Mathematical modelling of the oxidation and dissolution of uranium carbide

James Spencer Shepherd

School of Chemical and Process Engineering

University of Leeds

Submitted in accordance with the requirements for the degree of

Doctor of Philosophy

15th October 2015

The candidate confirms that the work submitted is his/her own, except where work which has formed part of jointly authored publications has been included. The contribution of the candidate and the other authors to this work has been explicitly indicated below. The candidate confirms that appropriate credit has been given within the thesis where reference has been made to the work of others.

Chapter 4 includes work from the jointly authored publication, "Mathematical modelling of the pre-oxidation of a uranium carbide fuel pellet", by James S. Shepherd, Michael Fairweather, Peter J. Heggs and Bruce C. Hanson, published in *Computers & Chemical Engineering* and found at http://dx.doi.org/10.1016/j.compchemeng.2015.05.001. The contribution to this work by the candidate comprised researching the relevant literature, designing the model, writing the necessary software for the numerical solution and writing of the paper. The co-authors provided supervision and guidance throughout the process. This chapter also includes work from two publications in peer reviewed conference proceedings: "Mathematical modelling of the oxidation of uranium carbide fuel", and "Modelling of the oxidation of spent uranium carbide fuel", found in *Plutonium Futures: The Science 2014*, Vol. 33, pp. 317-319 and *ESCAPE 24*, Vol. 33, pp. 355-360, respectively. The contribution of the candidate to these publications is identical to the above.

Chapter 6 includes work from the jointly authored publication, "Mathematical model of the oxidation of a uranium carbide fuel pellet including an adherent product layer", by James S. Shepherd, Michael Fairweather, Bruce C. Hanson and Peter J. Heggs, submitted to *Applied Mathematical Modelling*. The contribution of the candidate is identical to the above.

Chapter 7 contains work from the jointly authored publication, "A two-dimensional, finite-difference model of the oxidation of a uranium carbide fuel pellet", by James S. Shepherd, Michael Fairweather, Bruce C. Hanson and Peter J. Heggs, accepted for publication in the AIP conference proceedings from *ICCMSE 2015* in Athens. Again, the work was completed by the candidate under the supervision of the co-authors.

Acknowledgements

I would like to express my deep gratitude to my project supervisors, Professors Michael Fairweather, Peter Heggs and Bruce Hanson, for guiding me through what has been an extremely rewarding and educational three years. I came to the department as a somewhat confused physicist, and leave with the (quite possibly misplaced) confidence that I could now pass as a chemical engineer. I therefore am hugely thankful for their extraordinary combined expertise and dedication.

I would like to give particular mention to Peter, for patiently guiding me through the rather intimidating world of numerical solution by finite difference, and politely tolerating the multitude of questions that inevitably, and regularly, arose.

I would also like to thank the Chemical and Process Engineering department at the University of Leeds as a whole, for providing me with a reliable and comforting support network and a number of lasting friends.

Finally, my gratitude also extends to the ASGARD project (European Union 7th Framework Programme FP7-Fission-2011-2.3.1), for their generous funding of the research included in this thesis and also for the number of successful scientific collaborations it allowed me to enjoy.

Abstract

Uranium carbide is a candidate fuel for Generation IV nuclear fission reactors due to its higher thermal conductivity and metal atom density than its oxide fuel counterpart. However, in order for carbide fuels to be implemented, a reprocessing method must be devised to increase fuel efficiency and limit the volume of nuclear waste produced.

Currently, nuclear fuel is reprocessed by first dissolving it in nitric acid. However, when carbide fuel is dissolved in this way, organic compounds are formed in the resulting solution. These organics have been observed to complex the plutonium (IV) and uranium (VI) ions in the solution making their extraction from the solution for further processing significantly more difficult. Therefore, a method of removing the organic compounds, or preventing their formation, must be found.

Mathematical models have been constructed that simulate both the dissolution of a UC/(U, Pu)C pellet in nitric acid, and a pre-oxidative process that implements a conversion into UO_2 removing the possibility of organic formation. Models have been built by mathematically describing the physical processes, particularly heat and mass transfer, involved followed by a numerical solution generated using finite difference methods. Available literature was consulted for reaction coefficients and information on reaction products initially, with experimental data then used where possible to derive new coefficients and compare to the literature values. Further models were then produced through the modification of commercial code that uses the Lattice Boltzmann Method to calculate fluid flow around the pellet and consider batch processes.

The completed models assist in characterising the proposed reprocessing method for carbide fuels by predicting reaction completion times under various initial conditions and therefore suggest the optimal oxidation and dissolution conditions. The result is a powerful tool for use by the nuclear industry in assessing the most feasible reprocessing method.

Contents

List of Figures

List of Tables

Nomenclature

Letters	Description	Units
a	Pore size	m
A	Surface area	m^2
Bi	Biot number	
c_p	Specific heat capacity	$J\,kg^{-1}\,K^{-1}$
C	Concentration	$mol\,m^{-3}$
C^B	Concentration in the bulk gas	$mol\,m^{-3}$
C_p	Heat capacity	$J\,K^{-1}\,m^{-3}$
d_c	Cylindrical pellet diameter	m
d_e	Spherical pellet diameter	m
D	Diffusivity	$m^2\,s^{-1}$
$\bar{D}$	Chemical diffusivity	$m^2\,s^{-1}$
$\mathcal{D}_K$	Knudsen diffusivity	$m^2\,s^{-1}$
e	Velocity	$m\,s^{-1}$
e_{max}	Maximum fluid velocity	$m\,s^{-1}$
E_A	Activation energy	$J\,mol^{-1}$
g	Coefficient used in modelling the concentration of HNO_2	$mol\,s\,dm^{-3}$
G	Heat generated per unit volume	$W\,m^{-3}$
h	Heat transfer coefficient	$W\,m^{-2}\,K^{-1}$
$\bar{h}$	Averaged heat transfer coefficient across a surface	$W\,m^{-2}\,K^{-1}$
i	An integer representing the radial increment	
p	An integer representing the maximum value of i	
k_C	First order reaction coefficient with a maximum of k_1	$m\,s^{-1}$
k_d	Dissolution rate coefficient	$dm^3\,mol^{-1}\,s^{-1}$
k_g	External film diffusion coefficient	$m\,s^{-1}$
L	Length	m
m	Mass	kg
M	Molar mass	$kg\,mol^{-1}$

n	Number of moles	mol
Nu	Nusselt number	
Pr	Prandtl number	
r	Radius within solid	m
r_1	Radius of unreacted core	m
r_2	Radius of unreacted core and product layer (Ch: 6), or the internal radius of an annular pellet (Ch: 7)	m
R	Rate of consumption of a species by reaction	$\mathrm{mol\,s^{-1}}$
R^*	Rate of transfer across a film layer of a species	$\mathrm{mol\,s^{-1}}$
R_g	Gas constant	$\mathrm{J\,mol^{-1}\,K^{-1}}$
$\bar{R}_g$	Gas constant	$\mathrm{m^3\,atm\,mol^{-1}\,K^{-1}}$
Re	Reynolds number	
Sc	Schmidt number	
Sh	Sherwood number	
t	Time passed since reaction started	s
T	Temperature	K
T_A	Ambient temperature	K
T_0	Initial solution temperature	K
$\bar{T}$	Average temperature	K
u_1, u_2, u_3	Solutions at increment sizes of h_1, h_2 and h_3 respectively	
u	Estimated solution using an infinitely small increment size	
U	Thermal transmittance	$\mathrm{W\,m^{-2}\,K^{-1}}$
V	Volume	$\mathrm{m^3}$
$\dot{V}_{in}$	Inlet volumetric flow rate	$\mathrm{m^3\,s^{-1}}$
$\dot{V}_{out}$	Outlet volumetric flow rate	$\mathrm{m^3\,s^{-1}}$
x_1	Half the length of the cylindrical carbide pellet in Ch. 7, and carbide powder height in Ch. 6	m
x_2	Total powder bed height	m

Greek Letters

α	Thermal diffusivity	$\mathrm{m^2\,s^{-1}}$
ΔH	Enthalpy of a reaction	$\mathrm{J\,mol^{-1}}$
ϵ	Emissivity	
Ω	Collision integral in bulk diffusion calculation	
λ	Thermal conductivity	$\mathrm{W\,m^{-1}\,K^{-1}}$
μ	Fluid dynamic viscosity	$\mathrm{kg\,m^{-1}\,s^{-1}}$

Ψ	A correction factor necessary to compensate for surface area inaccuracies when generating rounded structures from cubic voxels	
ρ	Density	$\mathrm{kg\,m^{-3}}$
$\dot{\rho}$	Molar density	$\mathrm{mol\,m^{-3}}$
σ	Stefan Boltzmann constant	$\mathrm{W\,m^{-2}\,K^{-1}}$
σ_D	Constant in the Lennard Jones potential energy function	Å
τ	Thermal time constant	s
θ	Dissolution time constant	$\mathrm{s^{-1}}$

Subscripts

CO	Carbon monoxide
d	Refers to a property of the overall domain in DigiPac$^{\mathrm{TM}}$
$fluid$	Oxidising fluid surrounding the pellet
g	Refers either to O_2 or CO
in	Designates effects on the internal radius of an annular cylinder
N	Refers either to HNO_2 or NO_3^-
HNO_3	Nitrous acid
HNO_3	Nitric acid
m	Represents either UC or UO_2 depending on the region under consideration
$plate$	Refers to a property of the heating plate
r	Denotes a 2D variable active in the radial direction
s	Refers to a property of the solid
ss	Stainless steel
UC	Uranium carbide
UO_2	Uranium dioxide
U_3O_8	Triuranium octoxide
x	Denotes a 2D variable active in the a length direction

Superscripts

B	A property of the bulk gas
n	An integer designating the current time step

p	Exponent used in Richardson's deferred approach to the limit

Abbreviations

BNFL	British Nuclear Fuel Limited
CEA	Commissariat à l'Énergie Atomique et aux Énergies Alternatives
CFD	Computational fluid dynamics
CN	Crank-Nicolson
DEM	Discrete element method
FIB	Fully implicit bacwkard
LBM	Lattice Boltzmann method
LES	Large eddy simulation
MD	Molecular dynamics
NIOC	Non-identified organic compounds
NNL	National Nuclear Laboratory
NS	Navier-Stokes
ODEs	Ordinary differential equations
PDEs	Partial differential equations
PUREX	Plutonium uranium redox extraction
RANS	Reynolds averaged Navier-Stokes
SCM	Shrinking core model

Chapter 1

Introduction

1.1 Background and motivation for research

Over the coming few decades, the nuclear industry will begin construction of the fourth generation of nuclear reactors. One of the most important design specifications for these Generation IV reactors is that they are significantly more sustainable than their predecessors. For a nuclear reactor, sustainability is dependent on the efficiency of fuel use and, perhaps more importantly, effectively reprocessing the potentially dangerous waste so that a small a fraction as possible requires long-term storage. In other words, the nuclear fuel cycle must be closed.

The nuclear fuel cycle is a term used to describe the lifetime of nuclear fuels from extraction of uranium via mining to the storage of spent fuel. Figure 1.1 provides a brief overview of the cycle. Closing of the fuel cycle is one of the primary goals of the nuclear industry and entails complete recycling of fuel used in the reactor through the re-use of fissile uranium and plutonium found in the spent fuel. Currently, this is achieved to a lesser extent using MOX (mixed-oxide) fuel fabricated from spent oxide fuels. This project, however, focusses on the reprocessing of mixed (uranium/plutonium) and uranium carbide as candidate fuels for Generation IV reactors. It is therefore concerned with the back end of the fuel cycle for carbide fuels and attempting to ensure fissile material can be extracted from the spent fuel efficiently.

Carbide fuels are being considered as a potential fuel for Generation IV reactors because they possess a higher thermal conductivity (approximately 10 times

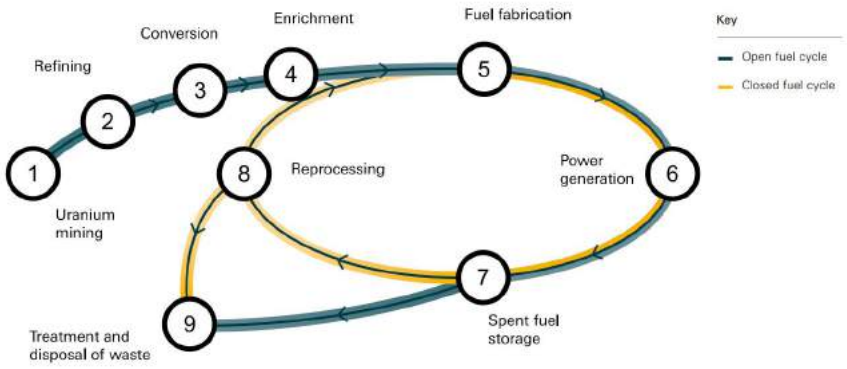

Figure 1.1: The nuclear fuel cycle (Royal Society, 2011).

that of the oxide counterpart, the current fuel of choice in most Generation III reactors) and undergo a smaller thermal expansion. Therefore, this allows reactors to be run at higher temperatures and increases flexibility in the fuel pin design. Another important characteristic of carbide fuels is their higher heavy metal density, hence their improved ability to produce plutonium upon fission an invaluable characteristic for any fuel used in a fast reactor.

Whilst the benefits of using carbide fuels are plain to see, there is currently no consensus on the reprocessing techniques that should be applied, posing a serious obstacle to their implementation. Ideally, they would be reprocessed in the same manner as oxide fuels to reduce the risk associated with novel methods and the need for new reprocessing plants. However, that is not without its complications.

The goal of reprocessing nuclear fuels is to attempt to extract as much of the unspent uranium, plutonium and minor actinides produced in the fission process from the irradiated fuel. It is also concerned with the separation and safe disposal of any volatile fission products and irradiated structural materials (fuel pellet cladding, for example). Therefore, providing a full, clear understanding of the reprocessing process is crucial to the efficiency and sustainability of a nuclear power plant utilising carbides, as well as making sure it is able to meet any emissions restrictions.

For oxide fuels the process is well developed, with most plants employing the PUREX (plutonium uranium redox extraction) process. Carbide fuels, however, present a unique problem when reprocessed in this way. Upon dissolution in nitric

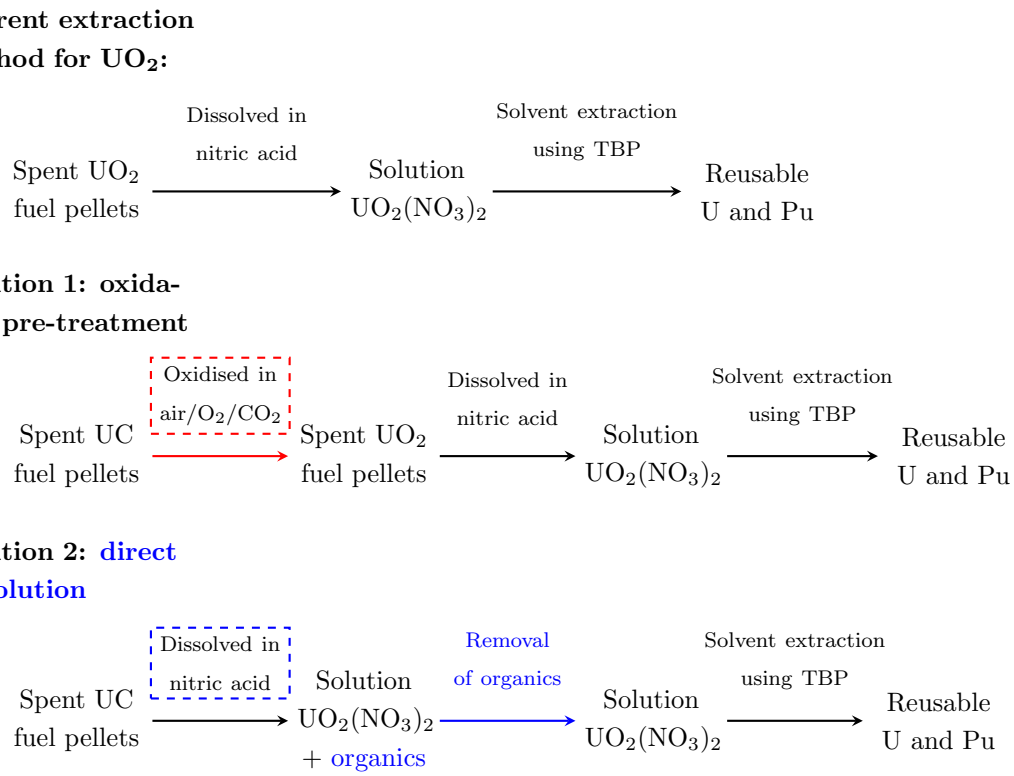

Figure 1.2: A simplified flow chart of the current method used to extract reusable U and Pu from spent oxide fuel, compared with two options for doing the same with carbide fuels.

acid, a standard head end step in oxide reprocessing, organic species are produced in the solution from the displaced carbon which greatly reduce the capability to extract uranium and plutonium. These organics are also expected to impede efficiency when the process is performed at an industrial scale, as they are likely to build-up on plant surfaces and reduce flow rates et cetera.

Solutions to the problem of organics can be divided into two different routes, as illustrated in Figure 1.2. The first is a pre-oxidative treatment, coloured in red, which entails oxidising the carbide fuel to an oxide fuel then reprocessing as a standard oxide fuel. The second, coloured in blue, is to carry out a direct dissolution in nitric acid as normal and then attempt to remove the organics from the solution via oxidative techniques. The processes outlined in dashed lines designate the two processes to be examined in this work. Neither process

has revealed itself to be the better as of yet, so helping to decide between the two is part of the scope of this project.

1.2 Aims and objectives

The aim of this project is to provide two mathematical models: the first is to model the oxidation of uranium carbide in air, and the second for its dissolution in nitric acid.

The oxidation model will specify the conditions necessary to keep the reaction within a specified safety envelope by predicting the temperature output of the reaction at different initial temperatures and reactant concentrations and quantities. It will also carry out the more general aims of predicting reaction rate, the time until complete oxidation and the composition of the reaction products. The dissolution model has similar aims, but the focus will be on the reaction products and how they are affected by the initial conditions of the dissolution, rather than the temperature output, which is less of a concern for dissolution. Both models will approximate the carbide fuel as a spherical pellet allowing the system to be considered one-dimensionally.

The models will start by bringing together information available in current literature, such as reaction kinetics for the reactions of uranium carbide with air and nitric acid. Mathematical methods will be used to calculate the heat and mass transfer to the reaction interface at the surface of the carbide pellet, as well as through the pellet in the case of heat transfer. These models will be constructed using novel software written in Fortran. Upon completion on a one-dimensional approximation of a fuel pellet as a sphere, the two dimensional case will be approached. This will allow the carbide fuel pellet to be modelled as an axisymmetric cylinder and will hopefully confirm the conclusions of the one dimensional models. It may also be necessary to produce an oxidation model considering UC in powdered form in order to compare the predictions against experimental data. The models will then be fitted to experimental data provided by the partners from the ASGARD programme, the CEA and the NNL, in order to derive new kinetics parameters and compare them to the existing values found in literature.

The models will then be furthered using commercial software to examine different aspects of the reactions. This will include using Lattice Boltzmann Method (LBM) software, DigiPac^{TM}, to examine the effects of fluid flow around the pellet on the oxidation. The source code used by DigiPac^{TM} has been made available, allowing its modification to make it more applicable to the cases involved in this project. Successful modification will allow the addition of oxidation kinetics and heat transfer through both the solid and the surrounding fluid to the code, which can then be used in conjunction with its packing algorithm to simulate batch pellet oxidations.

Such models would then be significantly more complex than the few available currently (assessment so far is that the two dimensional, simple models are already novel) and will be able to assist any future experimental work, hopefully allowing the suggestion of original improvements to the oxidation and dissolution methodologies.

1.3 Organisation of the thesis

The introduction and the literature review provided in Chapter 2 aim to introduce the reader to the subject and outline the current research available whilst stating what the goals of the thesis are. Chapter 3 then provides a summary of the methods used to achieve these goals. The remaining chapters, 4, 5, 6, 7 and 8, include the results produced from this work and some discussion of their significance. How these results chapters are structured is included as a flow chart in Figure 1.3. The conclusions and recommendations for future work on this subject can then be found in Chapter 9.

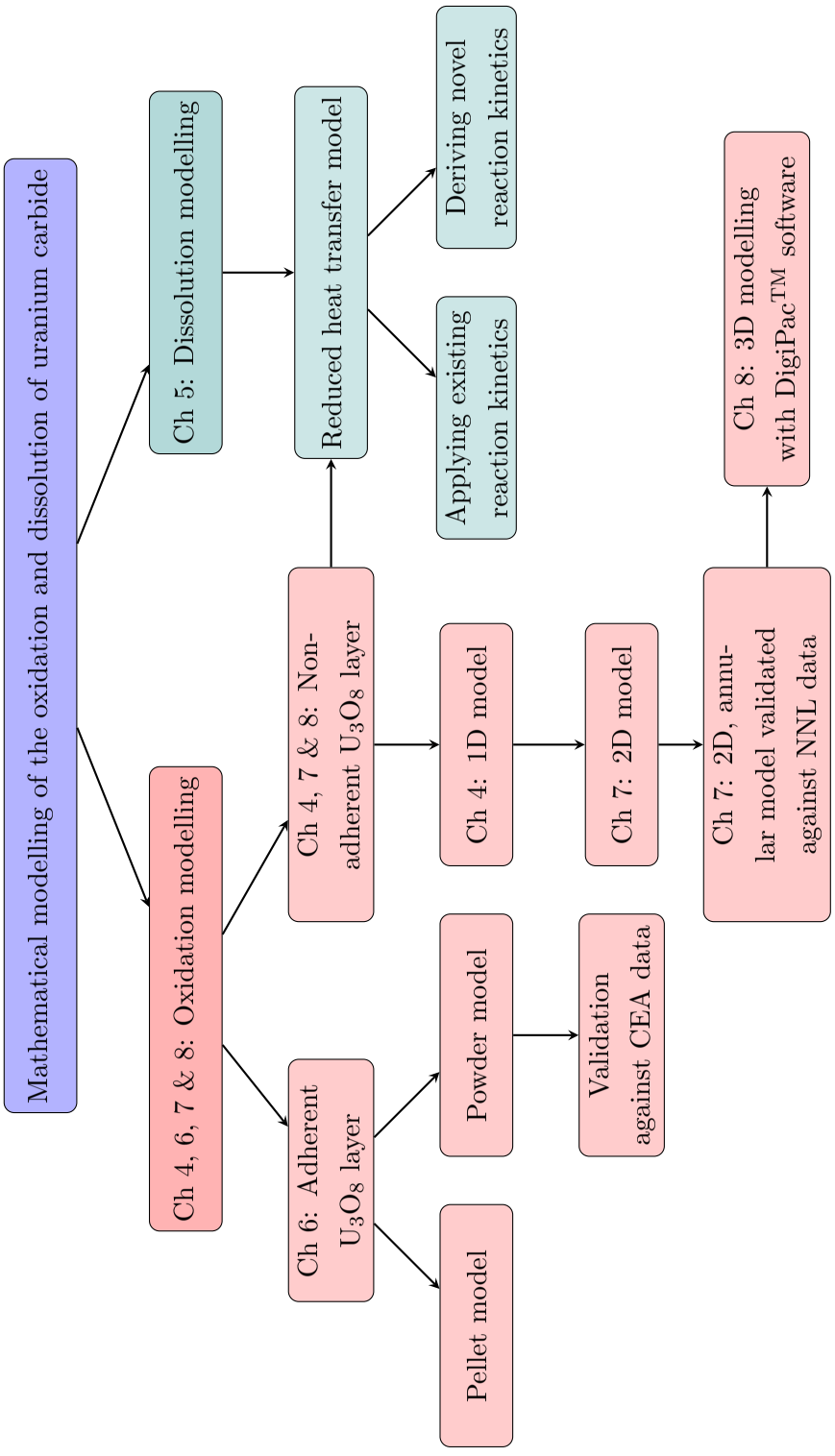

Figure 1.3: A flow chart outlining the general structure of this thesis.

Chapter 2

Literature review

2.1 Introduction

The aim of this chapter is to review and outline literature relevant to the present study, with additional focus on any similar models already in publication. Efforts have been made to collate as much experimental data as possible on the oxidation and dissolution of uranium carbide in order to gain a better understanding of the reactions. The kinetics and mechanism of each process are of particular interest from a modelling perspective, enabling reaction rates and products to be predicted. Also of significance is finding experiments that are able to validate, or at least provide a comparison for, the models produced in this investigation.

Firstly, however, the properties of uranium carbide itself will be briefly discussed.

2.2 Uranium carbide

Uranium monocarbide (UC) is an attractive fuel for Generation IV nuclear reactors on account of its higher thermal conductivity than oxide fuel (roughly $20\,\mathrm{W\,m^{-1}\,K^{-1}}$ for the carbide (De Coninck *et al.*, 1975) compared to $2\,\mathrm{W\,m^{-1}\,K^{-1}}$ for the oxide (Popov & Ivanov, 1957) at $1000°C$), and its higher metal atom density of $12.96\,\mathrm{Mg\,m^{-3}}$ resulting in it being more fissile (Gorlé *et al.*, 1974; Jones & Crosthwaite, 1973; Mazaudier *et al.*, 2010). Whilst it is now seeing a consider-

Table 2.1: Some of the properties of UC required to model its oxidation and dissolution found in literature. T is the temperature in Kelvin, and t the temperature in Celsius.

Property	Associated value	Source
Density ($\mathrm{kg\,m^{-3}}$)	$\rho_{UC} = 1.3630 \times 10^5$	(Rundle *et al.*, 1948)
Thermal conductivity ($\mathrm{W\,m^{-1}\,K^{-1}}$)	$\lambda_{UC} = 20.4 + 2.836 \times 10^{-6}(t - 570)$	(De Coninck *et al.*, 1975)
Spectral emissivity	$\epsilon_{UC} = 0.55 - 8.5 \times 10^{-5} t$	(De Coninck *et al.*, 1975)
Specific heat capacity ($\mathrm{W\,kg^{-1}\,K^{-1}}$)	$C_{p_{UC}} = 77.07 + 0.4883T - 4.907 \times 10^{-4}T^2 + 2.153 \times 10^{-7}T^3 - 3.220 \times 10^{-11}T^4$	(De Coninck *et al.*, 1975)

able resurgence in the volume of research towards its implementation, it has had limited use in the past with the only reactor to have used it thus far with any regularity being the Fast Breeder Test Reactor at Kalpakkam, India operating since 1985 (Ganguly *et al.*, 1986).

In order to simulate chemical processes involving UC fuel, some of it's properties must be defined in order to predict how it responds to physical phenomena, such as heat transfer, occurring during an oxidation or dissolution. Table 2.1 is a collection of the values of some of these properties extracted from literature that are of importance to the modelling process.

2.3 Difficulties associated with reprocessing uranium carbide

The purpose of this study is to examine ways in which the head end reprocessing, i.e. the early stages of the reprocessing cycle, of carbide fuels can be made viable. It is important, therefore, that the difficulties facing this process are summarised to provide the necessary context.

Firstly, the current reprocessing of oxide fuels will be outlined so that the difficulties specific to carbides can be pinpointed. The initial stage of uranium oxide reprocessing is the dissolution of spent fuel pellets in nitric acid. Upon completion of the dissolution, the insoluble fuel cladding is removed and the solution is fed forward for the extraction of fissile material (uranium and plutonium) for reuse. The extraction of uranium and plutonium is achieved by employing the PUREX process, which uses diluted tributyl phosphate (TBP) as an extractant (Ramanujam, 2001). The extracted material then undergoes further processing before being able to be reused as mixed oxide fuel.

Ideally, carbides would be reprocessed in the same manner so that current infrastructure and knowledge can be applied, making the introduction of carbides both easier and more cost effective. The difficulty is, however, that upon dissolving carbide fuel in nitric acid soluble organics are formed in solution from the displaced carbon (Donaldson *et al.*, 1963; Ferris & Bradley, 1965; Grenthe *et al.*, 2010; Legand *et al.*, 2014; Pauson *et al.*, 1963). These organics then complex the U(VI) and Pu(IV) ions in the solution, resulting in their incomplete extraction (Nayak *et al.*, 1988) and hence significant and unacceptable losses of fissile material.

The organics formed are primarily oxalic and mellitic acid, as found by Ferris and Bradley (Ferris & Bradley, 1965). The results of their investigation of the dissolution of uranium carbide are displayed in Table 2.2, where it can be seen that generally less than 50% of the carbon remains in solution as organics.

The amount of carbon remaining in the solution is disputed. Donaldson *et al.* (Donaldson *et al.*, 1963) report that dissolving UC in 2 M to 12 M HNO_3 results in 33% of the carbide carbon being converted to CO_2 whilst the remainder remains in solution. Pauson *et al.* (Pauson *et al.*, 1963), in rough agreement, report around 30% of the carbon evolving as CO_2 after dissolution in 6 M HNO_3. Legand *et al.*, however, report that 50% of the carbon is released as CO_2, which is more in line with the findings of Ferris and Bradley (Legand *et al.*, 2014). The products of the dissolution reaction observed by Legand *et al.* are displayed in Figure 2.1.

The general trends appear to be that higher nitric acid concentrations reduce the amount of carbon remaining in solution, and hence mitigates the problem of complexation of the U and Pu ions to some extent. However, there is still a

Table 2.2: Carbon distribution following the dissolution of UC in HNO_3 (Ferris & Bradley, 1965).

HNO_3 conc. (M)	Temp. (°C)	Amount of carbon as organic products (% of original)			
		Total C	Oxalic acid	Mellitic acid	Unidentified
4	40	44	8.9	8.9	27
4	105	35	2.6	8.4	24
4	105	32	1.6	5.9	24
4	105	40	5.4	2.6	32
4	105	44	4.6	2.4	37
16	25	35	10.8	3.8	20
16	120	21	0.0	7.9	23
16	120	26	0.0	4.0	22

significant presence of soluble organics that requires removing from the solution before the Purex process can be applied. This leads to the two processes described in Section 1.1 and Figure 1.2: either pre-oxidise the carbide fuel pellet to an oxide pellet and reprocess as normal, or dissolve and find a method to remove the soluble organics.

2.4 Oxidation

In order to circumvent the formation of organics completely, it is possible to oxidise the carbide fuel to an oxide allowing it to be dissolved in nitric acid without problem. Oxidation can occur at high temperatures with air/O_2, steam, or CO_2. The reaction with air can be highly exothermic, particularly if the carbide is in powder form, with reports claiming that self-ignition, thermal runaway and pyrophoricity have been observed (Berthinier *et al.*, 2009; Le Guyadec *et al.*, 2009; Naito *et al.*, 1976). Therefore, any pre-oxidative methods will need a comprehensive description of the conditions required to maintain a controlled oxidation. Another consideration is to make sure that any volatile fission products released can be contained in the off-gas system.

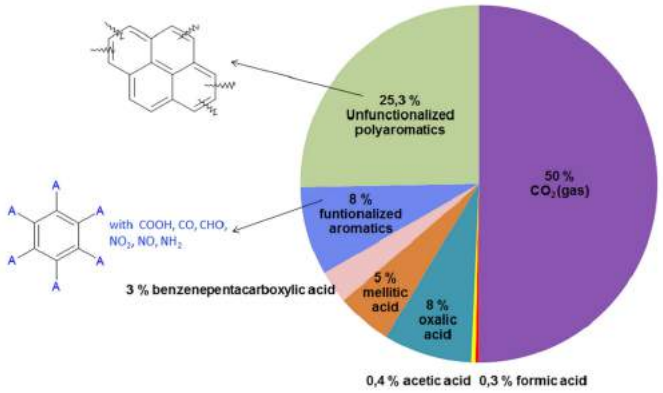

Figure 2.1: Mass balance of the produced carbon species by the dissolution of UC in HNO_3 (Legand *et al.*, 2014).

Figure 2.2 shows the possible steps involved in oxidative pre-treatment, as suggested by Fox and Maher (Fox & Maher, 2007). Initially, the pellet is placed in a kiln and oxidised by carbon dioxide, water or oxygen. Any volatile fission products are then captured by the direct off-gas system for safe removal. The carbide fuel, freshly converted to oxide fuel, is then dissolved in nitric acid as oxide fuel normally would be. The resulting solution is then centrifuged to remove the insoluble fission products and also the insoluble plutonium, which is then dissolved in a second dissolver and returned to the solution ready for solvent extraction.

This review will concentrate on the oxidation using air/O_2 as it seems the most viable option and the majority of the literature is focussed on it, but there will be a brief summary of the other methods. Before these reactions are considered in more detail, however, some theory on gas-solid reactions will be included.

2.4.1 Gas-solid reactions

A gas solid reaction is of the general form (Missen *et al.*, 1999):

$$A(g) + bB(s) \rightarrow \text{products}[(s),(g)] \tag{2.1}$$

where A and B are reactants and b is a stoichiometric coefficient.

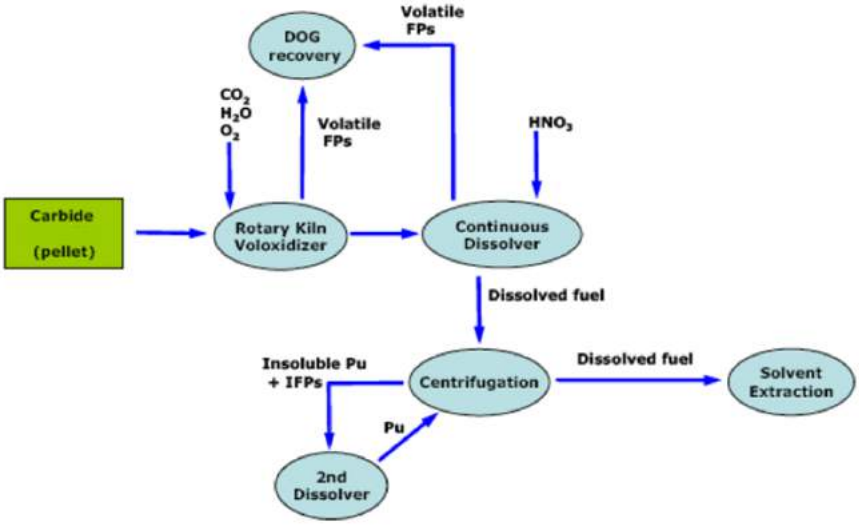

Figure 2.2: The possible steps involved in the pre-treatment of carbide fuel (Fox & Maher, 2007).

In order to consider the kinetics, the reactant solid is imagined as a single particle, B, reacting with an unlimited amount of gaseous species, A. The particle size is held constant, requiring the assumption that the solid product is of the same density as B.

The mass transfer involved in the reaction is dependent upon the porosity of the solid B and the solid product forming around it. If B is very porous, the reactant gas A faces no internal diffusional resistance and the reaction can be considered to be occurring uniformly throughout the pellet. If B and the product layer are moderately porous, then there is a concentration gradient of A from the surface of the solid to the centre. The reaction therefore occurs quickly at the surface and slower further into the pellet. The case that will be considered here however (due to the high theoretical density of the uranium carbide pellets that will be modelled) is when B has no porosity but the product layer does. In this case the reactant gas cannot penetrate the solid and the reaction must continue at the surface (Missen *et al.*, 1999).

In all three cases, however, there is mass transfer of A through an external gas film layer surrounding B from the bulk gas to the solid surface.

The kinetics for a gas-solid reaction where the solid is non-porous can be

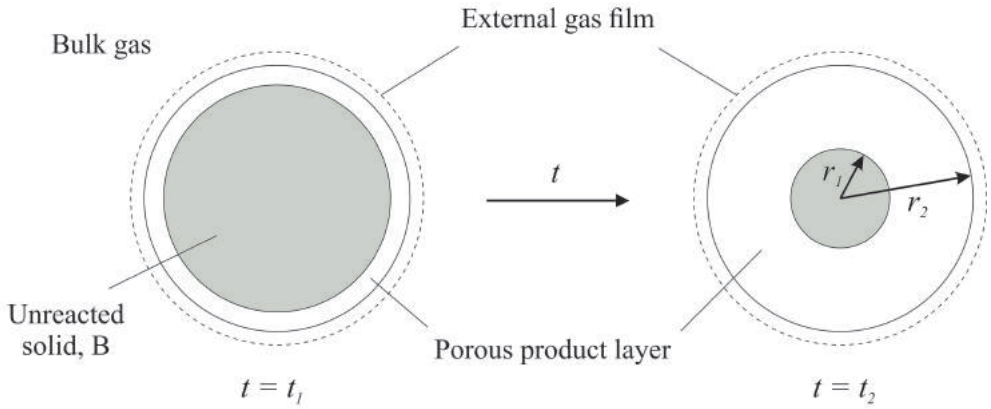

Figure 2.3: A diagram of the shrinking core model.

described by the shrinking core model (SCM) (Missen *et al.*, 1999), illustrated in Figure 2.3. Note that this is a shrinking core, constant particle size model (Safari *et al.*, 2009), assuming that the overall particle volume remains constant. Other assumptions usually present in a SCM are:

- The unreacted core remains spherical, enabling a one-dimensional approximation of the system along its radius.
- The product layer is adherent and porous.
- The solid-gas reaction is only occurring at the surface of the solid particle.

. The first step in the reaction kinetics is the external mass transfer of the reactant gas across the gas film layer surrounding the solid surface. Once on the solid surface, the gas then has to diffuse through the porous product layer (assuming the reaction has begun, as there may be no product initially) before reaching the solid surface to begin the surface reaction. The unsteady state diffusion of gas A through the product layer can be given as (Missen *et al.*, 1999):

For $r_1 \leq r \leq r_2$:

$$\frac{\partial C_A}{\partial t} = D_e \left(\frac{\partial^2 C_A}{\partial r^2} + \frac{2}{r} \frac{\partial C_A}{\partial r} \right) \tag{2.2}$$

where r_1 is the radius of the unreacted solid, B, r_2 is the external radius of the whole solid, D_e is the effective diffusivity of A through the porous product layer and C_A is the concentration of A.

The mass flux gas A through the external film layer can be considered as the outer boundary condition for Eq. 2.2 (Missen *et al.*, 1999).

For $r = r_2$:

$$D_e \frac{\partial C_A}{\partial r} = k_{g_A} \left(C_A^B - C_A|_{r_2} \right) \tag{2.3}$$

where k_{g_A} is the mass transfer coefficient for A diffusing through the film layer, C_B^A is the concentration of A in the bulk gas and $C_A|_{r_2}$ is the concentration of A at the solid surface.

Eqs. 2.2 and 2.3 describe the transfer of A from the bulk gas to the reaction interface on the surface of B. Once A reaches B, the surface reaction can proceed. Assuming that the reaction is first order, it can be written as:

$$R_A = -k_{s_A} A_S \, C_A|_{r_1} \tag{2.4}$$

where R_A is the rate at which A is consumed, k_{s_A} is the rate coefficient for the surface reaction, A_S is the surface area and $C_A|_{r_1}$ is the concentration of A at the reaction interface (the surface of B).

Eq. 2.4 can then be used as the inner boundary condition for Eq. 2.2 to describe how A is used up at the reaction interface:

For $r = r_1$:

$$D_e \frac{\partial C_A}{\partial t} = k_{s_A} \, C_A|_{r_1} \tag{2.5}$$

Eqs. 2.2, 2.3 and 2.5, therefore, describe the mass transfer of a reactant gas to the surface of the solid with which it reacts. Eq. 2.4 then describes the surface reaction occurring between the solid and the gas. The solid product from the reaction forms a porous layer around the solid reactant and any gaseous products diffuse out through it and the gas film layer. The diffusing gas products may form an extra barrier to the oxygen diffusing toward the solid. This can be accounted for in the diffusion coefficient, D_e (Smith, 1970).

Some specific examples of oxidation SCMs, investigating both UC and more general models, are included in Section 2.4.6 .

Table 2.3: The ignition temperatures of some different carbide materials (Sowden *et al.*, 1964).

Source of carbide	Physical treatment of UC	Carbon content (wt%)	Surface area ($m^2\,g^{-1}$)	Ignition temperature (°C)
Oxide-C	Ball milled	4.78	1.8	0
Oxide-C	Hand ground	4.78	0.48	180
Oxide-C	As prepared	4.78	0.13	210
Arc melted	Hand ground	4.72	0.09	390
Arc melted	As prepared	4.72	0.022	600
Oxide-C	Ball milled and sintered to $13.2\,g\,cm^{-3}$	4.86	0.02	> 600

2.4.2 Oxidation in air/oxygen

As mentioned previously, UC is known to oxidise readily in air. A number of studies investigating the ignition temperature have been carried out (Dell & Wheeler, 1967; Ewart & Findlay, 1972; Naito *et al.*, 1976; Nawada *et al.*, 1989; Sowden *et al.*, 1964), with the suggestion that it can be as low as 0 °C (Sowden *et al.*, 1964). It is dependent on particle size and surface area, hence if the carbide is in powdered rather than pellet form it is more likely to ignite. Ignition temperatures depending on surface area and preparation of the carbide sample are presented in Table 2.3.

Dell and Wheeler provide a list of twelve factors that affect the initiation and propagation of the ignition of carbides, determined from a series of oxidations of small pieces and sintered powders of UC in oxygen (Dell & Wheeler, 1967):

1. The sintering temperature used in preparation of the specimen.
2. Oxygen partial pressure/concentration.
3. Gas flow rate. Too low and the reaction is oxygen starved, too high and there is too much convective cooling.

4. Mass and geometry of the sample, affecting the rates of convective and radiative heat loss.
5. Particle size.
6. Thermal conductivity of the solid. Lower conductivity increases propensity to ignite.
7. Texture of oxide product. Affects the mass transfer of oxygen to the unreacted carbide.
8. Thermal pretreatment. Prior heating in a vacuum may result in recrystallisation of a protective oxide layer.
9. Rate of heating.
10. Atmosphere of heating.
11. Abrasion of specimens. May increase the surface area of the specimen.
12. Age of specimen. Over time, the carbide may be exposed to atmospheric conditions that roughen its surface.

These factors will require consideration in any model constructed, and may provide ideas for parameters to be investigated when sensitivity studies are carried out.

The effects of varying some of these factors are shown in Tables 2.4 to 2.6, the results from a set of experiments conducted by Iyer *et al.* (Iyer *et al.*, 1990). The experimental set up comprised a UC or (U, Pu)C pellet of approximately 350 g loaded into a crucible. Despite the main focus of this work being UC, the data pertaining to mixed carbides was included as it should exhibit similar trends. An oxygen/air mixture was passed over at a rate of $3\,\mathrm{ml\,min^{-1}}$.

The data displayed in Table 2.4 demonstrates the how increasing the partial pressure of oxygen increases the reaction rate. For these experiments, the temperature was 673 K and the theoretical density of the UC and (U, Pu)C pellets was $96 \pm 1\%$ and $90 \pm 1\%$ respectively. Note that the theoretical density in this

Table 2.4: Oxidation of UC and (U, Pu)C as a function of oxygen partial pressure (Iyer *et al.*, 1990).

Sample	pO_2 (kPa)	Time for 50% conversion (min)	Time for 75% conversion (min)	Time for 100% conversion (min)
UC	60.8	105	150	240
(U, Pu)C	25.3	180	350	600
(U, Pu)C	30.4	150	240	450
(U, Pu)C	40.5	120	200	380
(U, Pu)C	55.7	90	150	270
(U, Pu)C	60.8	70	110	200

case is the percentage of the density of solid uranium or mixed carbide. The lower the percentage suggests a higher pellet porosity.

Table 2.5 displays the effect of increasing the temperature on the oxidation rate of carbide fuels. For both uranium and mixed carbide fuels, a higher oxidation temperature leads to a higher reaction rate. The oxygen partial pressure was 60.8 kPa, and the theoretical density of the UC and (U, Pu)C pellets was again $96 \pm 1\%$ and $90 \pm 1\%$ respectively.

Table 2.6 displays a smaller number of experiments carried out to investigate the effect of the pellet's theoretical density. However, it is difficult to draw a conclusion of the effect that the density has due to there only being a single UC run, and the (U, Pu)C runs being carried out at different temperatures.

Berthinier *et al.* oxidised around 50 mg of UC powder in a cylindrical crucible in dry air. The sample was subjected to a heating ramp of $5\,^{\circ}\mathrm{C\,min^{-1}}$ up to 500 °C, but was stopped at different points in different experiments to examine the reaction products at that temperature via x-ray diffraction (Berthinier *et al.*, 2009). At around 120 °C on the heating ramp, the powder's temperature was observed to increase to ∼865 °C accompanied by the powder glowing and increasing in volume significantly. A second exothermic phenomenon was observed at around 375 °C, where the powder sparked and ejected some of itself from the crucible whist reaching 605 °C. On each run, the ignition temperature was noted,

Table 2.5: Oxidation of UC and (U, Pu)C as a function of temperature (Iyer *et al.*, 1990).

Sample	Temp. (K)	Time for 50% conversion (min)	Time for 75% conversion (min)	Time for 100% conversion (min)
UC	673	105	150	240
UC	723	80	125	195
(U, Pu)C	573	110	150	280
(U, Pu)C	623	95	135	220
(U, Pu)C	673	60	100	180
(U, Pu)C	723	50	80	140

Table 2.6: Oxidation of UC and (U, Pu)C as a function of theoretical density (Iyer *et al.*, 1990).

Sample	Density (%)	Temp. (K)	Time for 50% conversion (min)	Time for 75% conversion (min)	Time for 100% conversion (min)
UC	96	673	105	150	240
(U, Pu)C	90 ± 1	673	60	100	180
(U, Pu)C	85 ± 1	723	50	80	140

and the results are displayed in Table 2.7. The data displayed in Table 2.7 offer an interesting insight into the reaction mechanism of the oxidation of UC in O_2, and strongly suggest that the reaction products are dependent on the temperature at which the reaction is carried out.

Berthinier *et al.* also carried out an oxidation of UC at lower O_2 concentration, 3% volume O_2 in an N_2 atmosphere, to see if the ignition of the 1.5 g UC powder sample could be prevented or controlled (Berthinier *et al.*, 2009). Figure 2.4 is a plot of the temperature recorded by a thermocouple in the powder bed over time against the temperature of the heating plate on which the powder is positioned. The ignition can be observed to occur at approximately 120 °C

Table 2.7: Reaction products present after the oxidation of UC powder when the temperature ramp is stopped at different stages (Berthinier *et al.*, 2009). The emboldened phase forms the majority.

Shut down temperature (°C)	Ignition temperature (°C)	Phases present
170	none	**UC**
200	195	**UC**+U_3O_8+UO_{2+x}+U_3O_7
250	187	UC+**U_3O_8**+UO_{2+x}+U_3O_7
390	203	**U_3O_8**+UO_{2+x}+U_3O_7
430	170	**U_3O_8**
500	223	**U_3O_8**

causing a temperature rise in the powder of ∼100 °C, significantly lower than the oxidation in air. No ejection of powder from the crucible was observed (Berthinier *et al.*, 2009). The O_2 concentration is shown, therefore, to have a drastic effect on the ferocity of the oxidation of UC powder. As such it may be preferable from a safety perspective to carry out UC oxidations at low O_2 concentrations.

2.4.2.1 Reaction mechanism

Characterising the reaction mechanism that best fits the oxidation of uranium carbide in oxygen is an important step in understanding and modelling the reaction. Important considerations are the uranium oxides that are formed and what happens to the carbon released.

Mazaudier *et al.* carried out a short review on the oxidation of mixed carbides, and state that the oxidation products always consist of a finely divided powder made of two oxides: $(U, Pu)_{2+x}$ and $(U, Pu)_3O_8$ (Mazaudier *et al.*, 2010). The ratio of these oxides is dependent on the temperature and the availability of oxygen.

Although the Mazuadier work was concerned with mixed carbides, UO_2 and U_3O_8 are generally observed to be the oxide products for uranium carbides, with the UO_2 phase generally forming the intermediate step (Mukerjee *et al.*, 1994).

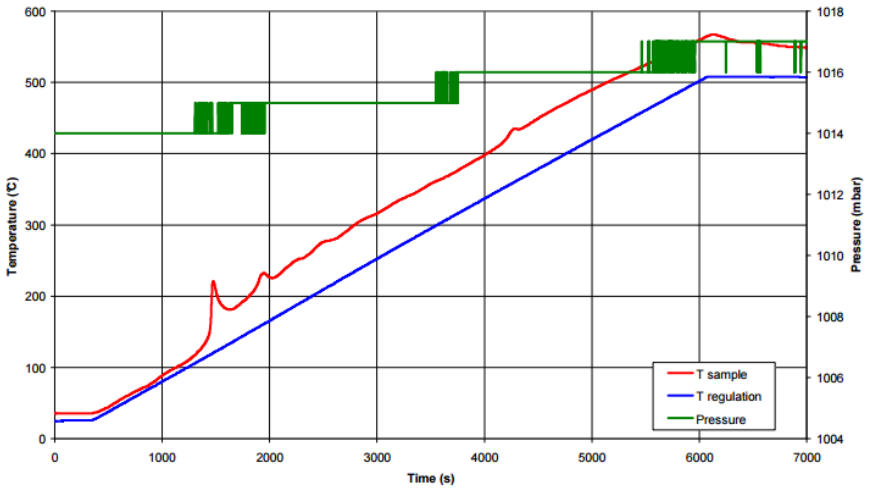

Figure 2.4: Measured powder temperature during oxidation under 3% O_2 in N_2 (Berthinier *et al.*, 2009).

Experiments carried out by Naito *et al.* on the oxidation of UC powder in varying oxygen partial pressures led to the conclusion that, at temperatures approximately 1200 °C and below, the reaction mechanism proceeds as follows (Naito *et al.*, 1976):

$$UC + (x/2)O_2 \rightarrow UC_{1-x}O_x + xC \tag{2.6}$$

$$UC_{1-x}O_x + (2 + x' - x)/2O_2 \rightarrow UO_{2+x} + (1 - x)C \tag{2.7}$$

$$C + O_2 \rightarrow CO_2 \tag{2.8}$$

$$UO_{2+x} + (2 - 3x' - z)/6O_2 \rightarrow (1/3)U_3O_8 \tag{2.9}$$

Eq. 2.6 is a partial oxidation of the carbide producing free carbon which is then itself oxidised in Eq. 2.8, producing CO_2. The part oxidised UC is then oxidised to UO_{2+x} in Eq. 2.7, which is then itself further oxidised to U_3O_8 in Eq. 2.9.

Similarly, Borchardt (Borchardt, 1959) reports that the oxidation proceeds through an intermediate oxide of UO_2, with U_3O_8 forming at temperatures above

$900°C$:

$$UC_x + (1 + x/8)\,O_2 \rightarrow UO_2 + (3x/4)C + (x/4)CO \quad (150 - 680\,°\mathrm{C}) \quad (2.10)$$

$$2C + O_2 \rightarrow 2CO \quad (680 - 900\,°\mathrm{C}) \quad (2.11)$$

$$3UO_2 + O_2 \rightarrow U_3O_8 \quad (900 - 970\,°\mathrm{C}) \quad (2.12)$$

Borchardt, in contrast to Naito *et al.*, states that the product of the carbon oxidation is CO rather than CO_2. In fact, it is possible that both cases are simplified and carbon is oxidised in a number of fashions. When examining a similar scenario, the oxidation of graphite fuels, Scott (Scott, 1966) claims that the following oxidations occur.

$$2C + O_2 \rightarrow 2CO \quad (2.13)$$

$$C + O_2 \rightarrow CO_2 \quad (2.14)$$

$$2CO + O_2 \rightarrow 2CO_2 \quad (2.15)$$

The implication is, therefore, that carbon present in the UC fuel can be oxidised either to CO or CO_2 (presumably depending on the temperature on local availability of oxygen), and is further oxidised to CO_2 eventually provided enough oxygen is available.

Whilst the reaction mechanisms published in literature differ slightly in a number of ways, the important aspects are that the UC is oxidised to U_3O_8 via the intermediate UO_2, and that the carbon is oxidised to CO_2 via CO. This is reflected by the simpler reaction mechanism proposed by Peakall and Antill (Peakall & Antill, 1962), who state that UO_2 is formed only as an intermediary with U_3O_8 formed at all temperatures within the range 350 °C to 1000 °C, in contrast to Borchardt. Note also that Berthnier *et al.* (Berthinier *et al.*, 2009) observed U_3O_8 as low as 250 °C.

$$3UC + 4O_2 \rightarrow U_3O_8 + 3C \quad (2.16)$$

$$C + O_2 \rightarrow CO_2 \quad (2.17)$$

The exact conditions at which each oxidation is able to occur is difficult to pin down due to often conflicting reports, but will be represented in the model by their respective activation energies.

Table 2.8: Standard heats of formation for some of the reactants and products present in the oxidation of UC.

Species	Standard heat of formation ($kJ\,mol^{-1}$)	Source
UC	-97.49 ± 3.8, -87.86 ± 4.18	(Storms & Huber Jr, 1967), (Farr *et al.*, 1959)
UO_2	-1085.1 ± 2.5	(Johnson & Steele, 1981)
U_3O_8	-3583.6	(Popov & Ivanov, 1957)

2.4.2.2 Exothermicity and activation energy

Given that the thermal output of the oxidation reaction is of concern, characterising the reaction enthalpy, ΔH_R, is important in calculating how much heat is released by the oxidation. Equally as important is a value for the activation energy of the reaction, which essentially controls the temperature at which the reaction rate becomes significant.

The reaction enthalpy is dependent on the reaction being considered, specifically the reactants and products involved. These can be calculated individually using the standard heats of formation for the species involved, the less commonly known of which are found in Table 2.8.

Activation energies for the oxidation can be found in the literature. Naito *et al.* (Naito *et al.*, 1976) found that the activation energy varied within in different regions of temperature. The specific values are displayed in Table 2.9.

Mukerjee *et al.* (Mukerjee *et al.*, 1994) calculated the activation energies of a number of different oxidations at oxygen partial pressures of 1-20 kPa, finding that the activation energy was between 92.0-117.5 $kJ\,mol^{-1}$. The difference in activation energy was due to different mechanisms. For example, at low oxygen partial pressures (1-5 kPa) the reaction was diffusion controlled, while at high partial pressures (20 kPa) the reaction is surface controlled.

Peakall and Antill (Peakall & Antill, 1962) use an Arrhenius plot of the reaction rates of O_2 with UC at different temperatures to calculate an activation energy. The experiments are carried out at temperatures of 350 °C to 1000 °C,

Table 2.9: Activation energies for the oxidation of UC in air found in literature and the temperature ranges in which they were reported.

Activation energy ($kJ\,mol^{-1}$)	Temperature range (°C)	Oxygen partial pressure (atm)	Source
6.7	< 800	7.0×10^{-4}–1.1×10^{-3}	(Naito *et al.*, 1976)
20.5	$800 - 1200$	7.0×10^{-4}–1.1×10^{-3}	(Naito *et al.*, 1976)
96	> 1200	7.0×10^{-4}–1.1×10^{-3}	(Naito *et al.*, 1976)
106.6	673 and 723	9.9×10^{-3}–2.0×10^{-1}	(Mukerjee *et al.*, 1994)
104.6 ± 16.7	350 - 550	1.0	(Peakall & Antill, 1962)

however the calculation is taken from the temperature range 350 °C to 550 °C. All experiments were carried out in 1 atm of O_2.

2.4.3 Oxidation in steam

At temperatures greater than 100 °C, water can be used to oxidise UC and (U, Pu)C (Flanary *et al.*, 1964, 1965) to give hydrated uranium oxides, hydrocarbons and hydrogen. Fragmented, 5 g samples of UC took 1 h to completely oxidise at 750 °C, 3 h at 700 °C and over 6 h at 650 °C (Flanary *et al.*, 1964). Only trace amounts of U_3O_8 were reported, with the reaction mechanism suggested to be as follows (Flanary *et al.*, 1964):

$$UC + H_2O \rightarrow UO_2 + C + 2H_2 \tag{2.18}$$

$$C + H_20 \rightarrow CO + H_2 \tag{2.19}$$

$$C + 2H_2O \rightarrow CO_2 + 2H_2 \tag{2.20}$$

The production of hydrogen means the reaction would need careful control. Flanary *et al.* (Flanary *et al.*, 1964) report that the reactor used was purged with nitrogen to eliminate air preventing a hydrogen-oxygen explosion.

2.4.4 Oxidation in carbon dioxide

Oxidation of carbide fuel in carbon dioxide is advantageous due to the reaction producing less heat than oxidation in oxygen (Huwyler & Bischoff, 1980). The calculated enthalpy of reaction for the oxidation in CO_2 is approximately $\Delta H = -250\,\mathrm{kJ\,mol^{-1}}$ whilst for the oxidation is O_2 it is approximately $\Delta H = -1360\,\mathrm{kJ\,mol^{-1}}$.

Oxidation in CO_2 forms UO_2 as the oxide product as opposed to U_3O_8 (Huwyler & Bischoff, 1980; Peakall & Antill, 1962). The reaction proceeds according to the mechanism below, found by both Murbach and Turner (Murbach & Turner, 1962) and Peakall and Antill (Peakall & Antill, 1962).

$$UC + 2CO_2 \rightarrow UO_2 + C + 2CO \tag{2.21}$$

$$CO_2 + C \rightarrow 2CO \tag{2.22}$$

Murbach and Turner report that Eq. 2.21 begins at 350 °C, and that the reduction of CO_2 in Eq. 2.22 occurs above 670 °C. Peakall and Antill (Peakall & Antill, 1962) report that this reduction of CO_2/oxidation of C can occur at 500 °C.

Huwyler and Bischoff (Huwyler & Bischoff, 1980) conducted a series of oxidations on 10 g samples of powdered UC in CO_2. The UC initially had 6.67 %, the change in which was recorded to observed the oxidation completion. These results are displayed in Table 2.10, where it can be seen that a temperature of 800 °C is required for a low carbon content.

The activation energy of the oxidation is reported to be $64.9 \pm 6.3\,\mathrm{kJ\,mol^{-1}}$ for a high density UC sample ($\sim 1.17 \times 10^4\,\mathrm{kg\,m^{-3}}$), and $37.7 \pm 8.4\,\mathrm{kJ\,mol^{-1}}$ for a low density one ($\approx 1.27 \times 10^4\,\mathrm{kg\,m^{-3}}$) (Peakall & Antill, 1962).

2.4.5 Oxide product layer behaviour

An important aspect of the oxidation reaction is the behaviour of the uranium oxide product: specifically, whether or not it adheres to the surface of the reacting carbide. If it does, it provides a barrier to the transfer of gaseous reactants from the bulk gas to the surface of the reacting carbide, leading to the diffusion of

Table 2.10: The oxidation of UC powder in CO_2 (Huwyler & Bischoff, 1980).

No.	Temperature (°C)	CO_2 flow ($l\,h^{-1}$)	Time (h)	Carbon analysis (%)
1	500	20	5	6.37
2	800	20	5	0.53
3	800	20	5	1.05
4	800	50	5	3.54
5	800	50	6	0.33

oxygen (or another oxidant of choice) through the oxide layer becoming the rate limiting step (Berthinier *et al.*, 2013; Mazaudier *et al.*, 2010).

Unfortunately, given the importance of this phenomenon to predicting the rate of oxidation, literature is contradictory as to whether the product layer does adhere. Mazaudier *et al.* (Mazaudier *et al.*, 2010) oxidised both powdered and porous solid samples of mixed carbides in 10 % or 20 % oxygen between 500 °C and 700 °C, and noted that no protective oxide layer was observed on the samples. However, the formation of a protective oxide layer is observed by Berthinier *et al.* (Berthinier *et al.*, 2009, 2013) and Le Guyadec *et al.* (Le Guyadec *et al.*, 2009) when oxidising powdered samples of UC.

Mukerjee *et al.* reported that the formation of a protective oxide layer is dependent on the partial pressure of oxygen (Mukerjee *et al.*, 1994). From visual observation of the oxidation of UC microspheres (diameter $\sim 500\,\mu m$) in oxygen, the sample is seen to retain its spherical shape and result in a swollen sphere comprising U_3O_8 at oxygen partial pressures between 1 and 5 kPa. The retention of the spherical shape implies that the oxide product adhered to the carbide microsphere. At intermediate oxygen partial pressures of 10 kPa to 15 kPa, the powdered product separated from the sample due to disintegration of the adherent product after the fraction of UC oxidised became greater than 0.5. At 20 kPa oxygen partial pressure, the product separated after the fraction of UC oxidised reached 0.2. Figure 2.5 is a schematic provided by Mukerjee *et al.* of the different mechanical behaviour of the oxide (Mukerjee *et al.*, 1994).

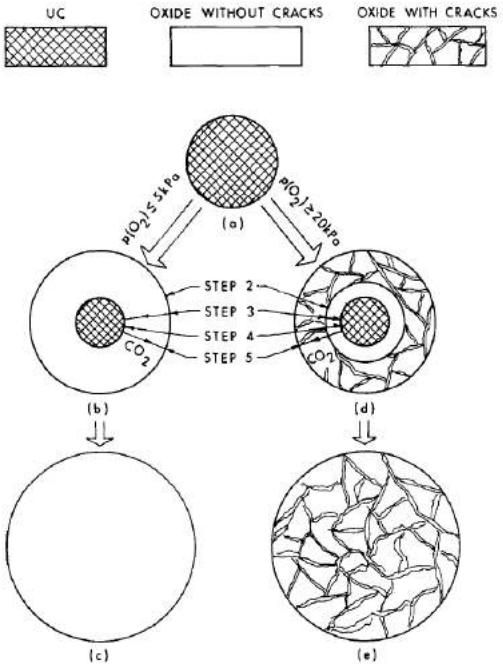

Figure 2.5: Schematic of the different routes for the oxidation of UC microspheres depending on O_2 partial pressure (Mukerjee *et al.*, 1994).

Note that 20 kPa is roughly equivalent to 20 % oxygen in air at 1 atm, the conditions used by Mazaudier *et al.* (Mazaudier *et al.*, 2010) assuming standard pressure was used, suggesting that there is agreement between the two experiments on no oxide layer forming at high oxygen concentrations. There is still a slight dispute however as Mukerjee *et al.* report the product layer adhering up until an oxidation fraction of 0.2 whilst one is never observed by Mazaudier *et al.*.

Due to literature reporting both the oxide product layer adhering and not adhering, it was decided that the models constructed in this investigation will take into account both the possibilities.

2.4.5.1 Diffusion of oxygen through the oxide layer

If the oxide product layer does adhere, diffusion of oxygen through it becomes the rate limiting step. Therefore, in order to predict the oxidation rate, a description of the rate of this diffusion is necessary.

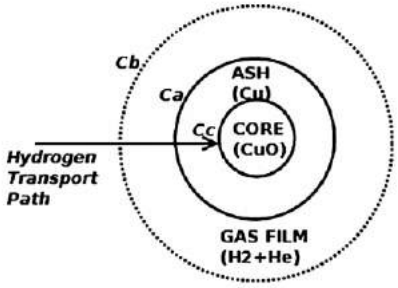

Figure 2.6: Schematic diagram of the SCM of CuO reduction by H_2 (Bhattacharyya *et al.*, 2015).

Berthinier *et al.*, during the oxidation of UC powder, note that it is the diffusion of O_2 through the intermediate oxide, UO_2, that is the rate limiting step (Berthinier *et al.*, 2013). A rate for the chemical diffusion of oxygen for stoichiometric UO_2 across the temperatures $300 < T < 2500\,\mathrm{K}$ is modelled and compared to existing literature to a good degree of agreement and provided below (Berthinier *et al.*, 2013):

$$log_{10}(\bar{D}_o) = -\frac{5596}{T} - 3.4391 \tag{2.23}$$

where $\bar{D}_o$ is the chemical diffusion coefficient of O_2 through UO_2 in $\mathrm{m^2\,s^{-1}}$ and T is the temperature in K.

2.4.6 Oxidation models

The following section will discuss SCMs present in open literature, relating firstly to metal particle oxidations and then specifically to UC oxidation.

2.4.6.1 Metal oxidation

SCM models, as described in Section 2.4.1 have been applied across a number of gas-solid particle reactions. For the scope of this work, metallic oxidations are of particular interest due to their closeness to UC oxidation. Examples of such SCMs will be presented in this section to provide an outline of what processes they are capable of simulating.

One such SCM found in open literature is presented by Bhattacharyya *et al.* (Bhattacharyya *et al.*, 2015), where copper oxide (CuO) pellets are reduced by hydrogen (H_2) in a hydrogen/helium mix. A schematic diagram of this process is included in Figure 2.6. The chemical reaction is given as:

$$CuO + H_2 \rightarrow Cu + H_2O \tag{2.24}$$

with an enthalpy of $\Delta H_{Cu} = -130.5\,\mathrm{kJ\,mol^{-1}}$.

In this case, the modelled particle comprises an unreacted core of CuO, and adherent layer of copper (Cu) metal. H_2 must therefore diffuse through this Cu layer to the reaction site at the surface of the unreacted core. The rate at which the reaction in Eq. 2.24 occurs is given as (Bhattacharyya *et al.*, 2015):

$$-R_{H_2} = \frac{k_r C_c^n}{r_1} \tag{2.25}$$

where R_{H_2} is the rate of the reduction reaction, $\mathrm{mol\,m^{-3}\,s^{-1}}$, k_r is the intrinsic surface rate constant, $\mathrm{mol^{0.4}\,m^{-0.2}\,s^{-1}}$, C_c^n is the H_2 concentration at the reaction site at a time n, $\mathrm{mol\,m^{-3}}$ and r_1 is the core radius, m. The surface rate constant, k_r, is given as (Bhattacharyya *et al.*, 2015):

$$k_r = 1.0 \times 10^{-4} exp\left(\frac{-33000}{8.314T}\right) \tag{2.26}$$

where T is the temperature in K.

The mass transfer of H_2 from the bulk gas has to account for three fluxes: external convective flux from the gas to the solid surface, diffusive flux through the Cu shell layer and consumption at the surface of the unreacted core. They are represented by Bhattacharyya *et al.* as (Bhattacharyya *et al.*, 2015):

$$M_1 = 4\pi r_2 k_g \left(C_b - C_a\right) \tag{2.27}$$

$$M_2 = \frac{4\pi r_1 D_e \left(C_a - C_c\right)}{\left(1 - r_1/r_2\right)} \tag{2.28}$$

$$M_3 = 4\pi r_1^2 k_r C_c^n \tag{2.29}$$

where M_1, M_2 and M_3 are the rates of film diffusion, Cu layer diffusion and surface reaction, respectively, $\mathrm{mol\,s^{-1}}$, r_2 is the particle radius, m, k_g is the external convective mass transfer coefficient, $\mathrm{m\,s^{-1}}$, C_a and C_b are the H_2 concentrations

at the particle surface and in the bulk gas respectively, $\mathrm{mol\,m^{-3}}$, and D_e is the effective diffusivity of H_2 through the porous Cu layer.

The convective mass transfer coefficient is calculated from a correlation for convective mass transfer to an external sphere (Bhattacharyya *et al.*, 2015):

$$\mathrm{Sh} = \frac{2k_g r_2}{D_{AB}} = 2 + 0.6\mathrm{Sc}^{0.33}\mathrm{Re}_p^{0.5} \tag{2.30}$$

where Sh is the dimensionless Sherwood number, D_{AB} is the diffusivity of H_2 through helium, $\mathrm{m^2\,s^{-1}}$, Sc is the dimensionless Schmidt number and $\mathrm{Re_p}$ is the dimensionless Reynolds number for the particle.

Bhattacharyya *et al.* (Bhattacharyya *et al.*, 2015) then assume that the system is in a pseudo steady state, such that $M_1 = M_2 = M_3$. This allows the concentration of H_2 at the unreacted core surface, C_c, to be expressed in terms of the bulk concentration, C_b, by eliminating C_a:

$$C_c + \frac{r_1 k_r C_c^n \left(1 - r_1/r_2\right)}{D_e} = C_b - \frac{r_1^2 k_r C_c^n}{r_2^2 k_g} \tag{2.31}$$

Therefore, for a given bulk H_2 concentration, temperature and particle size, a reaction rate and hence a rate of the CuO depletion can be calculated. Examples of this model's ability to predict reaction rates are included in Figure 2.7, where reaction profiles are included at different temperatures with 1.5% H_2 in the feed stream and a particle radius of 0.003 m.

Comparing Bhattacharyya *et al.*'s model to the general format of a SCM discussed in Section 2.4.1 illustrates the emphasis on defining the reaction kinetics specific to the case in question when constructing a novel SCM, as the structure of the model is largely the same. Another variable is whether to represent the mass transfer through the shell layer as a steady or unsteady state. Bhattacharyya *et al.*'s model is capable of predicting a rate of reaction at different temperatures using reaction kinetics in open literature. There is only a calculation of mass transfer, and no consideration of heat transfer and temperature released by the surface reaction which is significant in the UC oxidation.

Apart from being developed to simply simulate a process, SCMs can be used to estimate properties of the examined system, such as the diffusivity of the reactant through the adherent shell layer, if the necessary experimental data is

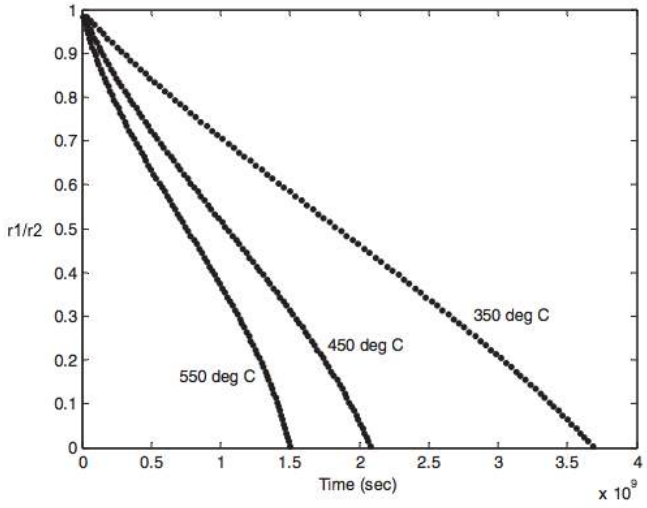

Figure 2.7: Reaction profiles of a CuO particle at different temperatures with 1.5% H_2 and a particle radius of 0.003 m (Bhattacharyya *et al.*, 2015).

provided. Zhao *et al.* (Zhao *et al.*, 2012) carried out such an investigation, using a SCM to estimate an effective diffusion coefficient of oxygen in magnesia-carbon (MgO-C) refractories. The two oxidative processes assumed to be occurring in Zhao *et al.*'s model are (Zhao *et al.*, 2012):

$$2C(s) + O_2(g) = 2CO(g) \tag{2.32}$$

$$C(s) + MgO(s) = CO(g) + Mg(g) \tag{2.33}$$

Zhao *et al.*'s investigation focuses on a cylindrical particle, but the one-dimensionality of the SCM is maintained by an oxidation resistant coating on the ends of the particles so that the oxidation processes only require consideration radially (Zhao *et al.*, 2012). Figure 2.8 illustrates the particle shape and the position of the coating used, and a schematic of the SCM used is included in Figure 2.9, which also presents a representation of the relative oxidant concentration levels through the system.

Zhao *et al.*'s model assumes that the same three mass transfer steps are occurring along the system's radius: external mass transfer from the bulk gas to the particle, diffusion in and out of the adherent, porous product layer and consumption by the reaction at the surface of the unreacted core (Zhao *et al.*, 2012).

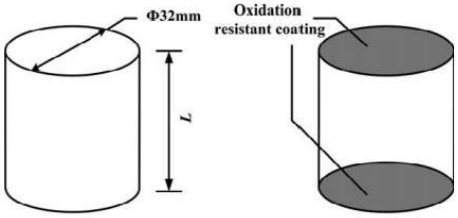

Figure 2.8: The shape of the particles oxidised (left) and the coverage of the oxidant resistant coating (right) (Zhao *et al.*, 2012).

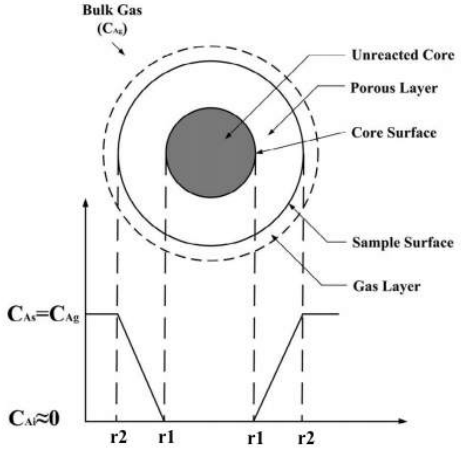

Figure 2.9: Diagram of the SCM for the oxidation of an MgO-C refractory (Zhao *et al.*, 2012).

It is assumed that due to their being a clear boundary between the unreacted core and the oxidised layer that the effective diffusivity, D_e, of O_2 through the layer is the rate determining step. This assumption allows the rate of diffusion of O_2 through the oxidised layer to be expressed as (Zhao *et al.*, 2012):

$$\frac{\mathrm{d}n_{O_2}}{\mathrm{d}t} = 2\pi r l D_e \frac{\mathrm{d}C_{O_2}}{\mathrm{d}r} \tag{2.34}$$

where n_{O_2} is the number of moles of O_2 in through the porous layer, mol, D_e is the effective diffusivity of O_2 through the layer, $\mathrm{cm^2\,s^{-1}}$, t is the time, s, r and l are the radius and length of the cylindrical particle respectively, m, and $\frac{\mathrm{d}C_{O_2}}{\mathrm{d}r}$ is the concentration gradient of O_2 along the radius, $\mathrm{mol\,cm^{-4}}$.

Integrating Eq. 2.34 along the radius between the surface of the unreacted core, r_1, and the particle surface, r_2, gives (Zhao *et al.*, 2012):

$$-\frac{\mathrm{d}n_{O_2}}{\mathrm{d}t} = \frac{2\pi l D_e \left(C_{O_2}|_{r_1} - C_{O_2}|_{r_2}\right)}{\ln r_1 - \ln r_2} \tag{2.35}$$

Zhao *et al.* then assume that if convection is present at the particle surface, the O_2 concentration at the surface is equivalent to the bulk concentration. Eq. 2.35 therefore becomes:

$$-\frac{\mathrm{d}n_{O_2}}{\mathrm{d}t} = \frac{2\pi l D_e C^B_{O_2}}{\ln r_1 - \ln r_2} \tag{2.36}$$

where $C_{O_2}^B$ is the bulk gas O_2 concentration, $\mathrm{mol\,cm^{-3}}$.

The effect that the oxidation reaction has on the O_2 concentration can be expressed as:

$$-\frac{\mathrm{d}n_{O_2}}{\mathrm{d}t} = \frac{4\pi r_1 l\rho\left(\theta_1 w_1 + \theta_2 w_2\right)}{M_C}\frac{\mathrm{d}r_1}{\mathrm{d}t} \tag{2.37}$$

where ρ is the appearance density of the sample, $\mathrm{g\,cm^{-3}}$, θ_1 and θ_2 are the weight percentages of graphite and phenolic resin, respectively, w_1 and w_2 are the carbon contents as a percentage of graphite and phenolic resin, respectively, and M_C is the mole mass of carbon, $\mathrm{g\,mol^{-1}}$.

Since diffusion through the product layer is assumed to be the rate limiting step, Eqs. 2.36 and 2.37 can be equated to give (Zhao *et al.*, 2012):

$$\frac{2\pi l D_e C_{O_2}^B}{\ln r_1 - \ln r_2} = \frac{4\pi r_1 l\rho\left(\theta_1 w_1 + \theta_2 w_2\right)}{M_C}\frac{\mathrm{d}r_1}{\mathrm{d}t} \tag{2.38}$$

Zhao *et al.* then manipulate Eq. 2.38 and integrate with respect to both time and radius, giving (Zhao *et al.*, 2012):

$$\frac{D_e M_C C_{O_2}^B}{2\rho\left(\theta_1 w_1 + \theta_2 w_2\right)}t = \frac{1}{2}r^2\left(\ln\frac{r}{r_2} - \frac{1}{2}\right) + \frac{1}{4}r_2^2 \tag{2.39}$$

Expressing the the oxidation rate of the cylindrical sample, x_B, as:

For $0 \leq x_B \leq 1$:

$$1 - x_B = \left(r/r_2\right)^2 \tag{2.40}$$

and the appearance density as:

$$\rho = \frac{m_0}{\pi r_2^2 l} \tag{2.41}$$

where m_0 is the initial particle mass, allows 2.39 to be expressed as (Zhao *et al.*, 2012):

$$\frac{2\pi l D_e M_C C_{O_2}^B}{m_0\left(\theta_1 w_1 + \theta_2 w_2\right)}t = (1 - x_B)\ln(1 - x_B) + x_B \tag{2.42}$$

Then, letting:

$$k = \frac{2\pi l M_C C_{O_2}^B}{m_0\left(\theta_1 w_1 + \theta_2 w_2\right)}D_e \tag{2.43}$$

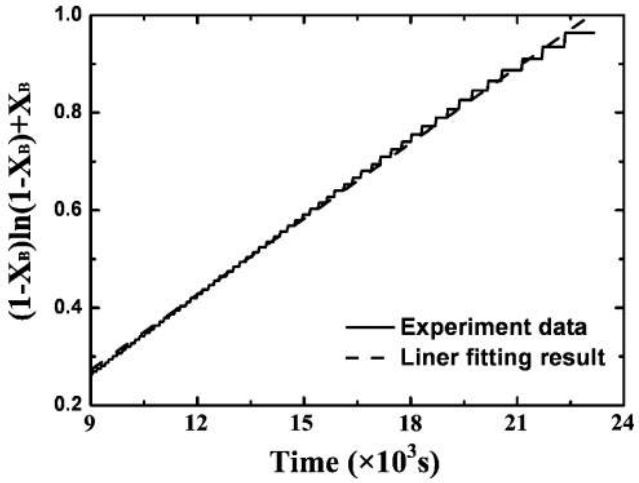

Figure 2.10: Fitted SCM model result and experimental measurement of $(1 - x_B)\ln(1 - x_B) + x_B$ versus time (Zhao *et al.*, 2012).

Table 2.11: Input parameters and the results for the calculation of the effective diffusion coefficient from Zhao *et al.*'s SCM (Zhao *et al.*, 2012).

Sample	k ($\times 10^{-5}$ s^{-1})	m_0 (g)	l (mm)	Start time ($\times 10^3$ s)	End time ($\times 10^3$ s)	D_e ($\times 10^{-1}$ $cm^2\,s^{-1}$)
Mg-1%	5.15	74.632	35.539	9	24	3.23
Mg-3%	5.47	74.724	35.925	9	24	3.55

gives:

$$kt = (1 - x_B)\ln(1 - x_B) + x_B \tag{2.44}$$

where k is the slope of $(1 - x_B)\ln(1 - x_B) + x_B$ versus time (Zhao *et al.*, 2012).

Therefore, fitting of the simulated slopes to experimental data allows a value for k, and hence D_e, to be derived. An example of such a fitting from Zhao *et al.*'s study is presented in Figure 2.10, and some derived diffusion coefficients are included in Table 2.11 (Zhao *et al.*, 2012).

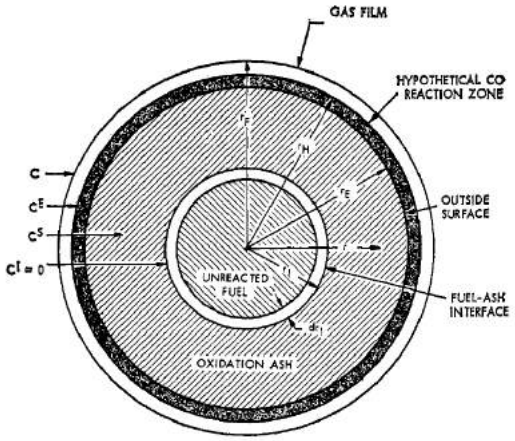

Figure 2.11: Scott's representation of a graphite fuel piece (Scott, 1966).

2.4.6.2 Uranium carbide oxidation

Only one existing model of the oxidation of UC in O_2 could be found in the literature by Scott (Scott, 1966). Scott published a model on the oxidation of graphite-uranium fuel spheres, assumed to be analogous to UC fuel spheres, in a fixed or moving bed in O_2. The model is roughly a SCM as illustrated in Figure 2.11, and begins by giving a first order reaction rate for the surface reaction between the oxygen and the graphite:

$$R_C = k_C A_{UC} C_{O_2} \tag{2.45}$$

where R_C is the rate of O_2 reaction with carbon to form CO in $\mathrm{gmol\,s^{-1}}$, A_{UC} is the area available for reaction in $\mathrm{cm^2}$, C_{O_2} is the O_2 partial pressure in the bulk gas in atm and k_C is the rate coefficient given as $20000exp(-21400/T)$ $\mathrm{gmol\,cm^{-2}\,s^{-1}\,atm^{-1}}$. From this Arrhenius expression for k_C, multiplying the value of -21400 by the ideal gas constant, R_g, gives an activation energy of $177.8\,\mathrm{kJ\,mol^{-1}}$ for the reaction.

The next effect considered is the external mass transport of the O_2 in the bulk gas to the external surface of the fuel sphere across a stagnant gas film. The rate of mass transport is expressed as:

$$R = k_g A_{UC} \left(C_{O_2} - C^B_{O_2} \right) \tag{2.46}$$

where R is the rate of O_2 transfer in $\mathrm{gmol\,s^{-1}}$, k_g is the external mass transfer constant in $\mathrm{gmol\,cm^{-2}\,s^{-1}\,atm^{-1}}$ and $C^B_{O_2}$ is the oxygen partial pressure in the bulk gas in atm. Note that the units for R and k_g are not specified by Scott and have been inferred from later comparison of the mass transfer rate, R, to the surface reaction rate, R_C, for which the units are provided.

Scott then describes the mass transfer of O_2 through the adherent product layer as Fickian diffusion:

$$\frac{\partial C^S_{O_2}}{\partial t} = D_E \Delta^2 C^S_{O_2} \tag{2.47}$$

where $C^S_{O_2}$ is the oxygen concentration within the solid oxidation ash, as can be seen in Figure 2.11, and D_E is the effective diffusivity in $\mathrm{cm^2\,s^{-1}}$.

For any small increment of time the diffusional process can be steady state. Coupling this with the assumption that the fuel pellet is spherical Scott reduces Eq. 2.47 to:

$$\frac{\partial}{\partial r}\left(r^2 \frac{\partial C^S_{O_2}}{\partial r}\right) = 0 \tag{2.48}$$

where r represents the radial position within the sphere in cm.

The following boundary conditions that assume the surface reaction rate is irreversible and unimportant to the overall reaction rate (i.e. that it is relatively fast compared to the mass transfer) are then stated:

$$\text{For } r = r_E: \qquad C^S_{O_2} = C^E_{O_2} \tag{2.49}$$

$$\text{For } r = r_I: \qquad C^S_{O_2} = 0 \tag{2.50}$$

where r_E is the external radius and r_I the radius of the reaction interface.

These boundary conditions can then be used to solve Eq. 2.48 for $C^S_{O_2}$:

$$C^S_{O_2} = \frac{r_E C^E_{O_2}\,(r - r_I)}{r\,(r_E - r_I)} \tag{2.51}$$

Then, Scott equates the reaction rate of oxygen with carbon to the rate of O_2 diffusing to the reaction surface:

$$R_C = -4\pi r_I^2 \alpha D \left(\frac{\partial C^S_{O_2}}{\partial r}\right)_{r=r_I} \tag{2.52}$$

where α is the effective porosity of the solid phase and D the molecular diffusivity of O_2.

The partial derivative of $C^S_{O_2}$ can then be evaluated at the reaction interface to give:

$$\left(\frac{\partial C^S_{O_2}}{\partial r}\right)_{r=r_I} = \frac{r_E C^E_{O_2}}{r_I\,(r_E - r_I)} \tag{2.53}$$

which, when substituted into Eq. 2.52, gives the oxidation rate limited by internal diffusion:

$$R_C = \frac{4\pi r_E \alpha D r_I C^E_{O_2}}{(r_E - r_I)} \tag{2.54}$$

Using the above reaction rate, Scott was then able to describe the shrinking radius of the UC sphere, and hence the reaction completion time, through the following equation:

$$\frac{\mathrm{d}r_I}{\mathrm{d}t} = -\frac{R_C}{A_{UC}\dot{\rho}_{UC}} \tag{2.55}$$

where $\dot{\rho}_{UC}$ is the molar density of the UC pellet in $\mathrm{g\,gmol^{-1}}$. The factor of 2 is included to represent the stoichiometry of the reaction equation, $2C + O_2 \rightarrow 2CO$, as R_C is the rate of O_2 consumption rather than UC.

Note that these equations are one dimensional considering only spherical pellets. The models produced may require elaboration on Scott's work to model a 2D system that allows the pellet to be considered as a cylinder rather than a sphere; a shape more common in current fuel pellets.

Scott assumes that the surface reaction rate will be irrelevant once external diffusion is considered making the external diffusion the controlling factor. This may be the case, as mentioned in Section 2.4.5, however the surface reaction rate may still have a small effect on the overall rate, especially at the beginning of the oxidation prior to the oxide layer reaching a significant thickness. External diffusion, and hence a dependence on k_g, are also not included in this model.

The models constructed in this work will aim to calculate the actual O_2 distribution through the porous oxide layer instead of applying the boundary conditions in Eqs 2.49 and 2.50. They also will not separate the reaction rates based on internal and external diffusion, but combine them into one system.

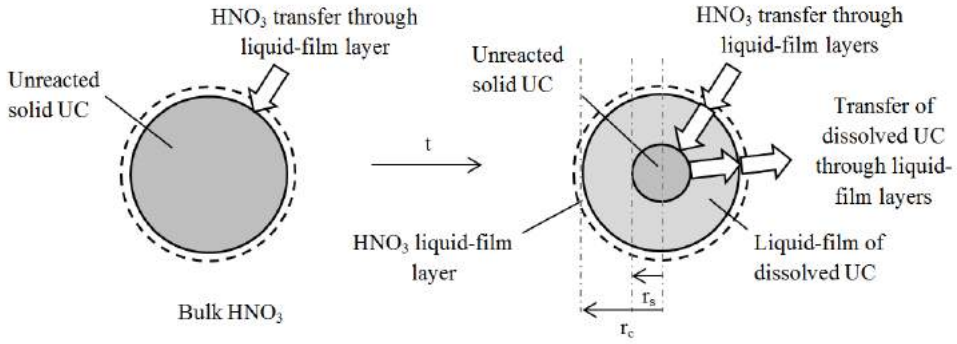

Figure 2.12: A diagram of the dissolution of a UC sphere in HNO_3.

The secondary oxidation of CO to CO_2 in the bulk gas and the effects it has on the bulk gas composition and temperature will also be considered.

2.5 Dissolution

Rather than pre-oxidising the spent UC fuel to its oxide form, another possibility is to dissolve the pellet in nitric acid and then remove the soluble organics from the solution. This section of the literature review will consider the dissolution process itself in line with what is to be modelled. Methods of removing the organics from the solution will be discussed briefly, however.

Similarly to the review of oxidative methods, a brief discussion of the theory of liquid-solid reactions is included.

2.5.1 Liquid-solid and solid dissolution reactions

The reaction between any fluid and a solid is generally dependent on mass transfer (Fogler, 1999). In the case of a solid dissolving in a liquid, there are a number of mass transfer processes that must be considered.

At time $t \leq 0$, before the dissolution reaction has begun, the solid, UC in this case, is surrounded by an external liquid film layer as illustrated by the left side image in Figure 2.12. This layer presents the first region across which mass transfer occurs. In order for the dissolution to begin, HNO_3 molecules must

diffuse through this layer to reach the UC surface. Fick's 1st law can be used to calculate the flux of nitric acid across this external boundary in terms of the bulk HNO_3 concentration, $C^B_{HNO_3}$ (Fogler, 1999):

For $r = r_C$:

$$D_e \frac{\partial C_{HNO_3}}{\partial r} = k_g \left(C^B_{HNO_3} - C^S_{HNO_3} \right) \tag{2.56}$$

where r is the radial position in m, r_C is the radius of the solid and any dissolved UC present, C_{HNO_3} is the concentration of nitric acid in $\mathrm{mol\,m^{-3}}$, $C^S_{HNO_3}$ is the nitric acid concentration at the solid surface, D_e is the diffusivity of nitric acid through the film layer in $\mathrm{m^2\,s^{-1}}$ and k_g is the mass transfer coefficient across the film layer in $\mathrm{m\,s^{-1}}$.

Once the HNO_3 has reached the solid surface and adsorbed onto it, the surface reaction can begin. The reaction can be assumed to only occur at the surface, given that the theoretical density of the carbide pellets used in the remainder of the literature review is generally $> 95\,\%$ leaving little to no porosity. If the surface reaction kinetics are assumed to be first order with respect to both UC and HNO_3, it can be represented by the general reaction rate (Missen *et al.*, 1999):

For $r = r_S$:

$$R_C = k_d A C^S_{HNO_3} \tag{2.57}$$

where r_S is the radius of the solid surface, R_C is the rate of HNO_3 consumption at the surface in $\mathrm{mol\,s^{-1}}$, k_d is the surface reaction rate coefficient in $\mathrm{m\,s^{-1}}$ and A is the surface area of the solid in $\mathrm{m^2}$.

The surface reaction between UC and HNO_3 causes the UC to dissolve. The reaction products desorb from the solid surface and begin to diffuse away from the surface into the solution. The dissolved UC now surrounding the pellet, diffusing away from the pellet according to the concentration gradients, presents an extra barrier to the HNO_3 diffusing toward the solid surface (see Figure 2.12). The diffusion of HNO_3 through the layer of dissolved UC can be expressed using Fick's 2nd law, written as (Missen *et al.*, 1999):

For $r_S \leq r \leq r_C$:

$$\frac{\partial C_{HNO_3}}{\partial t} = D_e \left(\frac{\partial^2 C_{HNO_3}}{\partial r^2} + \frac{2}{r} \frac{\partial C_{HNO_3}}{\partial r} \right) \tag{2.58}$$

If Eq. 2.56 is taken to be the boundary condition for Eq. 2.58 at $r = r_C$, then the provision of a boundary condition at $r = r_S$ would provide a complete description of the mass transfer of HNO_3 to the solid surface. This can be done using the rate coefficient from Eq. 2.57, k_d, to account for the rate at which HNO_3 is being used up at the solid surface:

For $r = r_S$:

$$D_e \frac{\partial C_{HNO_3}}{\partial t} = k_d C^S_{HNO_3} \tag{2.59}$$

The solution of Eqs. 2.56, 2.58 and 2.59 would therefore provide the HNO_3 distribution from the bulk liquid to the solid surface, and hence allow a calculation of the dissolution rate.

2.5.2 Dissolution in nitric acid

This dissolution reaction of UC in HNO_3 was briefly discussed in Section 2.3 but with a focus on the carbon content remaining in the solution and the ramifications that had for the Purex process. This section will be more concerned with attaining a better understanding of the reaction kinetics and mechanism of the dissolution in order to model it accurately.

Ferris and Bradley (Ferris *et al.*, 1964) dissolved 1 g to 4 g UC samples at 90 °C in 2 M to 16 M HNO_3. They observed that the dissolution will not occur in dilute concentrations of HNO_3, 0.001 M to 0.5 M, but will proceed at concentrations greater than 1 M and proceeds rapidly between 2 M to 16 M. From visual observation, they concluded that the dissolution of the UC sample was complete when the gas evolved over time plot, Figure 2.13, changed abruptly. Further gas release beyond this point is due to oxidation of the soluble organics in the solution. The total dissolutions times at different HNO_3 concentrations are displayed in Table 2.12, and it can be observed that increasing the nitric acid concentration has a large effect on the reaction completion time.

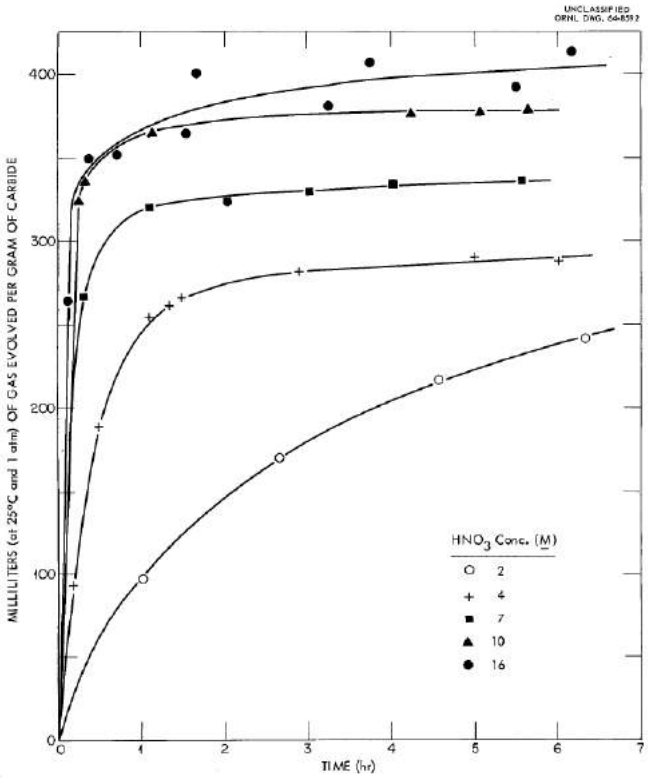

Figure 2.13: Gas evolution of the reactions of 1 g to 4 g specimens of UC with HNO_3 solutions at 90 °C carried out by Ferris and Bradley (Ferris *et al.*, 1964).

Table 2.12: The effect of HNO_3 concentration on the dissolution completion time at 90 °C (Ferris *et al.*, 1964).

HNO_3 conc. (M)	Dissolution time (h)
2	10
4	3
7	2
10	1.5

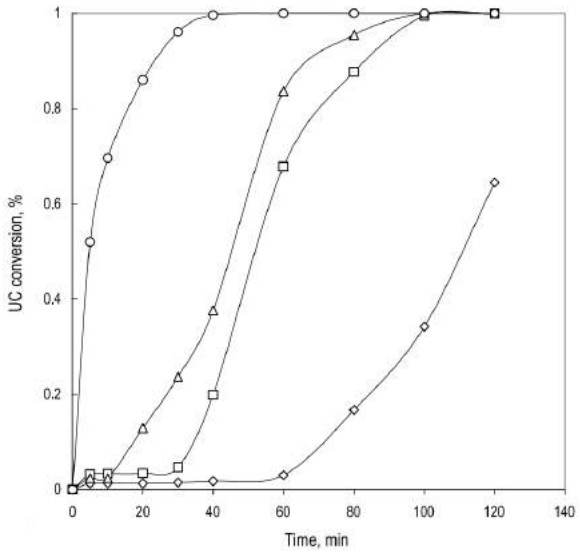

Figure 2.14: Dissolution curves of powdered, 1 g UC samples at different nitric acid concentrations (Maslennikov *et al.*, 2009). ◇ 2 M, □ 3 M, △ 4 M and ○ 6 M.

Maslennikov *et al.* (Maslennikov *et al.*, 2009) dissolved ∼1 g samples of powdered UC in 2 M to 6 M HNO_3 at 22 °C. It was found that the production of nitrous acid (HNO_2) by the reaction in Eq. 2.60 catalyses the dissolution increasing the rate rapidly.

$$UC \xrightarrow{NO_3^-, k_{NO_3^-}} U(VI) + NIOC + CO_2 + HNO_2 \tag{2.60}$$

where $NIOC$ represents non-identified organic compounds and $k_{NO_3^-}$ is a rate constant for the dissolution of UC by HNO_3.

The catalysis by HNO_2 leads to induction periods and S-shaped curves at lower nitric acid concentrations ($\leq$ 4 M), as illustrated in Figure 2.14, due to the reaction not accelerating until a significant quantity of HNO_2 is produced in the solution (Maslennikov *et al.*, 2009). Figure 2.15 is a plot of the HNO_2 concentration over time at different HNO_3 concentrations, that when combined with Figure 2.14, helps to confirm this suggestion.

The dissolutions carried out by Maslennikov *et al.* appear to happen a lot faster than those by Ferris and Bradley (Ferris *et al.*, 1964), despite the lower

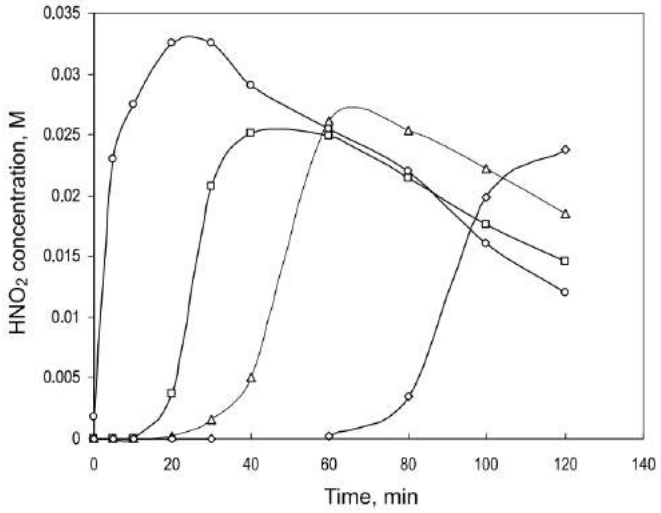

Figure 2.15: Production curves of HNO_2 at different initial nitric acid concentrations (Maslennikov *et al.*, 2009). ◇ 2 M, □ 3 M, △ 4 M and ○ 6 M.

HNO_3 concentrations and the significantly lower temperature. This may be because Maslennikov uses a powdered UC sample. However, it is not clear what form the UC sample used by Ferris and Bradley is in to confirm this.

2.5.2.1 Reaction mechanism

The exact reaction mechanism of the dissolution of UC in HNO_3 is difficult to identify due to the large variety of reaction products and different dissolution reactions. A significant feature, however, is the rapid catalysis of the dissolution by HNO_2 produced by the dissolution with HNO_3.

In addition to Eq. 2.60, Maslennikov *et al.* describe the dissolution of UC by different species in solution by the following equations (Maslennikov *et al.*, 2009):

$$UC \xrightarrow{n_{HNO_2},k_{HNO_2}} U(VI) + NIOC + CO_2 + NO \tag{2.61}$$

$$UC \xrightarrow{n_{O_2},k_{O_2}} U(VI) + NIOC + CO_2 \tag{2.62}$$

$$UC \xrightarrow{n_{H_2O},k_{H_2O}} U(VI) + NIOC + H_2 + CH_4 \tag{2.63}$$

$$UC \xrightarrow{n_{H^+},k_{H^+}} U(VI) + NIOC + H_2 + CH_4 \tag{2.64}$$

where k_{HNO_2}, k_{O_2}, k_{H_2O} and k_{H^+} are the rate constants of UC dissolution by the respective species and n_{HNO_2}, n_{O_2}, n_{H_2O} and n_{H^+} are the reaction orders.

Maslennikov *et al.* observed from the dissolution of UC in $HClO_4$ that the contribution of the dissolution rates from Eqs. 2.62 and Eqs. 2.63 was negligible, meaning that the dissolutions to be considered are those with HNO_3 and HNO_2.

Glatz *et al.* (Glatz *et al.*, 1990) proposed a two-stage reaction mechanism and defined a stoichiometric equation for each. Initially, HNO_3 reacts with the UC pellet to produce HNO_2, the slower stage responsible for the induction period, followed by the reaction of UC with both HNO_3 and HNO_2.

$$UC(cr) + 7HNO_3(sln) \rightarrow \{UO_2(NO_3)_2 + 5HNO_2 + H_2O\}(sln) + CO_2(g) \quad (2.65)$$

$$UC(cr) + \{10HNO_2 + 2HNO_3\}(sln) \rightarrow \{UO_2(NO_3)_2 + 6H_2O\}(sln) + \{CO_2 + 10NO\}(g) \quad (2.66)$$

where cr, sln and g stand for crystal, solution and gas respectively.

Whilst the reaction mechanism represented in Eqs. 2.65 and 2.66 maybe a simplification (no organics compounds are mentioned as reaction products, for example), it is a necessary one if a realistic model is to be constructed. The important aspect with respect to a dissolution model is that Glatz *et al.* provide a stoichiometry for the two reactions, meaning that the volume of HNO_3 and HNO_2 required to dissolve a UC pellet of a certain mass can be calculated.

2.5.3 Dissolution models

The following section will detail UC dissolution models found in literature, as well as some models that describe the dissolution of a UO_2 pellet via fragmentation as this physical mechanism would be largely similar for a UC pellet.

Fukusawa and Ozawa (Fukasawa & Ozawa, 1986) studied the dissolution of unspent UO_2 pellets in nitric acid, taking in careful consideration of the porosity of the pellets. It was found that the changing surface area during the reaction greatly influenced the reaction speed.

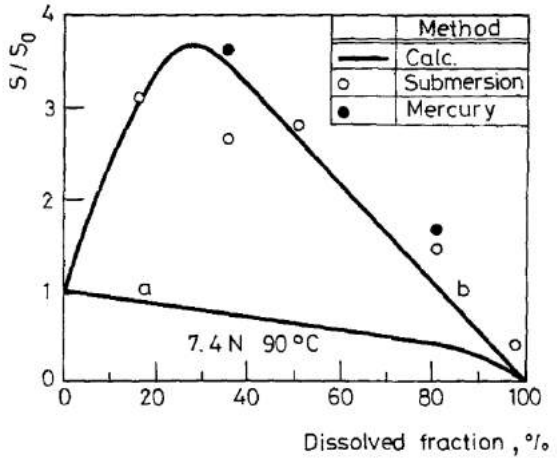

Figure 2.16: The surface area of a UO_2 pellet changing during dissolution in HNO_3. Line a assumes uniform dissoltution while line b assumes a constant dissolution rate (Fukasawa & Ozawa, 1986).

Figure 2.16 is a plot of two curves, a and b, of the normalised effective surface area (S/S_0) against the dissolved fraction of the oxide pellet. In curve a, where the assumption is made that the pellet dissolves uniformly from the surface, the effective surface area decreases slowly until reaction completion. Curve b, however, assumes that the dissolution rate per unit effective surface area was constant, and shows a rapid increase in surface area as the smooth surface of the pellet is eroded to form pores. It then decreases rapidly as well as the pellet dissolves. The dots are experimental data plots, and line up much more accurately with curve b, the one with the constant dissolution rate per unit effective surface area.

The data points were taken by removing the pellet from the nitric acid at certain stages of dissolution and measuring its surface area by the submersion or mercury impregnation methods (Fukasawa & Ozawa, 1986).

The submersion method involves weighing the pellet after the nitric acid has been dried (W_1), while it was placed in distilled water (W_2) and after it had been removed from the water and had the surface water removed (W_3). The open porosity ratio, ϵ, was then calculated as:

$$\epsilon = \frac{porosity\ volume}{porosity + pellet\ volume} = \frac{W_3 - W_1}{W_3 - W_2} \tag{2.67}$$

The effective surface area could then, using the open porosity ratio, be expressed as:

$$S = S_0 \left[(1-x)^{2/3} + \frac{49.68\epsilon(1-x)}{1-\epsilon} \right] \tag{2.68}$$

where S is the effective surface area in m^2, S_0 is the initial surface area also in m^2 and x is the dissolved fraction.

The mercury impregnation method involves submerging the pellet in mercury and gradually applying pressure. The pore radius is calculated by:

$$P\Delta X = -2\sigma cos\theta \tag{2.69}$$

where P is the pressure applied, Pa, ΔX is the pore radius, m, σ is the surface tension of mercury, $kg\,m\,s^{-2}$, and θ is the contact angle between the mercury and the sample (130°).

Knowing the pore radius, the surface area of the pellet can then be calculated from the volume of mercury in the pores:

$$S = \frac{2V_g}{\Delta X} \tag{2.70}$$

where V_g is the volume of mercury in the pores, m^3.

The equation Fukusawa and Ozawa use for the initial dissolution rate is (Fukasawa & Ozawa, 1986):

$$R = 6.3 \times 10^7 M^{2.8} exp(-15.2/KT) \tag{2.71}$$

where R is the initial dissolution rate, $mg\,cm^{-2}\,min^{-1}$, M is the initial HNO_3 concentration, $mol\,l^{-1}$, K is the ideal gas constant, $cal\,K^{-1}\,mol^{-1}$, and T is the absolute temperature, K.

The apparent activation energy for the dissolution is contained in the above Arrhenius expression as $15.2\,cal\,mol^{-1}$. It is doubtful, however, that this value would be the same for the dissolution of a carbide pellet.

From the fact that curve b (Figure 2.16) aligns well with the experimental data, Fukusawa and Ozawa conclude that the dissolution rate per unit surface area, R, is constant throughout the dissolution process (Fukasawa & Ozawa,

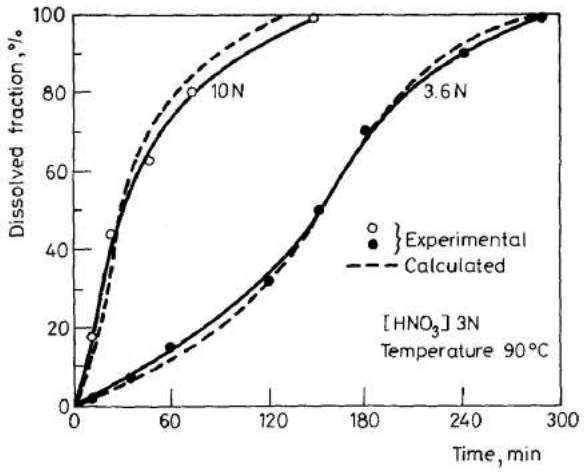

Figure 2.17: Simulations of the dissolution of UO_2 pellets in HNO_3 compared to experimental data (Fukasawa & Ozawa, 1986).

1986). This is an important and helpful consideration to take when constructing the dissolution model.

In order to model how the rate of reaction then slows as the pellet's surface area depletes, the rate in Eq. 2.71 must be made dependent on surface area. Fukusawa and Ozawa use the following equation to this end:

$$\Delta W_i = RS\Delta t \tag{2.72}$$

where ΔW_i is the change in weight of the dissolving pellet, mg, over the time period Δt, min.

Figure 2.17 is a plot of the S-shaped dissolution curves produced from such a model, and compares them to experimental data (Fukasawa & Ozawa, 1986). The reaction rate speeds up at first due to the increasing surface area as the smooth surface is eroded, and then decreases as the UO_2 depletes, aligning with curve b in Figure 2.16. Increasing the concentration of the nitric acid, expressed in Figures 2.16 and 2.17 as normality, N, decreased the dissolution completion time.

The model proposed by Fukusawa and Ozawa, therefore, offers a good description of the dependence of the dissolution rate on the changing surface area of the pellet. Unfortunately, it doesn't consider the effect that nitrous acid has on

the reaction kinetics, an effect also important in the dissolution of UO_2, meaning it may be limited.

Hodgson (Hodgson, 1987) produced a similar model on the dissolution of UO_2 that also focuses on physical, rather than kinetic, aspects of the reaction. Hodgson suggests the dissolution occurs by penetration of the acid along cracks of grain boundaries in the pellet. The model gives the same s-shaped curves as shown in Figure 2.17, but describes a dissolution process controlled by the propagation of the dissolution front along a crack.

The fuel pellet is considered to be made up of dissolving grains that have been exposed to the acid and non-dissolving grains which have not yet been exposed. At any instant, the reaction rate is proportional to the weight of fuel exposed at that instant (Hodgson, 1987):

$$\frac{\mathrm{d}\Delta m(t)}{\mathrm{d}t} = \frac{m_e(t)}{\theta} \tag{2.73}$$

where m_e is the instantaneous mass of fuel exposed to the acid, kg, Δm is the total mass of fuel dissolved up to time t, kg, and $1/\theta$ is a dissolution rate constant, s^{-1}.

The dissolution of fuel exposes more fuel grains to dissolution. The propagation of dissolution along a crack is assumed by Hodgson be proportional to the ratio of exposed to unexposed fuel, and the rate at which fuel is exposed is proportional to the dissolution rate:

$$\frac{\mathrm{d}m_u(t)}{\mathrm{d}t} = -f\frac{m_e(t)}{\theta}\frac{m_u(t)}{m_e(t)} = -f\frac{m_u(t)}{\theta} \tag{2.74}$$

where m_u is the mass of unexposed fuel at time t, kg, and f is a dimensionless constant. For an ideal fuel with uniformly dispersed grains, $f = 1$.

Exposed fuel is removed according to Eq. 2.73 and created according to Eq. 2.74. A mass balance then gives the rate of change of exposed fuel as (Hodgson, 1987):

$$\frac{\mathrm{d}m_e(t)}{\mathrm{d}t} = f\left(\frac{m_u(t)}{\theta} - \frac{m_e(t)}{\theta}\right) \tag{2.75}$$

Eqs. 2.73 and 2.75 are then computed for a specific rate constant, θ.

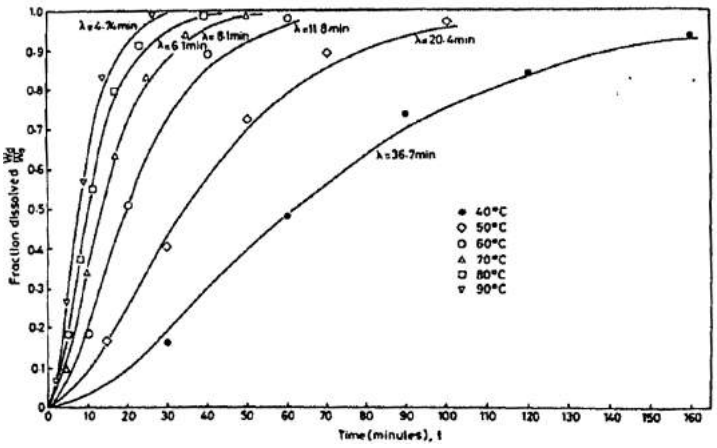

Figure 2.18: Dissolution curves of UO_2 pellets at different temperatures (Hodgson, 1987).

The general solution, expressed as the fraction of fuel dissolved, is given in Eq. 2.76. Note an ideal fuel is assumed (i.e. $f = 1$).

$$\frac{\Delta m(t)}{m_0} = 1 - \left(\frac{t}{\theta} + 1\right) exp\left(-\frac{t}{\theta}\right) \tag{2.76}$$

where m_0 is the initial mass of fuel, kg.

Hodgson then fits Eq. 2.76 to experimental data of UO_2 pellets being dissolved in HNO_3 at different temperatures (Hodgson, 1987), as illustrated in Figure 2.18. Different rate constants are deduced from the fits, and the typical S-shaped dissolution curve can be observed.

The final model to be considered the product of Maslennikov *et al.* (Maslennikov *et al.*, 2009), published in tandem with the experimental data displayed in Figures 2.14 and 2.15.

A more kinetic approach is considered, with the focus being on the reaction rate dependent on the concentration of two main reacting species, HNO_3 and HNO_2. As such, the concentration of both in the solution also requires calculating.

The overall equation for the fraction of UC powder dissolved is given as:

$$\frac{\Delta m(t)}{m_0} = \left(k_{H^+}\left[H^+\right]^{n_{H^+}} + k_{HNO_2}\left[HNO_2\right]^{n_{HNO_2}} + k_{NO_3^-}\left[NO_3^-\right]^{n_{NO_3^-}}\right) t^n \tag{2.77}$$

where $\Delta m(t)$ is the mass of UC dissolved at time t, g, m_0 is the initial mass, g, k_{H^+}, k_{HNO_2} and $k_{NO_3^-}$ are the rate constants dependent on H^+ ions, HNO_2 and

NO_3^- ions respectively, min^{-1}, n_{H^+}, n_{HNO_2} and $n_{NO_3^-}$ are partial reaction orders and n an additional reaction order.

Maslennikov then considers specifically the dissolution in an $HClO_4$-HNO_2 solution, calculating the decreasing HNO_2 concentration as an exponential decay (Maslennikov *et al.*, 2009):

$$[HNO_2]_t = [HNO_2]_0 \exp\left(-k^{SD}_{NO_3^-} t\right) \tag{2.78}$$

where $[HNO_2]_t$ is the HNO_2 concentration at time t, $[HNO_2]_0$ is the initial concentration and $k^{SD}_{NO_3^-}$ is a rate constant for the depletion on HNO_2, min^{-1}.

Whilst Eq. 2.78 is not accurate for the dissolution of UC in HNO_3 it is thought that a similar representation could be used to match the curves in Figure 2.15. For example, reversing the sign of the rate constant to give an exponential increase in the HNO_2 concentration over time, followed by a roughly linear decrease.

For the dissolution in the $HClO_4$-HNO_2 , Maslennikov *et al.* track the HNO_3 concentration by using the equilibrium in Eq. 2.79.

$$3HNO_2 \rightleftharpoons NO_3^- + 2NO + H^+ + H_2O \tag{2.79}$$

Combined with the rate of change in the HNO_2 concentration, the stoichiometry of Eq. 2.79 is used to calculate the time dependent HNO_3 concentration (Maslennikov *et al.*, 2009):

$$\left[NO_3^-\right]_t = k_{NO_3^-} - \frac{[HNO_2]_0}{3} \exp\left(-k^{SD}_{NO_3^-} t\right) \tag{2.80}$$

Given that the contribution to the reaction rate by the H^+ ions is negligible (Maslennikov *et al.*, 2009), Eqs. 2.80 and 2.78 then allow the solution of Eq. 2.77 and hence a calculation of the reaction rate.

Unfortunately, the partial rate constants and reaction orders provided by Maslennikov *et al.* relate to the dissolution in the $HClO_4$-HNO_2 solution, meaning that for this model to be applied to HNO_3, experimental data would be required to fit the necessary parameters.

Maslennikov *et al.* carried the dissolutions out at one temperature only, meaning that the dependence of the reaction kinetics on temperature is not included in this model. Also, the concentration range considered is also quite narrow, meaning that dissociation effects of the acids that occur at higher temperatures and concentrations are not included.

2.6 Applicable modelling techniques

This section of the literature review is concerned with examining modelling methods potentially applicable to this investigation. Of particular interest are codes that are able to simulate the packing of solid structures that would allow batch processing of UC fuel pellets to be considered, and codes that simulate fluid flow enabling the inclusion of flow into the models produced.

Efforts are made in the following sections to briefly examine the different computational methods available for packing and flow modelling with a view to determining the most applicable technique to this investigation.

2.6.1 Packing algorithms

A packing algorithm, in this context, is a computational method designed to simulate the arranging of a number of particles into a specified volume. Such algorithms have a wide range of application to engineering and industry, and so there exists a variety of different methods (Cumberland & Crawford, 1987; Gray, 1968). Packing algorithms, strictly, refers to the class of computational methods aiming to generate a packed structure within only geometric constraints. Therefore, the simulation of the physical processes occurring such as gravity and inter-particle effects, that would perhaps be modelled through molecular dynamics (MD) or discrete element method (DEM) modelling, can be ignored (Jia & Williams, 2001). This methodology is preferred due to its relative computational ease and that the scope of this investigation requires only a simple packing; for example, a handful of cylinders arranged within a vessel.

There are a large number of packing algorithms in publication coming in three basic forms as described by Jia and Williams in a review of geometric packing algorithms (Jia & Williams, 2001):

1. *Ballistic algorithms*. Particles follow defined trajectories to meet a resting place within the packing. An advantage of this method is its computational efficiency but it can be difficult to implement for containers with complex geometries. A good example of a ballistic packing algorithm for hard spheres is given by Webb and Davis (Webb & Davis, 2006).

2. *Random placement algorithms.* Particles are inserted individually into the packing at a random position. If an incoming particles does not overlap with one already in place, it is allowed to stay and added to the packing. Given its simplicity, this method is easily implemented but can be time consuming. Davis and Carter published such an algorithm designed to calculate packing fractions of arbitrarily sized and arbitrarily dense spherical particles (Davis & Carter, 1990).

3. *Growth algorithms.* Packing is produced by number of 'growing' points within it. Points are allowed to grow until reaching a set size or coming into contact with another point. A difficulty often faced by this method is an uneven size distribution caused by some points having more room to expand into. Kansal *et al.* describe a growth model where polydisperse, hard spheres expand to form a dense packing (Kansal *et al.*, 2002). In this case, the difficulty of the resulting particle size distribution is controlled by making the growth rate proportional to the particle's initial radius.

The vast majority of algorithms of these forms in publication are limited to the packing of analytical, regular shapes such as spheres (Berryman, 1983; Davis & Carter, 1990; Kansal *et al.*, 2002; Nolan & Kavanagh, 1992; Soppe, 1990; Webb & Davis, 2006) and cylinders (Coelho *et al.*, 1997; Nolan & Kavanagh, 1995), making it difficult to pack arbitrary shapes and possibly requiring the use of different algorithms for different shapes. Since the use of packing algorithms in this investigation is to pack UC fuel pellets, and although they will likely be in cylindrical form, it would be preferable to be able to consider a variety of geometries. Therefore, a highly versatile algorithm presented by Jia and Williams (Jia & Williams, 2001) that employs a digital approach to packing is chosen for use.

By digitising both the input structures and the container into collections of pixels for two-dimensional packing or voxels for three-dimensional cases, almost any arbitrarily shaped structure can be packed into an arbitrarily shaped container. Such an algorithm would then be highly flexible in simulating different processing methods for the batch oxidation of UC fuel. The details of the algorithm itself are included as a part of the methodology chapter of this thesis, in

Section 3.2.1. Furthermore, the algorithm is wholly interoperable with a digital DEM packing algorithm by Caulkin *et al.* (Caulkin *et al.*, 2009), allowing scope for a more complex, physically realistic packing should one become desired. The DEM algorithm works by calculating the forces the particles exert on each other and the forces between the particles and the container walls. This is achieved by allowing minor overlap between the solids upon contact and calculating the resulting force exerted from the spring-dashpot model (Xu *et al.*, 2006):

$$F_{n,t} = \left(-k_{n,t}\sigma_{n,t} - \eta_{n,t}\nu_{n,t}\right)\bar{n}_{n,t} \tag{2.81}$$

where F is the force from a pixel-pixel or voxel-voxel contact, k is the stiffness, σ the overlap, η the dumping coefficient and ν is the relative velocity component. The subscripts n and t denote that each property has component in the normal, $\bar{n}_n$, and tangential, $\bar{n}_t$, directions, respectviely (Caulkin *et al.*, 2009; Xu *et al.*, 2006).

Due to this inclusion of particle interaction forces, the DEM algorithm is not only capable of more accurate packing structures but also able to include physical processing phenomena such as stirring, shaking and vibrating containers.

2.6.2 Fluid flow modelling

There are a huge variety of mathematical and computational tools available for simulating fluid flow around solids, together constituting the highly active field of computational fluid dynamics (CFD). Therefore, a user has to choose which method is expected to provide the most accurate solution to their specific scenario. This following section will describe a number of CFD methods used to model turbulent flows, outlining their general advantages and disadvantages and some of their applications. A conclusion will then be drawn on which method is the most appropriate for this investigation.

2.6.2.1 Direct numerical simulation (DNS)

The vast majority of the CFD methods aim to solve the Navier-Stokes (NS) equations that describe the motion of viscous fluids (Caboussat *et al.*, 2011; Moin

& Mahesh, 1998), derived from Newton's second law and expressed in tensor notation as (Ferziger & Peric, 2012; Tu *et al.*, 2008):

$$\underbrace{\frac{\partial u_i}{\partial t}}_{\text{local acceleration}} + \underbrace{u_j \frac{\partial u_i}{\partial x_j}}_{\text{advection}} = - \underbrace{\frac{1}{\rho}\frac{\partial p}{\partial x_i}}_{\text{pressure gradient}} + \underbrace{v \frac{\partial^2 u_i}{\partial x_j \partial x_j}}_{\text{diffusion}} \tag{2.82}$$

with the continuity equation included as:

$$\frac{\partial u_j}{\partial x_j} = 0 \tag{2.83}$$

where x_i, with $i = 1, 2, 3$, are the Cartesian coordinates, u_i is the fluid velocity component in the i direction, t the time, v is the kinematic viscosity, ρ is the fluid density and p the pressure. Where two of the same index occur in the same term, e.g. the advection term, it is implied by tensor notation to sum the effects in each Cartesian coordinate. Note that this formulation of the Noyes-Whitney equations assumes that the fluid is incompressible and therefore has constant density.

When considering turbulent flows, it is impossible to find an analytical solution to the NS equation. A numerical solution is therefore required, and can be found using a method known as DNS to directly discretise the NS equations and solve using finite difference or finite element methods (Caboussat *et al.*, 2011; Moin & Mahesh, 1998). Such an all-inclusive solution requires solving the NS equations at all scales of motion, hence requiring finite difference meshes, or grids, across the domain to be extremely fine in order to capture the smallest scales of motion (Caboussat *et al.*, 2011) making it computationally laborious. Given that increasing the Reynolds number, the measure of flow turbulence, increases the range of scales of motion, DNS is only feasible with current computational technology only at low Reynolds numbers and with simple geometries (at which it is very accurate). DNS is therefore extremely limited in its application to engineering problems and is as such rarely used despite being the most conceptually simple solution to the NS equations (Ferziger & Peric, 2012). It does, however, experience some use as a research tool to examine specific issues such as the effects of compressibility and combustion on turbulent flows (Ferziger & Peric, 2012).

The flow systems that would be applied in this work would involve the flow of air of HNO_3 around one or many UC pellets. The flow rate would likely be low,

but the complex geometry of a packed bed of pellets may result in DNS being overly computationally expensive so it is unlikely to be used. It remains worthy of inclusion though due to its importance in understanding how and why other CFD methods are developed.

2.6.2.2 Large eddy simulation (LES)

LES is a CFD method designed to ease the computational expense of solving the NS equations by removing the need to solve explicitly at every scale. A spatial filter of a size relative to the computational grid size of a particular simulation is applied, and only the set of scales larger than the spatial filter are calculated explicitly with numerical methods (Moeng & Sullivan, 2002). The smaller scales, termed the subgrid-scale (SGS), are modelled to give an estimated solution. The concept of LES makes two important assumptions (Caboussat *et al.*, 2011):

- Most flow features are governed by the larger scale effects.
- Small-scale turbulences tend to local isotropy, i.e. are orientation independent, meaning general models can be applied.

The use of SGS models to shoulder some of the computational weight makes LES a preferable and more viable alternative to DNS for flows with higher Reynolds numbers and/or more complex geometries. The most widely used SGS models for LES simulations are the Smagorinsky-Lilly and Deardorff's turbulence kinetic energy models described in an LES review by Moeng and Sullivan (Moeng & Sullivan, 2002), and a slightly more sophisticated, dynamic model by Germano *et al.* (Germano *et al.*, 1991).

The following mathematical description of LES is taken largely from the book *Computational methods for fluid dynamics* by Ferziger and Peric (Ferziger & Peric, 2012). The spatial filter used in LES is applied mathematically by defining the quantities requiring precise computation rather than SGS modelling. This is done by filtering the velocity field, a process in which the large scale field is taken to be a local average of the complete velocity field. The filtered velocity is defined as:

$$\bar{u}_i(x) = \int G(x, x')\, u_i(x')\, \mathrm{d}x' \tag{2.84}$$

where $G(x, x')$ is a function called the filter kernel. Examples are Gaussian functions, a box filter (a simple local average) and a cutoff (a filter eliminating Fourier coefficients above a specified cutoff). Every filter has a designated length scale, Δ. Flow phenomena, such as eddies, with a scale of motion larger than Δ are computed numerically whilst those with a smaller scale of motion are modelled.

Applying this velocity filtering to the momentum conservation NS equation results in:

$$\frac{\partial(\rho\bar{u}_i)}{\partial t} + \frac{\partial\rho\overline{u_i u_j}}{\partial x_j} = -\frac{\partial\bar{p}}{\partial x_i} + \frac{\partial}{\partial x_j}\left[\mu\left(\frac{\partial\bar{u}_i}{\partial x_j} + \frac{\partial\bar{u}_j}{\partial x_i}\right)\right] \tag{2.85}$$

Since $\overline{u_i u_j} \neq \bar{u}_i\bar{u}_j$, the left side of Eq. 2.85 is not easily solved. Therefore the concept of subgrid-scale Reynolds stress, $\tau^s_{i,j}$, must be introduced:

$$\tau^s_{i,j} = -\rho\left(\overline{u_i u_j} - \bar{u}_i\bar{u}_j\right) \tag{2.86}$$

SGS Reynolds stress physically represents the large scale momentum flux caused by the small scale flow effects acting on the fluid. It is approximated using the SGS models mentioned previously, which compute it by considering properties of the local large scale velocity field and the past history of the fluid. The Smagorinsky model (Smagorinsky, 1963), for example, is an eddy viscosity model that assumes the principal effects of SGS Reynolds stress are on dissipation and transport of the fluid. As these phenomena are dependent on viscosity, the SGS Reynolds stress can be computed using the eddy viscosity and the strain rate of the large scale velocity field. For the sake of the brevity of this literature review, this SGS model and others will not be discussed in much further detail but detailed descriptions are easily available (Ferziger & Peric, 2012; Germano *et al.*, 1991; Moeng & Sullivan, 2002; Smagorinsky, 1963).

Similarly to DNS, the computational cost of LES rises significantly with Reynolds number as significant proportion of the length scales still require explicit solution. However, due to the approximation of the SGS scales, it is much more widely used. For example, it is frequently used in simulating turbulence in the Earth's atmosphere (Kumar *et al.*, 2006; Speziale, 1991), turbulent flow through jet engines (Blin *et al.*, 2003) and in modelling impinging jets (Tsubokura *et al.*, 2003). However, it is still a concern that LES modelling may also be unnecessarily computationally expensive for this investigation.

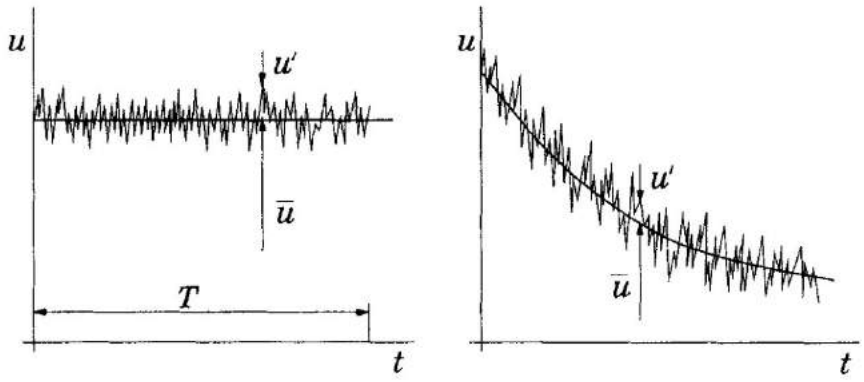

Figure 2.19: Time averaging of a steady flow (left) compared to ensemble averaging of an unsteady flow (right). Taken from *Computational methods for fluid dynamics* by Ferziger and Peric (Ferziger & Peric, 2012).

2.6.2.3 Reynolds-averaged Navier-Stokes equations (RANS)

The RANS method attempts to lower computational cost yet further by not explicitly solving the NS equations at all, and instead averaging every fluid variable over time (Ferziger & Peric, 2012; Gatski & Bonnet, 2009). Turbulence models are then introduced to 'close' the equations generated by averaging variables in the NS equations. Again, the book *Computational methods for fluid dynamics* by Ferziger and Peric (Ferziger & Peric, 2012) is used to in the following section to provide a mathematical explanation of RANS modelling.

The averaging method applied depends on whether the simulated flow is steady or unsteady. For a steady flow, every variable can be expressed as the sum of its time averaged value and a fluctuation about that value. Take a variable ϕ, representing a conserved property per unit mass of the fluid:

$$\phi(x_i, t) = \bar{\phi}(x_i) + \phi'(x_i, t) \tag{2.87}$$

where the time averaged component is calculated as:

$$\bar{\phi}(x_i) = \lim_{T\to\infty} \frac{1}{T} \int_0^T \phi(x_i, t)\, \mathrm{d}t \tag{2.88}$$

where t is time and T the time averaging interval. T must be large with respect to the fluctuation intervals in order to provide a reasonable approximation.

If the flow is unsteady, averaging of fluid variables over time is not possible. Instead, ensemble averaging must be carried out. The differences in the two concepts is illustrated in Figure 2.19. The ensemble averaged component of Eq. 2.87 is calculated as:

$$\bar{\phi}(x_i, t) = \lim_{N\to\infty} \frac{1}{N} \sum_{n=1}^{N} \phi(x_i, t) \tag{2.89}$$

where N is the number of members in the ensemble and must be large enough to eliminate the effects of fluctuations.

The term Reynolds averaging is used to refer to either of these forms of averaging, and applying it to the NS equations gives the RANS equations. The momentum conservation RANS can be expressed for incompressible flows in tensor form as:

$$\frac{\partial(\rho\bar{u}_i)}{\partial t} + \frac{\partial}{\partial x_j}\left(\rho\bar{u}_i\bar{u}_j + \rho\overline{u_i'u_j'}\right) = -\frac{\partial\bar{p}}{\partial x_i} + \frac{\partial\tau_{i,j}}{\partial x_j} \tag{2.90}$$

where $\tau_{i,j}$ is the Reynolds stress tensor given as:

$$\tau_{i,j} = \mu\left(\frac{\partial\bar{u}_i}{\partial x_j} + \frac{\partial\bar{u}_j}{\partial x_i}\right) \tag{2.91}$$

The averaged conservation equation is expressed as:

$$\frac{(\partial\bar{u}_i)}{\partial x_i} = 0 \tag{2.92}$$

The RANS equations, however, cannot be solved as they are not yet closed: there are more variables than equations. Closure, and hence solution, is achieved through the application of one of many turbulence models to approximate the Reynolds stress term, $\tau_{i,j}$, similar to the application of SGS models in LES. Eddy viscosity models are again one such applicable method for modelling the Reynolds stress, resting on the same idea that the viscosity of a flow mediates it's momentum, mass transport and energy etc. Further models of increasing complexity such as the $k-\epsilon$ (Mohammadi & Pironneau, 1993) and $k-l$ (Mellor & Herring, 1973) models are discussed in detail in a review of RANS turbulence models by Speziale (Speziale, 1991).

Of the three CFD methods mentioned thus far, RANS is the most commonly utilised on account of its versatility and relatively short computational times whilst continuing to give satisfactorily accurate predictions. It finds application in a huge variety of engineering disciplines, from wind turbine behaviour (Simms *et al.*, 1999) to preparing off-shore platforms for extreme weather (Oakley *et al.*, 2005). It therefore appears suitable for use in this work, but the lattice-Boltzmann method is in fact preferred due to its compatibility with other modelling needs as discussed in the following section.

2.6.2.4 Lattice-Boltzmann method (LBM)

The final CFD method to be outlined is LBM. LBM differs fundamentally from conventional CFD methods in that instead of solving filtered or averaged NS equations, it examines the physical phenomena occurring at the microscopic or mesoscopic scales (Chen & Doolen, 1998). Averages of microscopic calculations taken across a domain can then be used to predict macroscopic properties of a flow, and in effect recover the NS equations. The mathematics behind LBM are detailed in the methodology chapter of this work, in Section 3.2.2 on Page 72, whilst this section will simply discuss the applications of LBM and its suitability to this investigation.

LBM is can be applied to most CFD problems, but it is especially attractive when considering complex geometries as will be done in this work when examining fluid flow through a packing of fuel pellets (Chen & Doolen, 1998; Succi *et al.*, 1989). Put simply, this is a result of LBM essentially being a particle tracking technique, and hence intricacies at fluid-solid boundaries can be handled easily in terms of particle reflections and interactions (Succi *et al.*, 1989). Making an analogue between a packed structure of pellets and porous media, numerous studies have been carried out using LBM in complex geometries showing excellent agreement with experimental data (Ferreol & Rothman, 1995; Soll *et al.*, 1994; Spaid & Phelan Jr, 1997).

LBM is of further interest to this project as it has been shown to be easily coupled to Jia and Williams' (Jia & Williams, 2001) digital packing algorithm by Caulkin *et al.* (Caulkin *et al.*, 2012) creating an ideal tool to examine flow

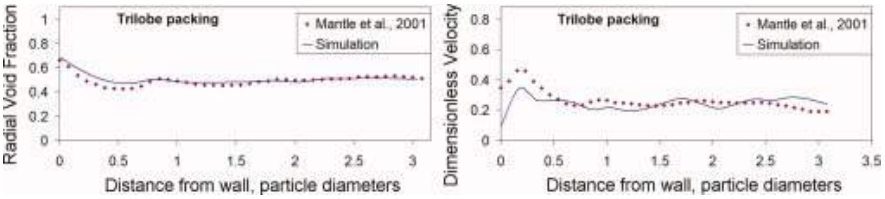

Figure 2.20: Validation of the digital packing algorithm and subsequent LBM simulations through the packing (Caulkin *et al.*, 2012).

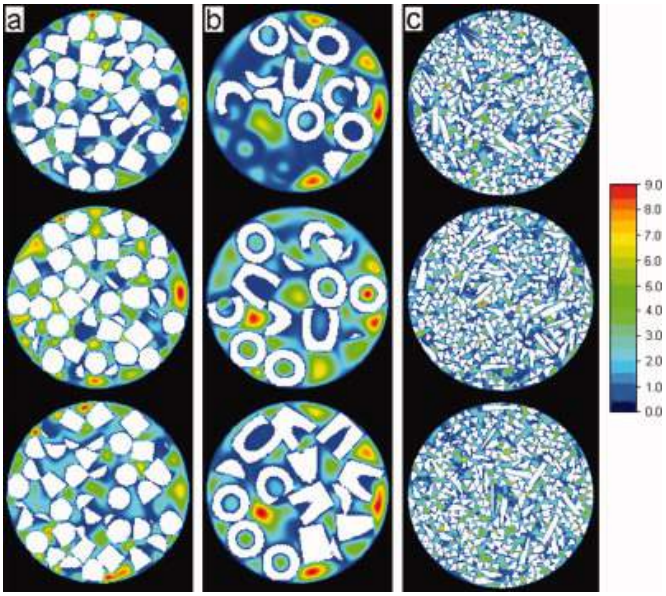

Figure 2.21: Cross sectional images of fluid flow through packed cylinders (a), Raschig rings (b) and trilobe pellets (c) (Caulkin *et al.*, 2012).

through a packing of UC fuel pellets. Figure 2.20 is a plot published by Caulkin *et al.* (Caulkin *et al.*, 2012) of the validation of both the packing algorithm and subsequent flow through it simulated using LBM against data by Mantle *et al.* (Mantle *et al.*, 2001), showing good agreement. Figure 2.21 illustrates the capability of this technique by provide velocity profiles of fluid flow through various packings, and demonstrating how it is ideally suited for the purposes of this investigation (Caulkin *et al.*, 2012).

2.7 Concluding remarks

The literature review detailed in this chapter has demonstrated the need for models that can accurately simulate the oxidation and dissolution of uranium carbide, with neither process having a comprehensive model present in the literature.

The oxidation of UC, whilst reasonably well studied, requires further investigation into a number of parameters due to contradicting reports on the activation energy and the behaviour of the oxide product. In terms of a model for the process, the only one found that relates to the particular oxidation was that by Scott (Scott, 1966). This model, whilst a good basis for the models that may be produced in this work, leaves plenty of room for elaboration. For example, it assumes an oxide layer is present which has been shown to not be the case at higher O_2 concentrations (Mukerjee *et al.*, 1994), and assumes a reaction product of only UO_2 with no higher oxides.

Despite there being a number of models for the dissolution of UO_2, the only model of the dissolution of UC is Maslennikov *et al.*'s. The rate constants used in this model, however, pertain to the dissolution of UC in a different solution to HNO_3, $HClO_4$-HNO_2, and as such would require a different set of experimental data and some tweaks to the kinetic equations to be pertinent. A lack of temperature dependence also limits the model's applicability.

Therefore, it is deemed that accurate models produced for both the dissolution of UC in HNO_3 and the oxidation in air would be significant developments in the field. The models present in the literature may be used as starting points, or it may be decided that different approaches may be required. In any case, the aim will be to produce models that are capable of providing more detailed simulations of each process, factoring in a number of additional kinetic and physical processes that have been shown to occur in the reactions. More advanced techniques and software can also be applied to simulate the oxidation and dissolution under different fluid flow rates and examining batch processes using a coupling of a digital packing algorithm with LBM modelling.

Chapter 3

Methodology

The methods employed in this work, as outlined in Chapters 1 and 2, are entirely computational, with experimental data either being taken from relevant published literature or provided by collaborators. Different mathematical concepts are explored and implemented using a variety of computational techniques.

The majority of the work is carried out through the application of finite difference methods to mathematical equations with a subsequent numerical solution generated in original software. Other methods include the use of more general commercial software to examine different aspects of the reaction processes or enhance the level of detail. The discussion of these methods comprises the content of this chapter.

3.1 Finite difference methods

Science and engineering frequently use mathematics to calculate rates of change of one variable, temperature or concentration for example, with respect to another, such as time or spatial position. These rates of change are described by differential equations, which can be either ordinary (ODEs, dependent upon one independent variable) or partial (PDEs, dependent upon two or more).

However, it can often be extremely difficult to find analytical solutions for differential equations, particularly the more complex PDEs. In these cases, it is more practical to approximate a solution by applying finite difference methods. The scope of this work requires the solution of both ODEs and PDEs, so an

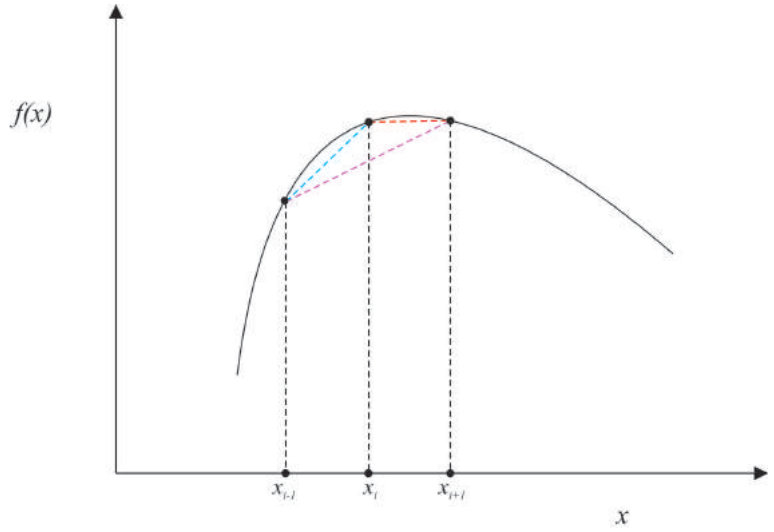

Figure 3.1: An example of different finite difference approximations of a function around the point x_i. The forward difference is coloured red, backward blue and central difference in purple.

explanation of the most appropriate finite difference approximations for each type of differential equation are included in the following sections.

3.1.1 Application to ODEs

Generally, finite difference methods estimate a solution to the differential equation by discretising the values that the variable can take, as illustrated in Figure 3.1. In Figure 3.1, a function with a single independent variable, $f(x)$, is plotted. The differential of $f(x)$ is represented by the ODE expressed in Eq. 3.1.

$$\frac{\mathrm{d}f(x)}{\mathrm{d}x} = f'(x) \tag{3.1}$$

In order to calculate an approximate solution to the differential of $f(x)$, x is discretised into a finite number of values, from say x_0 to x_{max}, allowing the differentiation of $f(x)$ between two points.

There are different methods of approximating $f'(x_i)$, the solution between these points, depending on which points are chosen to calculate the solution as highlighted by the coloured lines in Figure 3.1,.

The forward difference approximation of Eq. 3.1, i.e. the red dotted line in Figure 3.1, would then be:

$$\frac{f(x_{i+1}) - f(x_i)}{\Delta x} = f'(x_i) \tag{3.2}$$

allowing an estimation of the solution of the differential at x_i. Δx is the size of the increment between the discretised values of x.

The backward difference approximation (green) is expressed as:

$$\frac{f(x_i) - f(x_{i-1})}{\Delta x} = f'(x_i) \tag{3.3}$$

and the central difference (purple) as:

$$\frac{f(x_{i+1}) - f(x_{i-1})}{2\Delta x} = f'(x_i) \tag{3.4}$$

The accuracy of all three approximations is heavily dependent on the size of the increment between values of x, Δx. As it is reduced, the approximation becomes more accurate. However, when these calculations become more complex, the limit on reducing the increment size becomes how computationally expensive the calculations become due to the increased number of 'nodes' across the domain increasing the number of calculations required.

Different approximations can provide estimations of varying accuracy. For example, from Figure 3.1, it is clear that the forward difference approximation gives a closer fit to $f'(x)$ than that of the central difference. Choosing which finite difference approximation to apply to a problem is therefore important and highly contextual.

3.1.2 Application to PDEs

Finite difference approximations of PDEs require the discretisation of two or more independent variables, resulting in the domain of the relevant PDE being reduced to a multi-dimensional 'mesh'. The complexity of the approximation and the methods required to produce it depend upon the number of independent variables. For the purposes of this work, the maximum number of independent variables in a PDE reached is three, but this nonetheless requires different methodology than having two independent variables.

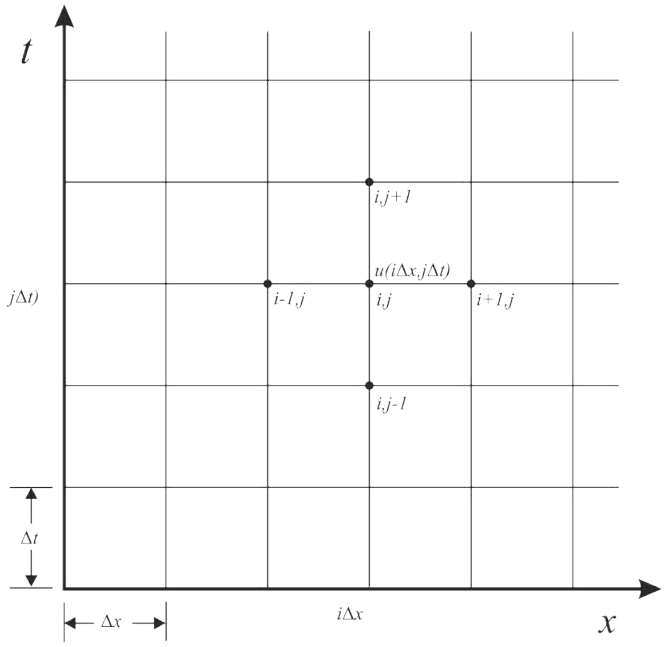

Figure 3.2: The discretisation of the domain of the function $u(x,t)$ over the $x-t$ plane (Smith, 1965).

3.1.2.1 Two independent variables

Consider the following parabolic function, $u(x,t)$:

$$\frac{\partial u(x,t)}{\partial t} = \frac{\partial^2 u(x,t)}{\partial x^2} \tag{3.5}$$

It is dependent on two independent variables, x and t, representing position and time respectively, and its two-dimensional discretisation is illustrated in Figure 3.2. The positions of different nodes across this domain are given by a combination of the two integers, i and j, where $i = j = 0$ at the origin, and the increment sizes for each variable are given by Δt and Δx. Therefore, $t = j\Delta t$ and $x = i\Delta x$.

The solution of Eq. 3.5 via finite difference approximation involves expressing unknown values of u across the mesh in Figure 3.2 in terms of known values of u (Smith, 1965). This can be done in a number of finite difference methods, similarly to the approximation of ODEs in the previous section. However, for the sake of brevity, only three methods will be considered presently: the explicit method,

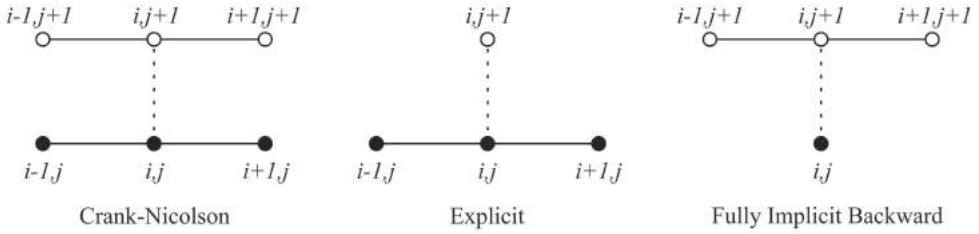

Figure 3.3: Examples of different finite difference methods (Smith, 1965). The known values are coloured black and the unknown in white.

the Crank-Nicolson (CN) implicit method and the fully implicit backward (FIB) method.

Each different method uses a different combination of known and unknown values of u, as illustrated in Figure 3.3. The initial known values are generally defined in the initial conditions when these methods are applied to a problem.

The explicit method calculates the solution, i.e. an unknown value of u, at one position using three known values of u. Applying the explicit method to Eq. 3.5 gives the following finite difference approximation (Smith, 1965):

$$\frac{u_{i,j+1} - u_{i,j}}{\Delta t} = \frac{u_{i+1,j} - 2u_{i,j} + u_{i-1,j}}{\Delta x^2} \tag{3.6}$$

which then allows the unknown value, $u_{i,j+1}$, to be expressed in terms of the known values:

$$u_{i,j+1} = u_{i,j} + \Delta t \left(\frac{u_{i+1,j} - 2u_{i,j} + u_{i-1,j}}{\Delta x^2} \right) \tag{3.7}$$

The CN method differs from the explicit method in that it uses the mean of the finite difference approximations of $\partial^2 u/\partial x^2$ along j and $j+1$:

$$\frac{u_{i,j+1} - u_{i,j}}{\Delta t} = \frac{1}{2} \left(\frac{u_{i+1,j+1} - 2u_{i,j+1} + u_{i-1,j+1}}{\Delta x^2} + \frac{u_{i+1,j} - 2u_{i,j} + u_{i-1,j}}{\Delta x^2} \right) \tag{3.8}$$

Grouping the unknowns of Eq. 3.8 on the left, and letting $r = \Delta t/\Delta x^2$, gives (Smith, 1965):

$$-ru_{i-1,j+1} + (2+2r)\,u_{i,j+1} - ru_{i+1,j+1} = -ru_{i-1,j} + (2+2r)\,u_{i,j} - ru_{i+1,j} \tag{3.9}$$

The CN method, when applied to across the domain, gives a set of equations similar to Eq. 3.9 that then require solving simultaneously to reach a solution (Smith, 1965).

The FIB method takes the approximation of $\partial^2 u/\partial x^2$ at $j+1$:

$$\frac{u_{i,j+1} - u_{i,j}}{\Delta t} = \frac{u_{i+1,j+1} - 2u_{i,j+1} + u_{i-1,j+1}}{\Delta x^2} \tag{3.10}$$

resulting in three unknown values to one known value. Rearranging for these unknowns gives:

$$-ru_{i-1,j+1} + (2+2r)\, u_{i,j+1} - ru_{i+1,j+1} = u_{i,j} \tag{3.11}$$

which again requires solving simultaneously with other equations of the same form across the domain.

Each of these methods presents its own advantages and disadvantages. Of particular importance, however, is the convergence and stability of each. A solution is convergent if reducing the increment sizes, Δt and Δx, towards zero causes the approximated solution to tend towards the analytical solution. Stability refers to whether or not the cumulative error introduced to the solution at each node invalidates the solution and is also dependent upon the increment sizes.

In order for the explicit method to be stable, a small time step size (Δt) is necessary for stability of the solution (Smith, 1965). The two implicit methods, however, are convergent and stable for all finite values of $\Delta t/\Delta x^2$ (Smith, 1965). Therefore, despite the increase in algebraic complexity demanded by the FIB and CN methods, numerical solutions derived using them will be overall computationally less expensive than those using the explicit method, as less calculations are required for the same period of time.

Both the CN and FIB methods are employed in the course of this work, but eventually the fully implicit backward method was preferred. This decision was made in response to the complexity of the CN approximation considering heat transfer at the boundary between two solids making the numerical solution difficult. It was found that the more simple approximation given by the FIB made the numerical solution significantly easier without compromising on the accuracy of the solution significantly.

Table 3.1: A comparison of the results provided by CN and FIB methods for the heating of a UC pellet.

	Surface Temperature ($°C$)	
Time (s)	CN Method	FIB Method
0	20.000	20.000
20	418.65	417.40
40	486.20	485.78
60	497.65	497.55

Table 3.1 and Figure 3.4 illustrate the results given by the CN and FIB methods when considering the thermal response of a spherical pellet under ambient conditions exposed to a gas at a temperature of $500°C$. The difference in the solutions calculated is negligible, justifying the use of the FIB method to ease the difficulty of the numerical solution.

3.1.2.2 Three independent variables

The previous section dealt with a PDE that had a dependence on a single spatial dimension, x, and time, t. However, if a transient system requires describing in two spatial dimensions, PDEs associated with it could involve three independent variables. Consider the following PDE:

$$\frac{\partial u(x,y,t)}{\partial t} = \frac{\partial^2 u(x,y,t)}{\partial x^2} + \frac{\partial^2 u(x,y,t)}{\partial y^2} \tag{3.12}$$

In order to generate a finite difference approximation to the solution of Eq. 3.12, it is necessary to discretise each independent variable: x, y and t. A sample of the resulting mesh is illustrated in Figure 3.5, where $x = i\Delta x$, $y = j\Delta y$ and $t = n\Delta t$.

Applying the FIB method to Eq. 3.12 results in the following expression:

$$\frac{u_{i,j,n+1} - u_{i,j,n}}{\Delta t} = \frac{u_{i+1,j,n+1} - 2u_{i,j,n+1} + u_{i-1,j,n+1}}{\Delta x^2} + \frac{u_{i,j,-1,n+1} - 2u_{i,j,n+1} + u_{i,j+1,n+1}}{\Delta y^2} \tag{3.13}$$

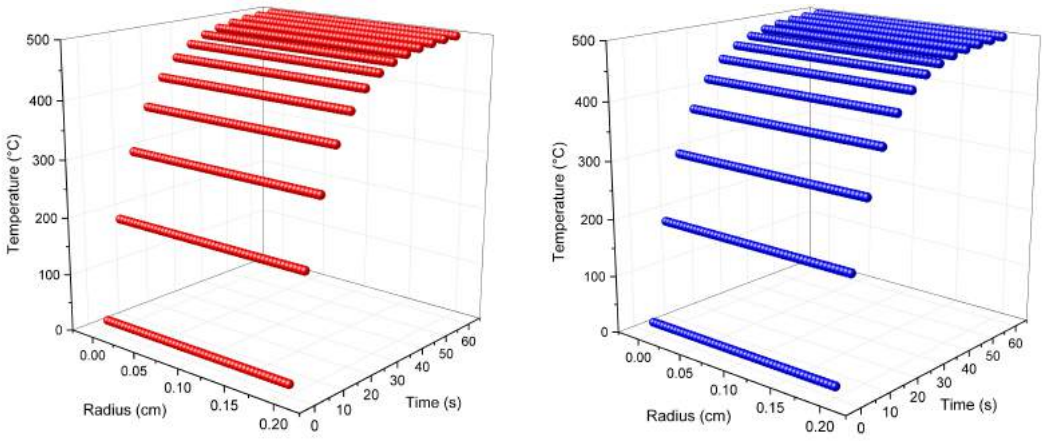

Figure 3.4: Radial temperature profiles across a spherical UC pellet under ambient conditions when exposed to a gas at a temperature of 500 °C calculated using the CN (red) and FIB (blue) finite difference methods.

Due to the larger number of unknowns present in the two-dimensional case than in the one-dimensional, arranging Eq. 3.13 into those of the form of Eq. 3.11 and solving simultaneously cannot be done. Therefore, a method known as the alternating directions method is applied (Smith, 1965).

Assume that at time $t = n\Delta t$, the solution to Eq. 3.12 is known. Then, as opposed to applying the FIB method to both spatial derivatives, the FIB is applied to only one for the solution at the time step $n+1$, $\partial^2 u/\partial x^2$ in this case, and the other, $\partial^2 u/\partial y^2$, is approximated explicitly:

$$\frac{u_{i,j,n+1} - u_{i,j,n}}{\Delta t} = \frac{u_{i+1,j,n+1} - 2u_{i,j,n+1} + u_{i-1,j,n+1}}{\Delta x^2} + \frac{u_{i,j,-1,n} - 2u_{i,j,n} + u_{i,j+1,n}}{\Delta y^2} \quad (3.14)$$

The number of unknowns is therefore reduced, and a solution can be found at the time step $n+1$. Advancing the solution from the time step $n+1$ to $n+2$ then requires solving in the alternate direction, the y direction, using the known values along x at $n+1$:

$$\frac{u_{i,j,n+2} - u_{i,j,n+1}}{\Delta t} = \frac{u_{i+1,j,n+1} - 2u_{i,j,n+1} + u_{i-1,j,n+1}}{\Delta x^2} + \frac{u_{i,j,-1,n+2} - 2u_{i,j,n+2} + u_{i,j+1,n+2}}{\Delta y^2} \quad (3.15)$$

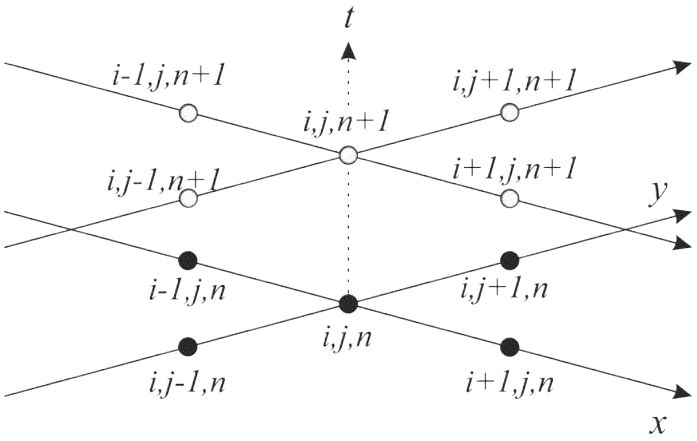

Figure 3.5: A finite difference mesh applicable to Eq. 3.12, covering two spatial dimensions, x and y, and time, t.

Eq. 3.15, similarly to Eq. 3.14, has a manageable number of unknowns at $n+2$ and is therefore solveable. The solution through time of Eq. 3.13 can then be solved by approximating in each direction alternatively.

3.2 Packing algorithm coupled with fluid flow calculation and reaction kinetics

More advanced software will be used to add complexity to the oxidation and dissolution models. Specifically, a software package collectively known as DigiPac^{TM} that incorporates a multitude of functions. The functions that will be of use to this investigation can primarily be considered to be:

- A packing algorithm
- Fluid flow modelling using the lattice-Boltzmann method (LBM)
- Application of reaction kinetics

These capabilities can be used in tandem to create a powerful modelling tool. For example, one application could be to use the packing algorithm to pack a number of fuel pellets into a container, calculate the flow of oxidant/solvent

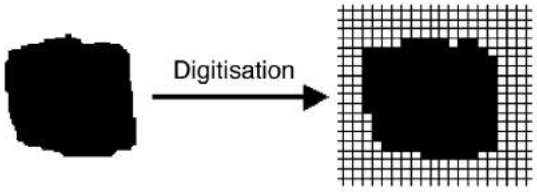

Figure 3.6: The digitisation of a particle to be used in a DigiPac^{TM} simulation (Jia & Williams, 2001).

through the structure and apply reaction kinetics dependent on the concentration of the reactants at any position. This would therefore allow simulation of a batch process.

3.2.1 Packing algorithm

DigiPac^{TM} has the capability to pack arbitrarily shaped particles into an arbitrarily shaped volume (Jia & Williams, 2001). This flexibility in the shape of the particles is allowed due to the digital nature of the algorithm, and DigiPac^{TM} in general. Input files describing the particle shape are digitised, or discretised, into 'voxels': a three dimensional, finite volume similar in concept to the two dimensional pixel used in televisions etcetera. The size of the voxel is chosen by the user and is a compromise between computational time and accuracy of the solution, similar to choosing a mesh increment size in finite-difference modelling. Figure 3.6 illustrates the process of digitising an arbitrarily shaped input particle into a collection of voxels (Jia & Williams, 2001). Once the particles to be packed have been digitised, they can then be inserted into a digital volume chosen by the user. For example, a hollow cylinder or a crucible shape.

The packing algorithm works by inserting the particles into the volume from the top of the domain. Each particle is then allowed to move randomly in one of 26 (6 orthogonal, 20 diagonal) directions in 3D (Gopinathan *et al.*, 2003). Each direction has an equal probability of being selected, except any movement with an upward component. Any upward movement is permitted only if it meets a 'rebounding probability', a value between 0 and 1 designed to limit the number of upwards movements and therefore simulate the effect of gravity (Jia &

Williams, 2001). A flow diagram of the DigiPac^{TM} packing algorithm is provided in Figure 3.7 (Gopinathan *et al.*, 2003).

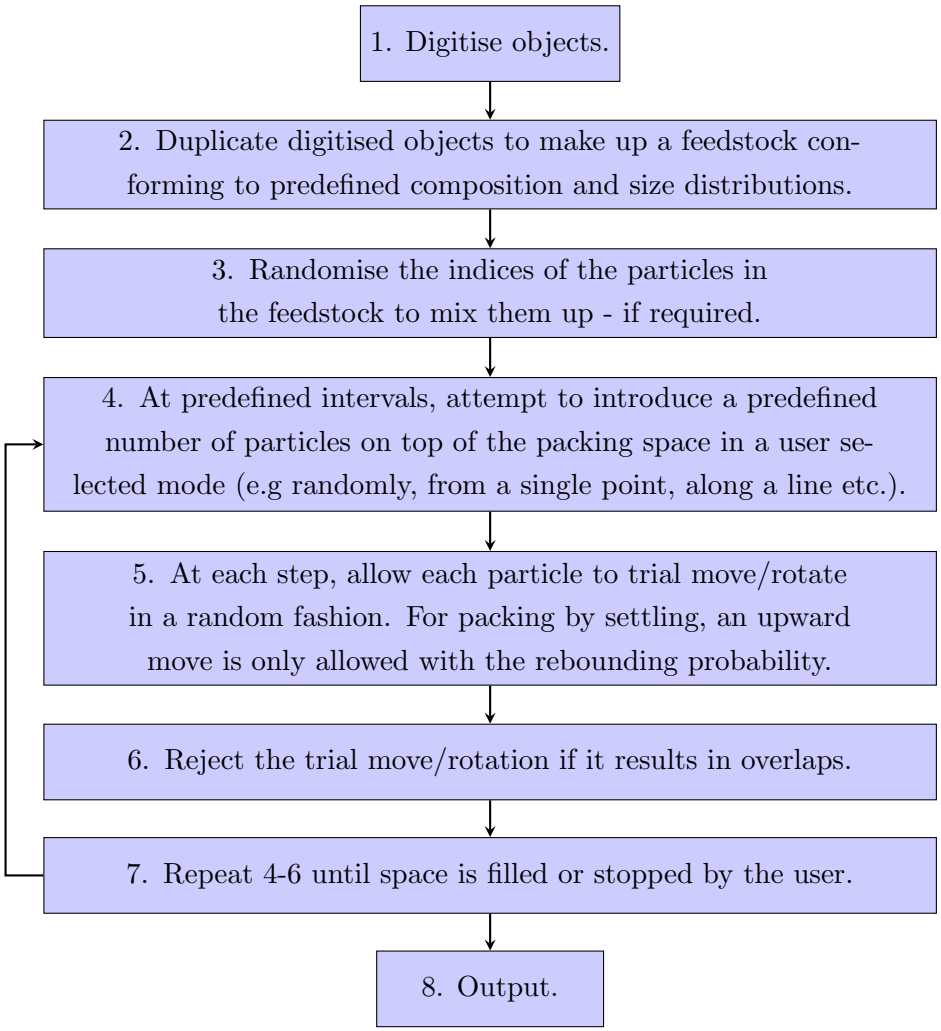

Figure 3.7: A flow diagram describing the steps employed by the DigiPac^{TM} packing algorithm (Gopinathan *et al.*, 2003).

The result is a directional (downwards) and diffusive motion of the particles that allows them to maximise the space available to create the packing. Figure 3.8 displays a completed packing simulation where 40 digitised, cylindrical pellets have been 'dropped' into a cylindrical volume using the 'hopper' method of introducing particles, where the inner diameter of the cylindrical volume is used to specify the region where pellets can be dropped from. The rebounding

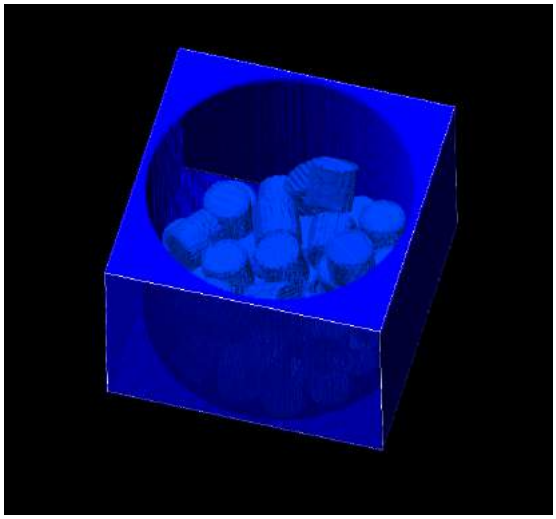

Figure 3.8: An example of the capability of the packing algorithm. 40 cylinders have been inserted into a cylindrical volume using DigiPac^{TM}.

probability, set to 0.4, then directs the cylinders down to emulate gravity and fill the space realistically. This is representative of how the DigiPac^{TM} packing algorithm will be employed in this work, as it will be used to examine the batch processing via oxidation of a number of UC pellets.

3.2.2 LBM flow modelling

DigiPac^{TM} software uses the LBM to calculate fluid flow around packings and single structures. This section will give a brief overview of the theory behind the LBM method.

The LBM method differs from the most computational fluid dynamics (CFD) methods in that it does not solve macroscopic equations such as the Navier-Stokes equations, but instead solves equations representing processes occurring at the microscopic or mesoscopic scales in an effort to then predict macroscopic effects (Chen & Doolen, 1998). Founded on kinetic theory of gas molecules being rigid spheres and elastically colliding, the LBM uses the particle velocity distribution function, the probability of a gas molecule to be found at a particular point in space with a particular velocity, to take a statistical approach to the properties of the fluid molecules being considered. From the velocity distribution function, a

number of macroscopic variables important to defining the nature of a fluid flow can be calculated, as shown in the list below. The velocity distribution function is written as $f(\mathbf{x}, \mathbf{e}, t)$, where $\mathbf{x} = (x, y, z)$, a particle's Cartesian position, and $\mathbf{e} = (e_x, e_y, e_z)$, its velocity (Aidun & Clausen, 2010).

- Mass density: $\rho(\mathbf{x}, t) = m \int f(\mathbf{x}, \mathbf{e}, t) d^3e$
- Flow velocity: $\mathbf{u}(\mathbf{x}, t) = \frac{m}{\rho} \int \mathbf{e} f(\mathbf{x}, \mathbf{e}, t) d^3e$
- Temperature: $T = \frac{m}{3R\rho} \int |\mathbf{e}|^2 f(\mathbf{x}, \mathbf{e}, t) d^3e$
- Stress tensor: $P_{\alpha\beta} = m \int (e_\alpha - u_\alpha)(e_\beta - u_\beta) f(\mathbf{x}, \mathbf{e}, t) d^3e$

where m is the mass of a molecule, d the domain size and R is the gas constant.

In order to calculate the velocity distribution function, the Boltzmann equation in the form described in Eq. 3.16 is used (Aidun & Clausen, 2010).

$$\left(\frac{\partial}{\partial t} + \mathbf{e} \cdot \nabla_{\mathbf{x}} \mathbf{a} \cdot \nabla_{\mathbf{e}} \right) f(\mathbf{x}, \mathbf{e}, t) = \mathbf{J} \tag{3.16}$$

where $\mathbf{a}$ is the acceleration of a particle, and $\mathbf{J}$ represents the effect of inter-particle collisions.

In order to solve the Boltzmann equation and use it in the LBM, Eq. 3.16 requires discretisation. This is done by restricting the velocities possessed by the particles in the simulation to a discrete set, $E = \{\mathbf{e}_0, ...\mathbf{e}_Q\}$, of Q different velocities (Aidun & Clausen, 2010). Eq. 3.16 then becomes:

For $i = 0, ..., Q$:

$$\partial_t f_i(\mathbf{x}, t) + \mathbf{e_i} \cdot \nabla f_i(\mathbf{x}, t) = \mathbf{J}_i(f) \tag{3.17}$$

where $f_i(\mathbf{x}, t) \equiv f(\mathbf{x}, \mathbf{e_i}, t)$ gives the probability of a particle with a velocity $\mathbf{e} \in E$ in an interval dt at time t within a volume of $\mathbf{dx}$ and position $\mathbf{x}$. The collision operator can be simplified as:

$$\mathbf{J}_i(f) = -A_{ij} \left(f_j - f_j^{eq} \right) \tag{3.18}$$

where the distribution function, f_i, has been expanded in terms on the Knudsen number, Kn, into equilibrium, f_i^{eq}, and non-equilibrium, f_i^{ne}, components.

A_{ij} is the quasilinear scattering matrix (Aidun & Clausen, 2010). The equilibrium distribution, f_i^{eq}, refers to the scenario where all the particles in the model have the same speed, obey Fermi statistics and collide under the restrictions of mass and momentum conservation (Chen *et al.*, 1992).

To derive the lattice Boltzmann (LB) equation from the Boltzmann equation, diffusive scaling (Junk *et al.*, 2005) is applied to Eq. 3.17. This involves the use of a scaling parameter, ε, such that $r \to r/\varepsilon$ and $t \to t/\varepsilon^2$.

For $i = 0, ..., Q$:

$$\partial_t f_i(\mathbf{x}, t) + \frac{1}{\varepsilon}\mathbf{e}_i \cdot \nabla f_i(\mathbf{x}, t) = \frac{1}{\varepsilon^2}\mathbf{J}_i(f) \tag{3.19}$$

Integrating Eq. 3.17 along the characteristics then gives the finite-difference approximation of the discrete velocity equation:

$$f_i\left(\mathbf{x} + \mathbf{e}_i\Delta_t/\varepsilon, t + \Delta_t\right) - f_i(\mathbf{x}, t) = \frac{1}{\varepsilon^2}\int_0^{\Delta_t} \mathbf{J}_i(f)\left(\mathbf{x} + \mathbf{e}_i s/\varepsilon, t + s\right) ds \tag{3.20}$$

Using the left rectangle rule (Aidun & Clausen, 2010) to approximate the integral over the collision term, $\mathbf{J}_i$, gives:

$$f_i\left(\mathbf{x} + \mathbf{e}_i\Delta_x, t + \Delta_t\right) - f_i(\mathbf{x}, t) \approx \mathbf{J}_i(f)\left(\mathbf{x}, t\right) \tag{3.21}$$

Eq. 3.21 can then be projected on to a discrete spatial lattice $\{X\}$. Rescaling t and $\mathbf{x}$ such that $\Delta_x = \Delta_t = 1$(Aidun & Clausen, 2010) gives the general LB equation:

$$f_i\left(\mathbf{x} + \mathbf{e}_i, t + 1\right) - f_i(\mathbf{x}, t) \approx \mathbf{J}_i(f)\left(\mathbf{x}, t\right) \tag{3.22}$$

This form of the LB equation, however, is rarely used in simulations due to the excessive computational cost of the collision term taking into account multi-body collisions (rather than two-body). Taking the linearised form of Eq. 3.18 with a single relaxation time, τ, (Chen *et al.*, 1992) simplifies Eq. 3.22:

$$f_i\left(\mathbf{x} + \mathbf{e}_i, t + 1\right) - f_i(\mathbf{x}, t) = -\frac{1}{\tau}\left(f_i - f_i^{eq}\right) \tag{3.23}$$

Adjusting the the relaxation time, τ, and the equilibrium function, f_i^{eq}, allows the Navier-Stokes equations for incompressible fluids to be produced (Aidun & Clausen, 2010).

3.2.3 Applying reaction kinetics

As well as producing a packed structure and calculating fluid flows, DigiPac™ is capable of applying reaction kinetics to solids present in the system using the DigiDiss™ module. Specifically, the Noyes-Whitney equation for dissolution is used (Jia & Williams, 2007):

$$\frac{\mathrm{d}W}{\mathrm{d}t} = -kS\left(C_{sat} - C_B\right) \tag{3.24}$$

where W is the weight of the solid dissolved, kg, t is the time passed, s, k is the dissolution constant, $\mathrm{m\,s^{-1}}$, S is the surface area of the solid exposed, $\mathrm{m^2}$, C_{sat} is the saturation concentration of the solid in the solvent, $\mathrm{kg\,m^{-3}}$, and C_B is the bulk concentration of the solid, $\mathrm{kg\,m^{-3}}$.

The model scans across the domain of the simulation, until a voxel representing the solid that shares an interface with a fluid voxel is found. There, Eq. 3.24 is applied to calculate a weight loss for that particular solid voxel. Since the kinetics represent a dissolution, the 'weight', or concentration, of the solid that is removed is transferred into the fluid voxel it is in contact with. Note that it could be in contact with more than one fluid voxel, meaning that it would lose n times as much weight if it were in contact with n fluid voxels. This process is carried out across the domain over a number of time steps until the solid is dissolved or the saturation concentration of the solid in the fluid is achieved.

Upon dissolution, the dissolved solid is allowed to move through the fluid according to the convective diffusive equation given below in Eq. 3.25 (Jia & Williams, 2007). Figure 3.9 illustrates the convection and diffusion of the dissolved solid through the fluid occurring during the dissolution of an Aspirin tablet (Jia & Williams, 2007).

$$\frac{\partial C}{\partial t} + \left(e_x\frac{\partial C}{\partial x} + e_y\frac{\partial C}{\partial y} + e_z\frac{\partial C}{\partial z}\right) = D\left(\frac{\partial^2 C}{\partial x^2} + \frac{\partial^2 C}{\partial y^2} + \frac{\partial^2 C}{\partial z^2}\right) \tag{3.25}$$

where C is the concentration of dissolved solid, $kg\,m^{-3}$, e_x, e_y and e_z are the fluid velocity components calculated using the LBM component of the software, $\mathrm{m\,s^{-1}}$, and D is the diffusion constant, $\mathrm{m^2\,s^{-1}}$.

Eqs. 3.24 and 3.25 are then discretised across the voxel-based domain using finite-difference methods, and solved over the duration of the reaction. The use

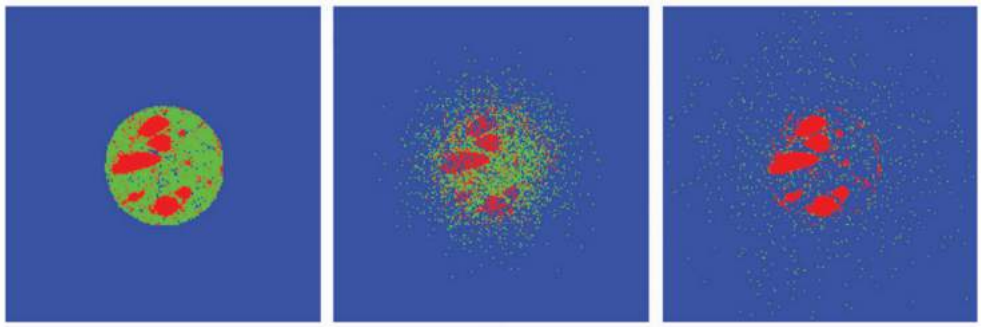

Figure 3.9: An example of a dissolution simulation using DigiDiss^{TM}. The cross section of an Aspirin tablet is shown on the left and its dissolved form on the right. The diffusion and convection of the dissolved solute can be observed in the latter two stages (Jia & Williams, 2007).

of voxels requires that when the model is solving at a particular position in the domain, it must consider effects occurring at each of the six faces of the voxel. The finite difference solution for Eqs. 3.24 and 3.25 used by DigiDiss^{TM} considers the effects occurring in the 6 directions and is given as (Structure Vision Ltd., 2013):

$$\begin{aligned} V\frac{C^{t+\Delta t}-C}{\Delta t} &= +ec_xA + ec_yA + ec_zA \\ &+ k_{i-1}A\left(C^s_{i-1}-C\right) + k_{i+1}A\left(C^s_{i+1}-C\right) \\ &+ k_{j-1}A\left(C^s_{j-1}-C\right) + k_{j+1}A\left(C^s_{j+1}-C\right) \\ &+ k_{k-1}A\left(C^s_{k-1}-C\right) + k_{k+1}A\left(C^s_{k+1}-C\right) \\ &+ DA\left(\frac{C_{i-1}-C}{\Delta x}+\frac{C_{i+1}-C}{\Delta x}\right) \\ &+ DA\left(\frac{C_{j-1}-C}{\Delta x}+\frac{C_{j+1}-C}{\Delta x}\right) \\ &+ DA\left(\frac{C_{k-1}-C}{\Delta x}+\frac{C_{k+1}-C}{\Delta x}\right) \end{aligned} \quad (3.26)$$

where $V = (\Delta x^3)$, representing the volume of a voxel, $A = (\Delta x^2)$, representing the surface area of a face of a voxel, and Δx is the width of a voxel in the x dimension where $\Delta x \equiv \Delta y \equiv \Delta z$ due to the cubic nature of the voxels. The subscripts i, j and k designate the position of the voxel relative to the current

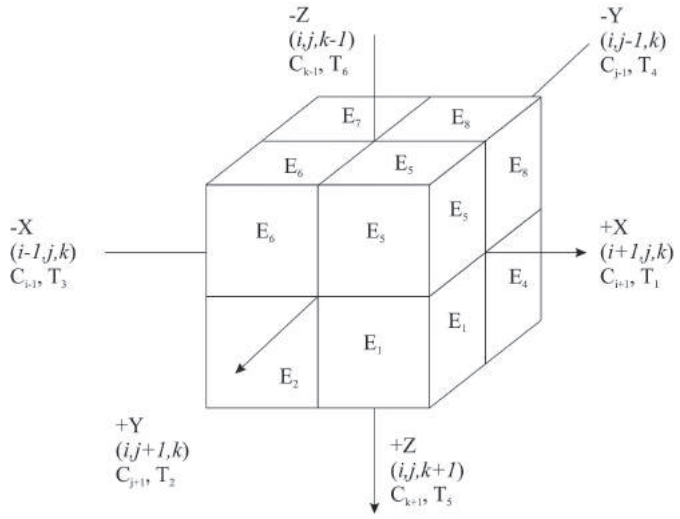

Figure 3.10: Naming conventions used in DigiPac^{TM} software. E=element (or voxel), nodes are designated by the coordinates.

voxel under consideration by the model at the coordinate (i, j, k), using the naming conventions illustrated in Figure 3.10. The values of ec_x, ec_y and ec_z are dependent on the direction of flow and given by:

$$ec_x = \begin{cases} |e_x| \left(C_{i-1} - C\right) & e_x > 0 \\ |e_x| \left(C_{i+1} - C\right) & e_x < 0 \end{cases} \tag{3.27}$$

$$ec_y = \begin{cases} |e_y| \left(C_{j-1} - C\right) & e_y > 0 \\ |e_y| \left(C_{j+1} - C\right) & e_y < 0 \end{cases} \tag{3.28}$$

$$ec_z = \begin{cases} |e_z| \left(C_{k-1} - C\right) & e_z > 0 \\ |e_z| \left(C_{k+1} - C\right) & e_x < 0 \end{cases} \tag{3.29}$$

Rearranging Eq. 3.26 for the new concentration at (i, j, k) and time $t = t + \Delta t$

gives (Structure Vision Ltd., 2013):

$$\begin{aligned} C^{t+\Delta t} &= C + \frac{\Delta t}{\Delta x}\left[ec_x + ec_y + ec_z\right] \\ &+ \frac{\Delta t}{\Delta x}\Big[k_{i-1}\left(C^s_{i-1} - C\right) + k_{i+1}\left(C^s_{i+1} - C\right) + k_{j-1}\left(C^s_{j-1} - C\right) \\ &+ k_{j+1}\left(C^s_{j+1} - C\right) + k_{k-1}\left(C^s_{k-1} - C\right) + k_{k+1}\left(C^s_{k+1} - C\right)\Big] \\ &+ \frac{D\Delta t}{\Delta x^2}\Big[(C_{i-1} - C) + (C_{i+1} - C) + (C_{j-1} - C) \\ &\qquad + (C_{j+1} - C) + (C_{k-1} - C) + (C_{k+1} - C)\Big] \end{aligned} \tag{3.30}$$

allowing calculation of the new concentration.

In order to use this software to consider the pre-oxidation of carbide fuel, it is necessary to modify the equation representing the reaction kinetics from the Noyes-Whitney equation to a more standard first order rate equation. The details of such a modification are included in Chapter 8.

3.2.4 Modelling heat transfer

The reaction kinetics necessary to simulate the oxidation also require the calculation of the temperature distribution through the system. DigiPac$^{\text{TM}}$ includes a separate module, DigiTherm$^{\text{TM}}$, designed to calculate the temperature distribution in a digital structure from convective and conductive heat transfer (Jia *et al.*, 2002; Structure Vision Ltd., 2012). This, therefore, helps form a basis for the inclusion of heat transfer into the DigiDiss$^{\text{TM}}$ module described in Chapter 8.

DigiTherm$^{\text{TM}}$ uses the Fourier equation for three-dimensional heat transfer given as:

$$C_p\frac{\partial T}{\partial t} = \frac{\partial}{\partial x}\left(k\frac{\partial T}{\partial x}\right) + \frac{\partial}{\partial y}\left(k\frac{\partial T}{\partial y}\right) + \frac{\partial}{\partial z}\left(k\frac{\partial T}{\partial z}\right) + G \tag{3.31}$$

where k is the thermal conductivity, C_p the heat capacity, T the temperature in K and G is the heat generated per unit volume.

Boundary conditions at the voxel faces can be of either Dirichlet (fixed value) or Neumann (representative of a flux) form, examples of which can be written as:

Dirichlet
$$T_0 = T_B \tag{3.32}$$

Neumann
$$-k\frac{\partial T}{\partial t} = h\left(T_0 - T_B\right) + q \tag{3.33}$$

where T_0 is the temperature of the solid at the position of interest, (i, j, k), T_B is the temperature at a boundary, h is the heat transfer coefficient at the boundary and q represents any additional heat fluxes present at that boundary.

The finite difference solution of Eq. 3.31 used is written as (Structure Vision Ltd., 2012):

$$\begin{aligned} C_p\frac{T_0^{t+\Delta t} - T_0}{\Delta t} &= k_1\frac{T_1 - T_0}{\Delta x^2} + k_2\frac{T_2 - T_0}{\Delta x^2} + k_3\frac{T_3 - T_0}{\Delta x^2} + k_4\frac{T_4 - T_0}{\Delta x^2} \\ &+ k_5\frac{T_5 - T_0}{\Delta x^2} + k_6\frac{T_6 - T_0}{\Delta x^2} + \frac{q_1 + q_2 + q_3 + q_4 + q_5 + q_6}{\Delta x} + G \\ &+ h_1\frac{T_1 - T_0}{\Delta x} + h_2\frac{T_2 - T_0}{\Delta x} + h_3\frac{T_3 - T_0}{\Delta x} \\ &+ h_4\frac{T_4 - T_0}{\Delta x} + h_5\frac{T_5 - T_0}{\Delta x} + h_6\frac{T_6 - T_0}{\Delta x} \end{aligned} \tag{3.34}$$

where T with a numerical subscript designates the temperature at a node with a position illustrated by Figure 3.10, k with a subscript is the conductivity at a particular node, q is the flux at a node and Δx is the voxel width with $\Delta x = \Delta y = \Delta z$ due to cubic voxels.

The heat transfer calculations contained within DigiTherm$^{\text{TM}}$ will require coupling to the DigiDiss$^{\text{TM}}$ module in order to use it for simulating the oxidation using temperature dependent reaction kinetics. Given the exothermicity of the oxidation, heat of reaction will have to be included into the heat transfer calculations as well as thermal radiation due to the high temperatures reached by the oxidation.

Chapter 4

One-dimensional oxidation model

4.1 Introduction

The model described in this chapter aims to simulate the oxidation of a uranium carbide fuel pellet in air and predict the temperatures reached by the pellet and reaction completion times under different initial conditions. The heat and mass transfer processes involved will be represented mathematically, and solved using the finite difference methods outlined in Section 3.1. The oxidation, assumed to be taking place in air, is written as the following two-step reaction:

$$2UC(s) + O_2(g) \rightarrow 2UO_2(s) + 2CO(g) \tag{4.1}$$

$$2CO(g) + O_2(g) \rightarrow 2CO_2(g) \tag{4.2}$$

The initial oxidation, Eq. 4.1 is a heterogeneous reaction assumed to be taking place at the surface of the carbide pellet and produces CO and UO_2. The CO is then further oxidised to CO_2 by a homogeneous reaction in the bulk gas, Eq. 4.2. For this model, the oxide product layer is assumed to instantaneously spall off from the carbide pellet surface, as suggested by Mazaudier *et al.* (Mazaudier *et al.*, 2010) and discussed in further detail in Section 6. This assumption, of an instantaneously spalling oxide product layer, allows the oxidation kinetics to be simply represented by Eq. 4.1 and 4.2. It is observed by Berthinier et al. (Berthinier *et al.*, 2009, 2011) that further oxidation of the UO_2 occurs under most conditions, producing higher oxides such as U_3O_8 and U_3O_7. However,

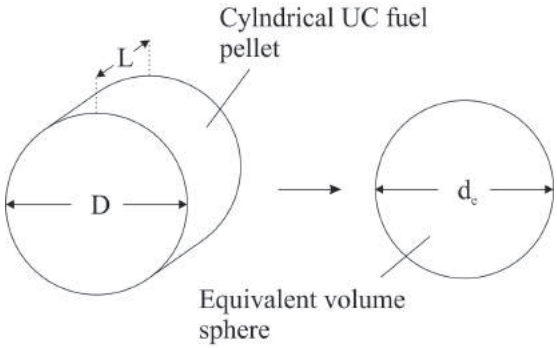

Figure 4.1: A one dimensional approximation of a UC pellet as an equivalent volume sphere.

since the UO_2 produced in the initial surface reaction is assumed to spall off, and hence not be present in this model, these further oxidations are not considered.

Another important assumption made, that is carried onto additional models in Chapters 5 and 6, is that the cylindrical uranium carbide pellet can be approximated as an equivalent volume sphere, as shown in Figure 4.1, allowing the oxidation reaction to be considered as a one-dimensional system. This assumption is deemed acceptable due to the majority of fuel pellet designs currently in use being approximately right cylinders, i.e. cylinders with length equal to their diameter, meaning that a right cylinder and its equivalent volume sphere will have equal initial volume to surface area ratios. The dimensions of the equivalent volume sphere can be calculated from the dimensions of the cylinder using the following equation:

$$d_e = 6d_c/(2d_c/L + 4) \tag{4.3}$$

where d_e is the diameter of the equivalent volume sphere, d_c is the diameter of the cylinder and L is the length of the cylinder.

Hence, for a right cylinder, where $d_c = L$, Eq. 4.3 reduces to:

$$d_e = d_c \tag{4.4}$$

Therefore, the diameter of the equivalent volume sphere is equivalent to the diameter (and length) of the right cylinder it is approximating. Importantly, the

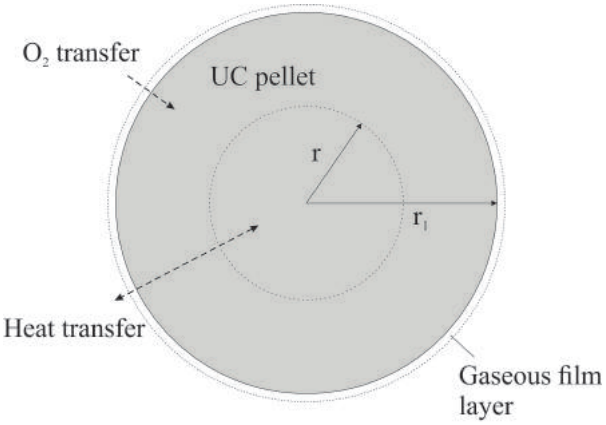

Figure 4.2: A one-dimensional diagram of the oxidation process with no adherent oxide layer present. The reaction is assumed to occur at the surface only, meaning that the only mass transfer process of importance is the diffusion of oxygen across a gaseous, external film layer surrounding the solid.

initial volume to surface area ratios of the cylinder and the sphere are equivalent in the case of a right cylinder which allows a justification of the equivalent sphere assumption.

The equivalent volume sphere assumption allows the model to be considered as a variation of the shrinking core model (Smith, 1970) as illustrated in Figure 4.2. At the surface of the carbide, i.e. where $r = r_1$, heat transfer between the solid and the bulk oxidising gas is included. The bulk gas can be assumed to be either an infinite medium at a constant temperature, or a finite volume with a variable temperature. In either case, however, there is no oxidant depletion during the reaction, the fluid is assumed to be stagnant and atmospheric pressure is assumed. The assumption of an infinite gaseous oxidant is removed at a later point to examine the effects of the secondary oxidation on the bulk gas composition, but should be assumed to be in place unless stated otherwise.

Oxygen transfers from the bulk gas to the reaction interface by diffusing through a gaseous film layer, assumed to comprise produced carbon monoxide, where it is consumed in the reaction given by Eq. 4.1. For the system shown in Figure 4.2, Figure 4.3a is a schematic of the radial O_2 and CO profiles through the gaseous film layer depicted in former figure. Additionally, Figure 4.3b is a

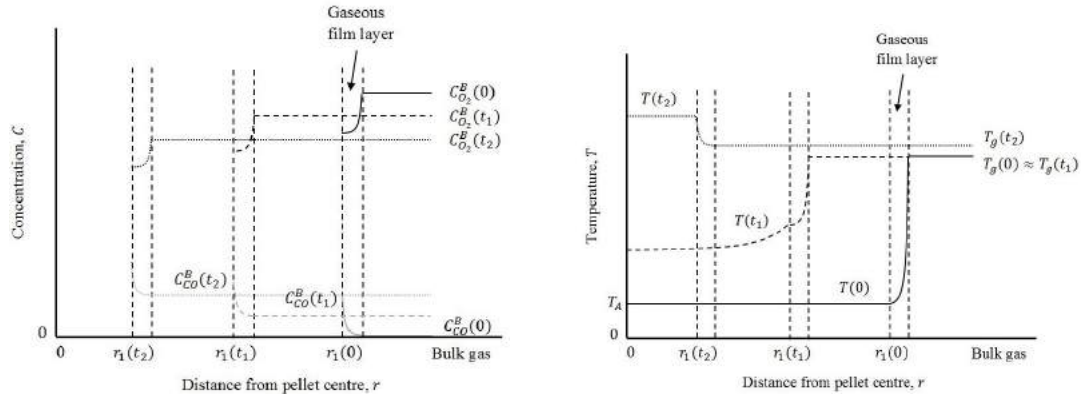

(a) O_2 and CO concentration (b) Temperature

Figure 4.3: Radial distributions of the concentration of gaseous species and temperature at three different instances during the reaction.

schematic of the radial temperature distribution. In both figures, the initial conditions are shown at time $t = 0$. The profiles are then shown at a later time $t = t_1$ and then at a further time $t = t_2$, where $t_2 > t_1$.

In Figure 4.3a, neither gas is present at $r < r_1$ due to the carbide being assumed to be non-porous. O_2 is consumed and CO generated at the reaction interface, $r = r_1$. If a finite volume of reactant gas is assumed, the bulk concentration of O_2 will deplete over time as shown. Depending on the temperature, the bulk concentration of CO will increase. This change in the composition of the bulk gas is discussed further in Section 4.2.2.

In Figure 4.3b, it can be seen that at time $t = 0$, the pellet is at ambient temperature. A short time later at $t = t_1$, a temperature gradient exists within the pellet due to sudden exposure of the pellet to the hotter bulk gas. After the reaction has been occurring for some time, at $t = t_2$, the pellet has become roughly isothermal due to the high thermal conductivity of UC and the more incremental nature of the temperature changes at the pellet surface. Due to the heat generated by the reaction, the pellet is now hotter than the bulk gas meaning that, depending on the gas volume, the bulk gas will heat up.

In both Figures 4.3a and 4.3b, the radial decrease of the carbide pellet over time is illustrated. A thickness for the gaseous film layer is not necessary as the layer is present in the model to simply represent the resistance to the mass and

heat transfer between the bulk gas and the pellet and is contained within the heat and mass transfer coefficients.

This summary provides a transient description of the temperature throughout the solid for the course of the reaction. Using this information, the reaction rate at the surface can be calculated as well as how the size of the pellet reduces over time.

Similar models are scarce in the present literature, with only one model found for the oxidation of UC (Scott, 1966) which is examined in Section 2.4.6. The present model provides a more detailed numerical method of oxidising uranium carbide, and also removes the assumption that an adherent oxide layer will form on the pellet. Mass transfer is therefore only considered to occur across the gas film layer surrounding the solid.

The non-linear set of coupled heat and mass partial differential equations comprising the model have been solved numerically through finite-difference approximations of the relevant differential equations and boundary conditions. The set of equations produced as a result were then solved using original software written in Fortran 90. The bulk of the mathematical equations used to model the physical processes that occur during the oxidation are detailed in the following section, Section 4.2. The numerical methods used to solve these equations are covered in Section 4.3, with the results and conclusions being presented in Sections 4.5 and 4.4, respectively.

4.2 Mathematical representation

The model can be thought of as a set of distinct, but dependent, sections, each requiring a solution for every time step, n:

1. Heat and mass transfer across an external gas film around the pellet.
2. Heat flow into the solid uranium carbide.
3. The resulting reaction rate and heat generated at the uranium carbide surface.
4. The resulting decrease in size of the pellet.

Due to their importance in modelling the heat and mass transfer, the reaction kinetics will be outlined first. The initial oxidation, Eq. 4.1, is a heterogeneous reaction assumed to be taking place at the surface of the carbide pellet and producing CO and UO_2. The reaction kinetics for this reaction can be described by the first order rate equation provided by Scott (Scott, 1966) in Eq. 4.5. An equation of the same form for the reaction kinetics was also suggested by (Marchand *et al.*, 2013).

$$R_C = k_C A C_{O_2}|_{r_1} \tag{4.5}$$

where R_C is is the rate of O_2 consumption at the carbide surface, A is the surface area of the reacting carbide, $C_{O_2}|_{r_1}$ is the oxygen concentration at the carbide surface and k_C, the reaction coefficient, can represented by the following Arrhenius expression (Scott, 1966):

$$k_C = k_1 \exp\left(-E_A / R T_{UC}|_{r_1}\right) \tag{4.6}$$

where k_1 is a constant provided by Scott (Scott, 1966) as $20000\,\mathrm{gmol\,cm^{-2}\,s^{-1}\,atm^{-1}}$, E_A is the activation energy reported to be $7000\,\mathrm{J\,mol^{-1}}$ (Naito *et al.*, 1976), R is the ideal gas constant and $T_{UC}|_{r_1}$ is the absolute temperature at the carbide surface.

The produced CO is then further oxidised to CO_2 by a homogeneous reaction occurring in the bulk gas, Eq. 4.2. The rate equation for this reaction, presented in Eq. 4.7, is provided by Howard *et al.* (Howard *et al.*, 1973).

$$\frac{R_{CO}}{V} = -\frac{\mathrm{d}C^B_{CO}}{\mathrm{d}t} = 1.3 \times 10^{14} \left[C^B_{CO}\right] \left[C^B_{O_2}\right]^{0.5} \left[C^B_{H_2O}\right]^{0.5} \exp\left(\frac{-30}{RT^B}\right) \tag{4.7}$$

where R_{CO} is the rate of CO oxidation, V is the volume of the surrounding gas, C^B_{CO}, $C^B_{O_2}$ and $C^B_{H_2O}$ are the concentrations of CO, O_2 and water vapour in the bulk gas, respectively, t is the time passed since the start of the reaction, R is the gas constant and T^B is the bulk gas temperature.

4.2.1 Heat and mass transfer

In order to calculate the reaction rate given by Eq. 4.5, it is necessary to know both the temperature, $T_{UC}|_{r_1}$, and concentration of oxidant, $C_{O_2}|_{r_1}$, at the reac-

tion interface through the use of heat and mass transfer equations. The conduction of heat through the solid is represented by the Fourier equation in spherical co-ordinates as:

For $t \geq 0$ and $0 < r \leq r_1(t)$:

$$\frac{\partial T_{UC}(r,t)}{\partial t} = \alpha_{UC}\left(\frac{\partial^2 T_{UC}(r,t)}{\partial r^2} + \frac{2}{r}\frac{\partial T_{UC}(r,t)}{\partial r}\right) \tag{4.8}$$

where r is the radius, $r_1(t)$ is the radius to the surface of the reacting carbide, $T_{UC}(r,t)$ is the temperature of the UC, and α_{UC} is the thermal diffusivity of UC.

The initial conditions for Eq. 4.8 are:

For $t = 0$:

$$r_1(0) > 0 \tag{4.9}$$

For $t = 0$ and $0 \leq r \leq r_1(t)$:

$$T_{UC}(r,0) = T_A \tag{4.10}$$

where T_A is the ambient temperature, assumed to be 25 °C.

Boundary conditions are then applied to Eq. 4.8 at the centre and the surface of the spherical pellet. When considering the boundary condition at the centre of the solid, where $r = 0$, Eq. 4.8 cannot be used as the second term on the right hand side is indeterminate as $\partial T/\partial r = 0$ and $r = 0$. L'Hôpital's rule must be applied to this term so that setting $r = 0$ allows Eq. 4.8 to be expressed as:

For $t \geq 0$ and $r = 0$:

$$\frac{\partial T_{UC}(0,t)}{\partial t} = 3\alpha_{UC}\left(\frac{\partial^2 T_{UC}(0,t)}{\partial r^2}\right) \tag{4.11}$$

Then, due to the symmetry of the sphere, the adiabatic heat transfer boundary condition at the centre of the sphere applicable to Eq. 4.11 is expressed as:

For $t = 0$ and $r = 0$:

$$\left.\frac{\partial T_{UC}(0,0)}{\partial r}\right|_0 = 0 \tag{4.12}$$

The boundary condition at the surface of the pellet, however, is more complex, requiring consideration of the heat and mass transfer between the solid and the bulk gas across a gaseous film layer assumed to comprise CO.

The heat flux experienced by the pellet at the surface can be written as the following boundary condition. Note that the effects of convective and radiative heat transfer, as well as heat generated by the reaction, are the terms involved.

For $t \geq 0$ and $r = r_1(t)$:

$$-\lambda_{UC} \left.\frac{\partial T_{UC}}{\partial r}\right|_{r_1} = h\left(T_{UC}|_{r_1} - T^B\right) + \epsilon_{UC}\sigma\left(T_{UC}|_{r_1}^4 - \left(T^B\right)^4\right) + \Delta H_R k_C \, C_{O_2}|_{r_1} \quad (4.13)$$

where λ_{UC} is the thermal conductivity of UC, h is the heat transfer coefficient, ϵ_{UC} the emissivity of UC, σ the Stefan-Boltzmann constant and ΔH_R is the enthalpy of the surface reaction, Eq. 4.5, calculated theoretically as $-1098\,\mathrm{kJ\,mol^{-1}}$.

The emissivity of uranium carbide is given by De Coninck et al (De Coninck *et al.*, 1975) as:

$$\epsilon_{UC} = 0.55 - 8.5 \times 10^{-5} \, T_{UC}|_{r_1} \quad (4.14)$$

The heat transfer coefficient is calculated from the Nusselt number according to Eq. 4.15:

$$h = \frac{\lambda_{fluid}\mathrm{Nu}}{2r_1} \quad (4.15)$$

where λ_{fluid} is the thermal conductivity of the fluid, usually air, surrounding the pellet, and Nu is the Nusselt number. The Nusselt number is obtained from the Ranz and Marshall correlation (Ranz & Marshall, 1952) as follows:

$$\mathrm{Nu} = 2.0 + 0.6\mathrm{Re}^{1/2}\mathrm{Pr}^{1/3} \quad (4.16)$$

where Re is the Reynolds number and Pr is the Prandtl number, given as:

$$\mathrm{Pr} = \frac{\mu c_{p_f luid}}{\lambda_{fluid}} \quad (4.17)$$

where μ is the dynamic viscosity of the fluid and $c_{p_{fluid}}$ is the specific heat capacity of the fluid.

The mass transfer, as mentioned previously, is the diffusion of oxygen through the surrounding film layer. This can be used in order to express the unknown,

time dependent variable of $C_{O_2}|_{r_1}$ with the known constant value of $C^B_{O_2}$, the O_2 concentration of the bulk gas.

Mass transfer through the film layer is expressed as:

For $t \geq 0$:

$$R^*_C = k_g A \left(C^B_{O_2} - C_{O_2}|_{r_1}\right) \tag{4.18}$$

where R^*_C is the rate of O_2 diffusion, k_g is the external diffusion coefficient and $C^B_{O_2}$ the bulk gas O_2 concentration.

The rate of this external diffusion through the gas film layer is expressed using the external diffusion coefficient:

$$k_g = \frac{D_{O_2-CO}\mathrm{Sh}}{2r_1} \tag{4.19}$$

where D_{O_2-CO} is the bulk diffusivity of O_2 through CO, and Sh is the Sherwood number.

The bulk diffusivity of oxygen through carbon monoxide can be calculated from the molecular mass of each species using the following formula given by Smith (Smith, 1970):

$$D_{O_2-CO} = \frac{1.8583 \times 10^{-7} \left(T^B\right)^{\frac{3}{2}} \left(\frac{1}{M_{O_2}} + \frac{1}{M_{CO}}\right)^{\frac{1}{2}}}{p\sigma_D \Omega} \tag{4.20}$$

where M_{O_2} and M_{CO} are the molecular weights in $\mathrm{g\,mol^{-1}}$ of oxygen and carbon monoxide respectively, p is the pressure in atm, σ_D is a constant in the Lennard-Jones potential energy function for the molecular pairing of O_2 and CO in Å and Ω is the collision integral. The assumption that the gaseous molecules are rigid spheres, made here, gives $\Omega = 1$.

The Sherwood number, similarly to the Nusselt number, can also be expressed via the Ranz and Marshall (Ranz & Marshall, 1952) correlation:

$$\mathrm{Sh} = 2.0 + 0.6\mathrm{Re}^{1/2}\mathrm{Sc}^{1/3} \tag{4.21}$$

where Sc is the Schmidt number. This is then calculated as:

$$\mathrm{Sc} = \frac{\mu}{\rho_o D_{O_2-CO}} \tag{4.22}$$

where ρ_o is the density of the fluid.

If it is assumed that the pellet is surrounded by stagnant oxidant, so $\mathrm{Re} = 0$, the Sherwood and Nusselt numbers reduce to 2.0 as reported by Rowe *et al.* (Rowe *et al.*, 1965) and deducible from Eqs. 4.16 and 4.21.

The concentration of O_2 at the UC surface $C_{O_2}|_{r_1}$ is then obtained in terms of the bulk gas O_2 concentration $C^B_{O_2}$ by equating Eqs. 4.5 and 4.18 for R_C and R^*_C respectively to give:

$$C_{O_2}|_{r_1} = \frac{k_g C^B_{O_2}}{k_g + k_1 \exp\left(-E_A/R\, T_{UC}|_{r_1}\right)} \tag{4.23}$$

This now allows the O_2 consumption rate at the reaction surface given in Eq. 4.5 to be expressed in terms of the bulk gas O_2 concentration:

$$R_C = \frac{k_1 \exp\left(-E_A/R\, T_{UC}|_{r_1}\right) A k_g C^B_{O_2}}{k_g + k_1 \exp\left(-E_A/R\, T_{UC}|_{r_1}\right)} \tag{4.24}$$

The boundary condition Eq. 4.13 now becomes:

$$-\lambda_{UC} \left.\frac{\partial T_{UC}}{\partial r}\right|_{r_1} = h\left(T_{UC}|_{r_1} - T^B\right) + \epsilon\sigma\left(T_{UC}|^4_{r_1} - \left(T^B\right)^4\right) + \Delta H_R \frac{k_1 \exp\left(-E_A/R\, T_{UC}|_{r_1}\right) k_g C^B_{O_2}}{k_g + k_1 \exp\left(-E_A/R\, T_{UC}|_{r_1}\right)} \tag{4.25}$$

Expressing the external boundary condition in this manner allows its non-linearity to be appreciated. This complicates the numerical solution which is discussed in the third section.

The Fourier heat conduction equation, Eq. 4.8, along with the initial conditions in Eqs. 4.9 and 4.10 and the boundary conditions in Eqs. 4.12 and 4.25, therefore, complete the description of the heat transfer into and through the pellet. Mass transfer across the film layer is described in Eq. 4.18, and is then used to express the reaction rate, Eq. 4.5, in terms of the bulk O_2 concentration.

4.2.2 Calculating the changing pellet size and gas composition

Eq. 4.24 provides the rate at which O_2 is consumed at the reaction interface. Using the stoichiometry of Eq. 4.1, this can be converted to the rate at which the UC depletes in $\mathrm{mol\,s^{-1}}$:

For $t \geq 0$:

$$\frac{\mathrm{d}n_{UC}}{\mathrm{d}t} = -\frac{R_C}{2} \tag{4.26}$$

where n_{UC} is the number of moles of UC.

The change in the number of moles of the uranium carbide can then be converted into a radial change by use of the molar density of uranium carbide, $\dot{\rho}_{UC}$. Therefore, to complete the model, the radius of the spherical pellet diminishes with time according to the following expression:

$$\frac{\mathrm{d}r_1}{\mathrm{d}t} = -\frac{k_1 \exp\left(-E_A/R\, T_{UC}|_{r_1}\right) k_g C^B_{O_2}}{2\dot{\rho}_{UC}\{k_g + k_1 \exp\left(-E_A/R\, T_{UC}|_{r_1}\right)\}} \tag{4.27}$$

The non-linearity of Eq. 4.25 is now further exacerbated, because both the film heat and mass transfer coefficients, h and k_g, increase with time due their dependency on the reciprocal of the pellet radius.

The effect that the secondary oxidation described in Eqs. 4.2 and 4.7 has on the composition of the bulk gas was also considered. The assumption that the bulk gas was infinite and stagnant was replaced with a finite and fixed volume (for the majority of simulations, the volume was taken to be $1\,\mathrm{m}^3$ that is not replenished.

The reaction rate provided in Eq. 4.7 has units of $\mathrm{mol\,m^{-3}\,s^{-1}}$ which was then converted to $\mathrm{mol\,s^{-1}}$ by multiplying by the total volume of gas, giving R_{CO}. The rate of CO_2 production was calculated using the stoichiometry of Eq. 4.2: for every mole of CO oxidised according to Eq. 4.7, a mole of CO_2 is produced. Oxygen depletion was included in the same fashion but combined with the effects of Eq. 4.1.

Figures 4.4a to 4.4c are plots of the changing number of moles of carbon monoxide and carbon dioxide in the bulk gas, as well as the number of moles of the solid carbide, at different bulk gas temperatures. In each case, the carbide is initially at room temperature, assumed here to be 20 °C, and the bulk oxygen concentration is $3.15\,\mathrm{mol\,m^{-3}}$ (corresponding roughly to the concentration of oxygen in air at a pressure of 1 atm). For the results depicted in Figures 4.4a, 4.4b and 4.4c, the assumption of an oxidant of infinite volume was removed.

At a bulk gas temperature of 20 °C, no CO_2 is produced as it is too cool for the reaction rate in Eq. 4.7 to reach a significantly large value to oxidise the CO. At 500 °C, the CO is completely oxidised after a small increase in concentration, and at 700 °C it is immediately oxidised to CO_2.

The effect that raising the bulk gas temperature has on increasing the rate at which the UC is consumed can also be observed in these figures.

4.3 Numerical solution

The results produced by the model, for example the plots illustrated in Figures 4.4a to 4.4c, were obtained from a numerical solution of the set of nonlinear partial and ordinary differential equations detailed in the previous section. These differential equations were solved by the application of finite-difference approximations, details of which are included in this section. Also in this section are the methods used to ensure numerical stability of the solution and to check that the solution is convergent.

The finite difference method used is known as the fully implicit backward (FIB) method (Smith, 1965), detailed in Section 3.1.1 on Page 65.

The FIB approximation of Eq. 4.8, the Fourier equation for heat transfer in a one dimensional sphere, is given by Eq. 4.28 as follows:

For $n \geq 0$ and $2 \leq i \leq k-1$:

$$\frac{T_i^{n+1} - T_i^n}{\Delta t} = \alpha_{UC} \left(\frac{v_i T_{i-1}^{n+1} - 2T_i^{n+1} + w_i T_{i+1}^{n+1}}{\Delta r^2} \right) \tag{4.28}$$

where n represents the number of time steps passed, i represents a node along the radius of the carbide, Δr is the radial increment size between these nodes, Δt is the time step size, $v_i = 1 - 1/i$, $w_i = 1 + 1/i$ and i is an integer representing the radial position where $i = 1$ at the pellet centre and $i = k$, the number of radial increments, at the solid surface. The subscript 'UC' has been dropped from the temperature, T, as the species in question is now defined by the radial position. In this model, however, only UC is present in the solid system anyway.

Eq. 4.28 is then applied across the solid. The number of radial increments, k, is held constant throughout the reaction, meaning that the radial increment

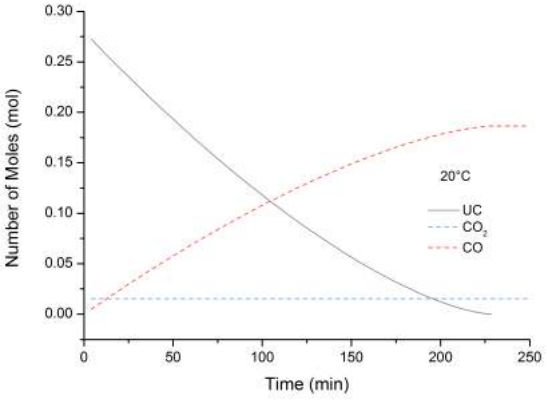

(a) A plot of the change in the number of moles of UC, CO_2, and CO at a bulk gas temperature of 20 °C.

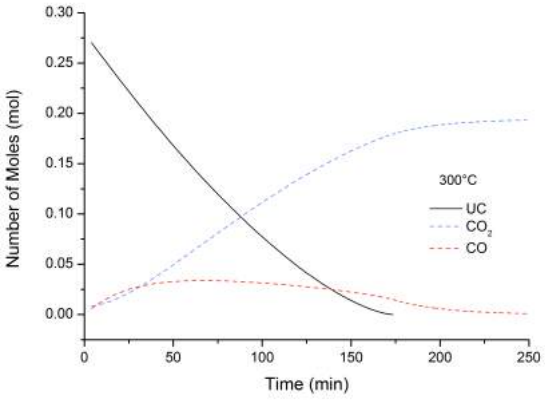

(b) A plot of the change in the number of moles of UC, CO_2 and CO at a bulk gas temperature of 300 °C.

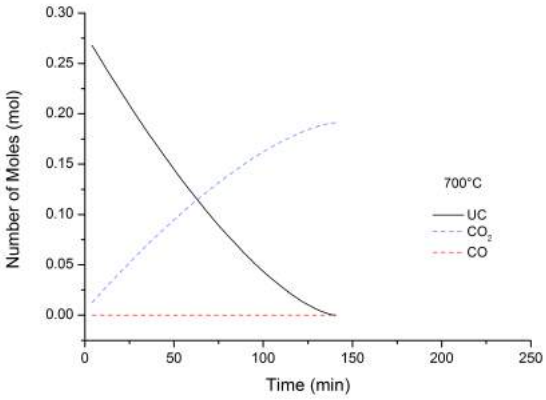

(c) A plot of the change in the number of moles of UC, CO_2 and CO at a bulk gas temperature of 700 °C.

Figure 4.4: Illustrations of the changing number of moles of carbon dioxide and carbon and monoxide in the bulk gas over time and at different temperatures. The depletion of uranium carbide can also be observed.

size varies with time. At the boundaries, where $i = 1$ or $i = k$, application of Eq. 4.28 creates imaginary points beyond the region on interest, $0 \leq r \leq r_1$. Finite-difference approximations of the boundary conditions must therefore be taken and applied to Eq. 4.28 at the relevant radial positions. When the appropriate boundary conditions and their finite-difference approximations have been taken into account, the resulting equations can be arranged into a tri-diagonal matrix. For this purpose, Eq. 4.28 is expressed in the form shown in Eq. 4.29 where the unknown terms are positioned on the left side of the equation:

For $n \geq 0$ and $2 \leq i \leq k - 1$:

$$-M_{UC} v_i T_{i-1}^{n+1} + (1 + 2M_{UC})\, T_i^{n+1} - M_{UC} w_i T_{i+1}^{n+1} = T_i^n \tag{4.29}$$

where $M_{UC} = \alpha_{UC} \Delta t / \Delta r^2$

The boundary condition at the centre of the solid is considered first, where the Fourier equation is replaced by Eq. 6.9 due to the application of L'Hôpitals rule. Applying the FIB method to Eq. 4.11allows it to be expressed as Eq. 4.30:

For $n \geq .0$ and $i = 1$:

$$\frac{T_1^{n+1} - T_1^n}{\Delta t} = 3\alpha_{UC} \left(\frac{v_1 T_0^{n+1} - 2T_1^{n+1} + w_1 T_2^{n+1}}{\Delta r^2} \right) \tag{4.30}$$

The problem term in Eq. 4.30 is T_0^{n+1}, occurring at the imaginary point $i = 0$. In order to remove it a central difference approximation of the boundary condition from Eq. 4.12 is used. Central difference approximations are used due to the FIB approximation of the Fourier equation being second order. The resulting approximation can be found below in Eq. 4.31:

For $n \geq 0$ and $i = 1$:

$$\frac{T_2^n - T_0^n}{2\Delta r} = 0 \tag{4.31}$$

Substituting Eq. 4.31 into Eq. 4.30 to remove T_0^{n+1} gives an equation that can be inserted into the first row of the tri-diagonal matrix:

For $n \geq 0$ and $i = 1$:

$$(1 + 6M_{UC})\, T_1^{n+1} - 6M_{UC} T_2^{n+1} = T_1^n \tag{4.32}$$

The other boundary condition requiring consideration is at the solid surface, where $i = k$. A central difference approximation is taken of Eq. 4.25:

For $n \geq 0$ and $i = k$:

$$\frac{T^n_{k+1} - T^n_{k-1}}{2\Delta r} = -\frac{h^n}{}(T^n_k - T^B) - \frac{\epsilon\sigma}{\lambda_{UC}}((T^n_k)^4 - (T^B)^4) - \frac{\Delta H_R}{\lambda_{UC}} \frac{k_1 \exp(-E_A/RT^n_k) k^n_g C^B_{O_2}}{k^n_g + k_1 \exp(-E_A/RT^n_k)} \quad (4.33)$$

Rearranging this equation for T^n_{k+1} and substituting that value into Eq. 4.29 with $i = k$ results in the following equation:

$$- 2M_{UC}T^{n+1}_{k-1} + \left(1 + 2M_{UC} + 2M_{UC}u_{UC} + \frac{2M_{UC}u_{UC}}{h^{n+1}}\epsilon\sigma(T^{n+1}_k)^3\right) T^{n+1}_k - \frac{2M_{UC}u_{UC}}{h^{n+1}}\epsilon\sigma(T^B)^4 + \frac{2M_{UC}u_{UC}\Delta H}{h^{n+1}} \frac{k_1 \exp(-E_A/RT^{n+1}_k) k^{n+1}_g C^B_{O_2}}{k^{n+1}_g + k_1 \exp(E_A/RT^{n+1}_k)} = T^n_k + 2M_{UC}u_{UC}T^B \quad (4.34)$$

where $u_{UC} = \Delta r w_k h/\lambda_{UC}$.

Eq. 4.34, however, is non-linear as solving for T^{n+1} requires prior knowledge of T^{n+1}_k in order to calculate the heat of reaction and radiation terms present. It must therefore be linearised by multiplying both the numerator and denominator of the heat of reaction term by T^{n+1}_k, allowing it to take the tri-diagonal form shared by Eqs. 4.29 and 4.32. This must also be done on the terms containing dependent on T^B, which can also be subject to change over time.The calculation is then iterated a number of times until a set tolerance limit is reached. For the first iteration, R_C is calculated assuming $T^{n+1}_k = T^n_k$. The solution is then recalculated at the same time step using the newly calculated value for T^{n+1}_k. Letting z represent the number of iterations starting at $z = 1$, Eq. 4.34 is re-

written as:

$$
\begin{aligned}
&- 2M_{UC}T_{k-1}^{n+1,z+1} + \Bigg\{ 1 + 2M_{UC} + 2M_{UC}u_{UC} + \frac{2M_{UC}u_{UC}}{h^{n+1}}\epsilon\sigma(T_k^{n+1,z})^3 \\
&- \frac{2M_{UC}u_{UC}}{h^{n+1}T_k^{n+1,z}}\epsilon\sigma(T^B)^4 \\
&+ \frac{2M_{UC}u_{UC}\Delta H}{h^{n+1}T_k^{n+1,z}} \frac{k_1 \exp\left(-E_A/RT_k^{n+1,z}\right) k_g^{n+1} C_{O_2}^B}{k_g^{n+1} + k_1 \exp\left(E_A/RT_k^{n+1,z}\right)} \Bigg\} T_k^{n+1,z+1} \\
&\qquad = T_k^n + 2M_{UC}u_{UC}T^B \quad (4.35)
\end{aligned}
$$

This iterative process is then carried out until the following criterion is satisfied:

$$
\frac{T_k^{n+1,z+1} - T_k^{n+1,z}}{T_k^{n+1,z+1}} < \text{Tolerance for all temperatures} \quad (4.36)
$$

The tolerance can be set to any value, generally around 0.1%, with the solution becoming more stable as it is decreased.

A further iterative step is also required due to the heat and mass transfer coefficients, h and k_g respectively, being dependent on the radius adding further non-linearity to the solution.

To solve the tri-diagonal matrix, values of h^{n+1} and k_g^{n+1}, present in Eq. 4.35, are required but are dependent on the radial increment size which is only known at the current time step, n. Similarly to the iteration of the temperature values, h^{n+1} and k_g^{n+1} are solved assuming $r^{n+1} = r^n$, and the entire solution, including the final radial change, is iteratively recalculated until a criterion similar to that in Eq. 4.36, but applied to the radius, is satisfied.

The resulting tri-diagonal matrix comprising Eq. 4.29 and bounded by Eqs. 4.32 and 4.34 is displayed in Eq. 4.39 on Page 97, with the unknown values of T^{n+1} included on the left hand side. It was solved at each time step using the Thomas algorithm (Chang, 1981), applied in original code written in Fortran 90, providing the temperature distributions at the time step $n+1$. This information could then be used to calculate the new carbide radius, r_1, at each time step using a backward difference approximation of Eq. 4.27:

$$
r_1^{n+1} = r_1^n - \frac{\Delta t k_1 \exp\left(-E_A/RT_k^{n+1}\right) k_g^{n+1} C_{O_2}^B}{2\dot{\rho}_{UC}\left\{k_g^{n+1} + k_1 \exp\left(-E_A/RT_k^{n+1}\right)\right\}} \quad (4.37)
$$

Table 4.1: The effect of varying the number of increments on the oxidation completion time as a test for convergence.

Number of radial increments	Oxidation completion time (min)	Computational time (s)
5	261.8	0.2028
10	262.3	0.5772
20	262.5	2.995
50	262.5	34.66
100	262.5	250.2
200	262.6	1984

The time loop was continued until the percentage of carbide oxidised became greater than 99%.

4.3.1 Ensuring numerical stability and convergence

When using finite-difference methods, it is vital to ensure that the solution remains stable so that the output can be trusted. The general stability criteria used in this work is the Courant-Friedrichs-Lewy rule (Smith, 1965), adapted for the various constants and increment sizes that affect stability in this particular case.

$$\Delta t = \frac{1}{2\alpha_{UC}} \Delta r^2 \tag{4.38}$$

The time step size is recalculated at every time step. The new values for the radial increment sizes and thermal and mass diffusion constants are worked out using the previous solution, including the iteration of the temperature and radial increment size, and applied to Eq. 4.38 to calculate the time step size. The solution is then converged using this time step and the process is repeated. Through this careful control of the time step size, it is ensured that the solution remains stable throughout.

In order to check for mathematical convergence, the model was run using the same input parameters but using a different number of radial increments and

$$
\begin{bmatrix}
1+6M_{UC} & -6M_{UC} & 0 & 0 & \cdots & \cdots & \cdots & 0 \\
-M_{UC}v_2 & 1+2M_{UC} & -M_{UC}w_2 & 0 & \cdot & \cdot & \cdot & 0 \\
0 & -M_{UC}v_3 & 1+2M_{UC} & -M_{UC}w_3 & \cdot & \cdot & \cdot & 0 \\
\vdots & \cdot & \ddots & \ddots & \ddots & \cdot & \cdot & \vdots \\
\vdots & \cdot & \cdot & \ddots & \ddots & \ddots & \cdot & \vdots \\
\vdots & \cdot & \cdot & \cdot & \ddots & \ddots & \ddots & \vdots \\
0 & 0 & \cdot & \cdot & 0 & -M_{UC}v_{k-1} & 1+2M_{UC} & -M_{UC}w_{k-1} \\
0 & 0 & \cdots & \cdots & 0 & 0 & -2M_{UC} & 1+2M_{UC}+2M_{UC}u_{UC}+fn(T_k^{n+1})
\end{bmatrix}
$$

$$
\times \begin{bmatrix} T_1^{n+1} \\ T_2^{n+1} \\ T_3^{n+1} \\ \vdots \\ \vdots \\ \vdots \\ T_{k_1}^{n+1} \\ T_k^{n+1} \end{bmatrix} = \begin{bmatrix} T_1^{n} \\ T_2^{n} \\ T_3^{n} \\ \vdots \\ \vdots \\ \vdots \\ T_{k-1}^{n} \\ T_k^{n}+2M_{UC}u_{UC}T^B \end{bmatrix} \tag{4.39}
$$

where $fn(T_k^{n+1}) = \frac{2M_{UC}u_{UC}}{h^{n+1}}\epsilon\sigma(T_k^{n+1})^3 - \frac{2M_{UC}u_{UC}}{h^{n+1}T_k^{n+1}}\epsilon\sigma(T^B)^4 + \frac{2M_{UC}u_{UC}\Delta H}{h^{n+1}T_k^{n+1}}\frac{k_1\exp\left(-E_A/RT_k^{n+1}\right)k_g^{n+1}C_{O_2}^B}{k_g^{n+1}+k_1\exp\left(E_A/RT_k^{n+1}\right)}$

hence different values for the initial increment size. The results of this can be seen in Table 4.1.

The minor changes observed in the solution upon varying the initial increment size showed that the model is convergent, especially when more than 50 increments are used. Richardson's deferred approach to the limit (Smith, 1965) can be used in this case to extrapolate the results from three different increment sizes to predict the solution for an infinitely small increment size. Taking the first three results from Table 4.1 and applying them to Eqs. 6.51 and 6.52 allows the prediction of such a solution:

$$u = \frac{h_2^p u_1 - h_1^p u_2}{h_2^p - h_1^p} \tag{4.40}$$

where u_1 and u_2 are the solutions (completion times) at initial radial increment sizes of h_1 and h_2, and p can be calculated from:

$$2^p = \frac{u_2 - u_1}{u_3 - u_2} \tag{4.41}$$

where u_3 is the solution at h_3, and $h_3 = \frac{1}{2}h_2 = \frac{1}{4}h_1$.

A value of $p = 1.322$ is obtained, leading to the calculation of $u = 262.6\,\text{min}$. This allows the conclusion that the model successfully converges on the solution as the number of increment sizes is increased.

4.4 Results

The complete oxidation model is capable of predicting the reaction completion time and the transient temperature distribution throughout the solid over the course of the reaction. An example of these capabilities can be seen in Figure 4.5 which displays the temperature distribution throughout the solid and the reduction in the solid radius over time, as well as the overall reaction completion time. Figure 4.6 examines the radial temperature gradient more closely at two instances of time during the reaction. For both figures, a pellet of radius 0.935 cm initially assumed to be at 25 °C is exposed to a bulk gas of a volume of $1\,\text{m}^3$ at an initial temperature of 500 °C. The bulk gas is taken to be air with an oxygen concentration of $3.15\,\text{mol}\,\text{m}^{-3}$.

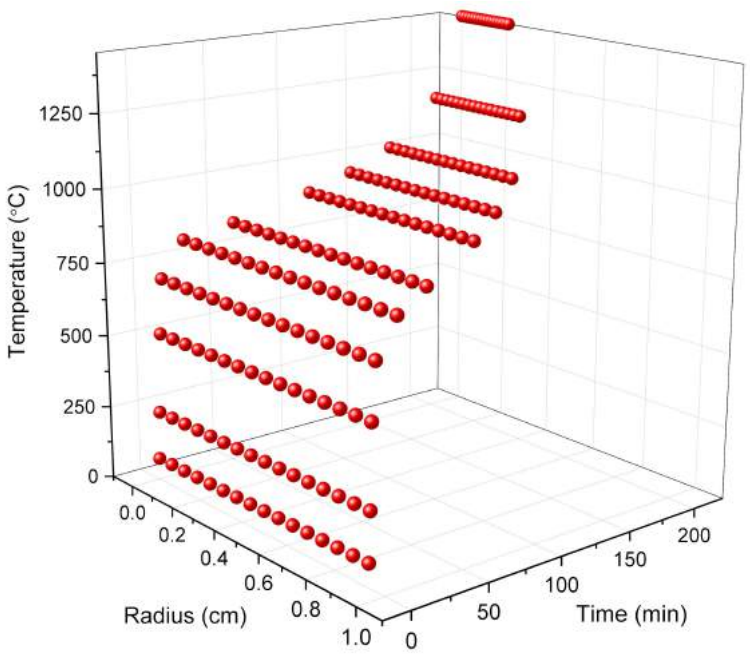

Figure 4.5: Radial temperature distribution over time illustrating both the shrinking radius and the thermal response of the pellet.

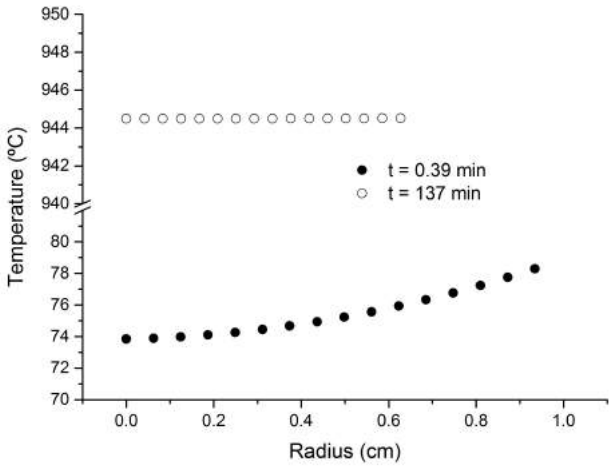

Figure 4.6: Two instantaneous temperature profiles plotting the temperature gradient across the carbide radius.

In Figure 4.5 an initial steep increase in the temperature along the radius is observed as the pellet experiences a large convective heat flux at the surface due to exposure to the hotter bulk gas. It overshoots the bulk gas temperature, however, due to the generation of heat from the oxidation reaction. There is then a rough plateau for the majority of the reaction as the heat generation is similar to the heat lost to the bulk gas. This is in part due to the effect of radiative heat loss becoming more significant at higher temperatures. Then, toward the end of the reaction as the pellet's radius becomes small, there is a temperature spike and a degree of thermal runaway.

Figure 4.6, a plot of two radial temperature profiles taken at different times during the reaction, illustrates the radial temperature gradient in the carbide in more detail. Initially, when the pellet is exposed to the hotter bulk gas, a temperature gradient exists with the surface of the carbide being hotter. As the reaction proceeds however, the temperature gradient becomes minimal due to the high conductivity of uranium carbide, as illustrated in the plot at $t = 137\,\mathrm{min}$.

The ignition effect displayed in Figure 4.5 can be explained through examination of the competing heat fluxes acting on the pellet: the heat generated by the reaction and the heat exchanged with the bulk gas. Figure 4.7 displays the heat exchanged with the bulk gas subtracted from the heat generated to create a value that is then compared against the surface temperature of the pellet over time.

Figure 4.7 shows that the overall heat flux into the pellet increases toward the end of the reaction, hence the sharp rise in surface temperature. This is due to heat generation from the reaction having a greater temperature dependence on the surface temperature than the heat loss via radiation and convection and therefore increases in magnitude faster with the steadily increasing surface area.

Sensitivity studies were carried out with the model to investigate the effects of varying the input parameters, such as bulk gas temperature and oxygen concentration, on the temperatures reached and reaction completion time.

Figure 4.8 is a plot showing how the surface temperature of the carbide pellet and the fraction of carbide oxidised increase over time. Each relationship is presented at three different bulk gas temperatures so that the effects of varying it can be observed. The oxygen concentration was again assumed to be $3.15\,\mathrm{mol\,m^{-3}}$,

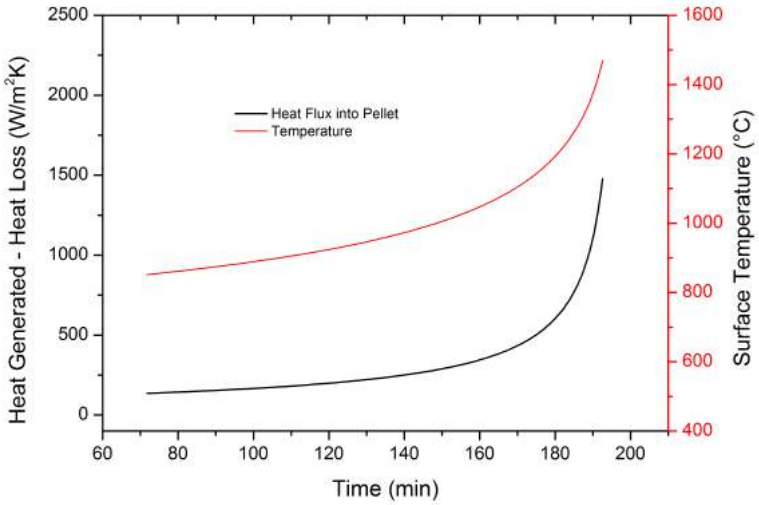

Figure 4.7: A plot of the difference between the heat generated and the heat lost to the bulk gas in black, and the surface temperature of the pellet in red, against time. The plot is taken from the latter stages of the reaction to concentrate on the region of interest.

the radius to be 0.935 cm and the initial temperature of the pellet was 25 °C. Table 4.2 provides more quantitative detail of the results.

Figure 4.8 and Table 4.3 indicate that increasing the initial temperature of the oxidising gas greatly decreases the reaction completion time, whilst also having a significant effect on the peak temperature reached. There is also a more significant increase in the final bulk gas temperature, most likely due to the hotter pellet and a faster rate of carbon monoxide oxidation in the gas. Figure 4.9 is a similar graph illustrating the effects of different bulk oxygen concentrations, using an initial bulk gas temperature of 250 °C and the same initial pellet conditions. Table 4.3 provides the numerical results.

Figure 4.9 and Table 4.3 illustrate that increasing the oxygen concentration in the bulk gas has a similar effect to increasing the temperature. When reduced to $0.788\,\mathrm{mol\,m^{-3}}$, the rate of oxidation is slowed significantly causing a much more modest temperature increase. The effects on the final bulk gas temperature are also slightly more unpredictable, as both the amount of time available for the secondary oxidation and the temperature at which it is occurring are factors.

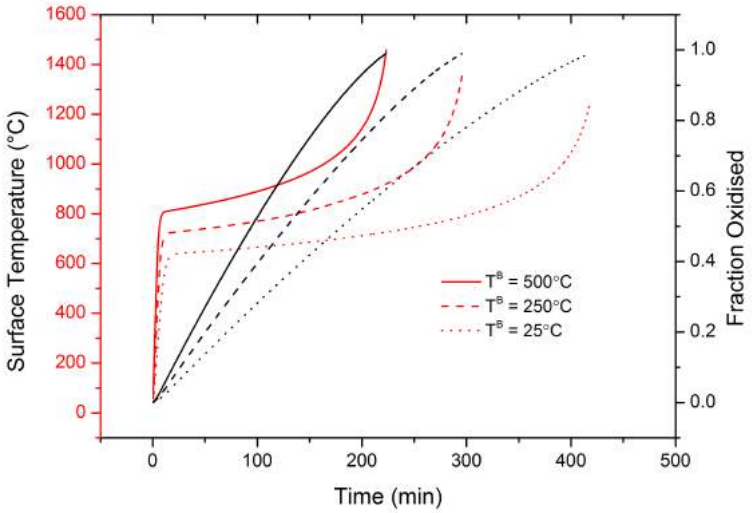

Figure 4.8: The surface temperature of the carbide (red) and the fraction oxidised (black) versus time, carried out at bulk gas temperatures of 25, 250 and 500 °C.

Another parameter that was varied to test the sensitivity of the model was the Reynolds number of the oxidising fluid surrounding the carbide pellet. Initially and for the previous results it has been assumed to have a value of Re = 0, indicating a stagnant fluid. Increasing the Reynolds number should have the effect of increasing the heat and mass transfer coefficients dictating the rate of heat and mass exchange between the bulk gas and the pellet, as described in Eqs. 4.15-4.16 and 4.19-4.21. Figure 4.10 illustrates how this increase leads to a faster reaction rate as the Reynolds number is increased. This increase is due

Table 4.2: The effects of the initial bulk gas temperature on the peak surface temperature, reaction completion time and the final bulk gas temperature.

Initial bulk gas temperature (°C)	Peak surface temperature (°C)	Reaction completion time (min)	Final bulk gas temperature (°C)
25.0	1253	418	57.0
250.0	1365	296	381.0
500.0	1458	223	644.8

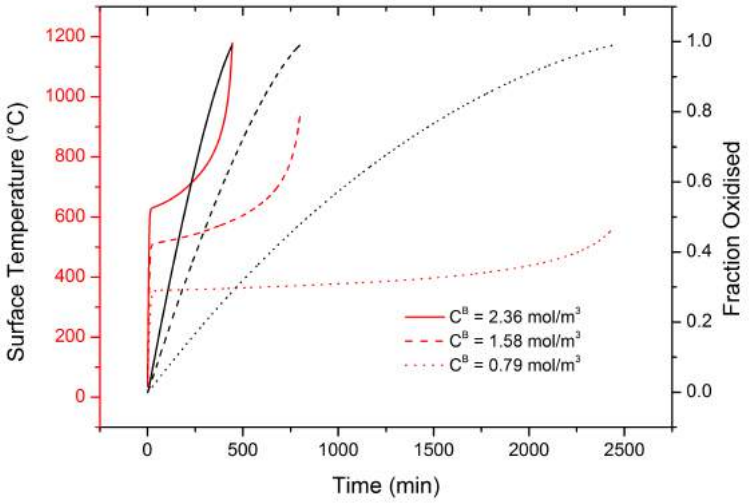

Figure 4.9: The surface temperature of the carbide (red) and the fraction oxidised (black) versus time, carried out at bulk gas oxygen concentrations of 0.788, 1.58 and 2.36 mol m^{-3}.

to the rate limiting step, the diffusion of oxygen across the external gas film, being accelerated by an increased value of the external diffusion coefficient, k_g. A bulk gas temperature of 250 °C was used with an initial oxygen concentration of 3.15 mol m^{-3} and a pellet of radius 0.935 cm.

The effect of decreasing the volume of oxidising fluid was also investigated. Due to depletion of the oxygen present in the fluid according to Eq. 4.24, a minimum volume required for complete oxidation of the carbide can be found. Figure 4.11 displays the effect of varying the volume of the bulk fluid on the fraction oxidised. At a bulk gas volume of 1 m^3, the oxygen consumption is minimal. When the volume of gas is decreased to 0.2 m^3, the change in rate of reaction is small, but there is a large decrease in the final oxygen concentration; from 2.78 mol m^{-3} at $V = 1$ m^3 to 1.31 mol m^{-3} at $V = 0.2$ m^3. If the volume is decreased by a factor of 10, to 0.1 m^3, it can be seen in Figure 4.11 that there is not enough oxygen present in the bulk gas to complete the oxidation.

In summary, the model predicts for a typical orthocylindrical pellet size of 9.35 mm that the oxidation generally takes between 200 min to 2000 min depending on the input parameters. Temperatures in the pellet reach a maximum as

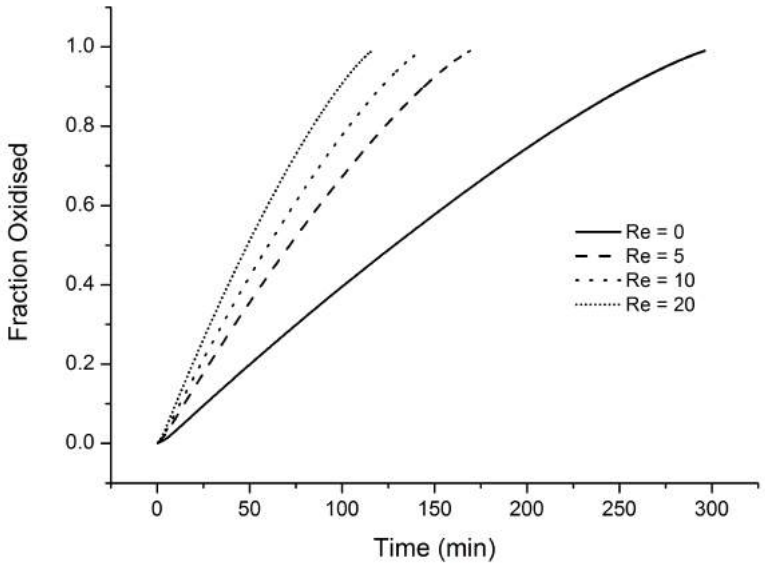

Figure 4.10: A plot of the fraction of uranium carbide oxidised versus time with the oxidising fluid flow at different Reynolds numbers.

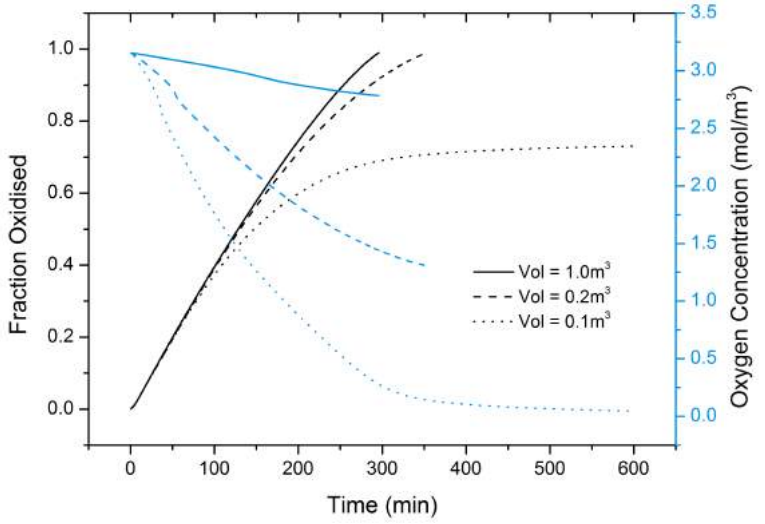

Figure 4.11: The fraction oxidised in black and the oxygen concentration in the bulk gas in blue versus time.

Table 4.3: The effects of the bulk gas oxygen concentration on the peak surface temperature, reaction completion time and the final bulk gas temperature.

Bulk gas oxygen concentration ($\mathrm{mol\,m^{-3}}$)	Peak surface temperature (°C)	Reaction completion time (min)	Final bulk gas temperature (°C)
0.788	563.5	2442	657.6
1.58	938.4	798.7	673.5
2.36	1179	444.2	663.2

the reaction completes and reached 1458 °C when the bulk gas was set to 500 °C, highlighting the high exothermicity of the reaction. Lower oxygen concentrations and bulk gas temperatures can reduce the temperature rise significantly. For example, a relatively small temperature peak of 563 °C at an initial gas temperature of 250 °C and oxygen concentration of $0.788\,\mathrm{mol\,m^{-3}}$ could suggest that these values represent safe operating conditions for the oxidation.

4.5 Conclusions

In this chapter, a transient mathematical model with a moving-boundary for the oxidation of a UC pellet coupled with a secondary oxidation of CO included in the surrounding gas phase is developed. The model for the UC is represented by the Fourier equation at any instant of time with a non-linear boundary condition at the outer surface that moves with time. This boundary condition accommodates the non-linear reaction rate term for the diffusion of species to and from the outer surface as well as heat transfer by convection and thermal radiation.

The partial and ordinary differential equations of the model are solved numerically by the application of implicit and explicit finite difference approximations. The resulting set of non-linear algebraic equations is highly non-linear, as shown in Eq. 4.34, and linearisation is used to obtain a solution at each time increment. Convergence at each time step is enforced before proceeding to the next time increment.

The numerical stability of the model is controlled by a dynamic time step size calculated from the Courant-Friedrichs-Lewy condition, which accommodates the change in the size of the radial increment. The numerical solution is checked for convergence by progressively increasing the number of radial increments and using Richardsons deferred approach to the limit methodology.

Reaction rate and completion time, temperature profiles in the pellet and gas composition changes can be predicted. Sensitivity studies have been carried out to establish the effect the input parameters can have on the predicted results. It is applicable to oxidations of UC pellets at higher O_2 partial pressures ($\geq$ 20 kPa): the range reported where the oxide product layer does not adhere by Mazaudier *et al.* (Mazaudier *et al.*, 2010) and Mukerjee (Mukerjee *et al.*, 1994). The model is therefore significant to the field by virtue of being valid at these higher O_2 partial pressures, unlike the only existing UC oxidation mode, Scotts model (Scott, 1966), that includes an adherent product layer.

However, the lack of a product layer means that the model is not applicable to lower O_2 partial pressures. Also, the model makes the assumption that UC pellets, which like most nuclear fuel pellets are cylindrical, can be accurately represented as spheres according to the equivalent volume sphere assumption. This assumption, as with any assumption of symmetry, is also prone to being inaccurate for damage pellets or pellets that disintegrate upon oxidation. Full symmetry also suggests that the pellet is not resting on a surface as would be expected in reality, but it suspended within the bulk gas. A further limitation of the model is that the reaction kinetics are simplified with only one uranium oxide phase, meaning heat outputs from the reaction may be different as different phases are produced. The age of rate constant found in the literature for the oxidation kinetics is also a concern, and could need updating should a new value or data useable for fitting be published.

Nonetheless, the model provides a valuable tool to UC fuel reprocessing, by allowing predictions of temperatures reached during oxidations at different conditions to outline safe operating conditions. Additionally, should new data arise, it is capable of being used to fit new oxidation parameters such as the rate constant. It also constitutes an excellent starting point from which further, more

case-specific models can be constructed from a stable, convergent and well-defined numerical solution.

Chapter 5

One-dimensional dissolution model

The model described in this section is designed to simulate the dissolution of a uranium carbide fuel pellet in nitric acid. This is achieved by employing similar methods to those used in modelling the oxidation of uranium carbide as described in Chapter 4. Specifically, the approximation of the carbide pellet as a one dimensional sphere and the heat transfer equations are virtually the same with the difference being in the reaction kinetics. Figure 5.1 is an illustration of how the dissolution system is considered for the model: a spherical, non-porous UC pellet is submerged in HNO_3 without contact with any vessel surface.

Given the lack of a temperature gradient within the UC pellet on account of its high thermal conductivity as discussed in Chapter 4, and the fact that the enthalpy change for the dissolution reaction is lower than that of the oxidation reaction ($\Delta H = -1098\,\mathrm{kJ\,mol^{-1}}$ to $\Delta H = -945\,\mathrm{kJ\,mol^{-1}}$), a reduced model for the heat transfer is employed. A description of this reduced model and how it can reduce computational time is included in Section 5.1.

5.1 Reduced heat transfer model

As indicated by the one dimensional oxidation model without an oxide layer present, the temperature gradient through the uranium carbide pellet is so minimal it can be reasonably assumed to be 0. It could, therefore, be assumed that

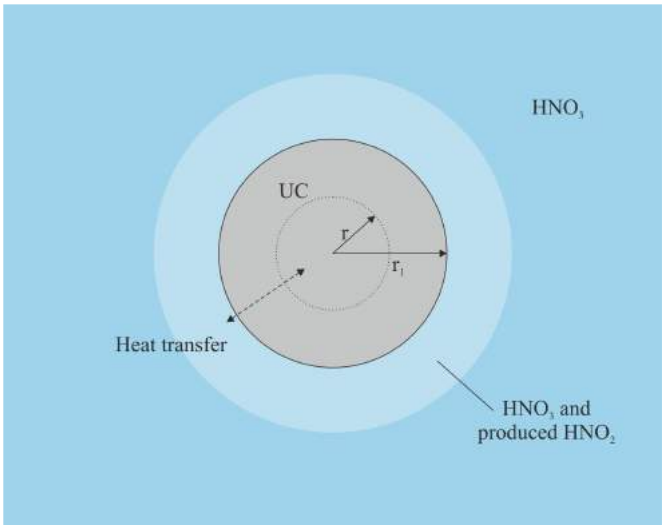

Figure 5.1: A representation of the dissolution of a uranium carbide pellet again assumed to be an equivalent volume sphere so the system can be approximated in one dimension. The reaction takes place at the surface with nitric acid and is strongly catalysed by the nitrous acid produced.

the temperature distribution through the pellet is represented by a single value, the *average* temperature within the carbide, rather than a number of values along the radius. This idea can be confirmed by calculating the Biot number, Bi, for the system and confirming that it is less than 0.1, the value at which the internal temperature gradient is negligible. It is calculated as:

$$\mathrm{Bi} = \frac{hr_1}{\lambda_{UC}} = 2.94 \times 10^{-3} \tag{5.1}$$

allowing confirmation that an insignificant temperature gradient within the UC pellet should be expected.

The assumption of a representative average temperature allows a reduced model to be produced in place of the heat transfer model characterised in the previous chapter, reducing the need for the computationally expensive solution of the tri-diagonal matrix. The assumption can be written as:

For $0 < r < r_1$ and $t \geq 0$:

$$\frac{\partial T_{UC}}{\partial r} = 0 \tag{5.2}$$

The average temperature is represented as:

$$\bar{T}_{UC} = \frac{\int_0^{r_1} 4\pi r^2 T_{UC} dr}{\int_0^{r_1} 4\pi r^2 dr} \tag{5.3}$$

where $\bar{T}_{UC}$ is the average temperature along the radius of the carbide pellet. Eq. 5.3 simplifies to:

$$\bar{T}_{UC} = \frac{3}{r_1^3} \int_0^{r_1} r^2 T_{UC} dr \tag{5.4}$$

To show how this assumption then simplifies the heat distribution calculations, first the one dimensional Fourier equation represented in Eq. 4.8 on page 86 must be integrated across the radius:

$$\int_0^{r_1} r^2 \frac{dT_{UC}}{dr} dr = \alpha_{UC} \int_0^{r_1} \frac{d}{dr}\left(r^2 \frac{dT_{UC}}{dr}\right) dr \tag{5.5}$$

$$\frac{d}{dt} \int_0^{r_1} r^2 T_{UC} dr = \alpha_{UC} \int_0^{r_1} \frac{d}{dr}\left(r^2 \frac{dT_{UC}}{dr}\right) dr \tag{5.6}$$

Then, substitute Eq. 5.4 into Eq. 5.6 to produce an equation describing the change in the average temperature of the carbide over time.

$$\frac{r_1^3}{3} \frac{d\bar{T}_{UC}}{dt} = \alpha_{UC} \left[r_1^2 \left. \frac{dlT_{UC}}{dr} \right|_{r_1} - r^2 \left. \frac{dT_{UC}}{dlr} \right|_0 \right] \tag{5.7}$$

Given that the two terms on the right hand side of Eq. 5.7 represent the boundary conditions at the surface and the centre of the pellet, Eqs. 4.12 and 4.25 can be substituted in to simplify Eq. 5.7

$$\frac{d\bar{T}_{UC}}{dt} = -\frac{3\alpha_{UC}}{\lambda_{UC} r_1} \left(h\left(\bar{T}_{UC} - T^B\right) + \sigma\varepsilon\left(\bar{T}_{UC}^4 - T^B\right) - \frac{\Delta H_R R_C}{A} \right) \tag{5.8}$$

Note that Eq. 5.8 requires clarifying the initial assumption of the reduced model to state that the average temperature, $\bar{T}$, is equal to the surface temperature of the carbide. Although $\bar{T}$ is referred to as an average, the temperature throughout the carbide is constant.

The radial change in the reduced model is calculated in the same manner as in the oxidation model from Chapter 4 using Eq. 4.27 from page 90. This pair of differential equations are then solved using the predictor corrector method. In the 'predictor' step, a forward difference approximation of Eqs. 5.8 and 4.27 is used to calculate $\bar{T}_{UC}^{n+1}$ and r_1^{n+1} using $\bar{T}_{UC}^{n}$ and r_1^n. These values are then used to recalculate the temperature and radius dependent variables in Eqs. 5.8 and 4.27. Then, as the 'corrector' step, more accurate values of $\bar{T}_{UC}^{n+1}$ and r_1^{n+1} are calculated with a central difference approximation using $\bar{T}_{UC}^{n}$ and r_1^n and the re-calculated reaction variables.

This process is then iterated until the difference between the $\bar{T}_{UC}^{n+1}$ and r_1^{n+1} values calculated by the corrector step are within a certain tolerance of the values calculated by the predictor step.

The method is carried out at each time step until the radius approaches zero similarly to the full model. Due to the reduced model not needing to increment the radius of the sphere and use the Thomas algorithm (Chang, 1981) to invert the tri-diagonal matrices to solve the temperature distribution, this model runs signigicantly faster without compromising on accuracy. A comparison between the reduced model simulating the oxidation reaction and the oxidation model from Chapter 4 is included in Table 5.1, where it can be seen the difference in the results, i.e. the reaction completion times, is negligible. For the simulations in this case, a pellet of diameter 9.35 mm was exposed to an infinite, stagnant bulk gas set to be air with a fixed oxygen concentration of $3.15\,\mathrm{mol\,m^{-3}}$. It can also be seen that the reduced model runs noticeably faster, although at the parameters set in this case the computational times are very quick regardless.

Given the how similar the results are between the two models, it was therefore decided to employ the reduced model to calculated the heat transfer for the dissolution model. With the heat transfer calculated, dissolution reaction kinetics can now be applied.

5.2 Applying existing reaction kinetics

The most significant change between the oxidation and dissolution models is the reaction kinetics that are applied. Whilst the oxidation at the surface of

Table 5.1: A comparison of reaction completion and computational times at different bulk gas temperatures between the full oxidation model and the simpler reduced model.

	Reduced model		Full model	
Bulk gas temperature (°C)	Reaction completion time (min)	CPU time (s)	Reaction completion time (min)	CPU time (s)
300	310.5	2.699	310.5	3.526
500	240.6	2.075	240.6	2.730
700	190.9	1.732	190.9	2.120

the carbide was a simple 1st order reaction with only one step, the dissolution reaction is strongly affected by nitrous acid produced by the reaction between uranium carbide and nitric acid requiring a more complex description of the reaction kinetics.

Initially, the reaction kinetics used in the dissolution model are extracted from existing literature and attached to the heat transfer model across a sphere of uranium carbide. Two mechanisms in particular are considered as mentioned in Chapter 2: the first by Hodgson (Hodgson, 1987) and the second by Maslennikov *et al.*(Maslennikov *et al.*, 2009). One variable assumed to be in common is the calculated enthalpy of reaction, $\Delta H_R = -1.337 \times 10^6\,\mathrm{J\,mol^{-1}}$, to be used in the heat transfer model. This was calculated from the enthalpies of formations for the species present in the stoichiometric equation, given in Section 2.5.2.1 as Eq. 2.66 (Glatz *et al.*, 1990):

$$UC(cr) + \{10HNO_2 + 2HNO_3\}(sln) \rightarrow \{UO_2(NO_3)_2 + 6H_2O\}(sln) + \{CO_2 + 10NO\}(g)$$

5.2.1 Hodgson's kinetics

The first reaction mechanism to be considered is that suggested by Hodgson (Hodgson, 1987). Hodgson's model is based around the fragmentation of a fuel

pellet, with the dissolution process controlled by the propagation of the dissolution front along cracks in the fuel pellet (Hodgson, 1987). The model, however, is desgined for a uranium oxide fuel pellet, and hence using Hodgson's reaction kinetics requires the assumption that uranium carbide dissolves in a physically similar way to uranium oxide.

The dependence of the weight of the oxide pellet on time as it dissolves, assuming that the dissolving grains within the pellet are dispersed uniformly throughout the pellet, is given in Eq. 2.76 and repeated below (Hodgson, 1987):

$$\frac{W_d}{W_0} = 1 - \left(\frac{t}{\lambda} + 1\right) exp\left(-\frac{t}{\lambda}\right)$$

In order to calculate the changing radial increment size across the carbide sphere, Eq. 2.76 must be converted to an expression of the dependence of the radius on time. This can be done through the use of the following expression true for a sphere:

$$W_d = \rho_{UC} V_{UC} = \rho_{UC} \frac{4}{3} \pi r^3 \tag{5.9}$$

Eq. 2.76, can therefore be rearranged as:

$$\frac{r_1}{r_0} = \sqrt[3]{1 - \left(\frac{t}{\lambda} + 1\right) exp\left(-\frac{t}{\lambda}\right)} \tag{5.10}$$

where r_0 is the value of r_1 at time $t = 0$, the beginning of the reaction.

A further rearranging of Eq. 2.76 is also necessary due to the heat transfer boundary condition at the reaction interface, Eq. 4.13, requiring a reaction rate term, R_C, in $\mathrm{mol\,s^{-1}}$. This is done by noting the number of moles present at each time step both before and after the new radius is calculated. This is done through the following expression similar to Eq. 5.11

$$n_{UC} = \dot{\rho}_{UC} V = \dot{\rho}_{UC} \frac{4}{3} \pi r^3 \tag{5.11}$$

where $\dot{\rho}$ is the molar density.

The change between the two values of n_{UC} over the one time step under consideration is then divided by the size of that time step, Δt, to gain a value of

R_C for that time step and hence allow a calculation of the heat released by the dissolution reaction.

Hodgson uses the variable λ as a reaction coefficient with units of s^{-1}. It's dependence on temperature can be seen in Chapter 2 in Figure 2.18. This dependence was plotted in order to characterise it quantitatively and allow predictions of it's value a temperatures different to those presented in Figure 2.18. The temperature dependence of λ was found to have the functional form described in Eq. 5.12:

$$\lambda = \lambda_0 \left(\exp \left(\frac{-E_A}{RT_{HNO_3}} \right) \right)^{-1} \tag{5.12}$$

where λ_0 is a constant with a value of $7.707 \times 10^{-4}\,s^{-1}$, E_A is the activation energy of the dissolution with a value of $3866\,J\,mol^{-1}$ and T_{HNO_3} is the temperature of the nitric acid initially.

Eqs. 5.10 and 5.12, when coupled to the heat transfer model described in Section 5.1, allow the dissolution to be modelled according to the reaction kinetics published by Hodgson. Plotting of the reaction coefficient, λ, allows Hodgson's results to be extrapolated to different initial temperatures of the nitric acid, and the heat transfer model allows prediction of the ensuing changes in temperature of the pellet. Figure 5.2 is a plot of the fraction of the pellet dissolved over time at different temperatures. The solid lines represent dissolution curves produced using the coefficients used by Hodgson, demonstrating its ability to reproduce the curves shown in Figure 2.18 on Page 48, and the dashed lines represent the use of extrapolated values of the coefficient to predict dissolution curves at different temperatures. These results are from a fixed nitric acid concentration of 8 M and a spherical pellet with an initial weight of 1 g.

The extra curves generated by the model at 45 °C, 55 °C and 65 °C predictably line up well with the original data due to the simple dependence of the reaction coefficient on the temperature of the nitric acid. The temperatures reached by the uranium carbide pellet during the reactions can be seen in Table 5.2. These maximum temperatures occurred at the surface of the pellet, where the reaction is occurring, and at the end of the reaction due to a continually rising temperature.

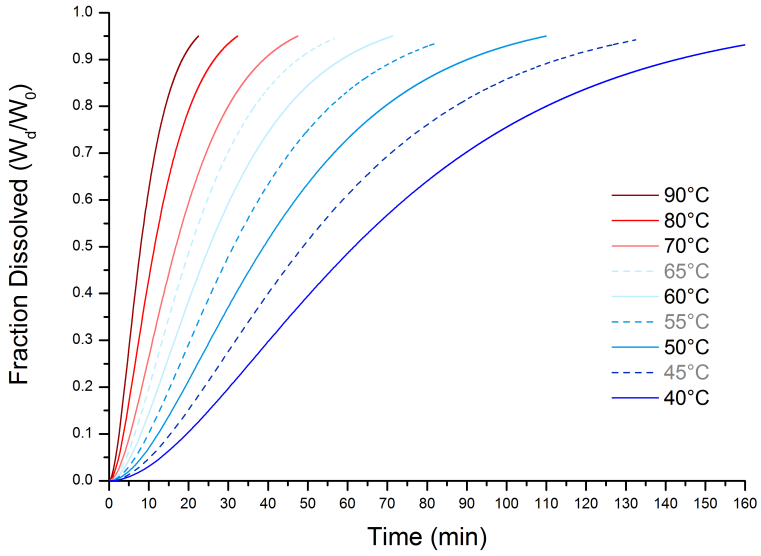

Figure 5.2: Repeating Hodgson's results from Figure 2.18 using the dissolution model (Hodgson, 1987). Extrapolating the reaction coefficient, λ, using Eq. 5.12, allows predictions of the dissolution rates at additional temperatures represented by the dashed lines. The HNO_3 concentration is 8 M and initial pellet weight is 1 g.

Table 5.2: Tabular data of the results shown in Figure 5.2, including the maximum temperature reached by the pellet during dissolution.

Temperature (°C)	Max. temperature reached by carbide (°C)	Completion time (min)
40	61	170
50	88	110
60	119	71
70	159	47
80	211	32
90	278	22
100	364	16

5.2.2 Maslennikov *et al.*'s kinetics

The second reaction mechanism to be applied to the one dimensional model is that suggested by Maslennikov *et al.* (Maslennikov *et al.*, 2009). As opposed to a physical mechanism like Hodgson's (Hodgson, 1987), Maslennikov *et al.* present kinetics dependent on the concentrations of the reactants involved. Importantly, Maslennikov *et al.*'s data relates to a UC sample in powdered form, meaning that it cannot be attached onto the heat transfer model that assumes a spherical, solid UC sample in the same manner Hodgson's kinetics could. The model is therefore an entirely kinetic one.

The overall reaction is represented as a change in mass in the uranium carbide sample given in Eq. 2.77 repeated below.

$$\frac{\Delta m}{m_0} = \left(k_{H^+}\left[H^+\right]^{n_{H^+}} + k_{HNO_2}\left[HNO_2\right]^{n_{HNO_2}} + k_{NO_3^-}\left[NO_3^-\right]^{n_{NO_3^-}}\right)t^n$$

where Δm is the change in mass since the beginning of the dissolution, k_{H^+}, k_{HNO_2} and $k_{NO_3^-}$ are rate constants for each species, n_{H^+}, n_{HNO_2} and $n_{NO_3^-}$ are the orders of reaction with respect to each species, t is the time passed and n the order of the reaction with respect to time.

For Eq. 2.77 to produce meaningful information, this means that the concentrations of H^+, NO_3^- and HNO_2 must be known over time. Maslennikov *et al.* provide expressions for the changing concentrations of HNO_2 and NO_3^- in Eqs. 2.78 and 2.80 when dissolving in a mixture of HNO_2 and $HClO_4$, again repeated below. It is assumed that $[H^+]$ remains roughly constant (Maslennikov *et al.*, 2009).

$$\left[HNO_2\right]_t = \left[HNO_2\right]_0 \exp\left(-k^{SD}_{NO_3^-}t\right)$$

$$\left[NO_3^-\right]_t = k_{NO_3^-} - \frac{\left[HNO_2\right]_0}{3}\exp\left(-k^{SD}_{NO_3^-}t\right)$$

where $\left[NO_3^-\right]_t$ and $\left[HNO_2\right]_t$ are the concentrations of nitrate ions and nitrous acid at time t respectively, $\left[NO_3^-\right]_0$ and $\left[HNO_2\right]_0$ are the concentrations at time $t = 0$ and $-k^{SD}_{NO_3^-}$ is a constant controlling the rate of nitrate ion depletion.

In lieu of a value provided for $-k^{SD}_{NO_3^-}$, it was decided to fit it to the nitrous acid production curves provided by Maslennikov *et al.* in Figure 2.15. However, it

was necessary to used modified expressions of a different form than that provided by Eq. 5.13, which allows HNO_2 to be generated and then to decay instead of just decay. This is because the simulation in this case is occuring in HNO_3 with no HNO_2 present initially, instead of a mixture of HNO_2 and $HClO_4$.

For $t \leq t_{decay}$:

$$[HNO_2]_t = \frac{a}{1 + exp\left(-k\left(t - x\right)\right)} \tag{5.13}$$

where a, k and x are constants and t_{decay} is the time at which the HNO_2 begins to decay in s.

Fitting Eq. 5.13 to the nitrous acid generation curves at different initial nitric acid concentrations in Figure 2.15 provides values for a, k and x at different nitric acid concentrations. These values are then plotted, as shown in Figure 5.3, and there dependency on nitric acid is expressed through the curve fits shown below.

$$a = 2.14 \times 10^{-2} + 1.72 \times 10^{-3} \left[NO_3^-\right]_0 \tag{5.14}$$

$$k = 2.59 \times 10^{-3} + 6.36 \times 10^{-5} \exp\left(\frac{\left[NO_3^-\right]_0 - 2}{7.10 \times 10^{-1}}\right) \tag{5.15}$$

$$x = -3.70 \times 10^{2} + 1.78 \times 10^{4} \exp\left(\frac{-\left[NO_3^-\right]_0}{1.78}\right) \tag{5.16}$$

However, it can be observed from Figure 2.15 that the HNO_2 begins a roughly linear decrease after a certain amount of time depending on the nitric acid. The rate of HNO_2 decay is roughly independent on the HNO_3 concentration and is assumed to be as such, but the time at which it begins is not. The time at which each curve from Figure 2.15 begins to decrease was plotted producing an expression for the time at which the decay begins depending on initial HNO_3 concentration.

$$t_{decay} = 1.05 \times 10^{3} + 3.19 \times 10^{4} \exp\left(\frac{-\left[NO_3^-\right]_0}{1.21}\right) \tag{5.17}$$

The decay of HNO_2 is expressed as a simple linear function given in Eq. 5.18. The gradient is calculated from the gradients of decay given in Figure 2.15.

For $t > t_{decay}$:

$$[HNO_2]_t = [HNO_2]_{t_{decay}} - 2.50 \times 10^{-6}\left(t - t_{decay}\right) \tag{5.18}$$

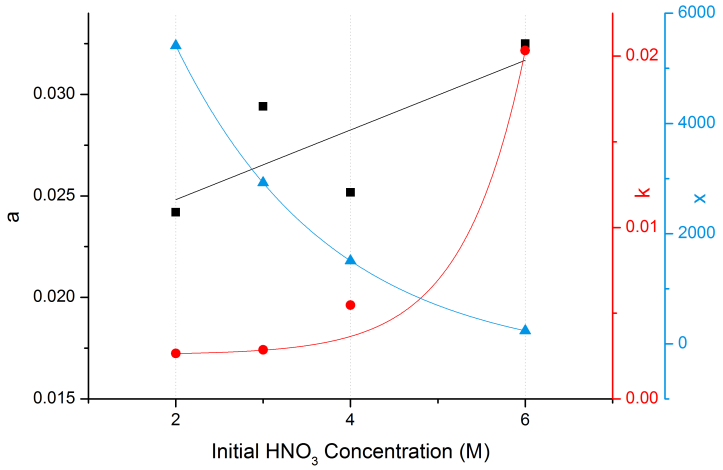

Figure 5.3: The values of the constants a, k and x plotted at different initial nitric acid concentrations. Curve fits are then applied to find their dependency on nitric acid.

Figure 5.4 depicts the HNO_2 production curves obtained from Eqs.5.13 and Eqs. 5.18 at different HNO_3 concentrations. The predicted curves are shown overlain against Maslennikov *et al.*'s results presented in Figure 2.15, and it can be seen that there is a good agreement. The limitation of this method of calculating the transient HNO_2 concentration is that its highly empirical nature means that any results generated outside of the HNO_3 concentrations for which there is data to compare against are difficult to defend. Therefore, it should be mentioned that this method for calculating the HNO_2 concentration is only valid at HNO_3 concentrations of $2, 3, 4$ and $6\,\mathrm{M}$.

Given that a different representation of $[HNO_2]_t$ is now used, an expression for the changing nitric acid concentration, $\left[NO_3^-\right]_t$, must be provided. Similar to Maslennikov *et al.*'s approach in Eq. 2.80, the stoichiometry of the equlibrium reaction between HNO_2 and NO_3^- in Eq. 2.79 is used to convert the production rate of the nitrous acid into a depletion rate for the nitric acid, as shown in Eq. 5.19.

$$\left[NO_3^-\right]_t = \left[NO_3^-\right]_0 - \frac{[HNO_2]_t}{3} \tag{5.19}$$

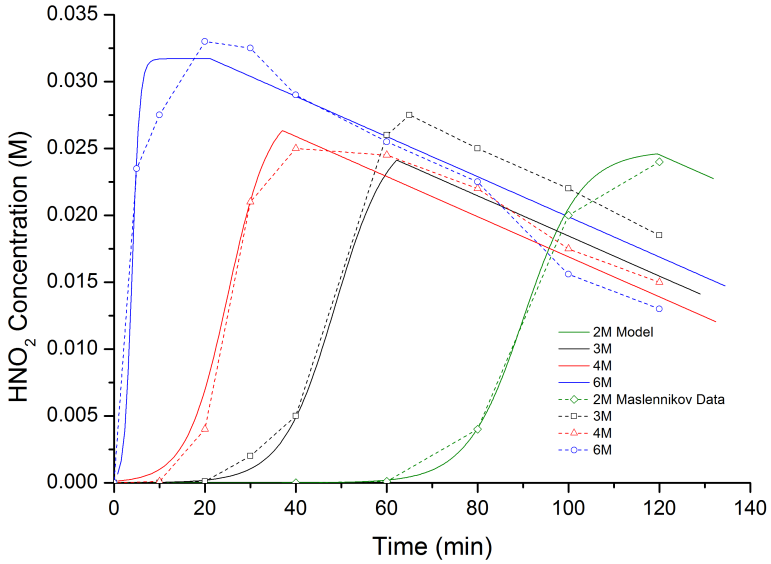

Figure 5.4: A comparison between the production of HNO_2 curves predicted by the model and Maslennikov *et al.*'s dissolution data (Maslennikov *et al.*, 2009) at different initial concentrations of HNO_3.

Substituting Eq. 5.19 into Eq. 2.77 allows it to be simplified by removing the time dependent nitric acid concentration, giving the equation:

$$\frac{\Delta m}{m_0} = \left(k_{H^+} \left[H^+\right]_t^{n_{H^+}} + k_{HNO_2} \left[HNO_2\right]_{t,B}^{n_{HNO_2}} + k_{NO_3^-} \left(\left[NO_3^-\right]_{0,B} - \frac{\left[HNO_2\right]_{t,B}}{3} \right)^{n_{NO_3^-}} \right) t^n \quad (5.20)$$

Using the assumption that $[H^+]$ remains constant over time with the known values of $\left[NO_3^-\right]_0$ and $[HNO_2]_t$ allows Eq. 5.20 to predict a reaction rate. It is again assumed to be only occuring at the surface of the reaction. Therefore, mass transfer of nitric and nitrous acid through a liquid film layer surrounding the carbide pellet is also considered.

$$R_N^* = k_N A \left([N]_{t,B} - [N]_{t,r_1} \right) \quad (5.21)$$

where R_N^* is the rate of transfer of acid across the liquid film layer, A is the surface area of the carbide pellet, $[N]_{t,r-1}$ can represent the concentration at the surface of the pellet of either NO_3^- or HNO_2 and $[N]_{t,B}$ is their concentrations in the bulk fluid.

The external diffusion coefficient of the two acid species through the film layer, k_N, is taken to be dependent the bulk diffusivity of each through a film layer comprising uranyl nitrate:

$$k_N = \frac{D_{N-UO_2(NO_3)_2}\mathrm{Sh}}{2r_1} \tag{5.22}$$

where $D_{N-UO_2(NO_3)_2}$ is the bulk diffusivity of each acid, given by Smith as (Smith, 1970):

$$D_{N-UO_2(NO_3)_2} = \frac{1.8583 \times 10^{-3} \left(T^B\right)^{\frac{3}{2}} \left(\frac{1}{M_H} + \frac{1}{M_{UO_2(NO_3)_2}}\right)^{\frac{1}{2}}}{p\sigma\Omega} \tag{5.23}$$

where M_H is the molecular weight of either nitric or nitrous acid in $g\,mol^{-1}$, and $M_{UO_2(NO_3)_2}$ is the molecular weight of uranyl nitrate in the same units.

Eq. 5.21 can then be used to express the concentration of nitrous acid in Eq. 5.20, $[HNO_2]$, in terms of its concentration at the surface of the pellet rather than in the bulk fluid. Rearranging Eq. 5.21 gives the following expression:

$$\left[HNO_2^-\right]_{t,B} = \left[HNO_2^-\right]_{t,r_1} + \frac{R^*_{HNO_2^-}}{k_{HNO_2^-}A} \tag{5.24}$$

Substituting Eq. 5.24 into Eq. 5.20 therefore allows the reaction rate to consider the mass transfer of nitrous acid to the reaction interface.

$$\begin{aligned}\frac{\Delta m}{m_0} = \Bigg(k_{H^+}\left[H^+\right]_t^{n_{H^+}} + k_{HNO_2}\left(\left[HNO_2^-\right]_{t,r_1} + \frac{R^*_{HNO_2^-}}{k_{HNO_2^-}A}\right)^{n_{HNO_2}} \\ + k_{NO_3^-}\left(\left[NO_3^-\right]_{0,B} - \frac{1}{3}\left(\left[HNO_2^-\right]_{t,r_1} + \frac{R^*_{HNO_2^-}}{k_{HNO_2^-}A}\right)\right)^{n_{NO_3^-}}\Bigg)t^n\end{aligned} \tag{5.25}$$

Eq. 5.25 offers a description of the reaction rate in terms of the variable, $\left[HNO_2^-\right]_{t,r_1}$. However, since the value of the order of the reaction with respect to nitric acid, $n_{NO_3^-}$, can take a non-integer value, Eq. 5.25 can be very difficult to expand and solve.

Firstly, a backward difference approximation of Eq. 5.25 is taken. The time variable is changed to a time step size rather than the total time passed allowing and the Δm_{UC} term therefore represents the change in the mass of UC over a time step. It is assumed that the order of the reaction with respect to time is 1. Values of $n_{H^+} = 0$, $n_{HNO_2} = 2$ and $n_{NO_3^-} = 0.1$ are taken from Maslennikov *et al.* (Maslennikov *et al.*, 2009).

The rate constants, k_{H^+}, k_{HNO_2} and $k_{NO_3^-}$, are dependent on the initial nitric acid concentration and were also provided by Maslennikov *et al.*(Maslennikov *et al.*, 2009). However, it was found that $k_{NO_3^-}$ had to be altered in order to fit the curves to the dissolution data provided by Maslennikov *et al.*, meaning that the results obtained were highly empirical. It was set to a constant, much smaller value of $k_{NO_3^-} = 1.25 \times 10^{-6}\,\mathrm{l\,mol^{-1}\,s^{-1}}$.

$$\frac{\Delta m_{UC}}{\Delta t} = R_D = m_0 \Bigg(k_{H^+} + k_{HNO_2} \left(\left[HNO_2^-\right]_{t,r_1} + \frac{R^*_{HNO_2^-}}{k_{HNO_2^-} A} \right)^2 + k_{NO_3^-} \left(\left[NO_3^-\right]_{0,B} - \frac{1}{3} \left(\left[HNO_2^-\right]_{t,r_1} + \frac{R^*_{HNO_2^-}}{k_{HNO_2^-} A} \right) \right)^{0.1} \Bigg) \quad (5.26)$$

where R_D is the mass of UC dissolved per second.

To solve Eq. 5.26, it must be treated as a function, fn, and solved using the bisection method. This requires rearranging Eq. 5.26 to the form shown in Eq. 5.27.

$$fn = R_D - m_0 \Bigg(k_{H^+} + k_{HNO_2} \left(\left[HNO_2^-\right]_{t,r_1} + \frac{R^*_{HNO_2^-}}{k_{HNO_2^-} A} \right)^2 + k_{NO_3^-} \left(\left[NO_3^-\right]_{0,B} - \frac{1}{3} \left(\left[HNO_2^-\right]_{t,r_1} + \frac{R^*_{HNO_2^-}}{k_{HNO_2^-} A} \right) \right)^{0.1} \Bigg) \quad (5.27)$$

A value for the upper and lower limits of the reaction rate, R_D, is then estimated. The average of these limits is then taken as the value of R_D and applied to Eq. 5.27 which can be solved in code to attain a value for fn. If $fn < 0$, the lower limit for R_D is adjusted to the averaged value of R_D used. If $fn > 0$, the upper limit is adjusted to the R_D value. This is continued until the difference

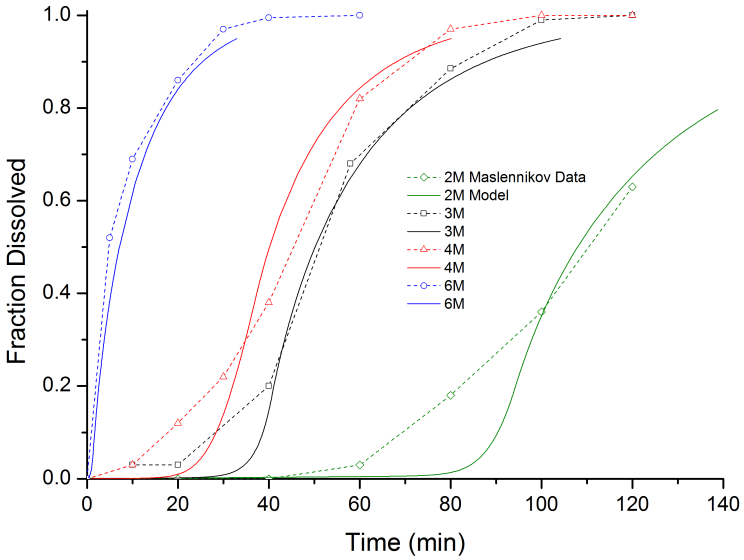

Figure 5.5: A comparison between the dissolution curves produced by the model using a modified version of Maslennikov *et al*'s reaction kinetics and Maslennikov's data (Maslennikov *et al.*, 2009) at different initial concentrations of nitric acid.

between the two limits becomes small enough to reach a tolerance criteria such as that given in Eq. 5.28.

$$\frac{R_{D_{upperlimit}} - R_{D_{lowerlimit}}}{R_D} \times 100 < \text{tolerance criteria} \tag{5.28}$$

Running the bisection method produces an estimate for the value for the reaction rate. This results in a dissolution model that factors the predicted generation of HNO_2 into a modified version of Maslennikov *et al.*'s dissolution kinetics, allowing a prediction of the dissolution time and rate at different initial HNO_3 concentrations.

Figure 5.5 illustrates the resulting dissolution curves obtained from the model using Eqs. 5.26 and 5.27 and compares them to Maslennikov *et al.*'s data from Figure 2.14. These simulations were carried out at a constant bulk fluid temperature of 22 °C a pellet with a powdered UC sample with an initial mass and temperature of 1 g and 20 °C. It can be seen that the model predicts smooth,

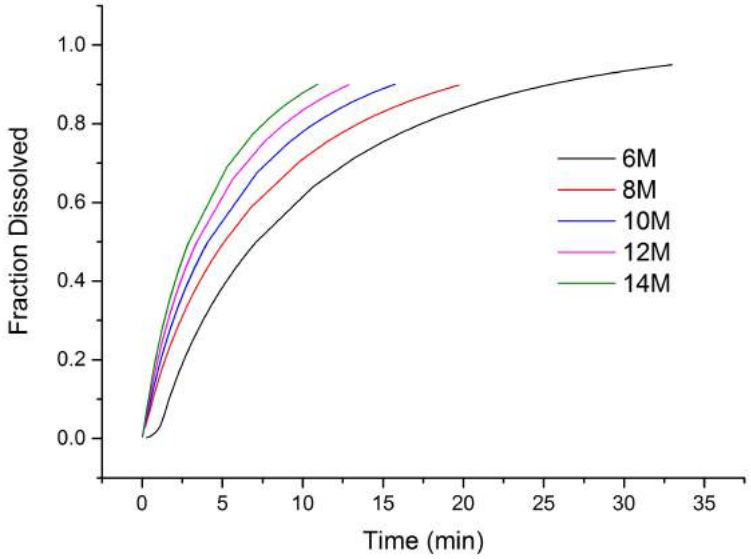

Figure 5.6: Dissolution curves produced by the model based on Maslennikov *et al.*'s kinetics at higher HNO_3 concentrations.

s-shaped curves characteristic of this dissolution process. The steep initial rise is caused by the generation of HNO_2 which catalyses the dissolution. The following rate decrease occurs due to the concentration of HNO_2. It was found that in order to make the tailing-off of the reaction rate significant enough to match the data provided by Maselennikov *et al.*, the mass transfer of acid from the bulk fluid to the reaction surface had to be included.

The most significant deviation of the simulated curves from the data is in the induction period, i.e. the period of time before there is enough HNO_2 for the reaction rate to become significant. In the simulation, there is virtually no reaction occurring during this time, whereas in the data, there is more of a reaction occurring before the curve steepens. This suggests that the model's reaction rate has too small of a dependence on the HNO_3 in the solution. If this is increases, however, the overall reaction completion time becomes faster and no longer aligns with the data. The final stages of the reaction where the rate is slowing agree well, as do the reaction completion times.

The model derived from Maslennikov *et al.*'s (Maslennikov *et al.*, 2009) kinetics can then be used to produce dissolution curves at different HNO_3 concen-

trations. Figure 5.6 is an example of the model based on Maslennikov *et al.*'s kinetics being used to simulate dissolutions at HNO_3 concentrations of 6 M to 14 M, where it is predicted that further increasing of the HNO_3 concentration increases the reaction rate and the induction period is removed.

5.3 Deriving novel reaction kinetics

Having applied reaction kinetics found in the relevant literature to the dissolution model, it was found that there were a number of notable limitations. Firstly, the Maslennikov *et al.* model (Maslennikov *et al.*, 2009) was the only model found specific to UC. Futhermore, Maslennikov *et al.* derived reaction kinetics from experiments using powdered UC rather than pellets, meaning that the kinetics cannot be coupled to the heat transfer model from Section 5.1, and did not investigate the effect of varying temperature. Similarly, Hodgson (Hodgson, 1987) investigated only the effect of temperature and not the effect of HNO_3 concentration.

In order to obtain a better understanding of the effects of both concentration and temperature on the dissolution of UC, in pellet form, in HNO_3, a series of dissolution experiments were carried out by the National Nuclear Laboratory (NNL). UC pellets, all with a mass of around 70 g, were dissolved in 6 M to 14 M HNO_3 between temperatures of 60 °C to 110 °C. The percentage of UC carbon present in the solution liquor was used as a measure of the dissolution completion, and the HNO_2 concentration in the solution was monitored due to its importance on the reaction kinetics.

This set of experiments provided further investigation into the reaction kinetics due to results dependent on both temperature and concentration, allowing a more advanced model for the dissolution reaction to be developed.

5.3.1 Modelling HNO_2 concentration

Given the important catalytic effect HNO_2 has on the dissolution, its concentration was modelled first as a basis for the dissolution model similarly to the approach taken by Maslennikov *et al.* (Maslennikov *et al.*, 2009).

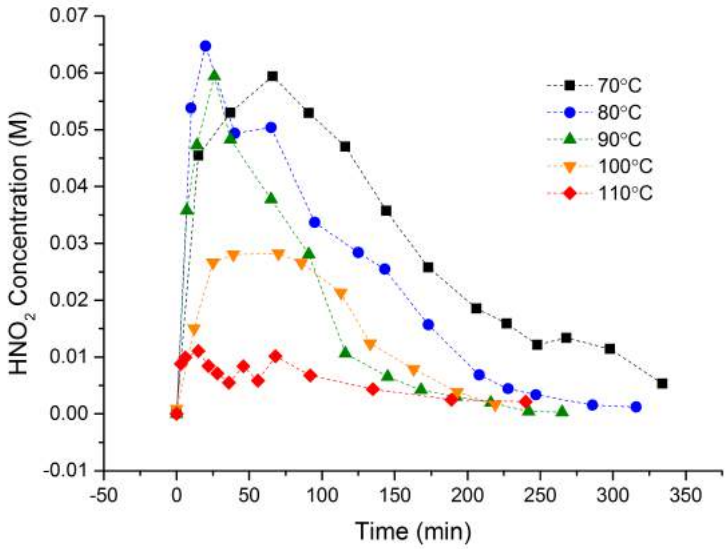

Figure 5.7: HNO_2 concentration in the solution over time at different temperatures from experiments carried out by the NNL. The initial HNO_3 concentration was 8 M in each case.

An example of how the HNO_2 concentration varies over time in the solution is provided by the plot in Figure 5.7, which also illustrates the effect of temperature. Initially, before the dissolution begins, there is no HNO_2 present. As the UC reacts with the HNO_3, HNO_2 is produced and its concentration increases and peaks between 0.01 M to 0.07 M depending on the temperature. The concentration then decreases due to a combination of consumption by the dissolution reaction and dissociation of HNO_2 into water and nitrogen oxides represented by the following equation (Fukasawa *et al.*, 1991; Kobayashi *et al.*, 1976; Park & Lee, 1988):

$$2HNO_2(sln) \rightarrow NO(g) + NO_2(g) + H_2O(sln) \tag{5.29}$$

One important observation is that at the higher temperatures, 100 and 110 °C, there is a sharp decrease in the production of HNO_2. This can be attributed to the rate of HNO_2 dissociation increasing significantly with temperature. If the rate of dissociation of HNO_2 is expressed as:

$$-\frac{\mathrm{d}\left[HNO_2\right]}{\mathrm{d}t} = k_{d_{HNO_2}}\left[HNO_2\right]^2 \tag{5.30}$$

Table 5.3: The dissociation coefficient of HNO_2 observed by Park and Lee (Park & Lee, 1988).

Temperature (°C)	$k_{d_{HNO_2}}$ ($dm^3\,mol^{-1}\,s^{-1}$)
10	3.46
22	13.4
30	28.6

where $k_{d_{HNO_2}}$ is a temperature dependent coefficient, then the temperature dependence can be quantified. For example, the values displayed in Table 5.3 for $k_{d_{HNO_2}}$ at low temperatures observed by Park and Lee (Park & Lee, 1988) illustrate the trend of increasing dissociation rate with temperature. Although the values are at a temperature range significantly lower than the range used for the NNL experiments, the demonstration of the dependence of dissociation rate on temperature would offer an explanation to the phenomena occurring in Figure 5.7.

Therefore, with the significance of HNO_2 dissociation highlighted, modelling the HNO_2 concentration in the solution would require consideration of three processes occurring:

1. Production of HNO_2 by the reaction of UC with HNO_3 according to Eq. 2.65.

2. Consumption of HNO_2 by its reaction with UC according to Eq. 2.66.

3. Dissociation of HNO_2 into water and gaseous nitrogen oxides according to Eq. 5.29.

Due to the complexity of modelling these three processes simultaneously, largely due to their co-dependency and different dependencies on temperature, it was found that it was simpler and more accurate to fit a mathematical expression to the concentration curves from plots such as the one in Figure 5.7.

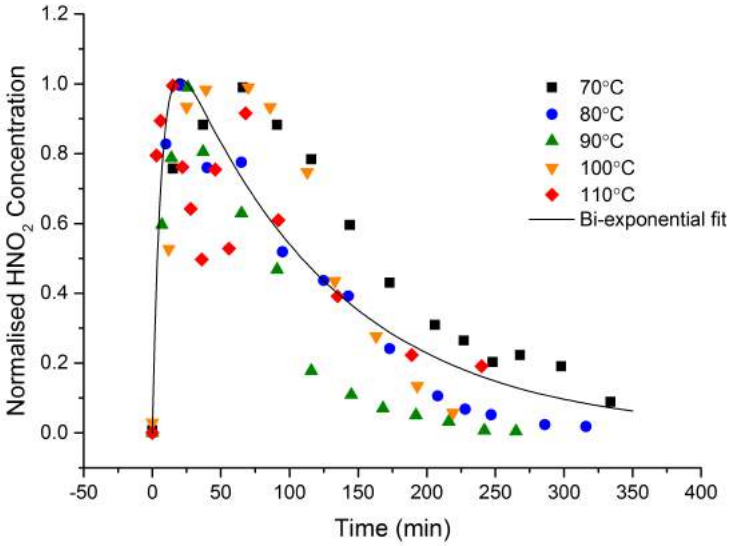

Figure 5.8: HNO_2 curves from Figure 5.7 normalised with respect to the y-axis, HNO_2 concentration. A bi-exponential line of best fit is then applied to the entire data set.

The functional form that was found to fit the HNO_2 concentration plots best is the bi-exponential, which allows a sharp peak followed by an exponential decay, described by the following equation:

$$[HNO_2]_t = g\frac{AB}{A-B}\left[exp\left(-Bt/60\right) - exp\left(-At/60\right)\right]C \tag{5.31}$$

where g is a temperature dependent coefficient, A, B and C are constants and t is the time in s.

In order to find the values of A, B and C and hence describe an overall shape of the curve, the curves from Figure 5.7 were normalised with respect to HNO_2 concentration, as illustrated in Figure 5.8. From the resulting bi-exponential fit of the data points, A, B and C were found to have values of 0.00863, 0.15 and 140 respectively, assuming that $g = 1$. With the functional form obtained, g could then be used as a multiplication factor to apply temperature dependence to the HNO_2 concentration. In order to express g as a function of temperature, the peak HNO_2 concentrations at each temperature were plotted as displayed in Figure 5.9.

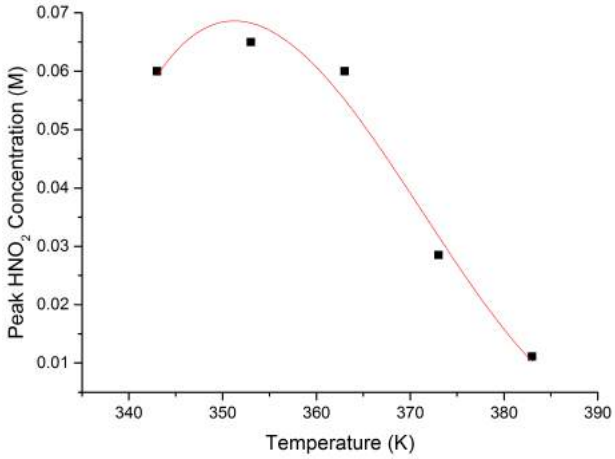

Figure 5.9: The peaks HNO_2 concentration observed at each temperature at an initial HNO_3 concentration of 8 M. A polynomial fit is applied to attain a temperature dependent value of g.

Due to the initial increase in the peak HNO_2 from 70 °C to 80 °C followed by the subsequent decrease at higher temperatures, a 3rd order polynomial was chosen to fit the points. This fit is included in Figure 5.9 and has a coefficient of determination of $r^2 = 0.92$. The resulting expression of g is written as:

$$g = -101.9806 + 828.8346T_0 - 2.237942 \times 10^{-3}T_0^2 + 2.008276 \times 10^{-6}T_0^3 \quad (5.32)$$

where T_0 is the initial solution temperature in K.

Applying the values of A, B, C and g to the bi-exponential expression in Eq. 5.31 can then be used to predict the HNO_2 concentrations at different temperatures for an initial HNO_3 concentration of 8 M. A comparison of these predictions to the NNL's data is displayed in Figure 5.10.

The model provides an acceptable fit to the HNO_2 concentrations, except for the experiment at 70 °C where the shape of the bi-exponential doesn't fit the corresponding data well. This is due to the peak HNO_2 concentration occurring at a later time at 70 °C than at the other temperatures, meaning that the line of best fit applied to the normalised data in Figure 5.8 does not fit well at 70 °C.

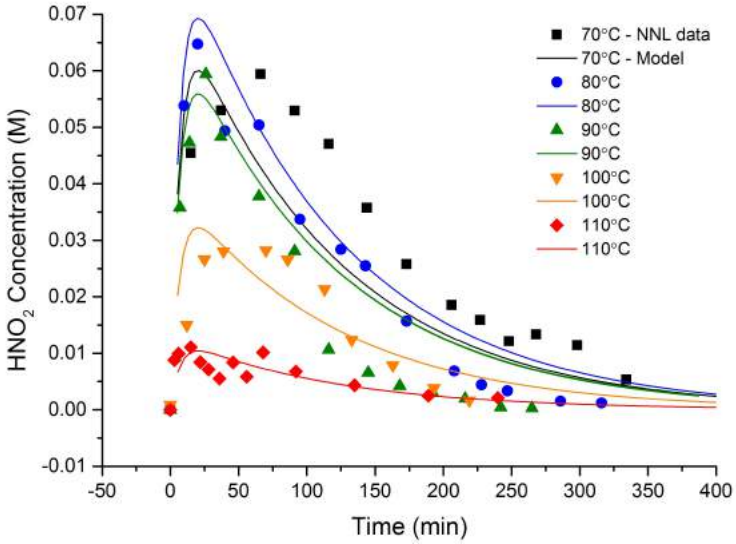

Figure 5.10: The modelled HNO_2 concentrations over time at different temperatures compared to the NNL data plotted using Eq. 5.31.

Therefore, the temperature range at which Eq. 5.31 can be considered to give a valid prediction of the transient HNO_2 concentration is 80 °C to 110 °C.

As well as characterising the dependence of the HNO_2 concentration on temperature, experiments carried out by the NNL at initial HNO_3 concentrations other than 8 M can be used to describe its dependence on HNO_3 concentration. However, due to the different dependencies on temperature at other initial HNO_3 concentrations, a different polynomial representing g is required at each concentration. The values of g valid at different HNO_3 concentrations are included in Table 5.4.

Applying the g values specified in Table 5.4 to Eq. 5.31 to the NNL data across different initial HNO_3 concentrations results in the plots displayed in Figure 5.11. Note that at the HNO_3 concentrations displayed in Figure 5.11, data only exists at three temperatures: 80, 100 and 110 °C. The significant decomposition of HNO_2 observed at the higher temperatures in Figure 5.7 is observable throughout Figure 5.11, and is again accommodated by the polynomial function, g, defined in Table 5.4.

The model's calculations provide a reasonable fit to the data, but are constrained by having to maintain the form of the bi-exponential function and hence

Table 5.4: Values for g and the HNO_3 concentration at which they are valid.

Initial HNO_3 concentration (M)	g ($\mathrm{mol\,s\,dm^{-3}}$)
6	$-126.5723 + 1.03668T_0 - 2.820 \times 10^{-3}T_0^2 + 2.55750 \times 10^{-6}T_0^3$
8	$-101.9806 + 828.835T_0 - 2.238 \times 10^{-3}T_0^2 + 2.00828 \times 10^{-6}T_0^3$
10	$-69.12822 + 0.54613T_0 - 1.430 \times 10^{-3}T_0^2 + 1.23333 \times 10^{-6}T_0^3$
12	$-416.4002 + 3.42577T_0 - 9.380 \times 10^{-3}T_0^2 + 8.54750 \times 10^{-6}T_0^3$
14	$-149.5218 + 1.22487T_0 - 3.340 \times 10^{-3}T_0^2 + 3.02500 \times 10^{-6}T_0^3$

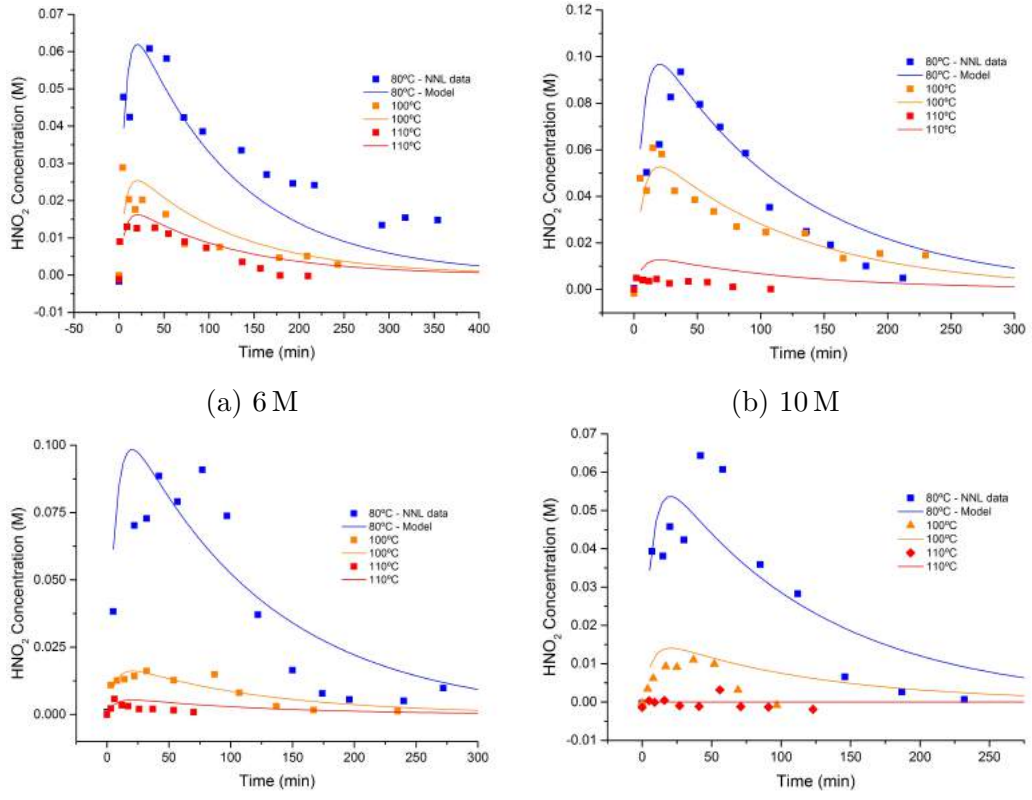

(a) 6 M (b) 10 M

(c) 12 M (d) 14 M

Figure 5.11: Modelled HNO_2 concentrations over time compared to NNL data at different temperatures across different initial HNO_3 concentrations.

fixing the position of the peak concentration. For example, in Figures 5.11c and 5.11d, the data points appear to indicated the peak HNO_2 concentration occurs at a later time to that calculated by the bi-exponential function. However, this disagreement between the time at which the peak occurs seems limited to the results at 80 °C, and the overall trend over time fits well. Therefore, the HNO_2 concentration calculated by the model was deemed to provide an acceptable fit to the NNL data. With this calculation complete, it is now possible to impose reaction kinetics dependent on this concentration calculation to model the dissolution rate of the UC pellet.

5.3.2 Modelling dissolution rate

The next step toward deriving reaction kinetics for the dissolution of UC in HNO_3 using the NNL's data, is to apply an equation capable of predicting the dissolution rate given the known HNO_2 concentration in solution. The resulting dissolution rate can be used to produce dissolution curves able to reproduce those in the NNL data, such as the example displayed in Figure 5.12. Figure 5.12 is a plot of the fraction of UC dissolved over time at different temperatures and an initial HNO_3 concentration of 8 M. The important effects to note are that the dissolution rate increases with temperature up to 110 °C where a dissolution rate almost identical to that at 100 °C is observed. This effect is due to the decomposition of HNO_2 examined in the previous section becoming significant at these temperatures. Therefore, the equation describing the dissolution rate must take into account both the temperature of the solution and the HNO_2 concentration.

The expression found to incorporate these variables whilst fitting the shape of the dissolution curves expresses the rate of reaction as the fraction of UC dissolved at a particular time, t:

$$\frac{\Delta m}{m_0} = -0.955 exp\left(\frac{[HNO_2]_{max}\, t}{60 k_{d_{UC}}}\right) + 0.998906 \tag{5.33}$$

where Δm is the mass of UC dissolved at time t, m_0 is the initial mass of UC at time $t = 0$, $[HNO_2]_{max}$ is the peak HNO_2 concentration and $k_{d_{UC}}$ is a coefficient dependent on temperature.

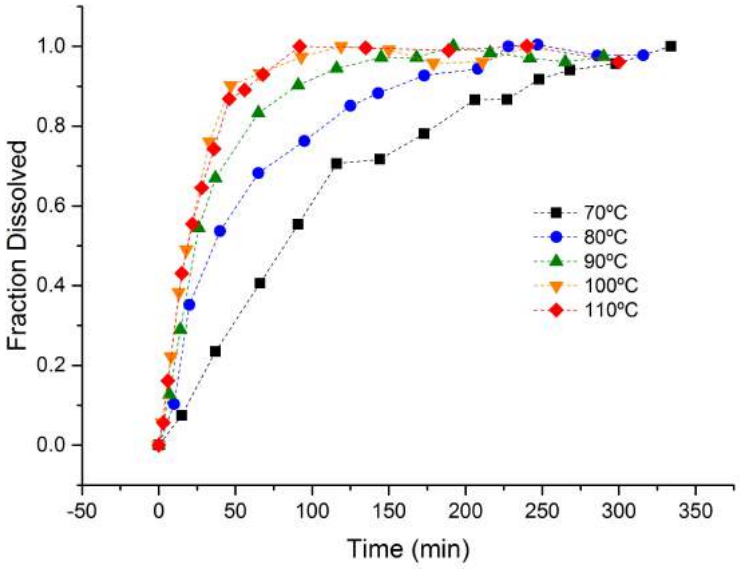

Figure 5.12: NNL data displaying the fraction of UC dissolved over time at different temperatures at an initial HNO_3 concentration of 8 M.

In order to calculate the heat transfer correctly using the model described in Section 5.1, this fractional change is converted to molar change per second, R_C, for use in Eq. 5.8 by calculating the mass dissolved at each time step and dividing the value by the molar mass of UC.

The coefficient $k_{d_{UC}}$ at an initial HNO_3 concentration of 8 M was calculated by determining what its necessary value is in order to fit the curve generated by Eq. 5.33 to the data in Figure 5.12. This fitting process was not carried out for the 70 °C run, due to the inability of the model to accurately reproduce the HNO_2 concentration at that temperature. The values of $k_{d_{UC}}$ found are present in Figure 5.13, where an exponential fit is applied to the values to determine a temperature dependent expression with an r^2 value of 0.99958. This expression is given as:

$$k_{d_{UC}} = 1.43676 \times 10^{11} exp\left(\frac{-T_0}{14.29727}\right) - 0.31036 \tag{5.34}$$

Similarly to the expression representing g for calculating the HNO_2 concentration, $k_{d_{UC}}$ requires a different expression at different initial HNO_3 concentrations

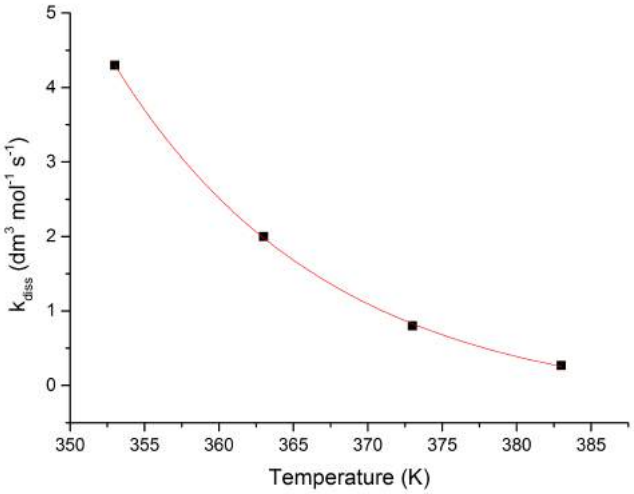

Figure 5.13: A plot of the $k_{d_{UC}}$ values required to fit the dissolution curve produced by the model to the NNL data at different temperatures at an initial HNO_3 concentration of 8 M. An exponential fit is then applied to provide an expression for $k_{d_{UC}}$.

due to the different temperature dependencies at different HNO_3 concentrations. The values of $k_{d_{UC}}$ at different HNO_3 concentrations are displayed in Table 5.5.

Eq. 5.33, with the values of $k_{d_{UC}}$ obtained from Table 5.5, can then be used to generate dissolution curves that can be compared against the NNL data. Figure 5.14 is such a comparison, using the data from Figure 5.12 produced at an initial HNO_3 concentration of 8 M and temperatures of $80, 90, 100$ and $110\,^{\circ}C$. The calculated dissolution curves fit very well to the data, indicating that the model is capable of accurately predicting both the rate of dissolution and the completion time. It successfully incorporates the increasing rate with temperature up to $100\,^{\circ}C$ and also the limited rate increase at $110\,^{\circ}C$ caused by the HNO_2 dissociation.

Figure 5.15 is a plot of the pellet temperature during the course of the dissolutions displayed in Figure 5.14. The NNL experiment did not monitor the pellet temperature, however, so it is not possible to validate these calculations and know if they are representative of the actual temperature of the pellet during the dissolution. Whilst the values predicted may therefore be inaccurate (pellet temperatures of $>350\,^{\circ}C$ seem unrealistic), the trend of the transient pellet

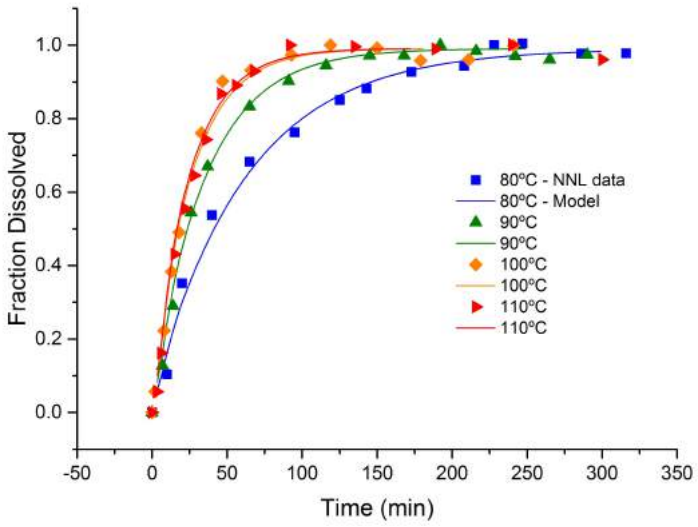

Figure 5.14: A comparison of the dissolution curves produced by the model against NNL data at an initial HNO_3 concentration of 8 M.

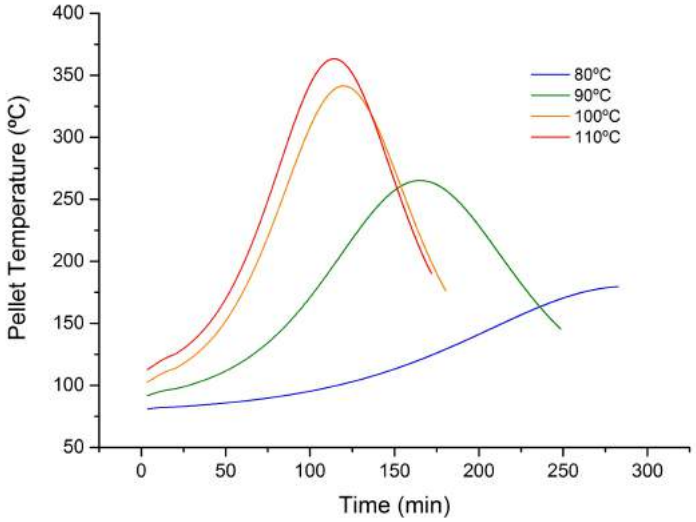

Figure 5.15: The pellet temperature over time calculated by the reduced heat transfer model coupled to the derived reaction kinetics at an HNO_3 concentration of 8 M.

Table 5.5: Values for $k_{d_{UC}}$ and the HNO_3 concentration at which they are valid.

Initial HNO_3 concentration (M)	$k_{d_{UC}}$ ($dm^3\,mol^{-1}\,s^{-1}$)
6	$3.16732 \times 10^{12} exp\left(\frac{-T_0}{12.89601}\right) + 0.39957$
8	$1.43676 \times 10^{11} exp\left(\frac{-T_0}{14.29727}\right) - 0.31036$
10	$2.08264 \times 10^{7} exp\left(\frac{-T_0}{22.93836}\right) - 0.81743$
12	$1.63902 \times 10^{19} exp\left(\frac{-T_0}{8.19296}\right) + 0.01826$
14	$1.38595 \times 10^{13} exp\left(\frac{-T_0}{11.97353}\right) - 0.17778$

temperature may still be worth noting. The model predicts that the pellet undergoes an initial temperature rise as the exothermic dissolution begins, but cannot maintain the temperature above the surrounding fluid as the reaction rate slows with depleting UC surface area. This effect causes a pronounced rise and fall in temperature at the higher solution temperatures.

Comparisons of the model's results with data taken at different HNO_3 concentrations are included in Figure 5.16. The temperature dependent $k_{d_{UC}}$ values can again be seen to model the temperature dependence of the dissolution rate well, with the reaction rate being limited at the higher temperatures. This effect is most notable in Figures 5.16a and 5.16c, where the dissolution curves at 100 °C and 110 °C are almost identical, both in the data and the model.

5.4 Conclusions

Mathematical models simulating the dissolution of UC in HNO_3 have been produced. Both existing and novel reaction kinetics were coupled to a reduced form of the heat transfer model described in Chapter 4, enabling the prediction of dissolution completion times and transient pellet temperature.

The first model was produced using kinetics published by Hodgson (Hodgson, 1987) that used the fracturing of a spherical pellet and subsequent and penetration of solvent to describe the dissolution process. The kinetics could be summarised in a single equation, Eq. 2.76, dependent on temperature but not

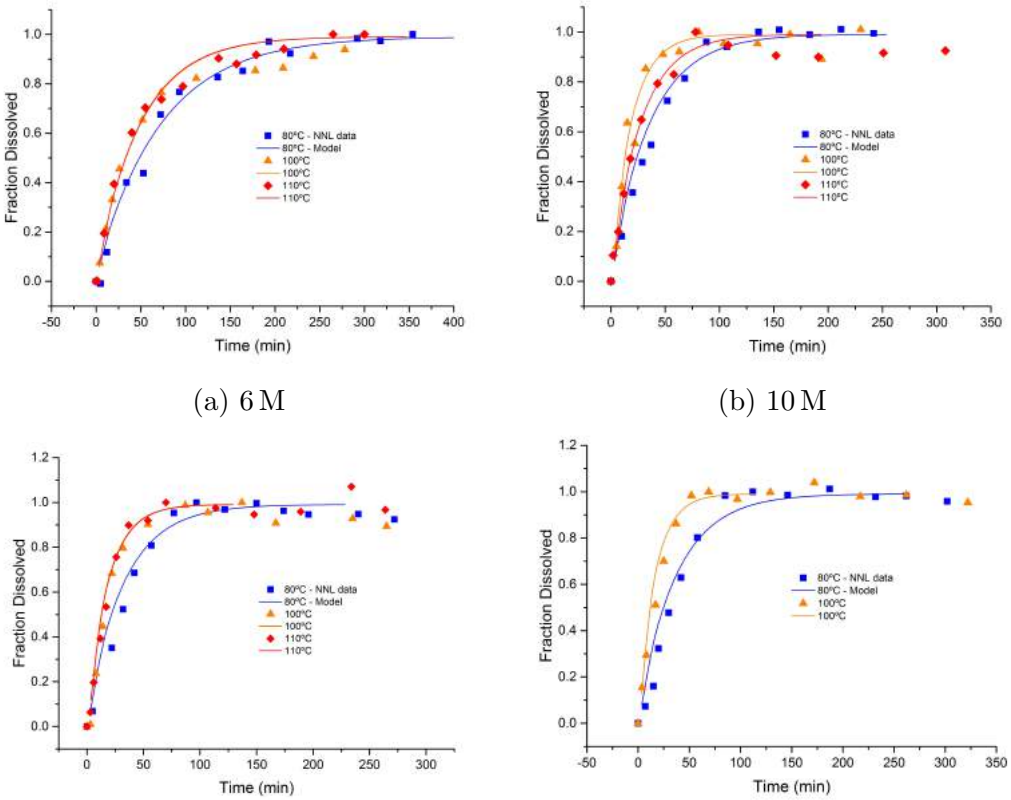

(a) 6 M (b) 10 M

(c) 12 M (d) 14 M

Figure 5.16: Modelled dissolution curves compared against NNL data across different temperatures and initial HNO_3 concentrations.

HNO_3 concentration. Extrapolating values for the reaction coefficient, λ, using Eq. 5.12 allows predictions for the dissolution rate at temperatures different to those initially used by Hodgson as illustrated in Figure 5.2. However, it should be kept in mind that the Hodgson model was designed to characterise the dissolution of UO_2. Despite it being a physical model, therefore, it may lose accuracy when considering UC. This, coupled with the inflexible HNO_3 concentration, means that this model constructed using Hodgson's kinetics may be limited.

The second, more detailed, model of the dissolution takes into account the important catalytic role produced HNO_2 has. A model published by Maslennikov *et al.* (Maslennikov *et al.*, 2009) describing the generation of HNO_2 in solution and the resulting reaction rate was modified to better fit the current investigation and

used to reproduced Maslennikov *et al.*'s data, as illustrated in Figures 5.4 and 5.5. Due to the powdered nature of the UC samples used to acquire this data, the reaction kinetics could not be couple to the reduced heat transfer model designed for a spherical pellet, making it a kinetics-only model. The reaction kinetics derived from Maslennikov *et al.*'s, whilst examining different HNO_3 concentrations, suffer from being independent of the solution temperature.

The final model employs novel reaction kinetics derived from data produced by the NNL in a similar fashion to the Maslennikov *et al.* model (Maslennikov *et al.*, 2009) in that the HNO_2 concentration is modelled and a subsequent reaction rate calculated. The HNO_2 concentration in the solution was found to fit the bi-exponential functional form the best, with a coefficient represented by a different polynomial at a number of HNO_3 concentrations used to provide temperature dependence. This method was able to incorporate an interesting effect elucidated by the NNL's data, where the dissolution rate was observed to stop increasing with temperature above 100 °C, by including the decomposition of HNO_2 occurring at these higher temperatures responsible for the limited reaction rate. An exponential expression dependent on the solution temperature and peak HNO_2 concentration was then used to calculate the fraction of UC dissolved over time at a number of HNO_3 concentrations. Conversion of this rate equation to a form in $\mathrm{mol\,s^{-1}}$ allowed coupling of these reaction kinetics to the heat transfer models, however the data necessary to validate the ensuing pellet temperature predictions is lacking.

Comparison between the models' results is difficult due to the differing UC samples being dissolved in the relevant data sets. For example, despite there being no overlap in the dissolution conditions in the models derived from Maslennikov *et al.*'s reaction kinetics (Maslennikov *et al.*, 2009) and the NNL's data (the highest HNO_3 concentration examined by Maslennikov *et al.* was 6 M and all experiments were carried out at 22 °C), the powdered UC sample can be seen to undergo a much faster dissolution. Similarly, the model using Hodgson's (Hodgson, 1987) kinetics uses 1 g UC pellets - significantly smaller than the 70 g samples examined by the NNL. As a result, Hodgson's kinetics predict reaction completion times of 32.3 and 22.5 min at temperatures of 80 and 90 °C and a HNO_3 concentration of 8 M, whereas the equivalent NNL experiments take 197 and 112 min, respectively.

Therefore, without changing size of the UC samples input into each model, it is not possible to make direct comparisons. However, given just how different the samples are, there is no guarantee that any of the reaction kinetics will be valid when using sample sizes appropriate for a different set of kinetics.

Chapter 6

One-dimensional oxidation model including an adherent product layer

6.1 Introduction

The model described in the this chapter represents the same oxidation reaction as that in Chapter 4, but allows the oxide product to adhere to the surface of the carbide. This requires a number of additional considerations, as the mass transfer of oxygen to and carbon monoxide away from the reaction interface via the adherent product layer must be included. Additionally, the presence of U_3O_8 must be accommodated if the oxide product remains within the reaction domain. However, the overall method of describing the heat and mass transfer processes occurring and subsequent numerical solution is similar. Note that the reduced heat transfer model characterised in Section 5.1 cannot be applied though, as there exists a concentration gradient and a minor temperature gradient through the product layer now constituting part of the solid system.

The reaction mechanism is based upon the observations made by Naito *et al.*, Borchardt and Peakall and Antill (Borchardt, 1959; Naito *et al.*, 1976; Peakall & Antill, 1962) covered in Section 2.4.2.1 on Page 19, but with the assumption that the intermediate UO_2 oxide formed is further oxidised to U_3O_8 significantly faster than it is produced. This assumption is made primarily due to the O_2 availability

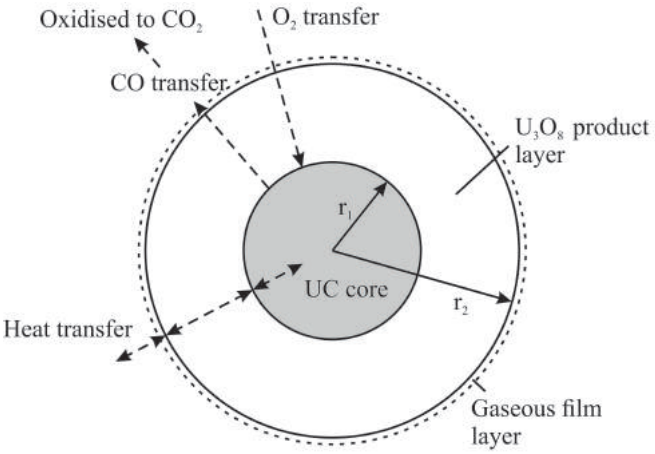

Figure 6.1: A representation of the oxidation reaction in one dimension with an adherent oxide layer present. Mass and heat transfer through this layer now require consideration, as well as how it changes in size over time.

at the two sites: any O_2 diffusing from the bulk gas through the product layer to the UC surface will have to pass through the UO_2 region, where a significant quantity will be consumed.

The model, therefore, will consider the reactions occurring in Eqs. 2.6 to 2.7 to be expressed as an overall equation written as Eq. 6.1, and the product layer will be assumed to comprise only U_3O_8, as illustrated in Figure 6.1. As indicated by Figure 6.1, the model makes the same equivalent volume sphere approximation as in Chapter 6.

$$3UC + 5.5O_2 \rightarrow U_3O_8 + 3CO \tag{6.1}$$

6.2 Mathematical representation

The model can be separated into distinct sections that are solved at each time step, n:

1. Heat and mass transfer across an external gas film around the pellet.
2. Heat flow through the solid system (both the oxide layer and the carbide).
3. Mass transfer of O_2 and CO in opposite directions through the oxide layer.

4. The resulting reaction rate and heat generated at the UC-U_3O_8 interface.

5. The resulting depletion and reduction in size of the carbide pellet and at the same time the expansion of the U_3O_8 layer.

The reaction kinetics are again provided by Scott (Scott, 1966) in Eq. 4.5 for the initial oxidation occurring at the reaction interface, $r = r_1$, and by Howard *et al.* (Howard *et al.*, 1973) in Eq. 4.7 for the bulk gas oxidation of CO.

6.2.1 Heat and mass transfer

The presence of the adherent product layer requires a more complex heat and mass transfer model than that in Chapter 4. Diffusion of CO and O_2 as well as conduction of heat through the oxide product must now be included in order to calculate the distribution of gaseous species and temperature so that a reaction rate can be calculated. A full description of how these effects are incorporated into the oxidation model is included in this section.

For the general heat transfer through the solid, the Fourier equation for heat conduction in a one dimensional sphere is used:

For $t \geq 0$ and $0 \leq r \leq r_1(t) \leq r_2(t)$:

$$\frac{\partial T_m(r,t)}{\partial t} = \alpha_m \left(\frac{\partial^2 T_m(r,t)}{\partial r^2} + \frac{2}{r} \frac{\partial T_m(r,t)}{\partial r} \right) \tag{6.2}$$

where $r_1(t)$ is the radius of the reacting carbide, $r_2(t)$ is the radius of the carbide and adherent oxide layer, m designates whether the oxide layer or carbide pellet is under consideration and α is the thermal diffusivity.

$$\begin{aligned} &\text{For } 0 \leq r < r_1(t) && : \quad m = UC \\ &\text{For } r_1(t) \leq r \leq r_2(t) && : \quad m = U_3O_8 \end{aligned}$$

The diffusion of O_2 and CO through the product layer are similarly represented by Fick's second law. Note that the range doesn't include the carbide region, $r < r_1(t)$, as it is assumed to be non-porous.

For $t \geq 0$ and $r_1(t) \leq r \leq r_2(t)$:

$$\frac{\partial C_g(r,t)}{\partial t} = D_g \left(\frac{\partial^2 C_g(r,t)}{\partial r^2} + \frac{2}{r} \frac{\partial C_g(r,t)}{\partial r} \right) \tag{6.3}$$

where C_g is the concentration, g designates whether O_2 or CO is being considered and D_g is the effective diffusivity of O_2/CO through the product layer.

For the diffusivity of O_2 through the U_3O_8 product layer, D_{O_2}, a value is provided by Jeong *et al.* (Jeong *et al.*, 2006) given in Eq. 6.4. Jeong *et al.* (Jeong *et al.*, 2006) determined the diffusivity from oxidising UO_2, where the rate limiting step is also the diffusion of O_2 through a U_3O_8 product layer.

$$D_{O_2} = D^+_{O_2} exp\left(-\frac{E^+_A}{R\bar{T}_{U_3O_8}}\right) \tag{6.4}$$

where $D^+_{O_2}$ is a constant with a value of $1.71 \times 10^{-5}\,\mathrm{m^2\,s^{-1}}$(Jeong *et al.*, 2006), E^+_A is the activation enthalpy for the diffusion of O_2 through U_3O_8 with a value of $1.6\,\mathrm{kJ\,mol^{-1}}$ (Jeong *et al.*, 2006) and $\bar{T}_{U_3O_8}$ is the average temperature within the oxide product layer.

For the diffusivity of CO through the product layer, D_{CO}, Knudsen diffusion is assumed. Assuming that Knudsen diffusion is the dominant diffusion mechanism means that the vast majority of particle collisions take place between the diffusing CO molecules and the walls of the pores present in the oxide product (Smith, 1970). This occurs when the mean free path of the diffusing molecules is comparable to the pore length, and is in contrast to Fickian diffusion where most of the collisions are molecule-molecule which generally occurs at higher pressures. The Knudsen diffusivity is defined, in $\mathrm{cm\,s^{-1}}$, by Smith as (Smith, 1970):

$$1 \times 10^4 D_{CO} = (\mathcal{D}_K)_{CO} = 9.70 \times 10^3 a \left(\frac{\bar{T}_{U_3O_8}}{M_{CO}}\right)^{\frac{1}{2}} \tag{6.5}$$

where a is the pore size of the oxide layer in cm, M_{CO} is the molecular weight of CO in $\mathrm{g\,mol^{-1}}$ and $\mathcal{D}_{KCO}$ is the Knudsen diffusivity in $\mathrm{cm^2\,s^{-1}}$. To obtain the diffusivity of CO, therefore, the Knudsen diffusivity is converted into $\mathrm{m^2\,s^{-1}}$ simply by dividing by a factor of 1×10^4.

The initial conditions for Eqs. 6.2 and 6.3 are:

For $t = 0$:

$$r_1(0) = r_2(0) - r_{ox} > 0 \tag{6.6}$$

For $t = 0$ and $0 \leq r \leq r_2(t)$:

$$T_m(r, 0) = T_{Amb} \tag{6.7}$$

For $t = 0$ and $r_1(t) \leq r \leq r_2(t)$:

$$C_g(r, 0) = 0 \tag{6.8}$$

where r_{ox} represents a very thin oxide layer present at the beginning of the reaction. This is an assumption made to allow computational times to be significantly shortened.

There are three positions in the solid where boundary conditions must be applied to Eq. 6.2: the centre of the solid, the interface between the oxide and the carbide, and the solid surface. For Eq. 6.3, only the latter two conditions are required.

When considering the boundary condition at the centre of the solid, where $r = 0$, Eq. 6.2 cannot be applied as the second term on the right hand side is indeterminate as $\partial T/\partial r = 0$ and $r = 0$. Applying L'Hôpital's rule to this term and setting $r = 0$ allows Eq. 6.2 to be expressed as:

For $t \geq 0$ and $r = 0$:

$$\frac{\partial T_{UC}(0, t)}{\partial t} = 3\alpha_{UC} \left(\frac{\partial^2 T_{UC}(0, t)}{\partial r^2} \right) \tag{6.9}$$

The adiabatic heat transfer boundary condition at the centre of the system applicable to Eq. 6.9 can then be described as follows:

For $t \geq 0$ and $r = 0$:

$$\left. \frac{\partial T_{UC}}{\partial r} \right|_0 = 0 \tag{6.10}$$

At the reaction interface, where $r = r_1(t)$, the boundary conditions must allow for the heat generated, O_2 consumed and CO produced by the oxidation. Intimate thermal contact between the carbide and the oxide is assumed as stated in Eq. 6.11. Fick's first law is applied for the mass transfer boundary conditions, and due to the prior assumption of Knudsen diffusion for the CO within the U_3O_8 layer, the diffusion coefficient at the interface is taken to be the bulk diffusion of either O_2 through CO or vice-versa occurring within the pores of the product layer.

For $t \geq 0$ and $r = r_1(t)$:

$$T_{UC}(r_1, t) = T_{U_3O_8}(r_1, t) \tag{6.11}$$

$$-\lambda_{UC}\left.\frac{\partial T_{UC}}{\partial r}\right|_{r_1} - \frac{\Delta H_R R_C}{A_{UC}} = -\lambda_{U_3O_8}\left.\frac{\partial T_{U_3O_8}}{\partial r}\right|_{r_1} \tag{6.12}$$

$$D_{O_2-CO}\left.\frac{\partial C_{O_2}}{\partial r}\right|_{r_1} = \frac{R_C}{A_{UC}} \tag{6.13}$$

$$D_{CO-O_2}\left.\frac{\partial C_{CO}}{\partial r}\right|_{r_1} = -\frac{6R_C}{11A_{UC}} \tag{6.14}$$

where $\lambda_{U_3O_8}$ is the thermal conductivity of U_3O_8, provided by Pillai *et al.* (Pillai *et al.*, 2001), ΔH_R is the enthalpy of the oxidation reaction and D_{g-g} is the bulk diffusivity of one gaseous species, g, through another. The factor of 11/6 included in Eq. 6.14 stems from the stoichiometry of Eq. 6.1 where 11 moles of O_2 consumed by the reaction produces 6 moles of CO at the carbide surface.

At the solid surface, where $r = r_2(t)$, the boundary conditions represent the transfer of heat and mass from the solid to the bulk gas and vice versa. Due to the assumption of an oxide layer being present from $t = 0$, the surface boundary conditions use variables relevant to U_3O_8.

For $t \geq 0$ and $r = r_2(t)$:

$$-\lambda_{U_3O_8}\left.\frac{\partial T_{U_3O_8}}{\partial r}\right|_{r_2} = h\left(T_{U_3O_8}|_{r_2} - T^B\right) + \epsilon_{U_3O_8}\sigma\left(T_{U_3O_8}|_{r_2}^4 - \left(T^B\right)^4\right) \tag{6.15}$$

$$-D_g\left.\frac{\partial C_g}{\partial r}\right|_{r_2} = k_g\left(C_g|_{r_2} - C_g^B\right) \tag{6.16}$$

where h is the heat transfer coefficient, $\epsilon_{U_3O_8}$ is the emissivity of U_3O_8, σ is the Stefan-Boltzmann constant, k_g and C_g^B are the external diffusion coefficient and bulk gas concentration of the gaseous species represented by g, either O_2 or CO, and T^B is the temperature of the bulk gas.

The heat transfer coefficient, h, is calculated from the Nusselt number according to Eq. 6.17:

$$h = \frac{\lambda_{fluid}\mathrm{Nu}}{2r_1} \tag{6.17}$$

where λ_{fluid} is the thermal conductivity of the fluid (air) surrounding the pellet and Nu is the Nusselt number, calculated as in Eq. 4.16.

Due to difficulties in finding any published values for the emissivity of U_3O_8 it was assumed to have the same value as that of UO_2, provided by Fink (Fink, 2000) as:

$$\epsilon_{U_3O_8} \approx \epsilon_{UO_2} = 0.836 + 4.321 \times 10^{-6} \left(T_{U_3O_8}|_{r_1} - 3120 \right) \tag{6.18}$$

The external diffusion coefficients represented by k_g control the rate of diffusion of O_2 and CO across the external gas film layer, assumed to comprise CO, surrounding the pellet to the solid surface:

$$k_g = \frac{D_{g-CO}\mathrm{Sh}}{2r_1} \tag{6.19}$$

where Sh is the Sherwood number, calculated as in Eq. 4.21.

6.2.2 Calculating the changing pellet size

The above heat and mass transfer calculations allow $T_{U_3O_8}|_{r_1}$ and $C_{O_2}|_{r_1}$ to be known over time. This allows a calculation of the reaction rate provided by Scott (Scott, 1966) in Eq. 4.5 giving the rate of O_2 consumed. Combining this with the stoichiometry of Eq. 6.1 gives both the rate of UC depletion and the rate of U_3O_8 production.

For $t \geq 0$:

$$\frac{\mathrm{d}n_{UC}}{\mathrm{d}t} = -\frac{6R_C}{11} = -\frac{6k_1 \exp\left(-E_A/R\, T_{U_3O_8}|_{r_1}\right) A_{UC}\, C_{O_2}|_{r_1}}{11} \tag{6.20}$$

$$\frac{\mathrm{d}n_{U_3O_8}}{\mathrm{d}t} = \frac{2R_C}{11} = \frac{2k_1 \exp\left(-E_A/R\, T_{U_3O_8}|_{r_1}\right) A_{UC}\, C_{O_2}|_{r_1}}{11} \tag{6.21}$$

where $n_{U_3O_8}$ is the number of moles of U_3O_8. Again, stoichiometric factors are included as R_C represents the moles of U_3O_8 consumed.

The rate of change in the number of moles of each species can be converted to show how the radius of the carbide pellet depletes and the overall solid expands, due to the density decrease from UC to U_3O_8, over time as follows:

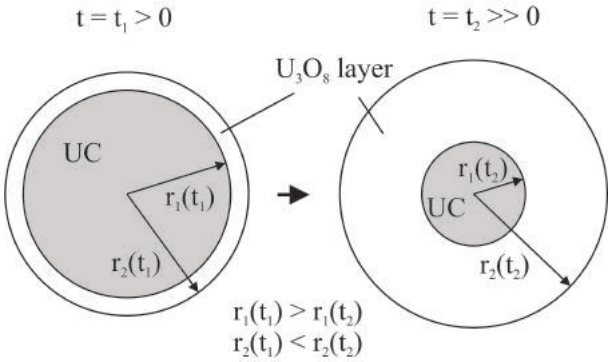

Figure 6.2: The changing shape of the pellet over time. Over the time interval $\Delta t = t_2 - t_1$, the carbide radius, r_1, decreases while the overall radius of the solid, r_2, increases due to U_3O_8 having a lower density than UC.

For $t \geq 0$:

$$\frac{\mathrm{d}r_1}{\mathrm{d}t} = -\frac{6k_1 \exp\left(-E_A/R\, T_{U_3O_8}|_{r_1}\right) C_{O_2}|_{r_1}}{11\dot{\rho}_{UC}} \tag{6.22}$$

$$\frac{\mathrm{d}r_2}{\mathrm{d}t} = \frac{2k_1 \exp\left(-E_A/R\, T_{U_3O_8}|_{r_1}\right) r_1^2 A_{U_3O_8}\, C_{O_2}|_{r_1}}{11r_2^2} \left(\frac{1}{\dot{\rho}_{U_3O_8}} - \frac{1}{\dot{\rho}_{UC}}\right) \tag{6.23}$$

where $\dot{\rho}_{UC}$ and $\dot{\rho}_{U_3O_8}$ are the molar densities of UC and U_3O_8 respectively.

Eqs. 6.22 and 6.23 also highlight the non-linearity of this model, given that both r_1 and r_2 are time dependent.

6.3 Numerical solution

The set of equations detailed in Section 6.2.1 are solved using the FIB method (Smith, 1965), illustrated in Figure 3.3. In the case of Eq. 6.2, the solution is complicated by the need to solve across two solid species that are changing in size differently. In order to model the shrinking carbide and expanding oxide, the radial increment sizes across each, Δr_{UC} and $\Delta r_{U_3O_8}$, are allowed to change whilst the number of radial increments across each is held constant. A FIB approximation of Eq. 6.2, therefore, must be considered across two different regions.

For $n \geq 0$, $2 \leq i \leq p-1$ and $p+1 \leq i \leq k-1$:

$$\frac{T_i^{n+1} - T_i^n}{\Delta t} = \alpha_m \left(\frac{v_i T_{i-1}^{n+1} - 2T_i^{n+1} + w_i T_{i+1}^{n+1}}{\Delta r_m^2} \right) \tag{6.24}$$

where i is an integer representing the radial increment across the solid, $v_i = 1 - 1/i$ and $w_i = 1 + 1/i$. At the solid centre, $i = 1$, at the reaction interface, $i = p$, and at the solid surface, $i = k$.

The radial increment sizes are therefore calculated as:

For $n \geq 0$ and $1 \leq i \leq p-1$:

$$\Delta r_{UC} = \frac{r_1^n}{k-2} \tag{6.25}$$

For $n \geq 0$ and $p \leq i \leq k$:

$$\Delta r_{U_3O_8} = \frac{r_2^n - r_1^n}{(p-1) - k} \tag{6.26}$$

The FIB representation of Eq. 6.3, the mass transfer through the oxide layer, is of the same form as Eq. 6.24.

For $n \geq 0$ and $k+1 \leq i \leq p$:

$$\frac{(C_g)_i^{n+1} - (C_g)_i^n}{\Delta t} = D_g \left(\frac{v_i (C_g)_{i-1}^{n+1} - 2(C_g)_i^{n+1} + w_i (C_g)_{i+1}^{n+1}}{\Delta r_{U_3O_8}^2} \right) \tag{6.27}$$

Eqs. 6.24 and 6.27 are rearranged in order to organise them into separate tri-diagonal matrices, each requiring a solution at every time step.

For $n \geq 0$ and $2 \leq i \leq p-1$:

$$-M_{UC} v_i T_{i-1}^{n+1} + (1 + 2M_{UC})\, T_i^{n+1} - M_{UC} w_i T_{i+1}^{n+1} = T_i \tag{6.28}$$

For $n \geq 0$ and $p+1 \leq i \leq k-1$:

$$-M_{U_3O_8} v_i T_{i-1}^{n+1} + (1 + 2M_{U_3O_8})\, T_i^{n+1} - M_{U_3O_8} w_i T_{i+1}^{n+1} = T_i^n \tag{6.29}$$

$$-M_{O_2} v_i (C_{O_2})_{i-1}^{n+1} + (1 + 2M_{O_2})\, (C_{O_2})_i^{n+1} - M_{O_2} w_i (C_{O_2})_{i+1}^{n+1} = (C_{O_2})_i^n \tag{6.30}$$

$$- M_{CO} v_i (C_{CO})_{i-1}^{n+1} + (1 + 2M_{CO}) (C_{CO})_i^{n+1} - M_{CO} w_i (C_{CO})_{i+1}^{n+1} = (C_{CO})_i^n \quad (6.31)$$

where $M_{UC} = \alpha_{UC} \Delta t / \Delta r_{UC}^2$, $M_{U_3O_8} = \alpha_{U_3O_8} \Delta t / \Delta r_{U_3O_8}^2$, $M_{O_2} = D_{O_2} \Delta t / \Delta r_{U_3O_8}^2$ and $M_{CO} = D_{CO} \Delta t / \Delta r_{U_3O_8}^2$.

To complete the tri-diagonal matrices and allow them to be solved, finite difference approximations of the boundary conditions must be included to remove imaginary points that occur outside the domain of Eqs. 6.28-6.31. A central difference approximation is used for all following boundary condition approximations due to the FIB approximations of the Fourier equation and Fick's second law being second order.

Applying the FIB method to Eq. 6.9, the format of the Fourier heat transfer equation applicable at the centre of the pellet and derived using L'Hôpital's rule, allows it to be expressed as:

For $n \geq 0$ and $i = 1$:

$$\frac{T_1^{n+1} - T_1^n}{\Delta t} = 3\alpha_{UC} \left(\frac{v_1 T_0^{n+1} - 2T_1^{n+1} + w_1 T_2^{n+1}}{\Delta r_{UC}^2} \right) \quad (6.32)$$

The problem term in Eq. 6.32 is T_0^{n+1}, occurring at the imaginary point $i = 0$. In order to allow its removal, a central difference approximation of the heat transfer boundary condition at the centre of the solid is given in Eq. 6.33.

For $n \geq 0$ and $i = 1$:

$$\frac{T_2^n - T_0^n}{2\Delta r_{UC}} = 0 \quad (6.33)$$

Eq. 6.33 therefore allows the removal of the imaginary point, $i = 0$, from Eq. 6.28 when $i = 1$, resulting in Eq. 6.28 taking the form of Eq. 6.34 when $i = 1$.

For $n \geq 0$ and $i = 1$:

$$(1 + 6M_{UC}) T_1^{n+1} - 6M_{UC} T_2^{n+1} = T_1^n \quad (6.34)$$

The next set of boundary conditions that require approximating are those at the UC/U_3O_8 interface, represented by Eqs. 6.12, 6.13 and 6.14. For the heat transfer boundary condition, it is necessary to simplify Eq. 6.12 using the assumption provided in Eq. 6.11 that there is intimate thermal contact between the two

solids. The finite difference approximations of the three boundary conditions at the interface are:

For $n \geq 0$ and $i = p$:

$$\left(\frac{\lambda_{UC}}{\Delta r_{UC}} - \frac{\lambda_{U_3O_8}}{\Delta r_{U_3O_8}}\right) \frac{T^n_{p-1} - T^n_{p+1}}{2\Delta r_{U_3O_8}} = -\Delta H_R k_1 \exp\left(-E_A/RT^n_p\right) (C_{O_2})^n_p \quad (6.35)$$

$$D_{O_2} \frac{(C_{O_2})^n_{p-1} - (C_{O_2})^n_{p+1}}{2\Delta r_{U_3O_8}} = k_1 \exp\left(-E_A/RT^n_p\right) (C_{O_2})^n_p \quad (6.36)$$

$$D_{CO} \frac{(C_{CO})^n_{p-1} - (C_{CO})^n_{p+1}}{2\Delta r_{U_3O_8}} = -\frac{6}{11} k_1 \exp\left(-E_A/RT^n_p\right) (C_{O_2})^n_p \quad (6.37)$$

Rearranging Eqs. 6.35, 6.36 and 6.37 for the imaginary values, T^n_{p-1}, $(C_{O_2})^n_{p-1}$ and $(C_{CO})^n_{p-1}$ and substituting into Eqs. 6.29, 6.30 and 6.31 results in the tri-diagonal matrices taking the following forms at $i = p$.

For $n \geq 0$ and $i = p$:

$$\left\{1 + 2M_{U_3O_8} + \frac{2M_{U_3O_8} y_{U_3O_8} \Delta H_R k_1 \exp\left(-E_A/RT^{n+1,z}_p\right) (C_{O_2})^{n+1,z}_p)}{T^{n+1,z}_k}\right\} T^{n+1,z+1}_k - 2M_{U_3O_8} T^{n+1,z+1}_{p+1} = T^n_k \quad (6.38)$$

$$\left\{1 + 2M_{O_2} + \frac{2M_{O_2} y_{O_2} k_1 \exp\left(-E_A/RT^{n+1,z}_p\right) (C_{O_2})^{n+1,z}_p}{(C_{O_2})^{n+1,z}_k}\right\} (C_{O_2})^{n+1,z+1}_k - 2M_{O_2} (C_{O_2})^{n+1,z+1}_{p+1} = (C_{O_2})^n_k \quad (6.39)$$

$$\left\{1 + 2M_{CO} + \frac{12M_{CO} y_{CO} k_1 \exp\left(-E_A/RT^{n+1,z}_p\right) (C_{O_2})^{n+1,z}_p}{11(C_{CO})^{n+1,z}_k}\right\} (C_{CO})^{n+1,z+1}_k - 2M_{CO} (C_{CO})^{n+1,z+1}_{p+1} = (C_{CO})^n_k \quad (6.40)$$

where $y_{U_3O_8} = \Delta r_{U_3O_8} v_p / (\lambda_{UC} - \lambda_{U_3O_8})$, $y_{O_2} = \Delta r_{U_3O_8} v_p / D_{O_2}$ and $y_{CO} = \Delta r_{U_3O_8} v_p / D_{CO}$.

Here, z represents the number of iterations used to ensure the non-linearity of these boundary conditions does not destabilise the model. This is necessary as solving for T^{n+1} and C_g^{n+1} requires prior knowledge of T_k^{n+1} and $(C_g)_k^{n+1}$, meaning that it is necessary to linearise the relevant equations. For example, Eq. 6.38 has been linearised by multiplying both the numerator and denominator of the heat of reaction term by T_k^{n+1} allowing it to take the tri-diagonal form shared by Eqs. 6.28 and 6.29. The calculation is then iterated a number of times until the tolerances characterised in Eqs. 6.41 and 6.42 are satisified.

For the first iteration, it is assumed that $T_k^{n+1} = T_k^n$ and $(C_g)_k^{n+1} = (C_g)_k^n$. The solution is then recalculated at the same time step, n, using the newly calculated values for T_k^{n+1} and $(C_g)_k^{n+1}$:

$$\frac{T_k^{n+1,z+1} - T_k^{n+1,z}}{T_k^{n+1,z+1}} < \text{Tolerance for all temperatures} \tag{6.41}$$

$$\frac{(C_g)_k^{n+1,z+1} - (C_g)_k^{n+1,z}}{(C_g)_k^{n+1,z+1}} < \text{Tolerance for all concentrations} \tag{6.42}$$

The final boundary conditions required to complete the matrices are those at the the solid surface, represented by Eqs 6.69 and 6.70.

For $n \geq 0$ and $i = k$:

$$\frac{T_{k+1}^n - T_{k-1}^n}{2\Delta r_{U_3O_8}} = -\frac{h^n}{\lambda_{U_3O_8}}(T_k^n - T^B) - \frac{\epsilon\sigma}{\lambda_{U_3O_8}}((T_k^n)^4 - (T^B)^4) \tag{6.43}$$

$$\frac{(C_g)_{k+1}^n - (C_g)_{k-1}^n}{2\Delta r_{U_3O_8}} = -\frac{k_g^n}{D_g}\left((C_g)_k^n - (C_g)^B\right) \tag{6.44}$$

Rearranging Eqs. 6.43 and 6.44 for the imaginary values, T_{k+1}^n and $(C_g)_{k+1}^n$, and substituting into Eqs. 6.29, 6.30 and 6.31 results in the tri-diagonal matrices taking the following forms at $i = k$.

For $n \geq 0$ and $i = k$:

$$-2M_{U_3O_8}T_{k-1}^{n+1,z+1} + \Bigg\{1 + 2M_{U_3O_8} + 2M_{U_3O_8}u_{U_3O_8} + \frac{2M_{U_3O_8}u_{U_3O_8}}{h^{n+1}}\epsilon\sigma(T_k^{n+1,z})^3 - \frac{2M_{U_3O_8}u_{U_3O_8}T^B}{T_k^{n+1,z}} - \frac{2M_{U_3O_8}u_{U_3O_8}}{h^{n+1}T_k^{n+1,z}}\epsilon\sigma(T^B)^4\Bigg\}T_k^{n+1,z+1} = T_k^n \tag{6.45}$$

$$-2M_{O_2}(C_{O_2})_{k-1}^{n+1,z+1}+\left\{1+2M_{O_2}+2M_{O_2}u_{O_2}-\frac{2M_{O_2}u_{O_2}(C_{O_2})^B}{(C_{O_2})_k^{n+1,z}}\right\}(C_{O_2})_k^{n+1,z+1} = (C_{O_2})_i^n \quad (6.46)$$

$$-2M_{CO}(C_{CO})_{k-1}^{n+1,z+1}+\left\{1+2M_{CO}+2M_{CO}u_{CO}-\frac{2M_{CO}u_{CO}(C_{CO})^B}{(C_{CO})_k^{n+1,z}}\right\}(C_{CO})_k^{n+1,z+1} = (C_{CO})_i^n \quad (6.47)$$

where $u_{U_3O_8} = \Delta r_{U_3O_8} w_k h/\lambda_{U_3O_8}$, $u_{O_2} = \Delta r_{U_3O_8} w_k k_g^n/D_{O_2}$ and $u_{CO} = \Delta r_{U_3O_8} w_k k_g^n/D_{CO}$.

The equations detailed in this section, therefore, provide the details on how to construct the three tri-diagonal matrices required to solve for: the temperature across the carbide and oxide layer, the concentration of O_2 through the oxide layer and the concentration of CO through the oxide layer. With these quantities now known at each time step, they can be used in backward difference approximations of the radial change equations, Eqs. 6.22 and 6.23. For $n \geq 0$:

$$r_1^{n+1} = r_1^n - \frac{\Delta t 6 k_1 \exp\left(-E_A/RT_p^{n+1}\right)(C_{O_2})_p^{n+1} k_g^{n+1}}{11\dot{\rho}_{UC}} \quad (6.48)$$

$$r_2^{n+1} = r_2^n - \frac{\Delta t 2 k_1 \exp\left(-E_A/RT_p^{n+1}\right)(C_{O_2})_p^{n+1}(r_1^{n+1})^2}{11(r_2^{n+1})^2}\left(\frac{1}{\dot{\rho}_{U_3O_8}} - \frac{1}{\dot{\rho}_{UC}}\right) \quad (6.49)$$

Using Eq. 6.48, therefore, the radial depletion over time can be calculated and hence the time until the reaction is completed. The simulation finishes when the percentage of carbide oxidised is 99%. It is held from fully completing because as the carbide increment size tends to zero, $\Delta r_{UC} \to 0$, so does the time step size, meaning that to fully oxidise the carbide would take an infinite amount of time. The details of the dependence of the time step size on the radial increment sizes are covered in the next section.

6.3.1 Ensuring numerical stability and convergence

The numerical stability of this model was maintained through use of the Courant-Friedrichs-Lewy rule (Smith, 1965), as in Chapter 4. It requires slight modification however to accommodate the differing radial increment sizes and the thermal

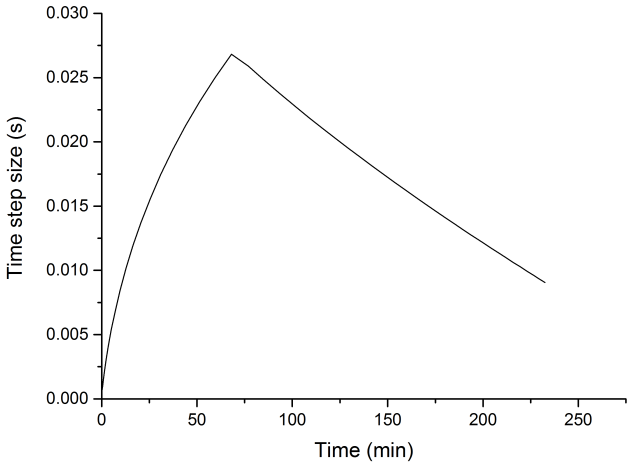

Figure 6.3: The variation of the time step size over reaction time. The initial increase is due to an expanding increment size of the oxide, $\Delta r_{U_3O_8}$, and the later decrease is due to the shrinking Δr_{UC} becoming dominant in Eq. 6.50.

and mass diffusivities involved in the solution. In order to maintain stability, the time step must be the smallest value possible from the array of values it can be calculated from. This can be seen in the part-logical, part-mathematical calculation of the time step that is used, given in Eq. 6.50:

$$\Delta t = \frac{1}{2MAX\left(\alpha_{UC}, \alpha_{U_3O_8}, D_{O_2}, D_{CO}\right)} MIN\left(\Delta r_{UC}^2, \Delta r_{U_3O_8}^2\right) \tag{6.50}$$

where $MAX()$ represents a function used in the model to select the largest value from the variables listed in the brackets, and $MIN()$ the smallest.

This equation is applied at the beginning of each time step once the relevant variables (increment sizes and diffusivities) have been calculated. Initially it is very small due to the small size of the oxide product layer. It then increases throughout the reaction before decreasing again as the radius of remaining carbide depletes. Despite this restriction slowing the simulation time of the oxidation greatly, it is necessary to ensure stability and confidence in the results.

How the time step size varies over time can be seen in Figure 6.3. It starts off small due to the thin, initial oxide layer having a small increment size, $\Delta r_{U_3O_8}$, across it and then increases as the product layer grows. Then, approximately

Table 6.1: The effect of varying the number of increments on the oxidation completion time as a test for convergence for the model with an oxide layer present.

Number of radial increments		Oxidation completion time (h)	Computational time (min)
Carbide core	Oxide layer		
5	5	9.043	0.046
10	10	10.25	0.183
20	20	10.82	0.743
40	40	11.09	2.861
80	80	11.24	12.04

midway through the reaction, when Δr_{UC} becomes smaller than $\Delta r_{U_3O_8}$ due to depletion of the carbide, it begins to decrease as Δr_{UC} does. This result was obtained using a carbide pellet with an initial radius of 0.20 cm and a bulk gas with a temperature of 900 °C and an O_2 concentration of 3.15 mol m^{-3}.

Convergence of the model was checked by varying the number of increments across both the carbide and oxide layers whilst maintaining the values of all other parameters. The results of this can be seen in Table 6.1.

Richardson's deferred approach to the limit (Smith, 1965) was used to extrapolate the results displayed in Table 6.1 to predict the solution for infinitely small increment sizes. Taking the first three results from Table 6.1 and applying them to Eqs. 6.51 and 6.52 facilitates the prediction of such a solution:

$$u = \frac{h_2^p u_1 - h_1^p u_2}{h_2^p - h_1^p} \tag{6.51}$$

where u_1 and u_2 are the solutions (completion times) at initial radial increment sizes of h_1 and h_2, and p can be calculated from:

$$2^p = \frac{u_2 - u_1}{u_3 - u_2} \tag{6.52}$$

where u_3 is the solution at h_3, and $h_3 = \frac{1}{2}h_2 = \frac{1}{4}h_1$.

Eqs. 6.51 and 6.52 yield a result of $u = 11.33$ h, which combined with the results in Table 6.1 indicate that the model is converging successfully.

The effect of time step size on the reaction completion time can also be seen from Table 6.1, as when the number of increments is increased the simulation completion time increases significantly.

6.4 Powdered variation

In addition to the spherical pellet oxidation model with an adherent product layer, a variant simulating a powdered UC sample was completed. The motivation was to fit kinetics coefficients, in particular the rate constant, k_1, and activation energy, E_A, to the experimental oxidation data published by Berthinier *et al.* (Berthinier *et al.*, 2009) that is briefly discussed in Section 2.4.2. This section will describe the design of the powdered variation of the oxidation model with an adherent product layer and how it was fit to the relevant experimental data.

6.4.1 Mathematical considerations

To represent a powdered UC sample, the mathematical representation of the model requires a number of significant adjustments. The core methodology was maintained, however, through the assumption that the powdered UC placed within the cylindrical crucible could be approximated as a porous solid. In order to make this approximation as accurate as possible, the geometry of the powder and crucible must be considered.

Following communication with the CEA, the organisation at which the work was carried out, some further detail was provided to Berthinier *et al.*'s paper (Berthinier *et al.*, 2009). The crucible was stainless steel 15 mm in diameter and 7 mm high. Approximately 1.5 g of UC powder was poured into the crucible without compression, resulting in a powder bed height of roughly 2 mm that was slightly higher in the centre. The particle size distribution is given as $D_{50} = 2.7\,\mu\text{m}$ with a polydispersity of ~ 0.7. An image of this arrangement is provided in Figure 6.4, and a diagrammatic interpretation in Figure 6.5. Assuming that the particles comprising the powder are spherical, this information allows an estimation of the porosity, ϵ_{UC}, of the cylinder representing the UC powder using

Figure 6.4: A photograph of the UC powder positioned within the crucible (Berthinier *et al.*, 2009).

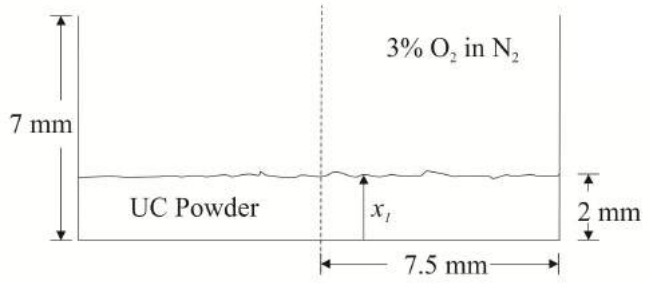

Figure 6.5: A cross-sectional diagram interpreting how the powder is arranged within the stainless steel crucible.

the following empirically-derived equation published by Rwifa (Rwifa, 2000):

$$\epsilon_{UC} = \left\{ \left(0.5710 + 0.144e^{(-0.8627D/D_{50})}\right) + \left[\left(\frac{x_1}{D_{50}} - 1\right) 0.386 + 0.141e^{(-0.6046D/D_{50})}\right] \right\} \Big/ \left(\frac{x_1}{D_{50}}\right) \quad (6.53)$$

where, in this case, D is the crucible diameter and x_1 is the bed height of the carbide powder. The resulting porosity estimate is $\epsilon_{UC} = 0.3867$.

For the powder model to function, the U_3O_8 product layer must also be approximated as a porous cylinder with its own porosity. Eq. 6.53 can again be used to estimate the U_3O_8 porosity, provided that an estimate of the overall powder height, x_2, can be made and assuming the particle size distribution remains the same. The height estimate is taken from the final height of U_3O_8 powder, and is assumed to be roughly twice that of the initial UC powder volume. This estimate is judged visually from Figure 6.6, an image of the powder before and after the oxidation, in lieu of any specific measurements taken of the final powder bed height. Both porosities, ϵ_{UC} and $\epsilon_{U_3O_8}$, are assumed to be constant throughout the oxidation.

The porosities of each species of powder can then be used to calculate the new values of various thermal and diffusive properties for the two species. For example, if ϕ_{UC}^{sol} is a property of solid UC, such as thermal conductivity, the

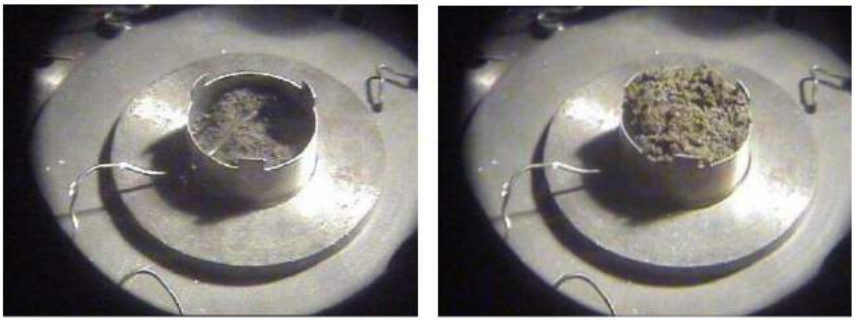

Figure 6.6: The UC powder prior to oxidation (left) and expanded, oxidised powder (right). Presented with permission from CEA Marcoule.

powdered equivalent. ϕ_{UC}^{pow}, can be calculated as:

$$\phi_{UC}^{pow} = \phi_{UC}^{sol}(1 - \epsilon_{UC}) + \phi_{N_2}\epsilon_{UC} \tag{6.54}$$

where ϕ_{N_2} is the value of the property in question belonging to gaseous N_2.

6.4.1.1 Dimensionality

Similarly to the spherical model, the powdered model was completed in one dimension along the height of the powder bed, x. In order to justify this approach given the existing assumption that both powder phases are approximated as porous cylinders, radial effects have to be shown to be negligible. Fortunately, mathematically, the crucible sides ensure that no solid-gas boundary exists along the radial surface of the powdered UC cylinder so no radial kinetic effects require inclusion. In theory, however, there could be radial heat loss at the crucible edges and hence a radial temperature profile in the powder. To examine this, a two-dimensional heat transfer model was constructed across the powder using a method described in the following chapter in Section 7.2. A 1.5 g powdered UC sample was then subjected to the heating ramp used by Berthiner (Berthinier *et al.*, 2009) at the base of the crucible and heat loss to the surrounding N_2 atmosphere fixed at 25 °C at the top; the powder surface. No reaction kinetics were included for simplicity.

Figure 6.7a presents the resulting temperature distributions along the powder radius at the mid-point of the UC powder's height, $x_1/2$. Symmetry around the

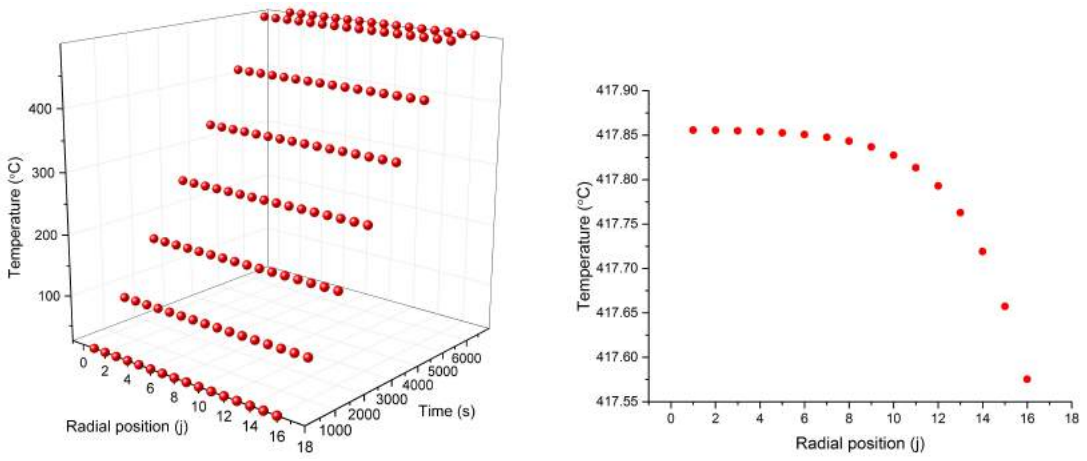

(a) (b)

Figure 6.7: Radial temperature profiles at the centre of the pellet's height, $x_1/2$, over time (a), and a closer examination at one of the instantaneous profiles at 5008 s (b).

powder's axis is assumed, and j designates the radial position within the powder with $j = 0$ at the axis and $j = 16$ at the crucible edge in this case. Figure 6.7b is a plot of a radial temperature distribution 5008 s into the simulation allowing a closer examination of the temperature gradient. A temperature difference of 0.48 °C between the powder axis and radial edge is predicted, indicating that the radial temperature loss is negligible and a one-dimensional approximation of the UC powder is acceptable.

6.4.1.2 Heat and mass transfer

The heat transfer throughout the powder bed was calculated in a similar fashion to the spherical model with a few adjustments. Firstly, the general Fourier equations for both heat and mass transfer, Eqs. 6.2 and 6.3, had to be modified to represent the fact that they considered effects occurring along the axis of the powder bed rather than a spherical radius. Thus the spherical component in the third term, $2/r$, is removed:

For $t \geq 0$ and $0 \leq x \leq x_1(t) \leq x_2(t)$:

$$\frac{\partial T_m(x,t)}{\partial t} = \alpha_m \left(\frac{\partial^2 T_m(x,t)}{\partial x^2} + \frac{\partial T_m(x,t)}{\partial x} \right) \tag{6.55}$$

where $x_2(t)$ is the bed height of the carbide and oxide powder and m designates whether the oxide or carbide is under consideration:

$$\begin{aligned} &\text{For } 0 \leq x < x_1(t) && : \quad m = UC \\ &\text{For } x_1(t) \leq x \leq x_2(t) && : \quad m = U_3O_8 \end{aligned}$$

The mass transfer requires similar modification: For $t \geq 0$ and $x_1(t) \leq x \leq x_2(t)$:

$$\frac{\partial C_g(x,t)}{\partial t} = D_g \left(\frac{\partial^2 C_g(x,t)}{\partial x^2} + \frac{\partial C_g(x,t)}{\partial x} \right) \tag{6.56}$$

New values for diffusivities, D_g, and thermal diffusivities, α_m, are calculated using Eq. 6.54. The initial conditions for Eqs. 6.55 and 6.56 are:

For $t = 0$:

$$x_1(0) = x_2(0) - x_{ox} > 0 \tag{6.57}$$

For $t = 0$ and $0 \leq x \leq x_2(t)$:

$$T_m(x,0) = T_{Amb} \tag{6.58}$$

For $t = 0$ and $x_1(t) \leq x \leq x_2(t)$:

$$C_g(x,0) = 0 \tag{6.59}$$

where x_{ox} represents a very thin oxide layer present at the beginning of the reaction, similar to r_{ox}.

There are again three positions in the solid where boundary conditions must be applied to Eq. 6.55: the base of the UC powder bed, the interface between the oxide and the carbide, and the powder surface. For Eq. 6.56, only the latter two conditions are required.

The boundary condition at the base, where $x = 0$, deviates the most from the spherical model. Rather than representing adiabatic heat transfer due to the

symmetry of a sphere, it must now represent heat transfer between the powder and the heating plate upon which it rests and include the resistance provided by the stainless steel crucible base separating the two:

For $t \geq 0$ and $x = 0$:

$$\left.\frac{\partial T_{UC}}{\partial x}\right|_0 = U\left(T_{plate} - T_{UC}|_0\right) \tag{6.60}$$

where U is the thermal transmittance and T_{plate} is the temperature of the hot plate heating the crucible.

The thermal transmittance is included to represent the rate of heat transfer from the plate to the powder across the stainless steel crucible's base. It is calculated as:

$$U = \frac{\lambda_{ss}}{\sigma c} \tag{6.61}$$

where λ_{ss} is the thermal conductivity of stainless steel and σ_c the thickness of the crucible base in the x direction.

The plate temperature, T_{plate}, increases over time according to the temperature ramp specified by Berthnier *et al.* (Berthinier *et al.*, 2009), illustrates in Figure 2.4 on Page 20. For the model's purposes, it is written as the following mathematical function:

For $t \leq 200\,\mathrm{s}$:

$$T_{plate} = 298 \tag{6.62}$$

For $200\,\mathrm{s} < t \leq 5700\,\mathrm{s}$:

$$T_{plate} = 298 + (0.0819(t - 200)) \tag{6.63}$$

For $t > 5700\,\mathrm{s}$:

$$T_{plate} = 773 \tag{6.64}$$

At the reaction interface, where $x = x_1(t)$, the boundary conditions are similar in form to those in the spherical model:

For $t \geq 0$ and $x = x_1(t)$:

$$T_{UC} = T_{U_3O_8} \tag{6.65}$$

$$-\lambda_{UC} \left.\frac{\partial T_{UC}}{\partial x}\right|_{x_1} - \frac{\Delta H_R R_C}{A_{UC}} = -\lambda_{U_3O_8} \left.\frac{\partial T_{U_3O_8}}{\partial x}\right|_{x_1} \tag{6.66}$$

$$D_{O_2-CO} \left.\frac{\partial C_{O_2}}{\partial x}\right|_{x_1} = \frac{R_C}{A_{UC}} \tag{6.67}$$

$$D_{CO-O_2} \left.\frac{\partial C_{CO}}{\partial x}\right|_{x_1} = -\frac{6R_C}{11A_{UC}} \tag{6.68}$$

where A_{UC} is the axial (face-end) surface area of the approximated UC cylinder calculated from the crucible's radius, r_c, as $A_{UC} = \pi r_c^2$. Note that due to both powder species being in the same crucible, $A_{UC} = A_{U_3O_8}$.

At the surface of the powder bed, where $x = x_2(t)$, the boundary conditions are again similar to the spherical model representing heat and mass transfer between the powder and bulk gas:

For $t \geq 0$ and $r = x_2(t)$:

$$-\lambda_{U_3O_8} \left.\frac{\partial T_{U_3O_8}}{\partial x}\right|_{x_2} = h\left(T_{U_3O_8}\big|_{x_2} - T^B\right) + \epsilon_{U_3O_8}\sigma\left(T_{U_3O_8}|_{x_2}^4 - \left(T^B\right)^4\right) \tag{6.69}$$

$$-D_g \left.\frac{\partial C_g}{\partial x}\right|_{x_2} = k_g\left(C_g|_{x_2} - C_g^B\right) \tag{6.70}$$

The bulk gas temperature within the furnace in which the powder was being oxidised was allowed to increase according to Eq. 6.71, taking into account heat emitted from the regions of the hot plate not covered by the crucible:

$$\begin{aligned}\frac{\mathrm{d}T^B}{\mathrm{d}t} = \Big\{&hA_{UC}\left(T_{U_3O_8}\big|_{x_2} - T^B\right) + \epsilon_{U_3O_8}\sigma A_{UC}\left(T_{U_3O_8}|_{x_2}^4 - \left(T^B\right)^4\right) \\ &+ hA_{UC}\left(T_{plate} - T^B\right) + \epsilon_{U_3O_8}\sigma A_{UC}\left(T_{plate}^4 - \left(T^B\right)^4\right)\Big\}/\rho_{N_2}c_{p_{N_2}}V\end{aligned} \tag{6.71}$$

where h_p is the heat transfer coefficient between the hot plate and the bulk gas, $A_p = A_{plate} - A_{UC}$, where A_{plate} is the surface area of the hot plate, representing the area of the region of the hot plate uncovered by the crucible, ρ_{N_2} and $c_{p_{N_2}}$ are the density and specific heat capacity of N_2, respectively, and V is the volume of the furnace.

6.4.1.3 Powder expansion

From the visual observation of the oxidised powder in Figure 6.6, it was estimated that the oxidised powder occupies twice the volume of the initial volume due, presumably, due to the density decrease from UC to U_3O_8 and increasing porosity of the powder due to the physical effects of the reaction. As such, it was initially decided to make the magnitude of $\mathrm{d}x_2/\mathrm{d}t$, the rate of overall powder expansion, equal to twice that of $\mathrm{d}x_1/\mathrm{d}t$, the rate of UC powder depletion, according to:

For $t \geq 0$:

$$\frac{\mathrm{d}x_1}{\mathrm{d}t} = -\frac{6k_1 \exp\left(-E_A/R\, T_{U_3O_8}|_{x_1}\right) C_{O_2}|_{x_1}}{11\dot{\rho}_{UC}} \tag{6.72}$$

$$\frac{\mathrm{d}x_2}{\mathrm{d}t} = -2\frac{\mathrm{d}x_1}{\mathrm{d}t} \tag{6.73}$$

However, this methodology could not match the phenomena observed during the CEA experiment, particularly the immediate cooling of the temperature spike caused by the initial steep temperature rise. Figure 6.8 is a plot of the temperature measured by a K-type thermocouple (Berthinier *et al.*, 2009) placed in the centre of the powder focussing on the early exothermic behaviour displayed in Figure 6.6. It illustrates the effect in question of the temperature spike immediately cooling off by ∼50 °C at around 1300 s. This effect is taken to be a result of the oxide layer forming on the powder surface, slowing the reaction and preventing the powder from being able to maintain the temperature reached through the exothermic reaction. With an oxide layer expanding slowly and steadily with the depletion of the carbide, this effect is difficult to replicate; instead producing an effect displayed in Figure 6.9. The effect is of the powder undergoing the temperature spike, but then steadily tending towards the plate temperature rather than experiencing the sharp temperature drop observed experimentally. This is taken to be due to the slowly expanding product layer not providing a thick enough diffusion barrier to slow the reaction significantly and cool the powder. Therefore, it was decided that a different approach to modelling the powder expansion should be taken - one involving an initial rapid expansion followed by only minor changes.

This approach was taken partly in part to achieve a better fit for the model, and partly due to observations made by Berthinier *et al.* (Berthinier *et al.*, 2009)

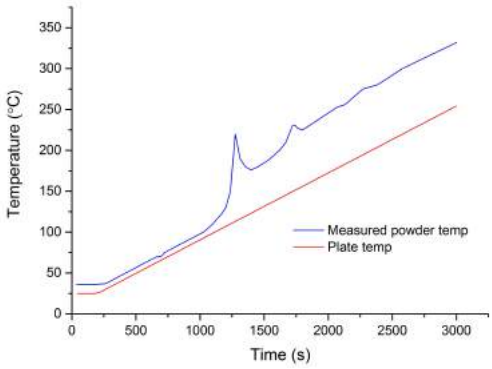

Figure 6.8: A closer examination of powder temperature rise resulting from the oxidation, taken from Figure 6.6.

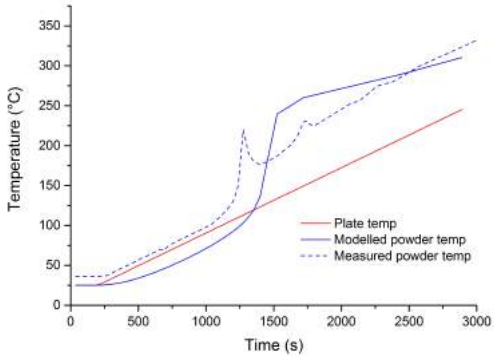

Figure 6.9: Powder temperature predicted when using a model with a steadily expanding U_3O_8 layer compared to Berthinier *et al.*'s (Berthinier *et al.*, 2009) measurements.

for the oxidation in air where a "major increase in volume was observed after ignition". Although the oxidation in 3% O_2 doesn't ignite in the same dramatic fashion, it is not unreasonable to assume that a significant volume expansion accompanies the initial exothermic peak at ∼1300 s. The expansion was implemented by defining the overall bed height, x_2, by the following conditions:

For $t < t_{ex}$:

$$x_2(t) = x_1(0) + x_{ox} \tag{6.74}$$

For $t \geq t_{ex}$:

$$x_2(t) = 2x_1(0) \tag{6.75}$$

where t_{ex} is the time at which the initial exothermic peak occurs, calculated in the model as the time at which the fraction of UC oxidised hits a threshold when the heat released from the reaction becomes significant ($\Delta m/m_0 = 0.015$), and $x_1(0)$ is the initial UC powder bed height.

This method of modelling the powder expansion, despite being more arbitrary, gives a much better fit to the experimental data than the steadily expanding oxide.

6.4.1.4 Monitoring powder temperature

Experimentally, the powder temperature was monitored through the use of a K-type thermocouple placed initially at the centre of the UC powder surface, roughly observable in the left image of Figure 6.6. As the oxide layer is generated and fills the crucible, the probe remains in roughly the same physical position and is submerged within the powder. In order to compare the modelled powder temperature against the measured value, therefore, readings must be taken from the equivalent physical position within the predicted temperature distribution.

The position of the thermocouple is expressed as:

For $t \geq 0$:

$$x_{probe} = x_1(0) \tag{6.76}$$

where x_{probe} is the position of the thermocouple, assumed to remain constant.

A subroutine is then included in the model's numerical solution that finds the node along the bed height, j, closest in position to x_{probe} at each time step. This value of the temperature is then output as the simulated thermocouple temperature for comparison to Berthinier *et al.*'s measurements (Berthinier *et al.*, 2009).

6.4.1.5 Numerical solution

The numerical solution to the mathematical formulation of the powder model is almost identical in methodology to that of the spherical case, barring the adjustment of one of the boundary conditions and a few other minor changes. Therefore, a separate description of the numerical solution for the powder model does not require inclusion.

6.5 Results

The results section of this chapter will be divided to distinguish results produced by the spherical, solid UC model and results from the powdered UC model.

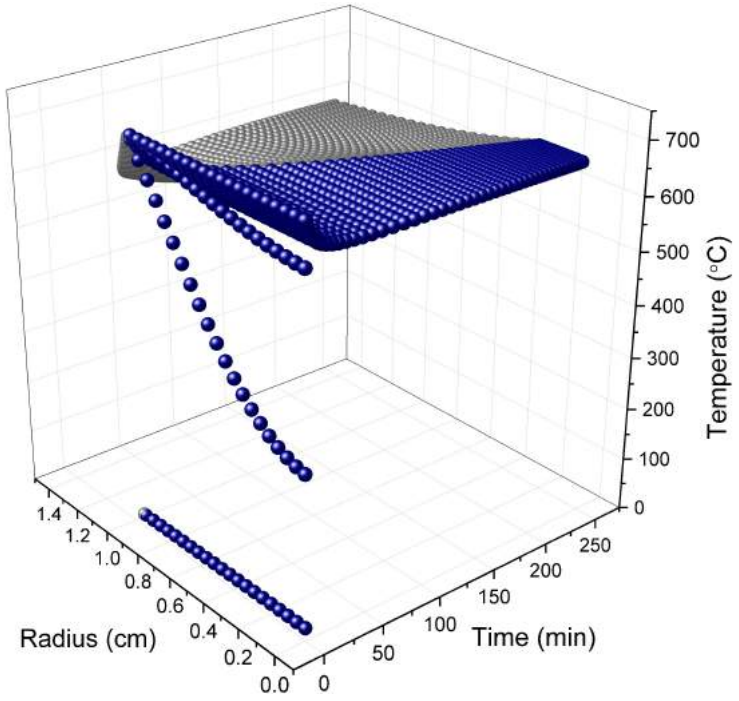

Figure 6.10: Radial temperature distribution over time illustrating the shrinking carbide in blue, the expanding oxide in grey and the thermal response of the solid.

6.5.1 Spherical model

The spherical model is capable of predicting the reaction completion time, as well as the transient temperature distribution through the solid system and the O_2 and CO concentration distributions through the oxide layer. An example of modelling the temperature distribution over time can be seen in Figure 6.10, and examples of the concentration distributions can be seen in Figures 6.11 and 6.12. For these results, a carbide pellet of radius $r_1 = 0.935\,\text{cm}$ was used initially at 25 °C and exposed to bulk gas with a volume of $1\,\text{m}^3$ and a temperature held constant at 500 °C. The bulk gas O_2 concentration at the beginning of the reaction was $3.15\,\text{mol}\,\text{m}^{-3}$, representing 21% O_2 in air at 1.01 bar, and the CO concentration was assumed to be constant and zero.

Figure 6.10 displays an initial steep temperature rise in the carbide, shown in blue, caused by both the exposure to the hotter bulk gas and the exothermic oxidation. It then peaks and begins to cool down slightly. This is due to the

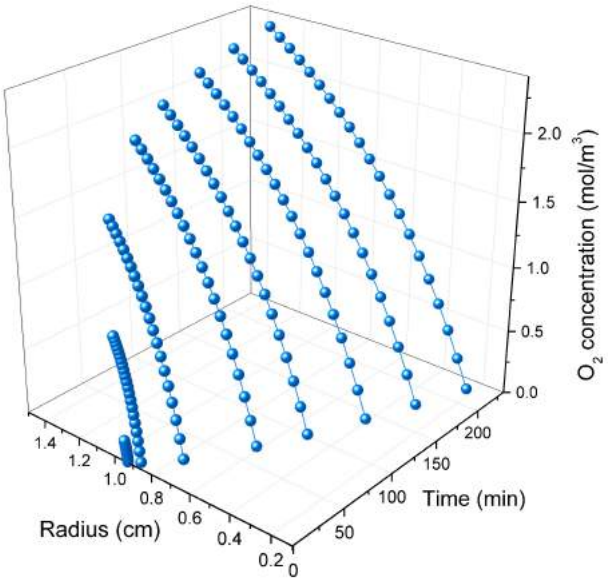

Figure 6.11: Radial O_2 distribution through the expanding oxide layer over time. The gradient is largely constant with time, and the minimal value at the oxide-carbide interface suggests O_2 diffusion is the rate limiting step.

formation of the U_3O_8 oxide layer retarding the initially rapid reaction rate, causing less heat to be generated by the reaction. The temperature throughout the solid then remains largely constant for the remainder of the reaction. Also observable in Figure 6.10 is the lack of a temperature gradient throughout the carbide due to its high thermal conductivity.

Figure 6.11 highlights the steep O_2 concentration through the product layer. At $r = r_2$, the solid surface, the O_2 concentration approaches the concentration of O_2 in the bulk gas (it remains lower, however, due to it having to diffuse across the external gas film layer). At $r = r_1$, the oxide-carbide interface, the O_2 concentration is essentially zero, with the value at $t = 233\,\text{min}$ being $C_{O_2}|_{r_1} = 4.78 \times 10^{-6}\,\text{mol}\,\text{m}^{-3}$. This suggests that the O_2 is being consumed by the surface reaction, R_C, significantly faster than it can diffuse from the bulk gas to the reaction site, allowing the conclusion that the reaction rate is limited and controlled by the rate of O_2 diffusion through the product layer, D_{O_2}.

Figure 6.12 illustrates the similarly steep concentration gradient of CO through the product layer, with the maximum occuring at $r = r_1$ where it is being gener-

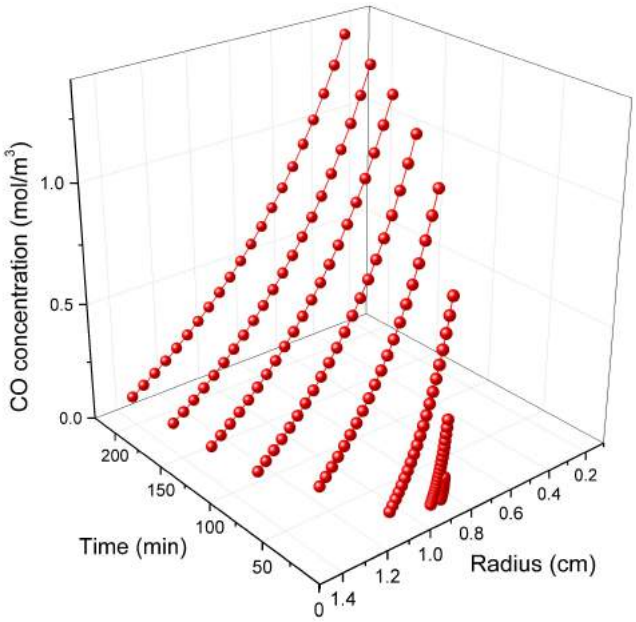

Figure 6.12: Radial CO distribution through the oxide layer. It is generated at the reaction interface and diffuses out to the bulk gas.

ated and a minimum at $r = r_2$ where it is lost to the bulk gas, assumed in this case to have a constant value of $C^B_{CO} = 0\,\mathrm{mol\,m^{-3}}$.

Figures 6.10, 6.11 and 6.12 also allow the expansion of the overall solid to be observed, with the initial solid radius of $r_2 = 0.945\,\mathrm{cm}$ increasing to $r_2 = 1.324\,\mathrm{cm}$.

A closer examination of the O_2 and CO distributions in the oxide layer at a time step late in the reaction, $t = 232.5\,\mathrm{min}$, can be observed in Figure 6.13.

Sensitivity studies were carried out on the model by varying input parameters to see what effects they have on the oxidation. Figure 6.14 is a plot of the effect of the bulk gas temperature on the reaction completion time, and Figure 6.15 plots the effect it has on the temperature at the reaction interface. A carbide pellet of radius 0.935 cm and initial temperature of 25 °C was used with an initial O_2 concentration in the bulk gas of $3.15\,\mathrm{mol\,m^{-3}}$ for all simulations, representing 21% O_2 in $1\,\mathrm{m^3}$ of air at 1.01 bar. An initial CO concentration of zero was assumed as was an initial oxide layer thickness of 0.01 cm. Table 6.2 quantifies the effects the gas temperature has on the completion time and the maximum

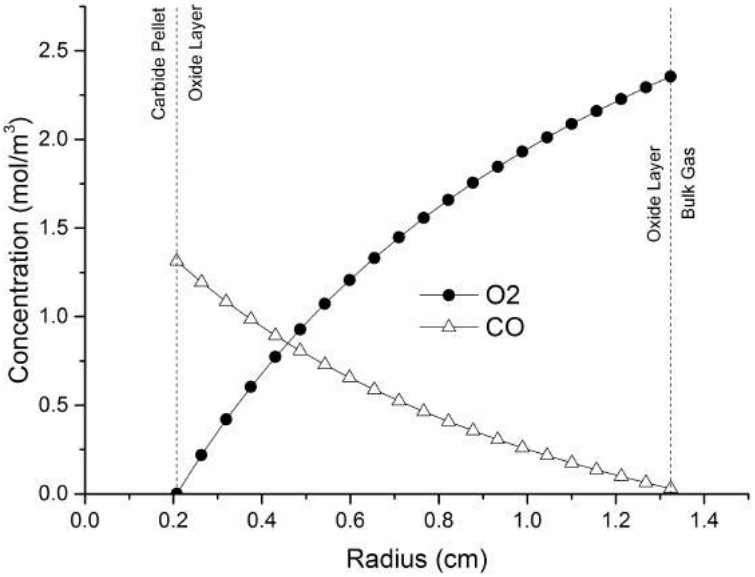

Figure 6.13: The O_2 and CO distributions through the oxide product layer towards completion of the reaction at $t = 232\,\text{min}$. At $t = 0$, $r_1 = 0.935\,\text{cm}$ and $r_2 = 0.935\,\text{cm}$.

interface temperature, which is the position within the solid that reaches the highest temperature.

Figure 6.14 and Table 6.2 indicate that increasing the gas temperature greatly reduces the oxidation completion time. Figure 6.15 demonstrates that the maximum temperature reached in the pellet, occurring at the UC/U_3O_8 interface, also increases significantly with the gas temperature.

Similar sensitivity studies were carried out on the effect of the initial O_2 concentration in the bulk gas with the results presented in Figures 6.16 and 6.17. For these results, the bulk gas temperature was 500 °C and a carbide pellet with an initial radius and temperature of 0.935 cm and 25 °C was assumed. The initial oxide layer present was again assumed to have a thickness of 0.01 cm, and the air pressure was 1.01 bar and its volume $1\,\text{m}^3$.

Figures 6.16 and 6.17 and Table 6.3 illustrate the effect that the O_2 concentration has on the reaction rate. The significant increase, and resulting increase in the temperature reached, was expected due to the suggestion that O_2 supply to the reaction is the rate limiting step. Increasing the O_2 concentration

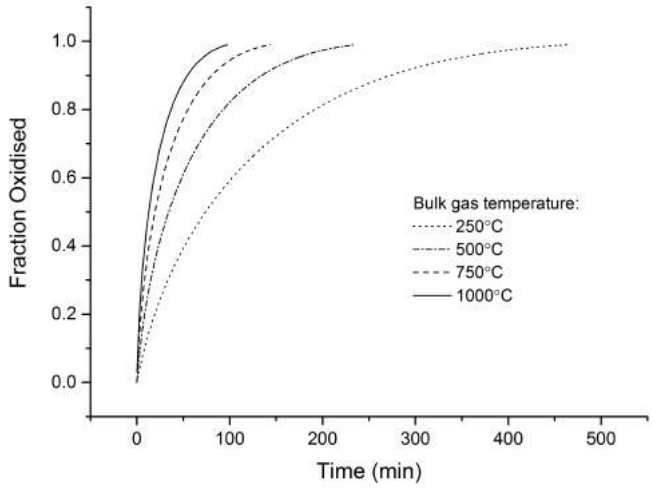

Figure 6.14: The effect of varying the bulk gas temperature, assumed to be constant, on the completion time of the oxidation reaction.

to 12.6 mol m^{-3}, for example, reduces the reaction completion time to 51.1 min compared to the 253 min in air.

Figure 6.17 is a logarithmic plot included to detail the O_2 concentration at the reaction interface over time. Due to the stated initial conditions, at $t = 0$, $C_{O_2}|_{r_1} = 0$. As O_2 then transfers into the product layer from the bulk gas, the concentration at the interface rises. This allows the oxidation reaction to proceed, which rapidly consumes the O_2. Continuous consumption of O_2 by the oxidation maintains the concentration at the interface as $C_{O_2}|_{r_1} \approx 0$.

6.5.2 Powder model

The powder model as described in Section 6.4 was then fit to Berthinier *et al.*'s (Berthinier *et al.*, 2009) data by adjusting the activation energy of the oxidation, E_A, and the first order reaction constant, k_1, until the modelled powder temperature matched the observed value. The best fit was achieved using values of $E_A = 51.0\,\mathrm{kJ\,mol^{-1}}$ and $k_1 = 2.0 \times 10^3\,\mathrm{m\,s^{-1}}$, with the results displayed in Figure 6.18. The dimensions of the crucible in which the powder was placed and the mass of UC powder were made equivalent to the values used by Berthinier *et al.* and the porosity of the powder calculated using Eq. 6.53. The surrounding gas tempera-

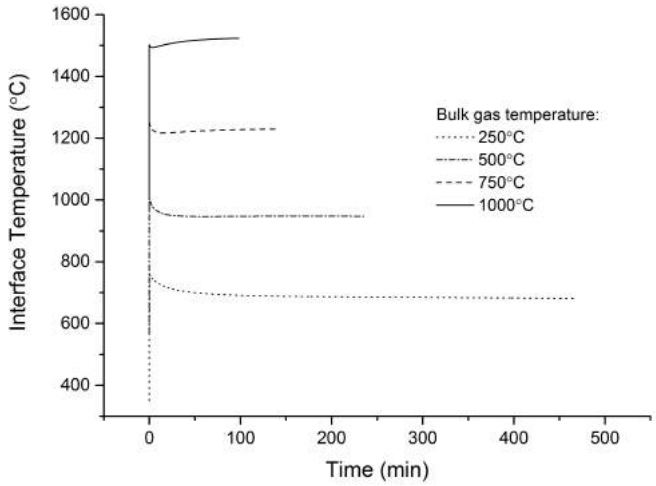

Figure 6.15: The effect of varying the bulk gas temperature on the temperature at the UC/U_3O_8 interface.

ture had an initial value of 25 °C and was allowed to rise according to Eq. 6.71. The O_2 concentration was fixed at 3% O_2 in a N_2 atmosphere at 1 atm.

The modelled powder temperature appears to fit the experimental observations well. The value of the activation energy, E_A, applied ensures the reaction starts to occur at around 100 °C and the rate constant, k_1, ensures the steepness of the temperature spike fits well. The expanding product layer then causes the temperature spike to dip: not quite as significantly as desired but a better fit than the steadily expanding oxide layer methodology presented in Figure 6.9. The modelled temperature then follows the steadily increasing measured temperature remaining around 60 °C hotter than the hot plate due to the on-going oxidation reaction. The model, however, is unable to replicate the second exothermic peak occurring. The cause of this peak is uncertain, and has been suggested to be a physical movement of the powder in the crucible exposing fresh carbide or perhaps a further oxidation reaction. In either case, the powder model would need to be significantly more advanced to account for it so this must be accepted as a limitation of the model.

Nonetheless, the model provides an acceptable fit to the observed powder temperature allowing some of its other capabilities to be examined. Figure 6.19 presents the temperature profiles along the powder bed height as the oxidation

Table 6.2: The dependence of the maximum temperature reached at the UC/U_3O_8 interface and the reaction completion time on the bulk gas concentration.

Bulk gas temperature, T^B ($mol\,m^{-3}$)	Maximum interface temperature, $T_{U_3O_8}\|_{r_2}$ (K)	Reaction completion time (h)
250	757.5	7.767
500	1004	3.922
750	1251	2.393
1000	1523	1.633

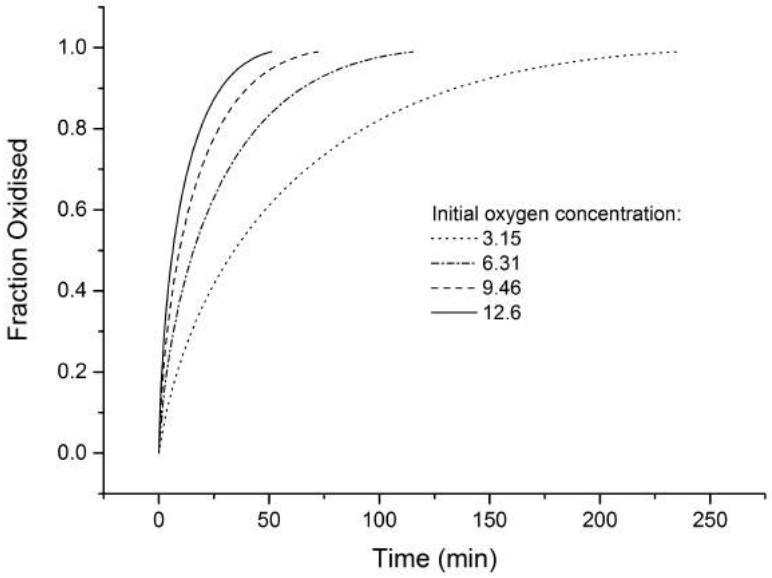

Figure 6.16: Curves representing fraction of uranium carbide oxidised over time at different initial O_2 concentrations in the bulk gas.

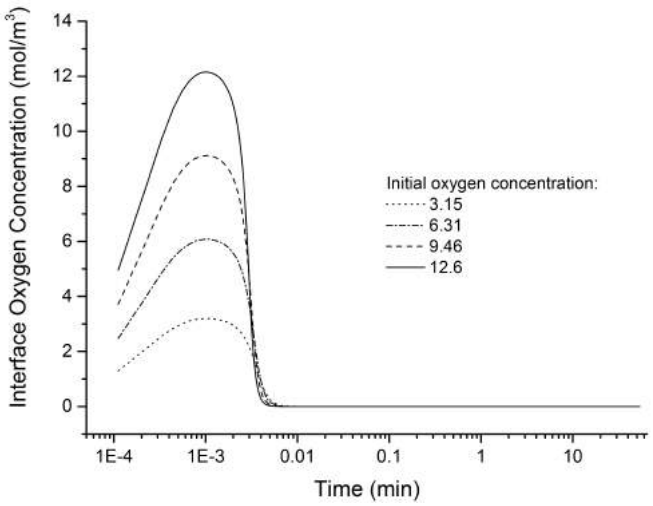

Figure 6.17: The effect of the bulk O_2 concentration on the O_2 concentration at the reaction interface over time.

proceeds from the same conditions used in producing Figure 6.18. The sudden expansion of the oxide layer, coloured grey, is illustrated, and the resulting dip in temperature across the entire solid is displayed. As the reaction proceeds and the carbide is depleted, the nodes across the carbide powder can be seen to draw closer as the increment size, Δx_{UC}, becomes smaller as dictated by the numerical solution applied in both the spherical and powdered models.

Figure 6.20 displays the O_2 concentration throughout the product layer from the same simulation as Figures 6.18 and 6.19, beginning when the product layer expansion occurs. In fact, there is O_2 present in the thin, initial product layer of thickness, x_{ox}, prior to expansion, but the concentration gradient is minimal and the value equivalent to the bulk concentration, $C^B_{O_2}$. These data were therefore omitted from Figure 6.20 to allow the more pertinent phenomena to be better displayed. Throughout the course of the oxidation, post-expansion, there is a steep O_2 concentration gradient from the powder surface to the reaction interface. This suggests again, despite the porosity of the oxide product increasing diffusivity of O_2 through it, that the oxidation rate is limited by the diffusion rate of O_2 from the bulk gas to the reaction site. After the product layer expansion, the O_2 concentration increases slightly across the powder bed height as the product layer slows the reaction. It then steadily decreases throughout the

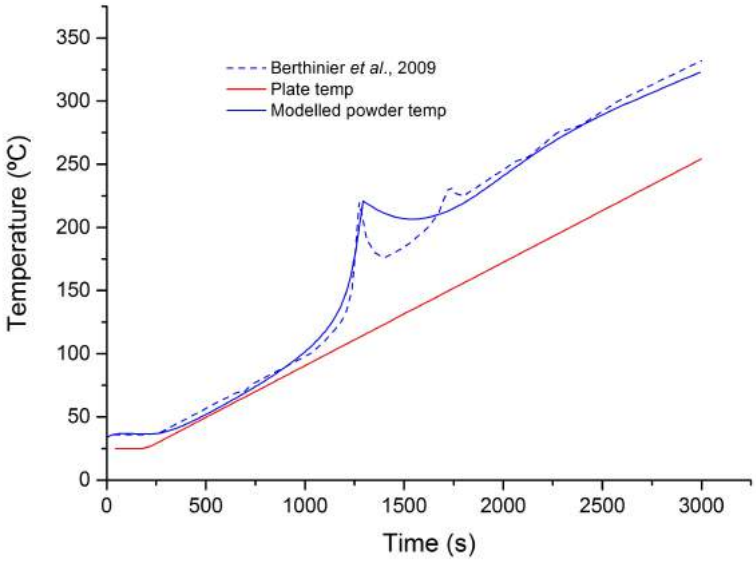

Figure 6.18: A comparison of the modelled powder temperature to experimental data during the initial stages of reaction.

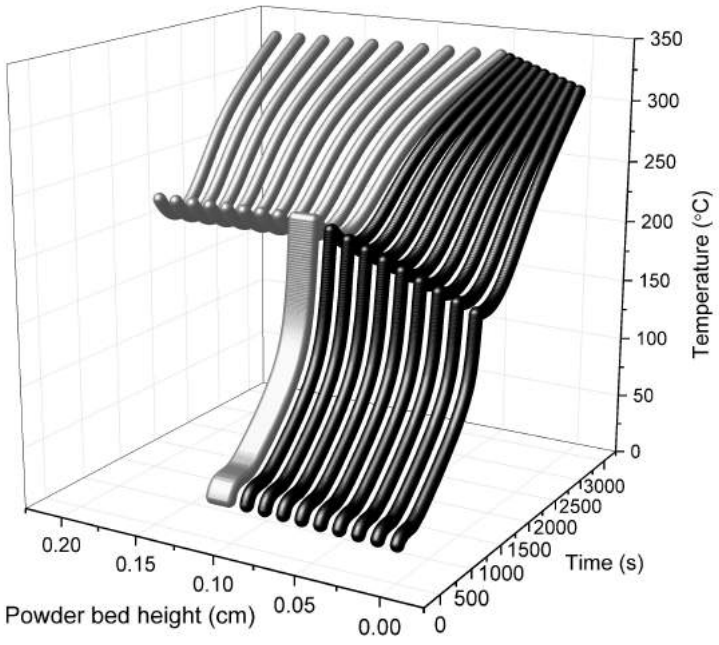

Figure 6.19: Temperature profiles along the carbide (black) and oxide (grey) powder bed height at different times. The immediate expansion of the oxide (in grey) can be seen to coincide with a dip in temperature across the solid.

Table 6.3: The dependence of the surface and interface temperatures on the bulk gas O_2 concentration, as well as the resulting reaction completion times.

Bulk gas oxygen concentration, $C^B_{O_2}$ ($\mathrm{mol\,m^{-3}}$)	Maximum interface temperature, $T_{U_3O_8}\vert_{r_2}$ (K)	Reaction completion time (min)
3.15 (21%)	1004	235.3
6.31 (40%)	1194	115.3
9.46 (60%)	1381	72.19
12.6 (80%)	1556	51.11

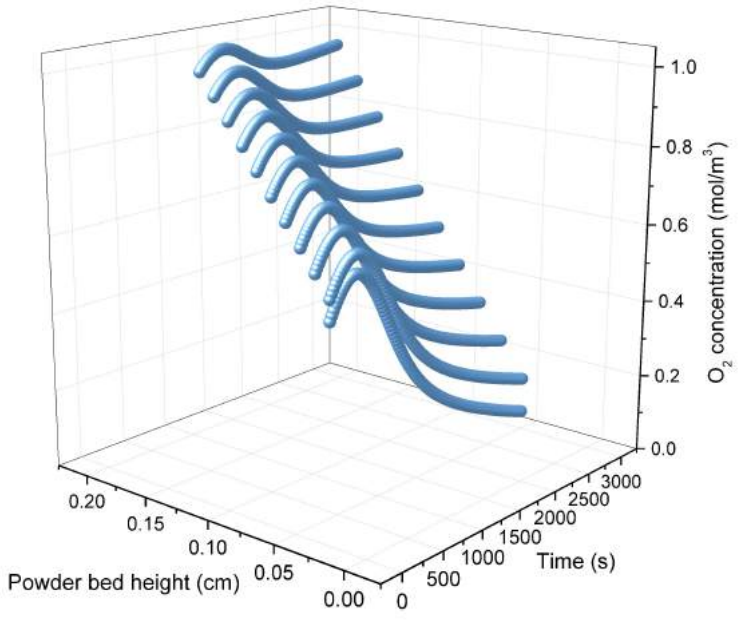

Figure 6.20: O_2 concentration profiles throughout the oxide layer at a number of instances, beginning after the oxide layer has expanded.

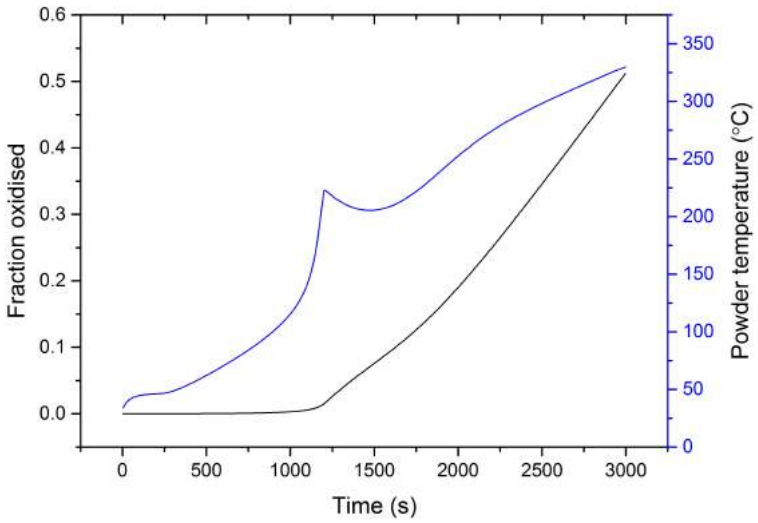

Figure 6.21: A plot of both the powder temperature and fraction of UC oxidised against time up to 3000 s.

reaction as the oxide layer expands as a result of the carbide shrinking and the total powder height remaining constant.

A prediction of the completion of the oxidation during the time period examined in Figures 6.18, 6.19 and 6.20 is plotted in Figure 6.21. Approximately 50 % of the UC powder is oxidised after 3000 s, with oxidation beginning concurrently with the temperature spike at 1200 s. The rate of oxidation then appears to increase, suggesting that the increasing temperature outweighs the slowing effect of the expanding product layer. It is possible, however, that the reaction rate will slow towards the completion of the oxidation as the oxide layer expands further and the plate temperature plateaus at 500 °C.

6.6 Conclusions

A transient mathematical model with two moving-boundaries and independent meshes for the oxidation of a UC pellet was developed. An adherent oxide product layer comprising U_3O_8 adheres and expands. Heat transfer through the solid and mass transfer through the U_3O_8 were represented by the Fourier equations at any instant of time, with non-linear boundary conditions at both the interface between

the UC and the U_3O_8 and at the solid surface. These boundary conditions are necessary for the processes of heat and mass transfer between the solid and the bulk gas, and for the generation of heat at the reaction interface.

The resulting set of partial and ordinary differential equations were solved numerically through implicit and explicit finite difference approximations. Linearisation of equations such as Eq. 6.38 at each time step was necessary to account for the high non-linearity. Convergence at each time step was enforced before proceeding to the next increment of time.

The numerical stability of the model was controlled by a dynamic time step size calculated from the Courant-Friedrichs-Lewy condition, which accommodates the change in the size of the radial increment. The numerical solution was checked for convergence by progressively increasing the number of radial increments and using Richardsons deferred approach to the limit methodology.

The stable model was then able to predict the temperature distribution through the solid and the concentrations of O_2 and CO through the U_3O_8 layer, and use them to predict the reaction completion times and the maximum temperatures reached. For a typical spherical UC pellet with a radius of 0.935 cm, the oxidation takes between 1 h to 20 h depending on the input parameters. The maximum temperature reached of 1556 °C occurred when a high O_2 content of 80% and a gas temperature of 500 °C was used. Lower O_2 concentrations and temperatures can be used to bring the maximum temperature down quite significantly, with a peak of 757.7 °C predicted at 21% O_2 and a gas temperature of 250 °C, suggesting that these parameters could provide safe operating conditions for the oxidation without compromising too much on the completion time.

Comparison of these predictions to those obtained from a model where the U_3O_8 layer does not adhere described in Chapter 4, indicates that the product layer slows the reaction. For example, at 500 °C, 21% O_2 and an initial radius of 0.935 cm, an increase in the reaction completion time from 3.71 h to 3.92 h is predicted. The cause for this increase in the completion time can be attributed to the need for the reacting oxidant to diffuse through the product layer before it reaches the reaction interface. Additionally, the slower reaction rate, especially toward the completion of the reaction as the product layer has thickened, causes

the maximum temperature reached to decrease from 1458 °C to 1004 °C when an adherent U_3O_8 layer is considered.

The model described in this chapter is applicable for the lower O_2 partial pressures that the model presented in Chapter 4 is not, as it considers an adherent oxide product layer. It provides an alternative to Scott's model of graphite fuel oxidation (Scott, 1966) in that it considers a U_3O_8 product layer, rather than UO_2, as is suggested to be the case in practice (Berthinier *et al.*, 2009; Mazaudier *et al.*, 2010; Peakall & Antill, 1962). It therefore predicts temperature outputs and a product layer expansion closer to the real oxidation. It also adds the calculation of the transient O_2 and CO gradients through the product layer, which is of importance as the rate limiting step.

A limitation of the model is that the kinetics are still a significant simplification, as the oxide layer will in reality likely be a combination of different uranium oxide phases at different degrees of oxidation. Incorporating these into a model using this methodology would require a different mesh for each species, so would be too numerically complex and computationally laborious for the scope of this work. Also, as with the model in Chapter 4, the one-dimensional assumption rests on the UC pellet undergoing no damage before or during the oxidation that would affect its symmetry. It may also be necessary to include a stress model for the U_3O_8 layer, so that the conditions at which it adheres and does not can be better understood rather than relying on suggestions in open literature that do not cover temperature dependence.

Further application of the methodology used in developing the adherent oxide layer model allowed the production of a model capable of simulating a UC sample in powdered form. The motivation for such a model was to enable the prediction of new values for the rate constant, k_1, and the activation energy of the oxidation, E_A, by fitting the powdered model's temperature predictions to experimental observation by Berthinier *et al.* (Berthinier *et al.*, 2009). Such a fit is presented in Figure 6.18, illustrating the capability of the powder model to simulate the bulk of the observed exothermic phenomena during the initial stages of a powder oxidation in 3% O_2 in a N_2 atmosphere. Additional capabilities of the powder model, such predicting temperature and concentrations through the powder, are illustrated in Figures 6.19 and 6.20.

Both powdered and pellet models provide predictions of maximum temperatures reached and the time necessary for complete oxidation that, when combined with the pellet model with no adherent layer, provide a comprehensive tool for designing a UC oxidation for reprocessing. Across a broad range of O_2 partial pressures, the necessary oxidation parameters for a safe and controlled oxidation can be predicted for both powdered and pellet samples. Additionally, both models constitute helpful tools for fitting and refining oxidation parameters should new, reliable data arise.

Chapter 7

Two-dimensional oxidation model

7.1 Introduction

In Chapters 4, 5 and 6, models describing the oxidation and dissolution of a UC fuel pellet approximated as an equivalent volume sphere to allow consideration in one dimension are detailed. This chapter aims to increase the complexity of the oxidation model without an adherent product layer as described in Chapter 4 by considering the pellet in two dimensions as an axisymmetric cylinder, as illustrated in Figure 7.1, hence requiring a significantly more complex mathematical description and numerical solution.

This representation of the pellet should increase the accuracy of the model by removing the equivalent volume sphere assumption, and therefore allowing the variation of temperature and O_2 concentration along the surface of the pellet. The assumption used instead is that the pellet is axisymmetric: it is completely symmetrical around its central, lengthwise axis. This allows the model to examine a plane, or a 'slice', taken from the pellet that is rotationally symmetrical around the axis as shown in Figure 7.1. Heat and mass transfer processes must now be considered in two directions: along the pellet's length and its radius.

The model described in this section uses the same reaction mechanism as that in Eqs. 4.1 and 4.2 provided on Page 80. All of the previous assumptions made for the one-dimensional model, except that the pellet is an equivalent volume sphere, are kept in place.

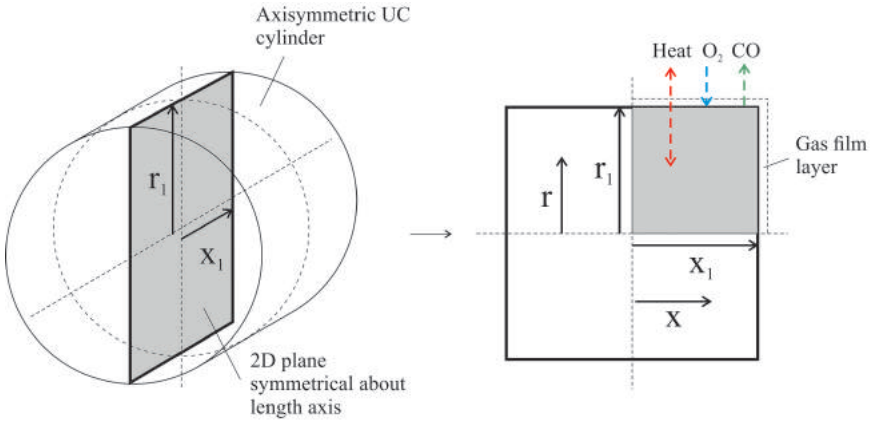

Figure 7.1: A two-dimensional approximation of a pellet as an axisymmetric cylinder. A rotationally symmetrical plane is taken from the cylinder as the domain of the model.

It was decided that the two-dimensional model would be completed without an adherent oxide layer due to difficulties in modelling the expansion of the oxide product layer in a manner representative of reality. These difficulties arose as diffusion through the product layer became the rate limiting step, and the two-dimensionality of the system meant that there was a significantly higher O_2 concentration at the corner of the plane being considered. The reaction rate is therefore faster at the corner, leading to a shape change in the cylindrical pellet as it tends towards a sphere as illustrated in Figure 7.2. In Figure 7.2, a pellet of a length and diameter of 4 mm was oxidised in air with a product layer allowed to adhere, but not to expand. Note that the model only solves over a quarter of the plane, and that the representation shown is produced by mirroring the results across the lines of symmetry along the radius and length.

The problem occurs when attempting to model the resulting expansion of the overall solid as the product layer is produced. As the most carbide is depleted at the corner, so should the most oxide produced be there. This would produce a strange effect where 'spikes' of oxide occur at the corners, rather than rounding off to a more spherical shape as might be expected. The mathematical complications and struggle to reconcile the oxide layer behaviour with reality led to the decision that a two-dimensional oxidation model with an adherent product layer would

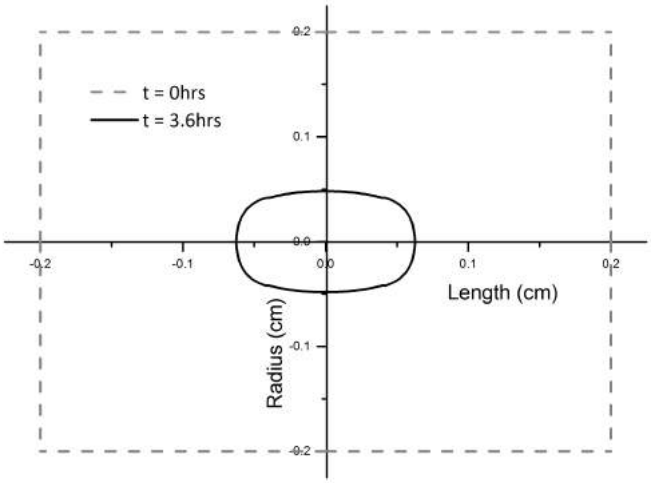

Figure 7.2: The change in position of the oxide-carbide interface after 3.6 h. At $t = 3.6$ h the dotted line also represents the position of the oxide layer as it isn't allowed to expand.

require more work than is feasible in the scope of this project.

7.2 Mathematical representation

As well as using the same reaction mechanism, Scott's (Scott, 1966) kinetics are again used to describe surface reaction rate. The mathematical description, however, is different due to the two-dimensionality of the system: the surface reaction occurs along both the face and length of the carbide cylinder.

For $0 \leq x \leq x_1$:

$$R_r = k_1 \exp\left(-E_A/RT_{UC}|_{x,r_1}\right) A_r \, C_{O_2}|_{x,r_1} \tag{7.1}$$

For $0 \leq r \leq r_1$:

$$R_x = k_1 \exp\left(-E_A/RT_{UC}|_{x_1,r}\right) A_x \, C_{O_2}|_{x_1,r} \tag{7.2}$$

where R_r and R_x are the rates of O_2 consumption along the radial and axial surfaces, respectively, x is the length position, with $x = 0$ at the centre of the pellet and $x = x_1$ at its surface, r is the radial position with $r = 0$ at the centre

and $r = r_1$ at the surface, and A_r and A_x are the surface areas exposed in the r and x directions, respectively.

Since the oxidation of CO occurs in the bulk gas, it is independent of the dimensionality of the pellet. Therefore, the rate of CO consumption remains in the same form as Eq. 4.7 provided by Howard *et al.* (Howard *et al.*, 1973) on Page 85.

7.2.1 Heat and mass transfer

In order to calculate the reaction rates provided in Eqs. 7.1 and 7.2, the temperature and O_2 concentration at the surface of the two-dimensional plane representing the axisymmetrical cylinder must be known.

The heat conduction through the pellet is represented by the two-dimensional, cylindrical Fourier equation:

For $t \geq 0$, $0 \leq r \leq r_1$ and $0 \leq x \leq x_1$:

$$\frac{\partial T_{UC}(r,x,t)}{\partial t} = \alpha_{UC}\left(\frac{\partial^2 T_{UC}(r,x,t)}{\partial x^2} + \frac{\partial^2 T_{UC}(r,x,t)}{\partial r^2} + \frac{1}{r}\frac{\partial T_{UC}(r,x,t)}{\partial r}\right) \quad (7.3)$$

The initial conditions for Eq. 7.3 are:

For $t = 0$ and $0 \leq x \leq x_1$:

$$r_1(0,x) > 0 \quad (7.4)$$

For $t = 0$ and $0 \leq r \leq r_1$:

$$x_1(r,0) > 0 \quad (7.5)$$

For $t = 0$, $0 \leq r \leq r_1$ and $0 \leq x \leq x_1$:

$$T_{UC}(r,x,t) = T_A \quad (7.6)$$

Boundary conditions are then applied along the surfaces, where $x = x_1$ and $r = r_1$, and along the lines of symmetry, where $x = 0$ and $r = 0$. Similarly to the

previous one-dimensional models, the heat transfer boundary conditions across the lines of symmetry are adiabatic. They can be written as:

For $t \geq 0$, $r = 0$ and $0 \leq x \leq x_1$:

$$\left.\frac{\partial T_{UC}}{\partial r}\right|_{x,0} = 0 \tag{7.7}$$

For $t \geq 0$, $0 \leq r \leq r_1$ and $x = 0$:

$$\left.\frac{\partial T_{UC}}{\partial x}\right|_{0,r} = 0 \tag{7.8}$$

The boundary conditions along the surfaces of the plane take the effects of heat transfer between the pellet and the bulk gas across a gaseous film layer into account. Eqs. 7.9 and 7.10 provide the mathematical representation of this heat exchange via conduction and radiation, as well as the heat generated by the surface reaction given in Eqs. 7.1 and 7.2.

For $t \geq 0$, $r = r_1$ and $0 \leq x \leq x_1$:

$$\begin{aligned} -\lambda_{UC}\left.\frac{\partial T_{UC}}{\partial r}\right|_{x,r_1} = {} & h_r\left(T_{UC}|_{x,r_1} - T^B\right) \\ & + \epsilon_{UC}\sigma\left(T_{UC}|^4_{x,r_1} - \left(T^B\right)^4\right) + \frac{\Delta H_R R_r}{A_r} \end{aligned} \tag{7.9}$$

For $t \geq 0$, $0 \leq r \leq r_1$ and $x = x_1$:

$$\begin{aligned} -\lambda_{UC}\left.\frac{\partial T_{UC}}{\partial x}\right|_{x_1,r} = {} & h_x\left(T_{UC}|_{x_1,r} - T^B\right) \\ & + \epsilon_{UC}\sigma\left(T_{UC}|^4_{x_1,r} - \left(T^B\right)^4\right) + \frac{\Delta H_R R_x}{A_x} \end{aligned} \tag{7.10}$$

where h_r and h_x are the heat transfer coefficients in the r and x directions, respectively, calculated according to Eqs. 7.11 and 7.12, and A_r and A_x are the radial and axial surface areas, respectively. The radial surface area and heat transfer coefficient vary both with time and axial position. Similarly, the axial surface area and heat transfer coefficient vary with time and radial position. This is an important effect to consider later when the numerical solution discretises the spatial dimensions. The dependence of each surface area at discretised positions

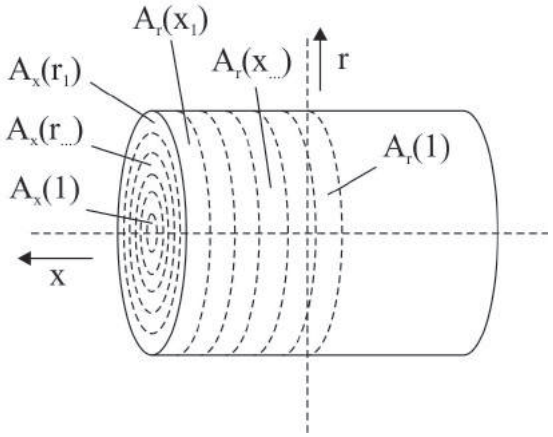

Figure 7.3: An illustration or how the radial surface area, A_r, varies with axial position, x, and how the axial surface area, A_x, varies with radial position, r.

is illustrated in Figure 7.3, and it can be seen that the axial surface area will vary quite significantly with radial position.

For $t \geq 0$ and $0 \leq x \leq x_1$:

$$h_r = \frac{\lambda_{fluid}\mathrm{Nu}}{2r_1} \tag{7.11}$$

For $t \geq 0$ and $0 \leq r \leq r_1$:

$$h_x = \frac{\lambda_{fluid}\mathrm{Nu}}{2x_1} \tag{7.12}$$

The Nusselt number is again calculated using the Ranz and Marshall correlation (Ranz & Marshall, 1952) in Eq. 4.16.

The mass transfer of oxygen from the bulk gas to the pellet surface across the gaseous film layer requires solving to obtain $C_{O_2}|_{x,r_1}$ and $C_{O_2}|_{x_1,r}$ from the bulk oxygen concentration $C^B_{O_2}$. It is expressed as:

For $t \geq 0$ and $0 \leq x \leq x_1$:

$$R^*_r = k_{g_r} A_r \left(C^B_{O_2} - C_{O_2}|_{x,r_1} \right) \tag{7.13}$$

For $t \geq 0$ and $0 \leq r \leq r_1$:

$$R^*_x = k_{g_x} A_x \left(C^B_{O_2} - C_{O_2}|_{x_1,r} \right) \tag{7.14}$$

where k_{g_r} and k_{g_x} are the external diffusion coefficients in the r and x directions respectively, calculated according to Eqs. 7.15 and 7.16.

For $t \geq 0$ and $0 \leq x \leq x_1$:

$$k_{g_r} = \frac{D_{O_2-CO}\mathrm{Sh}}{2r_1} \tag{7.15}$$

For $t \geq 0$ and $0 \leq r \leq r_1$:

$$k_{g_x} = \frac{D_{O_2-CO}\mathrm{Sh}}{2x_1} \tag{7.16}$$

The Sherwood number is also calculated using the Ranz and Marshall correlation (Ranz & Marshall, 1952) as described in Eq. 4.21.

Equating Eq. 7.13 with Eq. 7.2, and Eq. 7.14 with Eq. 7.1, provides the oxygen concentrations along each surface:

For $t \geq 0$ and $0 \leq x \leq x_1$:

$$C_{O_2}|_{x,r_1} = \frac{k_{g_r} C^B_{O_2}}{k_{g_r} + k_1 \exp\left(-E_A/R\, T_{UC}|_{x,r_1}\right)} \tag{7.17}$$

For $t \geq 0$ and $0 \leq r \leq r_1$:

$$C_{O_2}|_{x_1,r} = \frac{k_{g_x} C^B_{O_2}}{k_{g_x} + k_1 \exp\left(-E_A/R\, T_{UC}|_{x_1,r}\right)} \tag{7.18}$$

Allowing the rates of oxygen consumption at each surface to be expressed in terms of the bulk oxygen concentration:

For $t \geq 0$ and $0 \leq x \leq x_1$:

$$R_r = \frac{k_1 \exp\left(-E_A/R\, T_{UC}|_{x,r_1}\right) A_r k_{g_r} C^B_{O_2}}{k_{g_r} + k_1 \exp\left(-E_A/R\, T_{UC}|_{x,r_1}\right)} \tag{7.19}$$

For $t \geq 0$ and $0 \leq r \leq r_1$:

$$R_x = \frac{k_1 \exp\left(-E_A/R\, T_{UC}|_{x_1,r}\right) A_x k_{g_x} C^B_{O_2}}{k_{g_x} + k_1 \exp\left(-E_A/R\, T_{UC}|_{x_1,r}\right)} \tag{7.20}$$

The two-dimensional Fourier equation given in Eq. 7.3 coupled with the initial conditions in Eqs. 7.4, 7.5 and 7.6 and the boundary conditions in Eqs. 7.7, 7.8,

7.9 and 7.10 completes the description of the heat transfer through the quarter-plane illustrated in Figure 7.2, allowing calculations of the reaction rates given in Eqs. 7.19 and 7.20. These reaction rates can then be used to calculate the changing shape and size of the pellet during the reaction and predict a reaction completion time.

7.2.2 Calculating the changing pellet size

The reaction rates in Eqs. 7.19 and 7.20, when considered with the stoichiometry of Eq. 4.1, can then be used to calculate a rate of change of the positions of the radial and axial surfaces of the pellet.

For $t \geq 0$ and $0 \leq x \leq x_1$:

$$\frac{\mathrm{d}r_1(x)}{\mathrm{d}t} = -\frac{R_r}{2A_r\dot{\rho}_{UC}} = -\frac{k_1 \exp\left(-E_A/R\,T_{UC}|_{r_1}\right) k_{g_r} C^B_{O_2}}{2\dot{\rho}_{UC}\{k_{g_r} + k_1 \exp\left(-E_A/R\,T_{UC}|_{r_1}\right)\}} \tag{7.21}$$

For $t \geq 0$ and $0 \leq r \leq r_1$:

$$\frac{\mathrm{d}x_1(r)}{\mathrm{d}t} = -\frac{R_x}{2A_x\dot{\rho}_{UC}} = -\frac{k_1 \exp\left(-E_A/R\,T_{UC}|_{r_1}\right) k_{g_x} C^B_{O_2}}{2\dot{\rho}_{UC}\{k_{g_x} + k_1 \exp\left(-E_A/R\,T_{UC}|_{r_1}\right)\}} \tag{7.22}$$

7.3 Numerical solution

Finite difference methods are again used to approximate a numerical solution to the mathematical description of the oxidation. The addition of the axial dimension in the Fourier equation for heat transfer, Eq. 7.3, results in a partial differential equation with three independent variables: radial position, axial position and time. Therefore, the FIB method requires coupling with the alternating directions method discussed in Section 3.1.2.2 in order to accommodate the extra independent variable.

In this case, applying the method discussed in Section 3.1.2.2 involves advancing the solution across one time step, $n \rightarrow n+1$, whilst considering the temperature change in only one of the spatial dimensions, followed by the next time step, $n+1 \rightarrow n+2$, considering the temperature change across the alternate direction. The application of this method to Eq. 7.3 results in Eq. 7.24 solving across the first time step and Eq. 7.26 across the second.

For $n \geq 0$, $2 \leq i \leq k-1$ and $2 \leq j \leq p-1$:

$$\frac{T_{i,j}^{n+1} - T_{i,j}^{n}}{\Delta t} = \alpha_{UC}\left(\left.\frac{\partial^2 T_{UC}}{\partial x^2}\right|^{n+1} + \left.\frac{\partial^2 T_{UC}}{\partial r^2}\right|^{n} + \frac{1}{r}\left.\frac{\partial T_{UC}}{\partial r}\right|^{n} \right) \tag{7.23}$$

$$\frac{T_{i,j}^{n+1} - T_{i,j}^{n}}{\Delta t} = \alpha_{UC}\left(\frac{T_{i,j-1}^{n+1} - 2T_{i,j}^{n+1} + T_{i,j+1}^{n+1}}{\Delta x^2} + \frac{v_i T_{i-1,j}^{n} - 2T_{i,j}^{n} + w_i T_{i+1,j}^{n}}{\Delta r^2} \right) \tag{7.24}$$

where i is an integer representing the radial position with $i = 1$ when $r = 0$ and $i = k$ when $r = r_1$, j is an integer representing the radial position with $j = 1$ when $x = 0$ and $j = p$ when $x = x_1$, Δr and Δx are the increment sizes between these spatial positions, or nodes, in the r and x directions, respectively, $v_i = 1 - 1/i$ and $w_i = 1 + 1/i$. The real co-ordinate of each position in the carbide plane identifiable by values of i and j would be expressed as: $(r, x) = (i\Delta r, j\Delta x)$.

$$\frac{T_{i,j}^{n+2} - T_{i,j}^{n+1}}{\Delta t} = \alpha_{UC}\left(\left.\frac{\partial^2 T_{UC}}{\partial x^2}\right|^{n+1} + \left.\frac{\partial^2 T_{UC}}{\partial r^2}\right|^{n+2} + \frac{1}{r}\left.\frac{\partial T_{UC}}{\partial r}\right|^{n+2} \right) \tag{7.25}$$

$$\frac{T_{i,j}^{n+2} - T_{i,j}^{n+1}}{\Delta t} = \alpha_{UC}\left(\frac{T_{i,j-1}^{n+1} - 2T_{i,j}^{n+1} + T_{i,j+1}^{n+1}}{\Delta x^2} + \frac{v_j T_{i-1,j}^{n+2} - 2T_{i,j}^{n+2} + w_j T_{i+1,j}^{n+2}}{\Delta r^2} \right) \tag{7.26}$$

Eqs. 7.24 and 7.26 are then applied across the carbide solid by rearranging for the unknowns and producing two separate matrices, one solving in each direction. Considering the solution in the r direction first, Eq. 7.24 can be rearranged with the unknowns at $n+1$ on the left as:

For $n \geq 0$, $2 \leq i \leq k-1$ and $2 \leq j \leq p-1$:

$$-M_r v_i T_{i-1,j}^{n+1} + (1 + 2M_r)T_{i,j}^{n+1} - M_r w_i T_{i+1,j}^{n+1} = -M_x T_{i,j-1}^{n} + (1 + 2M_x)T_{i,j}^{n} - M_x T_{i,j+1}^{n} \tag{7.27}$$

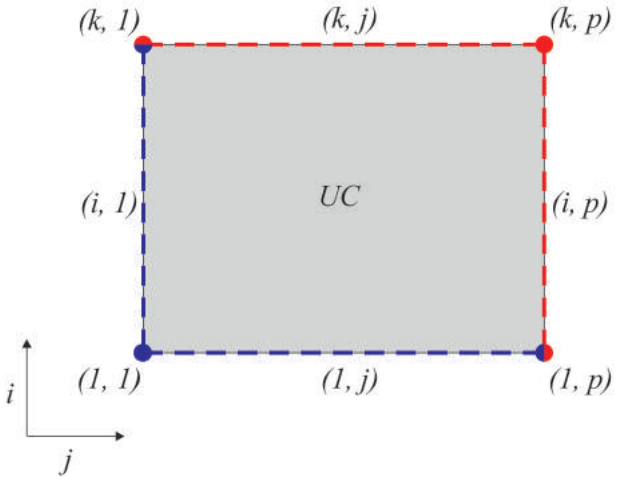

Figure 7.4: Labelled vertices and axes on the 2D carbide plane requiring unique boundary conditions. Adiabatic boundary conditions due to symmetry of the plane are coloured blue, and boundaries exposed to the bulk gas are coloured red.

where $M_x = \alpha_{UC}\Delta t/\Delta x^2$ and $M_r = \alpha_{UC}\Delta t/\Delta r^2$.

The left hand side of the matrix is therefore of a similar form to the one-dimensional case displayed in Eq. 4.39 on Page 97, but with a more complex right hand side dependent on the known values along the x direction. The two-dimensionality of the system also increases the complexity in that 8 different boundary conditions, rather than 2 in the one-dimensional case, require applying to Eq. 7.27 to complete the tri-diagonal matrix: 4 at each corner of the two-dimensional plane and 4 along each edge. The boundary conditions requiring consideration are illustrated in Figure 7.4 and consist of one (along a surface) or a combination (at corners) of two effects: adiabatic heat transfer across lines of symmetry within the solid, and the combined effect of heat generated by the reaction and exchanged with the bulk gas.

Central difference approximations of Eqs. 7.7, 7.8, 7.9 and 7.10 express the boundary conditions in terms of the imaginary point that requires eliminating at that boundary:

For $n \geq 0$, $i = 1$ and $1 \leq j \leq p$:

$$T^n_{0,j} = T^n_{2,j} \tag{7.28}$$

For $n \geq 0$, $1 \leq i \leq k$ and $j = 1$:

$$T^n_{i,0} = T^n_{i,2} \tag{7.29}$$

For $n \geq 0$, $i = k$ and $1 \leq j \leq p$:

$$T^n_{k+1,j} = T^n_{k-1,j} - 2\Delta r \frac{h^n}{\lambda_{UC}}(T^n_{k,j} - T^B) - \frac{\epsilon_{UC}\sigma}{\lambda_{UC}}((T^n_{k,j})^4 - (T^B)^4) - \frac{\Delta H_R}{\lambda_{UC}} \frac{k_1 \exp(-E_A/RT^n_{k,j}) k^n_{g_r} C^B_{O_2}}{k^n_{g_r} + k_1 \exp(-E_A/RT^n_{k,j})} \tag{7.30}$$

For $n \geq 0$, $1 \leq i \leq k$ and $j = p$:

$$T^n_{i,p+1} = T^n_{i,p-1} - 2\Delta r \frac{h^n}{\lambda_{UC}}(T^n_{i,p} - T^B) - \frac{\epsilon_{UC}\sigma}{\lambda_{UC}}((T^n_{i,p})^4 - (T^B)^4) - \frac{\Delta H_R}{\lambda_{UC}} \frac{k_1 \exp(-E_A/RT^n_{i,p}) k^n_{g_x} C^B_{O_2}}{k^n_{g_x} + k_1 \exp(-E_A/RT^n_{i,p})} \tag{7.31}$$

Substituting one of Eqs. 7.28, 7.29, 7.30 and 7.31 into Eq 7.27 at the appropriate boundary conditions removes the imaginary points encountered at this position. The resulting eight equations at each boundary suitable for inclusion into the r direction tri-diagonal matrix are included as follows:

For $n \geq 0$, $i = j = 1$:

$$(1 + 2M_r)T^{n+1}_{1,1} - 2M_r T^{n+1}_{2,1} = (1 + 2M_x)T^n_{1,1} - 2M_x T^n_{1,2} \tag{7.32}$$

For $n \geq 0$, $i = 1$ and $j = p$:

$$\begin{aligned}(1 + 2M_r)T^{n+1}_{1,p} - 2M_r T^{n+1}_{2,p} &= -2M_x T^n_{1,p-1} \\ &+ \left(1 + 2M_x + 2M_x u_x + \frac{2M_x u_x}{h^n_x}\epsilon\sigma(T^n_{1,p})^3\right) T^n_{1,p} \\ &- \frac{2M_x u_x}{h^n_x}\epsilon\sigma(T^B)^4 - 2M_x u_x T^B \\ &+ \frac{2M_x u_x \Delta H}{h^n_x} \frac{k_1 \exp(-E_A/RT^n_{1,p}) k^n_{g_x} C^B_{O_2}}{k^n_{g_x} + k_1 \exp(E_A/RT^n_{1,p})}\end{aligned} \tag{7.33}$$

where $u_x = \Delta x h_x/\lambda_{UC}$.

For $n \geq 0$, $i = k$ and $j = 1$:

$$
\begin{aligned}
&- 2M_r T_{k-1,1}^{n+1} + \left(1 + 2M_r + 2M_r u_r + \frac{2M_r u_r}{h_r^{n+1}} \epsilon\sigma (T_{k,1}^{n+1})^3\right) T_{k,1}^{n+1} \\
&- \frac{2M_r u_r}{h_r^{n+1}} \epsilon\sigma (T^B)^4 - 2M_r u_r T^B \\
&+ \frac{2M_r u_r \Delta H}{h_r^{n+1}} \frac{k_1 \exp(-E_A/RT_{k,1}^{n+1}) k_{g_r}^{n+1} C_{O_2}^B}{k_{g_r}^{n+1} + k_1 \exp(E_A/RT_{k,1}^{n+1})} = \\
&\qquad\qquad (1 + 2M_x) T_{k,1}^n - 2M_x T_{k,2}^n
\end{aligned} \tag{7.34}
$$

where $u_r = \Delta r w_k h_r / \lambda_{UC}$.

For $n \geq 0$, $i = k$ and $j = p$:

$$
\begin{aligned}
&- 2M_r T_{k-1,p}^{n+1} + \left(1 + 2M_r + 2M_r u_r + \frac{2M_r u_r}{h_r^{n+1}} \epsilon\sigma (T_{k,p}^{n+1})^3\right) T_{k,p}^{n+1} \\
&- \frac{2M_r u_r}{h_r^{n+1}} \epsilon\sigma (T^B)^4 - 2M_r u_r T^B \\
&+ \frac{2M_r u_r \Delta H}{h_r^{n+1}} \frac{k_1 \exp(-E_A/RT_{k,p}^{n+1}) k_{g_r}^{n+1} C_{O_2}^B}{k_{g_r}^{n+1} + k_1 \exp(E_A/RT_{k,p}^{n+1})} = \\
&- 2M_x T_{k,p-1}^n + \left(1 + 2M_x + 2M_x u_x + \frac{2M_x u_x}{h_x^n} \epsilon\sigma (T_{k,p}^n)^3\right) T_{k,p}^n \\
&- \frac{2M_x u_x}{h_x^n} \epsilon\sigma (T^B)^4 - 2M_x u_x T^B \\
&\qquad\qquad + \frac{2M_x u_x \Delta H}{h_x^n} \frac{k_1 \exp(-E_A/RT_{k,p}^n) k_{g_x}^n C_{O_2}^B}{k_{g_x}^n + k_1 \exp(E_A/RT_{k,p}^n)}
\end{aligned} \tag{7.35}
$$

For $n \geq 0$, $i = 1$ and $1 \leq j \leq p$:

$$
\begin{aligned}
&(1 + 2M_r) T_{1,j}^{n+1} - 2M_r T_{2,j}^{n+1} = \\
&\qquad\qquad - M_x T_{1,j-1}^n + (1 + 2M_x) T_{1,j}^n - M_x T_{1,j+1}^n
\end{aligned} \tag{7.36}
$$

For $n \geq 0$, $i = k$ and $1 \leq j \leq p$:

$$
\begin{aligned}
&- 2M_r T^{n+1}_{k-1,j} + \left(1 + 2M_r + 2M_r u_r + \frac{2M_r u_r}{h_r^{n+1}} \epsilon\sigma (T^{n+1}_{k,j})^3\right) T^{n+1}_{k,j} \\
&- \frac{2M_r u_r}{h_r^{n+1}} \epsilon\sigma (T^B)^4 - 2M_r u_r T^B \\
&+ \frac{2M_r u_r \Delta H}{h_r^{n+1}} \frac{k_1 \exp(-E_A/RT^{n+1}_{k,j}) k^{n+1}_{g_r} C^B_{O_2}}{k^{n+1}_{g_r} + k_1 \exp(E_A/RT^{n+1}_{k,j})} = \\
&\qquad - M_x T^n_{1,j-1} + (1 + 2M_x) T^n_{1,j} - M_x T^n_{1,j+1} \quad (7.37)
\end{aligned}
$$

For $n \geq 0$, $1 \leq i \leq k$ and $j = 1$:

$$
\begin{aligned}
&- M_r v_i T^{n+1}_{i-1,1} + (1 + 2M_r) T^{n+1}_{i,1} - M_r w_i T^{n+1}_{i+1,1} = \\
&\qquad (1 + 2M_x) T^n_{i,1} - 2M_x T^n_{i,2} \quad (7.38)
\end{aligned}
$$

For $n \geq 0$, $1 \leq i \leq k$ and $j = p$:

$$
\begin{aligned}
&- M_r v_i T^{n+1}_{i-1,p} + (1 + 2M_r) T^{n+1}_{i,p} - M_r w_i T^{n+1}_{i+1,p} = -2M_x T^n_{i,p-1} \\
&+ \left(1 + 2M_x + 2M_x u_x + \frac{2M_x u_x}{h_x^n} \epsilon\sigma (T^n_{i,p})^3\right) T^n_{i,p} - \frac{2M_x u_x}{h_x^n} \epsilon\sigma (T^B)^4 \\
&\qquad - 2M_x u_x T^B + \frac{2M_x u_x \Delta H}{h_x^n} \frac{k_1 \exp(-E_A/RT^n_{i,p}) k^n_{g_x} C^B_{O_2}}{k^n_{g_x} + k_1 \exp(E_A/RT^n_{i,p})} \quad (7.39)
\end{aligned}
$$

The tri-diagonal matrix composed from Eq. 7.27 and its bounds in Eqs. 7.32 to 7.39 can then be solved in the r direction for T^{n+1}. This is again achieved through use of the Thomas algorithm (Chang, 1981) applied in original code. It is then necessary to advance the solution to the time step, $n + 2$, by solving for the temperature distribution in the carbide in the x direction. Rearranging Eq. 7.24 with the unknown temperature values at $n+2$ on the left results in Eq. 7.40:

For $n \geq 0$, $2 \leq i \leq k - 1$ and $2 \leq j \leq p - 1$:

$$
\begin{aligned}
&- M_x T^{n+2}_{i,j-1} + (1 + 2M_x) T^{n+2}_{i,j} - M_x T^{n+2}_{i,j+1} = \\
&\qquad - M_r v_i T^{n+1}_{i-1,j} + (1 + 2M_r) T^{n+1}_{i,j} - M_r w_i T^{n+1}_{i+1,j} \quad (7.40)
\end{aligned}
$$

The solution in the x direction is subject to the same four boundary conditions illustrated in Figure 7.4 and detailed by the central difference approximations in

Eqs. 7.28, 7.29, 7.30 and 7.31. However, due to the difference in form between the FIB approximations of the Fourier equation in each direction, Eqs. 7.27 and 7.40, the equations constituting the tri-diagonal matrix for solution in the x direction are not of the same form. The eight boundary conditions, in tri-diagonal format, necessary for solution in the x direction are as follows:

For $n \geq 0$, $i = j = 1$:

$$(1 + 2M_x)T_{1,1}^{n+2} - 2M_x T_{1,2}^{n+2} = (1 + 2M_r)T_{1,1}^{n+1} - 2M_r T_{2,1}^{n+1} \tag{7.41}$$

For $n \geq 0$, $i = 1$ and $j = p$:

$$\begin{aligned} &- 2M_x T_{1,p-1}^{n+2} + \left(1 + 2M_x + 2M_x u_x + \frac{2M_x u_x}{h_x^{n+2}} \epsilon\sigma (T_{1,p}^{n+2})^3\right) T_{1,p}^{n+2} \\ &- \frac{2M_x u_x}{h_x^{n+2}} \epsilon\sigma (T^B)^4 - 2M_x u_x T^B \\ &+ \frac{2M_x u_x \Delta H}{h_x^{n+1}} \frac{k_1 \exp(-E_A/RT_{1,p}^{n+1}) k_{g_x}^{n+1} C_{O_2}^B}{k_{g_x}^{n+1} + k_1 \exp(E_A/RT_{1,p}^{n+1})} = \\ &\qquad (1 + 2M_r)T_{1,p}^{n+1} - 2M_r T_{2,p}^{n+1} \end{aligned} \tag{7.42}$$

For $n \geq 0$, $i = k$ and $j = 1$:

$$\begin{aligned} &(1 + 2M_x)T_{k,1}^{n+2} - 2M_x T_{k,2}^{n+2} = -2M_r T_{k-1,1}^{n+1} \\ &+ \left(1 + 2M_r + 2M_r u_r + \frac{2M_r u_r}{h_r^{n+1}} \epsilon\sigma (T_{k,1}^{n+1})^3\right) T_{k,1}^{n+1} - \frac{2M_r u_r}{h_r^{n+1}} \epsilon\sigma (T^B)^4 \\ &\qquad - 2M_r u_r T^B + \frac{2M_r u_r \Delta H}{h_r^{n+1}} \frac{k_1 \exp(-E_A/RT_{k,1}^{n+1}) k_{g_r}^{n+1} C_{O_2}^B}{k_{g_r}^{n+1} + k_1 \exp(E_A/RT_{k,1}^{n+1})} \end{aligned} \tag{7.43}$$

For $n \geq 0$, $i = k$ and $j = p$:

$$
\begin{aligned}
&- 2M_x T^{n+2}_{k,p-1} + \left(1 + 2M_x + 2M_x u_x + \frac{2M_x u_x}{h_x^{n+2}} \epsilon\sigma (T^{n+2}_{k,p})^3\right) T^{n+2}_{k,p} \\
&- \frac{2M_x u_x}{h_x^{n+2}} \epsilon\sigma (T^B)^4 - 2M_x u_x T^B \\
&+ \frac{2M_x u_x \Delta H}{h_x^{n+2}} \frac{k_1 \exp(-E_A/RT^{n+2}_{k,p}) k^{n+2}_{g_x} C^B_{O_2}}{k^{n+2}_{g_x} + k_1 \exp(E_A/RT^{n+2}_{k,p})} = \\
&- 2M_r T^{n+1}_{k-1,p} + \left(1 + 2M_r + 2M_r u_x + \frac{2M_r u_r}{h_r^{n+1}} \epsilon\sigma (T^{n+1}_{k,p})^3\right) T^{n+1}_{k,p} \\
&- \frac{2M_r u_r}{h_r^{n+1}} \epsilon\sigma (T^B)^4 - 2M_r u_r T^B \\
&\qquad + \frac{2M_r u_r \Delta H}{h_r^{n+1}} \frac{k_1 \exp(-E_A/RT^{n+1}_{k,p}) k^{n+1}_{g_r} C^B_{O_2}}{k^{n+1}_{g_r} + k_1 \exp(E_A/RT^{n+1}_{k,p})}
\end{aligned} \tag{7.44}
$$

For $n \geq 0$, $i = 1$ and $1 \leq j \leq p$:

$$
\begin{aligned}
&- M_x T^{n+2}_{1,j-1} + (1 + 2M_x) T^{n+2}_{1,j} - M_x T^{n+2}_{1,j+1} = \\
&\qquad (1 + 2M_r) T^{n+1}_{1,j} - 2M_r T^{n+1}_{2,j}
\end{aligned} \tag{7.45}
$$

For $n \geq 0$, $i = k$ and $1 \leq j \leq p$:

$$
\begin{aligned}
&- M_x T^{n+2}_{1,j-1} + (1 + 2M_x) T^{n+2}_{1,j} - M_x T^{n+2}_{1,j+1} = -2M_r T^{n+1}_{k-1,j} \\
&+ \left(1 + 2M_r + 2M_r u_x + \frac{2M_r u_r}{h_r^{n+1}} \epsilon\sigma (T^{n+1}_{k,j})^3\right) T^{n+1}_{k,j} - \frac{2M_r u_r}{h_r^{n+1}} \epsilon\sigma (T^B)^4 \\
&\qquad - 2M_r u_r T^B + \frac{2M_r u_r \Delta H}{h_r^{n+1}} \frac{k_1 \exp(-E_A/RT^{n+1}_{k,j}) k^{n+1}_{g_r} C^B_{O_2}}{k^{n+1}_{g_r} + k_1 \exp(E_A/RT^{n+1}_{k,j})}
\end{aligned} \tag{7.46}
$$

For $n \geq 0$, $1 \leq i \leq k$ and $j = 1$:

$$
\begin{aligned}
&(1 + 2M_x) T^{n+2}_{i,1} - 2M_x T^{n+2}_{i,2} = \\
&\qquad - M_r v_i T^{n+1}_{i-1,1} + (1 + 2M_r) T^{n+1}_{i,1} - M_r w_i T^{n+1}_{i+1,1}
\end{aligned} \tag{7.47}
$$

For $n \geq 0$, $1 \leq i \leq k$ and $j = p$:

$$
\begin{aligned}
&- 2M_x T_{i,p-1}^{n+2} + \left(1 + 2M_x + 2M_x u_x + \frac{2M_x u_x}{h_x^{n+2}} \epsilon\sigma (T_{i,p}^{n+2})^3\right) T_{i,p}^{n+2} \\
&- \frac{2M_x u_x}{h_x^{n+2}} \epsilon\sigma (T^B)^4 - 2M_x u_x T^B \\
&+ \frac{2M_x u_x \Delta H}{h_x^{n+2}} \frac{k_1 \exp(-E_A/RT_{i,p}^{n+2}) k_{g_x}^{n+2} C_{O_2}^B}{k_{g_x}^{n+2} + k_1 \exp(E_A/RT_{i,p}^{n+2})} = \\
&\qquad\qquad - M_r v_i T_{i-1,p}^{n+1} + (1 + 2M_r) T_{i,p}^{n+1} - M_r w_i T_{i+1,p}^{n+1} \quad (7.48)
\end{aligned}
$$

A second tri-diagonal matrix composed of Eq. 7.40 and the bounds in Eqs. 7.41 to 7.48 can then be solved to calculate T^{n+2} in the x direction. This is solved immediately after the first matrix solving in the r direction using the same method. The temperature distribution throughout the solid at $n+2$ is then used to calculate the reaction rates along each surface given in Eqs. 7.1 and 7.2 allowing the resulting change in size and shape of the two-dimensional carbide plane to be determined. The change in the radial and axial dimensions of the pellet is given by backward difference approximations of Eqs. 7.21 and 7.22:

For $t \geq 0$ and $1 \leq j \leq p$:

$$
r_{1_j}^{n+2} = r_{1_j}^{n} - \frac{2\Delta t k_1 \exp\left(-E_A/RT_{k,j}^{n+2}\right) k_{g_r}^{n+2} C_{O_2}^B}{2\dot{\rho}_{UC}\left\{k_{g_r}^{n+2} + k_1 \exp\left(-E_A/RT_{k,j}^{n+2}\right)\right\}} \quad (7.49)
$$

where r_{1_j} is the external pellet radius, r_1, at an axial position of j.

For $t \geq 0$ and $0 \leq i \leq k$:

$$
x_{1_i}^{n+2} = x_{1_i}^{n} - \frac{2\Delta t k_1 \exp\left(-E_A/RT_{i,p}^{n+2}\right) k_{g_x}^{n+2} C_{O_2}^B}{2\dot{\rho}_{UC}\{k_{g_x}^{n+2} + k_1 \exp\left(-E_A/RT_{i,p}^{n+2}\right)\}} \quad (7.50)
$$

where x_{1_i} is the pellet length, x_1, at an radial position of i.

The time loop is then continued until the percentage of carbide oxidised is greater than 99%.

7.3.1 Ensuring numerical stability and convergence

Numerical stability of the solution is again ensured through the use of the Courant-Friedrichs-Lewy rule (Smith, 1965). The criteria is adapted for the two-dimensional

Table 7.1: The effect of varying the number of increments on the oxidation completion time as a test for convergence.

Number of radial increments	Number of length increments	Oxidation completion time (min)	Computational time (min)
5	5	175.8	0.03
10	10	175.0	0.15
20	20	174.2	1.04
40	40	173.6	7.67
80	80	173.2	57.6
160	160	172.9	440

case by using the smaller of the two spatial increment sizes, Δr and Δx, in the calculation for the time step size.

$$\Delta t = \frac{1}{2\alpha_{UC}} \left\{ min \left(\Delta r_x, \Delta r_r \right) \right\}^2 \tag{7.51}$$

Due to the changes in the pellet size being calculated only at every 2^{nd} time step, the time step size is also only recalculated at every other time step. Nonetheless, it decreases significantly during the course of the oxidation, slowing the simulation toward completion of the oxidation.

Mathematical convergence was checked by running the model with the same input parameters but a different number of nodes and therefore different increment sizes. The results of this check for convergence are included in Table 7.1. The minor changes observed in the oxidation completion time with the number of increments suggests the model is convergent, but this can be confirmed by again using Richardson's deferred approach to the limit (Smith, 1965). Taking three results from Table 7.1 and applying Eqs. 6.51 and 6.52 from Page 153, gives an estimation of the solution using an infinitely small increment size - the converged, or analytical, solution. In this case, the converged solution is $u = 171.8\,\text{min}$, confirming that the results in Table 7.1 are converging.

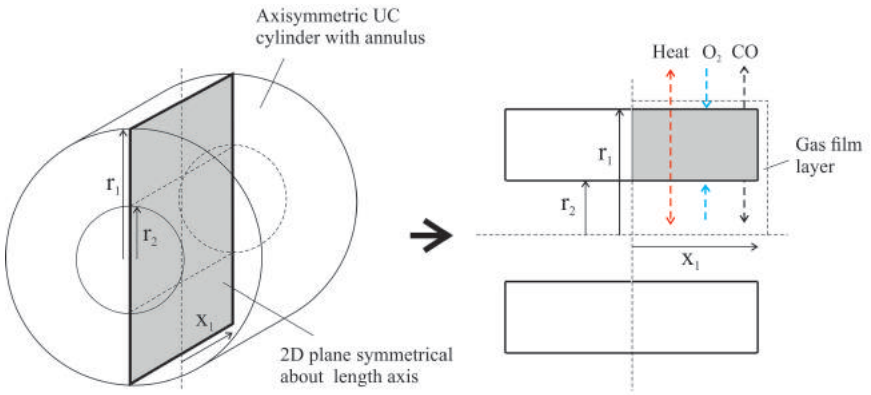

Figure 7.5: A two-dimensional approximation of an annular, cylindrical pellet as used in the NNL oxidation experiments. A rotationally symmetrical plane is taken from the cylinder and further lines of symmetry are used to reduce the domain of the model.

7.4 Fitting to experimental data

The provision of experimental oxidation data to this project by the National Nuclear Laboratory allowed the fitting of predictions made by the two dimensional model in order to derive values for certain parameters, such as the activation energy and oxidation rate constant. The data was provided in the form of a BNFL technical report (Coppersthwaite & Semeraz, 2003) explaining the methodology used in its acquisition, as well as raw data provided separately. It is applicable to the two-dimensional model only as the experiments used annular, cylindrical pellets, meaning that consideration of the additional reaction front along the inner radius is necessary: impossible using a one-dimensional, spherical approximation.

It was again assumed that the pellets used in the NNL experiments were axisymmetric, allowing a two-dimensional, rotationally symmetrical slice to be taken from the pellet and treated as the model's domains. This is illustrated in Figure 7.5, where the inclusion of heat and mass transfer effects on the inner radius of the annular pellet can also be observed.

7.4.1 Experimental method

Before the fitting of the two-dimensional oxidation model to the NNL data is discussed, it is necessary to include a brief description of the experimental methodology used in acquiring this data.

UC fuel pellets obtained from rejected fuel pins stored at Springfields were oxidised in air within a horizontal split tube furnace (Carbolite model HST 12/200) under different temperatures. The pellets had a diameter of 1.9 cm, a length of 2 cm, an annuli diameter of 0.45 cm and a density of $13.13 \pm 0.07\,\mathrm{g\,cm^{-3}}$. The pellets were then placed in alumina crucibles with an internal diameter of 3.75 cm and a height of 6 cm, which was in turn located in the hot zone of an alumina work tube, 6 cm in internal diameter and 20 cm in working length, mounted in the furnace. The work tube was sealed at either end using stainless steel flanges that allowed a flow of air through the tube at $10\,\mathrm{dm^3\,min^{-1}}$. A rough illustration of this set up is included in Figure 7.6. The changes in concentration of O_2, CO and CO_2 in the gas flow over the course of the oxidation were monitored by a Siemens Ultramat 23 infrared analyser. Temperature within the furnace was controlled by a programmable Eurotherm 2416CG.

There were then several experiments carried out at furnace temperatures of 530 °C and 950 °C for a period of 24 h. For all experiments, an initial heating period from approximately 18.5 °C to the desired furnace temperature lasting around 2 h was present. The composition of the off-gas was monitored to establish when the oxidation began and if it had completed within the 24 h duration. Temperatures within the furnace were measured using a type K thermocouple.

The solid oxidation product was then analysed for its total carbon content to be used as an indicator of oxidation completion, and to identify the oxide phases present.

7.4.2 Additional mathematical considerations

In order to fit the two-dimensional oxidation model to the NNL data, additional mathematics must be taken into consideration to account for the annular nature of the pellet. Specifically, the geometry of the two-dimensional plane must be modified from that in Figure 7.1 to that in Figure 7.5, and also the boundary

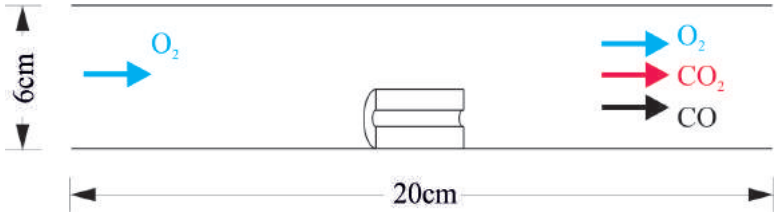

Figure 7.6: A diagram illustrating the position of the UC pellet within the work tube within the horizontal furnace.

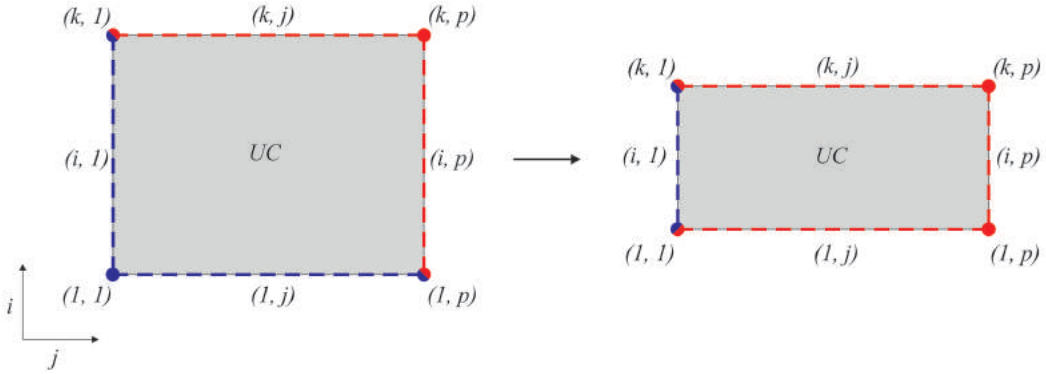

Figure 7.7: The modification to the domain of interest of the two-dimensional model necessary to model an annular pellet. The blue boundaries represent adiabatic boundary conditions along lines of symmetry in the pellet, and red boundaries represent those exposed to the bulk gas.

conditions require modifying to reflect the reaction front and heat and mass transfer along the inner radius of the pellet, where $r = r_2$.

As far as the two-dimensional model is concerned, the change in the domain of interest in the model is illustrated by Figure 7.7. This change is represented mathematically by the modification of Eq. 7.7, originally the adiabatic boundary condition at $r = 0$, to include the effects of the oxidation reaction and heat and mass transfer with the bulk gas at the position now labelled $r = r_2$:

For $t \leq 0$, $r = r_2$ and $0 \leq x \leq x_1$:

$$\lambda_{UC} \left.\frac{\partial T_{UC}}{\partial r}\right|_{x,r_2} = h_{r_{in}} \left(T_{UC}|_{x,r_2} - T^B \right) + \epsilon_{UC}\sigma \left(T_{UC}|^4_{x,r_2} - \left(T^B\right)^4 \right) + \frac{\Delta H_R R_{r_{in}}}{A_{r_{in}}} \quad (7.52)$$

where $h_{r_{in}}$ is the heat transfer coefficient at the internal radius, $R_{r_{in}}$ is the rate of O_2 consumption at the inner radius and $A_{r_{in}}$ is the carbide surface area exposed at the inner surface.

The internal heat transfer coefficient, $h_{r_{in}}$, is calculated using Eq. 7.53.

For $t \geq 0$ and $0 \leq x \leq x_1$:

$$h_{r_{in}} = \frac{\mathrm{Nu}_{in}\lambda_{fluid}}{r_1 - r_2} \tag{7.53}$$

where Nu_{in} is the Nusselt number at the internal surface, calculated from a correlation given by Sieder and Tate (Sieder & Tate, 1936) for laminar flow in circular tubes:

$$\mathrm{Nu}_{in} = 1.86 \left(\frac{2r_2\mathrm{RePr}}{2x_1}\right)^{1/3} \left(\frac{\mu^B}{\mu_{r_2}}\right)^{0.14} \tag{7.54}$$

where μ^B is the bulk fluid viscosity and μ_{r_2} is the fluid viscosity at the inner surface, affected by the temperature there.

The reaction rate at the inner radius, $R_{r_{in}}$, takes the form used by R_C with the only divergence being that the internal area, $A_{r_{in}} = 4\pi r_2 x_1$, is used.

As displayed in Figure 7.7, the introduction of Eq. 7.52 affects three of the eight boundary conditions necessary for numerical solution of the two-dimensional model, namely at the positions designated $(1,1)$, $(1,j)$ and $(1,p)$ where $i = 1$ (i.e. $r = r_2$). Taking Eqs. 7.34, 7.35, 7.37, 7.38 and 7.39 to still apply, the following three equations complete the tri-diagonal matrix necessary to solve the heat transfer across an annular, two-dimensional pellet in the r direction:

For $n \geq 0$, $i = j = 1$:

$$\begin{aligned}\left(1 + 2M_r + 2M_r u_r + \frac{2M_r u_r}{h_{r_{in}}^{n+1}}\epsilon\sigma(T_{1,1}^{n+1})^3\right) T_{1,1}^{n+1} - \frac{2M_r u_r}{h_{r_{in}}^{n+1}}\epsilon\sigma(T^B)^4 \\ - 2M_r u_r T^B + \frac{2M_r u_r \Delta H}{h_{r_{in}}^{n+1}} \frac{k_1 \exp(-E_A/RT_{1,1}^{n+1}) k_{g_{rin}}^{n+1} C_{O_2}^B}{k_{g_{rin}}^{n+1} + k_1 \exp(E_A/RT_{1,1}^{n+1})} \\ - 2M_r T_{2,1}^{n+1} = (1 + 2M_x)T_{1,1}^n - 2M_x T_{1,2}^n\end{aligned} \tag{7.55}$$

For $n \geq 0$, $i = 1$ and $1 \leq j \leq p$:

$$\left(1 + 2M_r + 2M_r u_r + \frac{2M_r u_r}{h_{r_{in}}^{n+1}} \epsilon\sigma (T_{1,j}^{n+1})^3\right) T_{1,j}^{n+1} - \frac{2M_r u_r}{h_{r_{in}}^{n+1}} \epsilon\sigma (T^B)^4$$
$$- 2M_r u_r T^B + \frac{2M_r u_r \Delta H}{h_{r_{in}}^{n+1}} \frac{k_1 \exp(-E_A/RT_{1,j}^{n+1}) k_{g_{rin}}^{n+1} C_{O_2}^B}{k_{g_{rin}}^{n+1} + k_1 \exp(E_A/RT_{1,j}^{n+1})}$$
$$- 2M_r T_{2,j}^{n+1} = -M_x T_{1,j-1}^n + (1 + 2M_x) T_{1,j}^n - M_x T_{1,j+1}^n \quad (7.56)$$

For $n \geq 0$, $i = 1$ and $j = p$:

$$\left(1 + 2M_r + 2M_r u_r + \frac{2M_r u_r}{h_{r_{in}}^{n+1}} \epsilon\sigma (T_{1,p}^{n+1})^3\right) T_{1,p}^{n+1} - \frac{2M_r u_r}{h_{r_{in}}^{n+1}} \epsilon\sigma (T^B)^4$$
$$- 2M_r u_r T^B + \frac{2M_r u_r \Delta H}{h_{r_{in}}^{n+1}} \frac{k_1 \exp(-E_A/RT_{1,p}^{n+1}) k_{g_{rin}}^{n+1} C_{O_2}^B}{k_{g_{rin}}^{n+1} + k_1 \exp(E_A/RT_{1,p}^{n+1})}$$
$$- 2M_r T_{2,p}^{n+1} = -2M_x T_{1,p-1}^n$$
$$+ \left(1 + 2M_x + 2M_x u_x + \frac{2M_x u_x}{h_x^n} \epsilon\sigma (T_{1,p}^n)^3\right) T_{1,p}^n - \frac{2M_x u_x}{h_x^n} \epsilon\sigma (T^B)^4$$
$$- 2M_x u_x T^B + \frac{2M_x u_x \Delta H}{h_x^n} \frac{k_1 \exp(-E_A/RT_{1,p}^n) k_{g_x}^n C_{O_2}^B}{k_{g_x}^n + k_1 \exp(E_A/RT_{1,p}^n)} \quad (7.57)$$

where $k_{g_{rin}}$ is the mass transfer coefficient at the internal radius given by:

For $t \geq 0$ and $0 \leq x \leq x_1$:

$$k_{g_{rin}} = \frac{D_{O_2-CO} \mathrm{Sh}}{r_1 - r_2} \quad (7.58)$$

Similarly, taking Eqs. 7.43, 7.44, 7.46, 7.47 and 7.48 to still apply, the following equations allow completion of the matrix solving in the x direction:

For $n \geq 0$, $i = j = 1$:

$$(1 + 2M_x) T_{1,1}^{n+2} - 2M_x T_{1,2}^{n+2} =$$
$$\left(1 + 2M_r + 2M_r u_r + \frac{2M_r u_r}{h_{r_{in}}^{n+1}} \epsilon\sigma (T_{1,1}^{n+1})^3\right) T_{1,1}^{n+1}$$
$$- \frac{2M_r u_r}{h_{r_{in}}^{n+1}} \epsilon\sigma (T^B)^4 - 2M_r u_r T^B$$
$$+ \frac{2M_r u_r \Delta H}{h_{r_{in}}^{n+1}} \frac{k_1 \exp(-E_A/RT_{1,1}^{n+1}) k_{g_{rin}}^{n+1} C_{O_2}^B}{k_{g_{rin}}^{n+1} + k_1 \exp(E_A/RT_{1,1}^{n+1})} - 2M_r T_{2,1}^{n+1} \quad (7.59)$$

For $n \geq 0$, $i = 1$ and $1 \leq j \leq p$:

$$
\begin{aligned}
&- M_x T_{1,j-1}^{n+2} + (1 + 2M_x) T_{1,j}^{n+2} - M_x T_{1,j+1}^{n+2} = \\
&\left(1 + 2M_r + 2M_r u_r + \frac{2M_r u_r}{h_{r_{in}}^{n+1}} \epsilon\sigma (T_{1,j}^{n+1})^3\right) T_{1,j}^{n+1} \\
&- \frac{2M_r u_r}{h_{r_{in}}^{n+1}} \epsilon\sigma (T^B)^4 - 2M_r u_r T^B \\
&\qquad + \frac{2M_r u_r \Delta H}{h_{r_{in}}^{n+1}} \frac{k_1 \exp(-E_A/RT_{1,j}^{n+1}) k_{g_{rin}}^{n+1} C_{O_2}^B}{k_{g_{rin}}^{n+1} + k_1 \exp(E_A/RT_{1,j}^{n+1})} - 2M_r T_{2,j}^{n+1}
\end{aligned} \tag{7.60}
$$

For $n \geq 0$, $i = 1$ and $j = p$:

$$
\begin{aligned}
&- 2M_x T_{1,p-1}^{n+2} + \left(1 + 2M_x + 2M_x u_x + \frac{2M_x u_x}{h_x^{n+2}} \epsilon\sigma (T_{1,p}^{n+2})^3\right) T_{1,p}^{n+2} \\
&- \frac{2M_x u_x}{h_x^{n+2}} \epsilon\sigma (T^B)^4 - 2M_x u_x T^B \\
&+ \frac{2M_x u_x \Delta H}{h_x^{n+1}} \frac{k_1 \exp(-E_A/RT_{1,p}^{n+1}) k_{g_x}^{n+1} C_{O_2}^B}{k_{g_x}^{n+1} + k_1 \exp(E_A/RT_{1,p}^{n+1})} = \\
&\left(1 + 2M_r + 2M_r u_r + \frac{2M_r u_r}{h_{r_{in}}^{n+1}} \epsilon\sigma (T_{1,k}^{n+1})^3\right) T_{1,k}^{n+1} \\
&- \frac{2M_r u_r}{h_{r_{in}}^{n+1}} \epsilon\sigma (T^B)^4 - 2M_r u_r T^B \\
&\qquad + \frac{2M_r u_r \Delta H}{h_{r_{in}}^{n+1}} \frac{k_1 \exp(-E_A/RT_{1,k}^{n+1}) k_{g_{rin}}^{n+1} C_{O_2}^B}{k_{g_{rin}}^{n+1} + k_1 \exp(E_A/RT_{1,k}^{n+1})} - 2M_r T_{2,k}^{n+1}
\end{aligned} \tag{7.61}
$$

With the inclusion of the six equations listed above into the two tri-diagonal matrices, the extra reaction front presented by the internal pellet surface is now included in the mathematical representation of heat transfer and the ensuing numerical solution.

Apart from the effect the extra reaction front has on the heat transfer, the effect it has on the geometry change over time must also be considered. A reaction occurring at the inner surface, $r = r_2$, as well as the outer surface, $r = r_1$, means that the pellet is shrinking in both radial directions as well as the length direction. The changes in pellet size are now represented by the ODEs in Eqs. 7.62, 7.63 and 7.64 listed below:

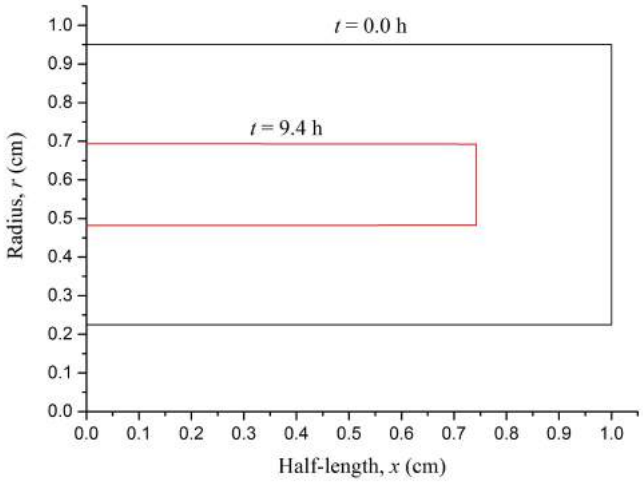

Figure 7.8: An example of how the two-dimensional plane taken from the annular pellet changes over time. The outline of the plane at $t = 0\,\mathrm{h}$ is in black, whilst the outline at $t = 9.4\,\mathrm{h}$ is coloured red.

For $t \geq 0$ and $0 \leq x \leq x_1$:

$$\frac{\mathrm{d}r_1(x)}{\mathrm{d}t} = -\frac{R_r}{2A_r\dot{\rho}_{UC}} = -\frac{k_1 \exp\left(-E_A/R\,T_{UC}|_{r_1}\right) k_{g_r} C_{O_2}^B}{2\dot{\rho}_{UC}\{k_{g_r} + k_1 \exp\left(-E_A/R\,T_{UC}|_{r_1}\right)\}} \tag{7.62}$$

For $t \geq 0$ and $0 \leq x \leq x_1$:

$$\frac{\mathrm{d}r_2(x)}{\mathrm{d}t} = \frac{R_{r_{in}}}{2A_{r_{in}}\dot{\rho}_{UC}} = \frac{k_1 \exp\left(-E_A/R\,T_{UC}|_{r_2}\right) k_{g_{rin}} C_{O_2}^B}{2\dot{\rho}_{UC}\{k_{g_{rin}} + k_1 \exp\left(-E_A/R\,T_{UC}|_{r_2}\right)\}} \tag{7.63}$$

For $t \geq 0$ and $r_2 \leq r \leq r_1$:

$$\frac{\mathrm{d}x_1(r)}{\mathrm{d}t} = -\frac{R_x}{2A_x\dot{\rho}_{UC}} = -\frac{k_1 \exp\left(-E_A/R\,T_{UC}|_{r_1}\right) k_{g_x} C_{O_2}^B}{2\dot{\rho}_{UC}\{k_{g_x} + k_1 \exp\left(-E_A/R\,T_{UC}|_{r_1}\right)\}} \tag{7.64}$$

An example of how the two-dimensional plane representing the axisymmetric, annular pellet changes with time is included in Figure 7.8. Similarly to the changing shape of the solid pellet, the annular pellet retains its shape during the reaction due to the conductivity of UC ensuring a uniform temperature distribution.

7.4.2.1 Gas flow and composition

Since the data provided by the NNL presents the results in the form of changes to the off-gas composition over time, it is important that the model calculates the gas flow through the sealed alumina work tube and the changes in its composition caused by the oxidation properly. The reaction mechanism presented in Eqs. 4.1 and 4.2 remains, where the surface reaction produces CO that is then oxidised to CO_2 in the gas phase, allowing the gas composition changes to be tracked. What remains to be added, then, is the flow through the tube and how it removes produced CO and CO_2 and replenishes O_2.

At the inlet, air flows in at a rate of $10\,\mathrm{dm^3\,min^{-1}}$. At the outlet, the off-gas, having passed over the oxidising UC and acquired CO and CO_2, flows out at the same rate. It is assumed that the flow is laminar. The work tube is then separated into regions, each assumed to be well mixed; the volume before the pellet, V_b, around the pellet, V_p, and after the pellet, V_a, as illustrated in Figure 7.9. The area of particular interest is the region after the pellet, V_a, as it is the gas composition in that region that will be taken represent the off-gas for fitting purposes. The concentration of the three gases of interest, O_2, CO and CO_2, in the after pellet region can be calculated from the flow rates, volumes and concentrations in the earlier regions. The initial conditions for the gas composition calculations are given as:

For $t \leq 0$:

$$C^b_{O_2} = C^p_{O_2} = C^a_{O_2} = \frac{0.21}{\bar{R}_g T^B} \tag{7.65}$$

where $C^b_{O_2}$, $C^p_{O_2}$ and $C^a_{O_2}$ are the O_2 concentrations in the regions before, around and after the pellet, respectively, and $\bar{R}_g$ is the ideal gas constant in $\mathrm{m^3\,atm\,mol^{-1}\,K^{-1}}$. It is assumed that the temperature is homogeneous throughout the work tube. For $t \leq 0$:

$$C^b_{CO} = C^p_{CO} = C^a_{CO} = 0 \tag{7.66}$$

$$C^b_{CO_2} = C^p_{CO_2} = C^a_{CO_2} = 0 \tag{7.67}$$

where C^b_{CO}, C^p_{CO} and C^a_{CO} are the CO concentrations across the regions of the cylinder and $C^b_{CO_2}$, $C^p_{CO_2}$ and $C^a_{CO_2}$ are the CO_2 concentrations.

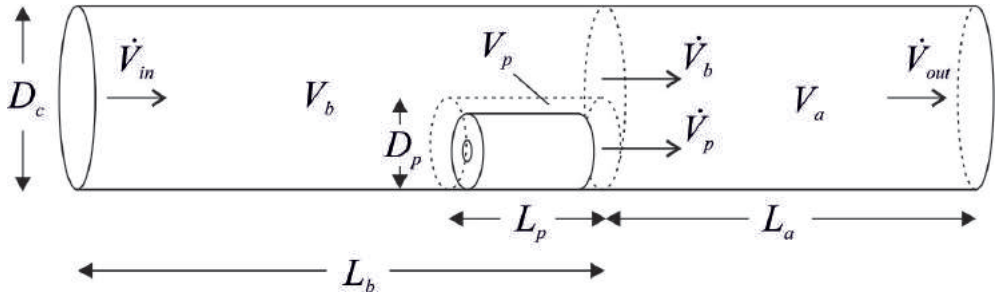

Figure 7.9: Diagram of the volumetric regions within the work tube used in gas composition calculations.

The volumetric flow rates and volumes remain constant for the duration of the reaction, and are expressed as:

For $t \geq 0$:

$$V_p = \pi D_p L_p \tag{7.68}$$

$$V_b = \pi D_c L_b - V_p \tag{7.69}$$

$$V_a = \pi D_c L_a \tag{7.70}$$

where V_p, V_b and V_a are the volumes of the regions, D_c and D_p are the diameters of the work tube and pellet region, respectively, and V_p, V_b and V_a are the region volumes.

For $t \geq 0$:

$$\dot{V}_{in} = \dot{V}_{out} = v_x \pi (D_c/2)^2 = 10\,\mathrm{dm^3\,min^{-1}} \tag{7.71}$$

$$\dot{V}_p = v_x \pi (D_p/2)^2 \tag{7.72}$$

$$\dot{V}_b = v_x \left(\pi (D_c/2)^2 - \pi (D_p/2)^2\right) \tag{7.73}$$

where $\dot{V}_{in}$ and $\dot{V}_{out}$ are the volumetric flow rates at the inlet and outlet, respectively, v_x is the constant flow velocity along the x (axial) direction and $\dot{V}_p$ and $\dot{V}_b$ are the volumetric flows rates exiting the pellet and before the pellet regions, respectively.

With the initial conditions, volumes and volumetric flow rates characterised, the concentrations in the off-gas (i.e. the region after the pellet) can be calculated:

For $t \geq 0$:

$$\frac{\mathrm{d}C^a_{O_2}}{\mathrm{d}t} = \frac{C^p_{O_2}\dot{V}_p}{V_p} + \frac{C^b_{O_2}\dot{V}_b}{V_b} - \frac{C^a_{O_2}\dot{V}_{out}}{V_a} - \frac{R_{CO}}{2V_a} \tag{7.74}$$

$$\frac{\mathrm{d}C^a_{CO}}{\mathrm{d}t} = \frac{C^p_{CO}\dot{V}_p}{V_p} + \frac{C^b_{CO}\dot{V}_b}{V_b} - \frac{C^a_{CO}\dot{V}_{out}}{V_a} - \frac{R_{CO}}{V_a} \tag{7.75}$$

$$\frac{\mathrm{d}C^a_{CO_2}}{\mathrm{d}t} = \frac{C^p_{CO_2}\dot{V}_p}{V_p} + \frac{C^b_{CO_2}\dot{V}_b}{V_b} - \frac{C^a_{CO_2}\dot{V}_{out}}{V_a} + \frac{R_{CO}}{V_a} \tag{7.76}$$

Whilst the majority of the CO oxidising to CO_2 occurs within the pellet region, the R_{CO} term designating the rate of CO oxidation is included for residual CO present in the after pellet region. The calculation of the gas concentrations within the pellet region are completed in the fashion used in Section 4.2.2 on Page 89, with the gas volume set as V_p. It is worth noting that Eqs. 7.74, 7.75 and 7.76 are all non-linear due to the changing concentration in the after-pellet region being dependent on itself. Therefore, calculation of the off-gas composition can be quite restrictive on computational time due to the necessary additional time step size constraints.

In order to simulate the heating of the furnace in the experimental data, the gas temperature in the work tube is represented by the following function (for the run at 950 °C):

For $t \leq 0$:

$$T^B = 291.5 \tag{7.77}$$

For $0 < t \leq 1.68\,\mathrm{h}$:

$$T^B = 1283 + \frac{25.92 - 1010}{1 + (t/1777)^{2.23}} \tag{7.78}$$

For $1.68\,\mathrm{h} < t \leq 24\,\mathrm{h}$:

$$T^B = 1223 \tag{7.79}$$

For $t > 24\,\mathrm{h}$:

$$T^B = 285.5 + 2.812 \times 10^{12} \exp\left(\frac{t}{3960}\right) \tag{7.80}$$

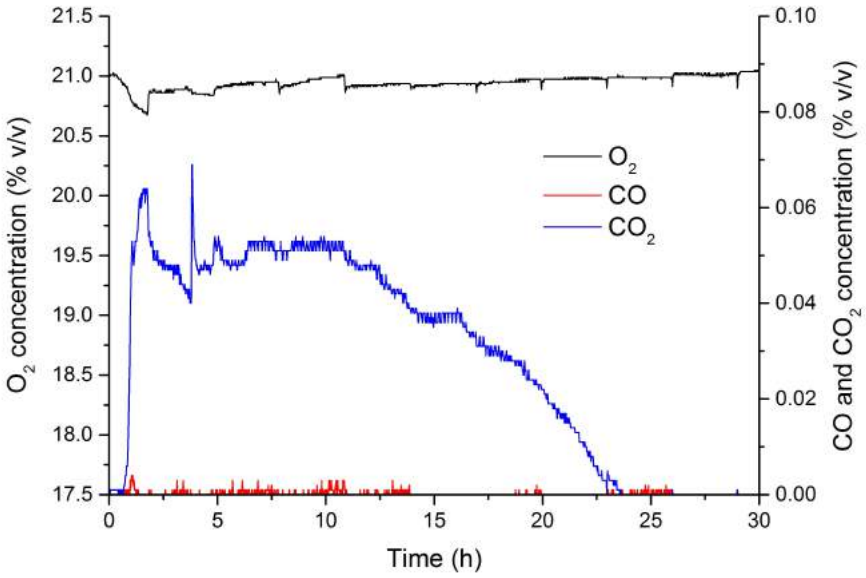

Figure 7.10: The off gas composition from a UC oxidation at 950 °C

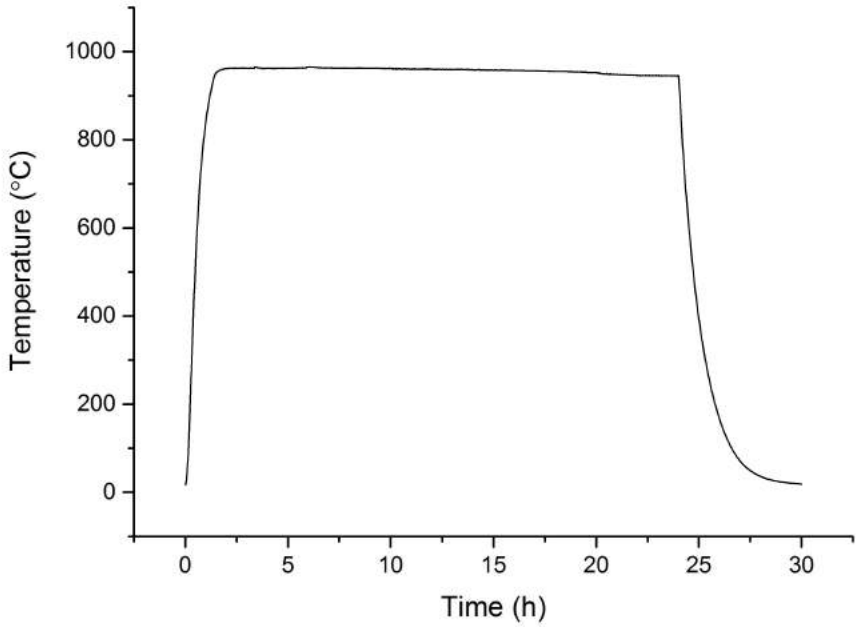

Figure 7.11: The furnace temperature during the oxidation.

7.4.3 Method of fitting

The experimental data to which the model's results will be fitted comes largely in the form of off-gas composition measurements. For example, Figure 7.10 is a plot of the off-gas for an oxidation of an annular UC pellet in air when subject to a furnace temperature in Figure 7.11. It is stated in the BNFL technical report accompanying the data that the regular, sharp decreases in O_2 concentration are measurement errors resulting from the equipment used (Coppersthwaite & Semeraz, 2003).

The changes in the off-gas composition can be used to determine both the duration of the oxidation by when the concentration of CO_2 returns to that in air, and the temperature at which the oxidation begins by when CO_2 is initially produced. By modifying the parameters associated with these two observations, specifically the rate constant, k_1, and the activation energy, E_A, the two-dimensional oxidation model can be fit to the data.

7.5 Results

The results for the two-dimensional model are displayed in two subsections: the first being for the solid pellet described initially, and the second for the annular pellet designed to be fit to experimental data.

7.5.1 Solid pellet model

Figure 7.12 displays the model's capability of calculating the temperature distribution across the two-dimensional plane taken from the axisymmetric cylinder over the course of the reaction. The shrinking in size of the plane during the reaction can also be observed. For this result, a pellet of radius 0.935 cm and length 1.87 cm assumed to have an initial temperature of 25 °C is exposed to a bulk gas with a temperature of 500 °C and an O_2 concentration of $3.15\,\mathrm{mol\,m^{-3}}$. Similarly to the minimal temperature gradient along the UC radius observed in the one-dimensional models, the two-dimensional plane is also largely isothermal throughout the majority of the reaction. Therefore, taking the maximum temperature present in the plane to be representative of the plane temperature

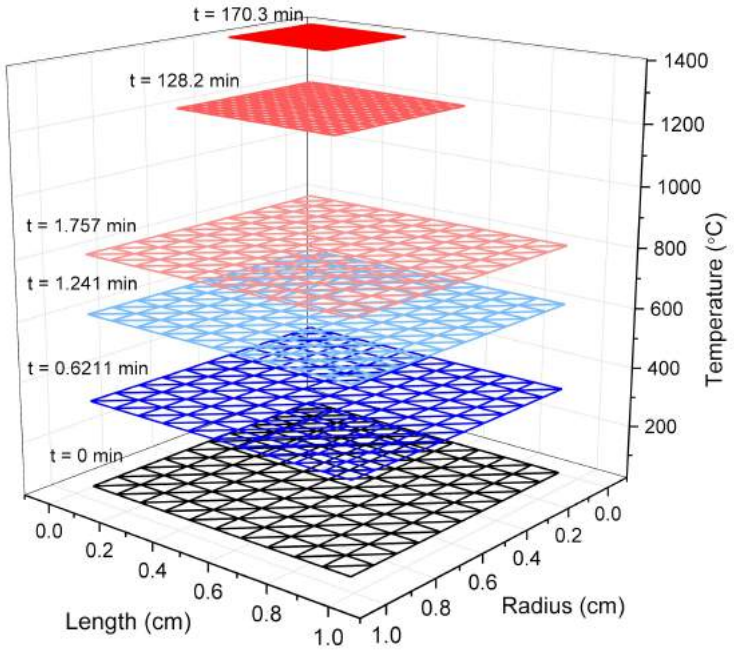

Figure 7.12: The temperature distribution through the 2D slice representing an axisymmetric, cylindrical UC pellet over time.

generally, Figure 7.13 gives a description of its value over time. Similarly to the one-dimensional model, an initial, sharp temperature rise is observed due to exposure to the hotter bulk gas and the oxidation beginning. A plateau is then reached as radial and convective heat losses to the bulk gas balance the heat production, followed by a degree of thermal runaway as the reaction completes. The thermal runaway is thought to occur as the decreasing pellet size provides a smaller heat sink for the reaction, causing the heat generated at the surface to overcome the heat lost to the gas.

During the initial stages of the reaction, immediately after the pellet has been exposed to the bulk gas, there does, however, exist a temperature gradient within the pellet for a short period of time. Figure 7.14a is the temperature profile through the plane quarter that forms the domain of the model at $t = 0.621\,\text{min}$ when the same conditions mentioned previously are used, and Figure 7.14b multiplies this results along the lines of symmetry to represent the full plane. Both figures illustrate the higher temperatures at the pellet corners as a result of the

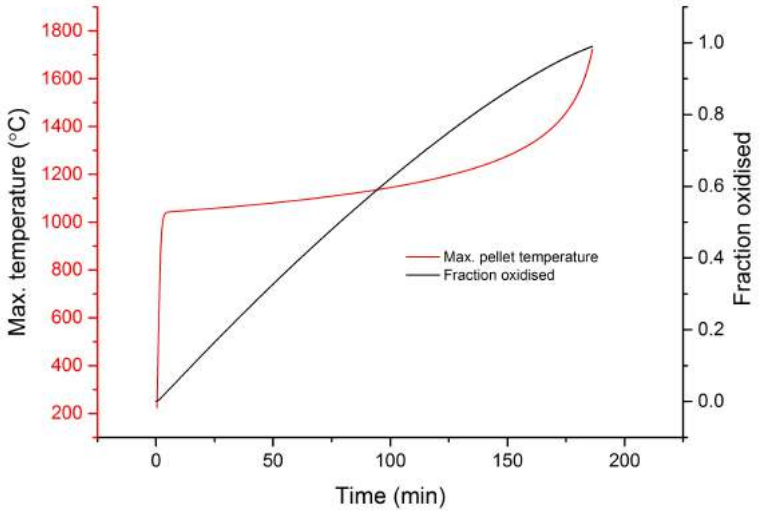

Figure 7.13: The maximum temperature within the UC pellet (red) and the fraction oxidised (black) over time.

increased rate of heat transfer. This faster heat transfer is due to the boundary conditions at the corner being subject to heat transfer in both the radial and axial directions, essentially doubling the heat flux at the corners.

Sensitivity studies were carried out using the two-dimensional model to demonstrate its dependence on the temperature and O_2 concentration of the bulk gas, the results of which are included in Figure 7.15. Again, a pellet with a of radius 0.935 cm and length of 1.87 cm was used and assumed to have an initial temperature of 25 °C. For the temperature variation results, shown in red, the initial O_2 concentration was fixed at 3.15 mol m^{-3}, and for the concentration variation, shown in black, an initial bulk gas temperature of 500 °C was used. Increasing both the temperature and O_2 concentration appears to have the effect of exponentially decreasing the reaction completion, mirroring the results predicted by the one-dimensional model. Tables 7.2 and 7.3 quantify the dependency of the reaction completion time on temperature and O_2 concentration whilst comparing the results to the one-dimensional model.

Generally, the two-dimensional model predicts a shorter oxidation completion time than the one-dimensional variant due to the higher temperatures predicted by the two-dimensional model. Figure 7.16 is a plot of the average temperatures

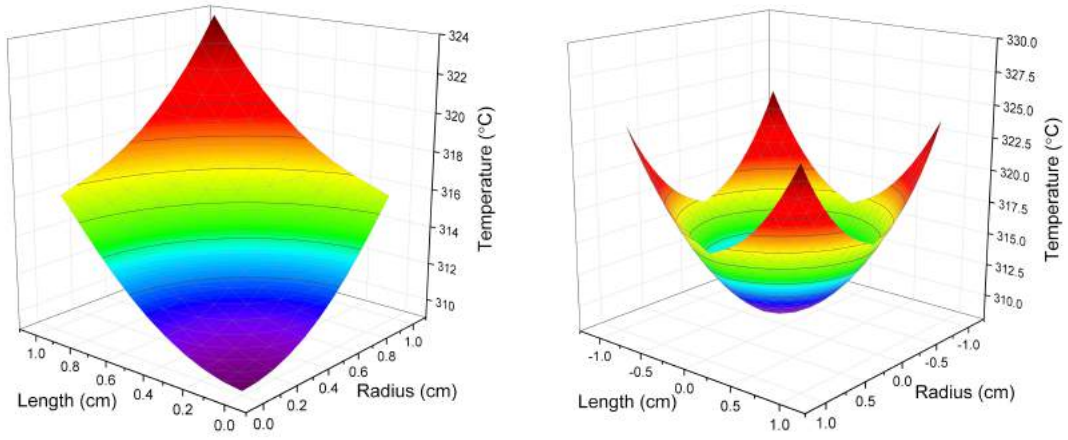

(a) Across a quarter of the plane.

(b) Multiplied along lines of symmetry to represent whole plane.

Figure 7.14: Temperature profiles across the two-dimensional plane at $t = 0.621$ min.

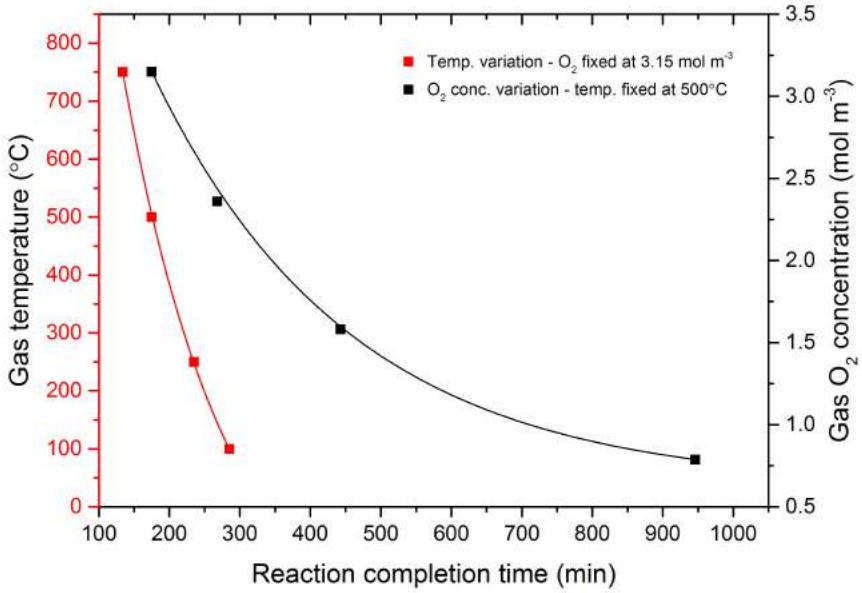

Figure 7.15: The dependence of the reaction completion time on the temperature and O_2 concentration of the bulk gas.

Table 7.2: The effects of the bulk gas temperature on the peak temperature reached within the UC plane and the reaction completion time.

Initial bulk gas temperature (°C)	Peak UC temperature (°C)		Reaction completion time (min)	
	1D	2D	1D	2D
100	1351	1636	373	277
250	1521	1700	296	229
500	1623	1824	223	172
750	1751	1956	170	133

Table 7.3: The effects of the bulk gas O_2 concentration on the peak temperature reached within the UC plane and the reaction completion time. The bracketed values give the percentage of O_2 in air represented by a particular concentration.

Bulk gas O_2 concentration ($\mathrm{mol\,m^{-3}}$)	Peak UC temperature (°C)		Reaction completion time (min)	
	1D	2D	1D	2D
0.788 (5%)	1663	1017	954	982
1.58 (10%)	1223	1337	608	435
2.36 (15%)	1427	1580	353	264
3.31 (21%)	1623	1824	223	172

within the one-dimensional sphere and two-dimensional cylinder over the course of the oxidation, demonstrating that the average temperature within the the cylinder is consistently hotter throughout. This effect is due to the cylindrical geometry of the two-dimensional pellet exposing it to multiple heat fluxes at the pellet surface, specifically at the corners where a heat flux is experienced in both the r and x directions.

Figure 7.17 is an examination of the finite difference mesh at the corner of the plane. For the point (k, j), there are two imaginary points, $(k+1, p)$ and $(k, p+1)$, that require removal to allow a numerical solution of the heat transfer. This requires the application of boundary conditions in both spatial directions,

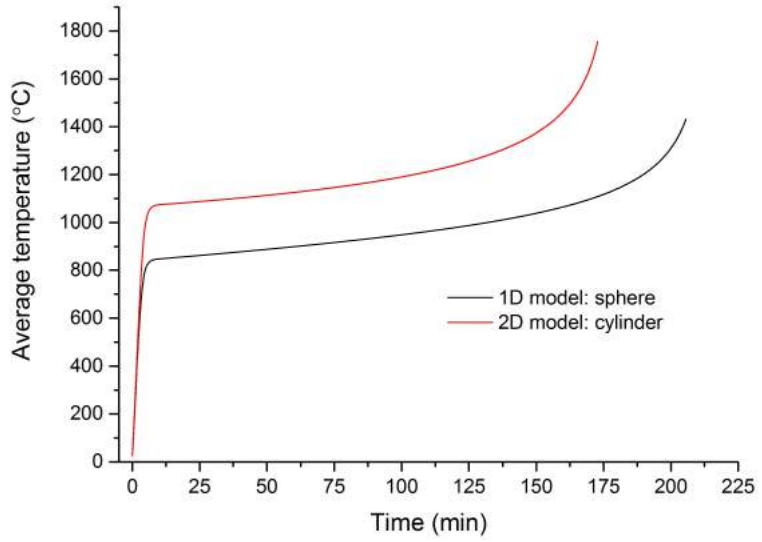

Figure 7.16: The average temperatures within the 1D sphere and the 2D cylinder versus time.

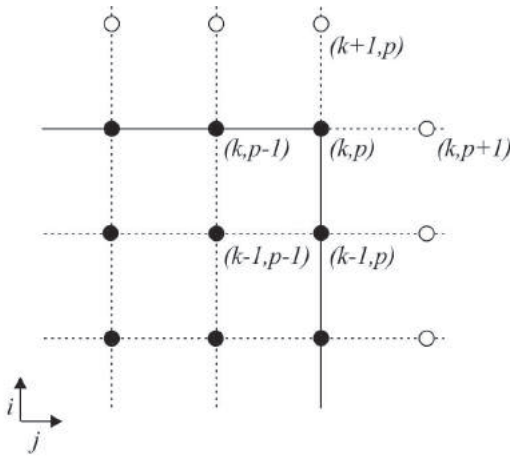

Figure 7.17: The finite difference mesh at the corner of the 2D plane region. Real points within the solid are designated by ●, and imaginary points requiring removal through the use of boundary conditions are designated by ○.

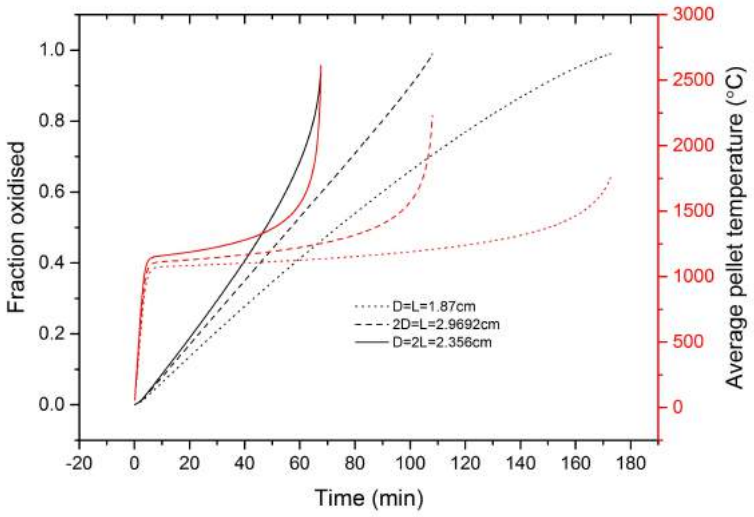

Figure 7.18: The effect of varying the diameter, D, to length, L, ratio of the oxidation rate and average pellet temperature.

and therefore subjects this point to twice the heat transfer and twice the heat of reaction. This extra heat is then conducted through the plane and raises the average temperature of the cylinder above that of the one-dimensional equivalent volume sphere.

Some further sensitivity studies were carried out using the two-dimensional model to investigate the effects of the cylinder's shape. Different ratios of the pellet's length and diameter were input into the model and the oxidation curves and average temperatures over time are plotted in Figure 7.18. Whilst the diameter to length ratio was varied, it was ensured that the pellet mass was constant. For the results shown in Figure 7.18, a bulk gas temperature of 500 °C and an O_2 concentration of $3.15\,\mathrm{mol\,m^{-3}}$ was used. Both the longer, thinner cylinder and the shorter, wider cylinder oxidise faster than the right cylinder with $D = L$. This is explained by the surface area varying with the changing geometries whilst the volume remains constant. At $D = L$, the surface area is $16.48\,\mathrm{cm^2}$, at $2D = L$ is is $17.22\,\mathrm{cm^2}$ and at $D = 2L$ it is $17.44\,\mathrm{cm^2}$.

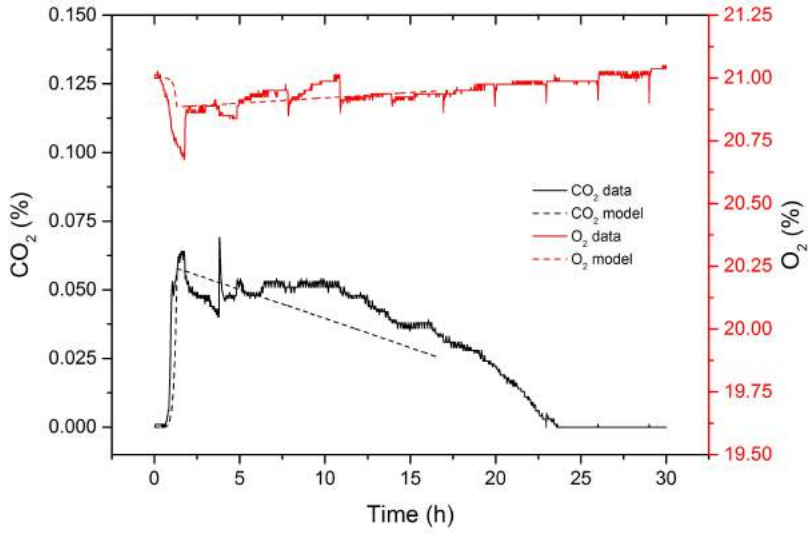

Figure 7.19: Comparison of the gas traces predicted by the annular pellet model to experimental data presented by the NNL (Coppersthwaite & Semeraz, 2003).

7.5.2 Annular pellet model

The annular pellet model was produced to allow fitting of its off-gas predictions to experimental data, such as that displayed in Figure 7.10. Fitting was achieved through modification of the Scott's (Scott, 1966) rate constant, k_1, and the activation energy, E_A, to replicate the duration of the oxidation and the temperature at which it begins, respectively. The results of the fitting are presented in Figure 7.19, where values of $k_1 = 23\,\mathrm{m\,s^{-1}}$ and $E_A = 93\,\mathrm{kJ\,mol^{-1}}$ were found to give the best results. In line with the experimental set-up (Coppersthwaite & Semeraz, 2003), the O_2 concentration at the work tube inlet was maintained at 21 % at a pressure of 1 atm, the inlet temperature was dictated by Eqs. 7.77 - 7.80 and a pellet of radius $9.50 \times 10^{-3}\,\mathrm{m}$, annular radius $2.25 \times 10^{-3}\,\mathrm{m}$ and length $1.00 \times 10^{-2}\,\mathrm{m}$ was oxidised. The initial pellet temperature was 18.5 °C.

The fit displayed in Figure 7.19 indicates a good approximation of the activation energy as the CO_2 release associated with the start of the reaction occurs at the same time, and hence at the same point on the temperature ramp. This allows the model to simulate accurately the temperature dependence of this oxidation. The rate of decline of the CO_2 concentration is also met reasonably, albeit in a

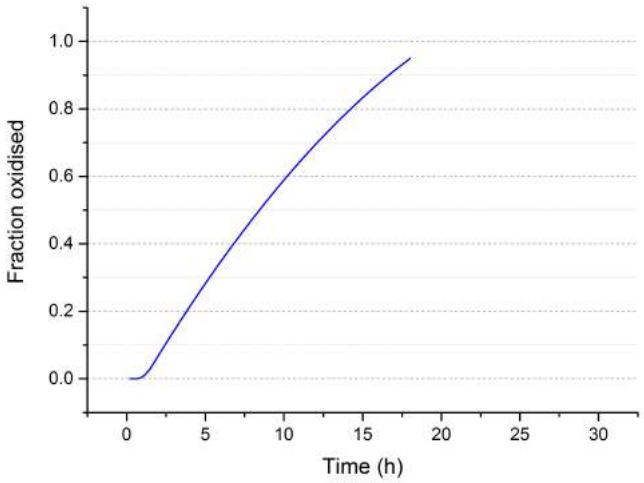

Figure 7.20: The fraction of the UC pellet oxidised in producing the gas traces displayed in Figure 7.19.

much more linear due to the nature of the model. In the model, this decline is a result of the oxidation rate slowing as the surface area of the pellet decreases whilst the flow rate of air through the tube remains constant and hence has a purging effect on the CO_2 concentration. Therefore, having the model match the rate of decline suggests the reaction rate constant, and hence the rate of CO_2 production, is roughly correct. The sharper drop off after around 18 h is presumed to be a result of the oxidation being largely completed and no more CO_2 being introduced to the system. As such, this is not included in the model which finishes upon completion of the oxidation.

Figure 7.20 is a plot of the fraction of UC oxidised during the simulation presented in Figure 7.19. The model completes upon reaching an oxidation fraction of 0.95, contrary to the value of 0.99 employed in previous models, due to the annular nature of the pellet meaning its magnitude is significantly greater in the length dimension than the radial. Therefore, as the oxidation progresses, the radial width of the pellet becomes very thin before the length direction is fully depleted. This causes the radial increment size to tend to zero, $\Delta r_{UC} \to 0$, hence $\Delta t \to 0$, meaning the simulation doesn't progress whilst there is still a reasonable amount of UC essentially spread along a thin, axial line. This effect is partially illustrated in Figure 7.8 on Page 201 where at an intermediate stage

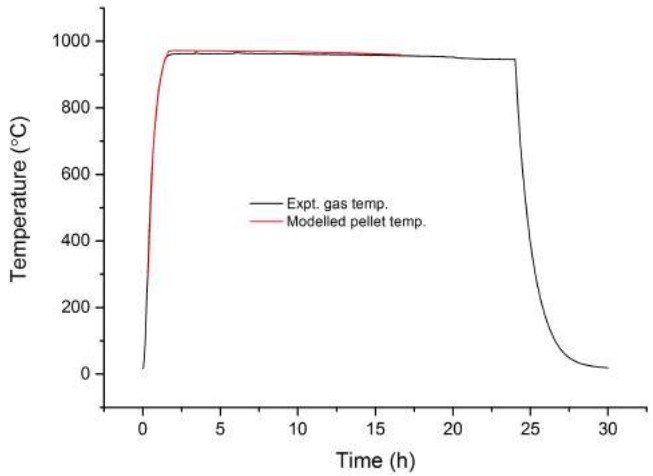

Figure 7.21: The experimental furnace temperature and the modelled pellet temperature throughout the oxidation.

of the reaction the radial width is closer to depletion than the pellets length.

Figure 7.21 displays the experimental furnace temperature, included in the model as the bulk gas temperature, T^B, and the modelled surface temperature at the pellet corner. The pellet only reaches temperatures around 10 °C higher than its surroundings as a result of the slower reaction rate used in the annular model than Scott's (Scott, 1966) kinetics used in the solid pellet model. The pellet temperature plot, similarly to the gas composition plot, finishes early as the time step size tends to zero near oxidation completion.

The effect of an additional exposed surface on the temperature distribution within the two-dimensional plane representing the axisymmetric cylinder is included in Figure 7.22. The temperature at the outer radial surface, where $r = r_1$, can be seen to be hotter, marginally due to the high conductivity of UC, than the inner radial surface, where $r = r_2$. This is thought to be an effect of the greater surface area along the outer radius ($\pi r_1 x_1 > \pi r_2 x_1$) resulting in a faster reaction rate, and therefore a large heat output. Figure 7.22b is a plot of the temperature distribution through the modelled quartile multiplied along the lines of radial and axial symmetry, illustrating the temperature distribution throughout the two-dimensional plane and the position of the annulus within it.

With the reaction kinetics of the two-dimensional, annular pellet model fit

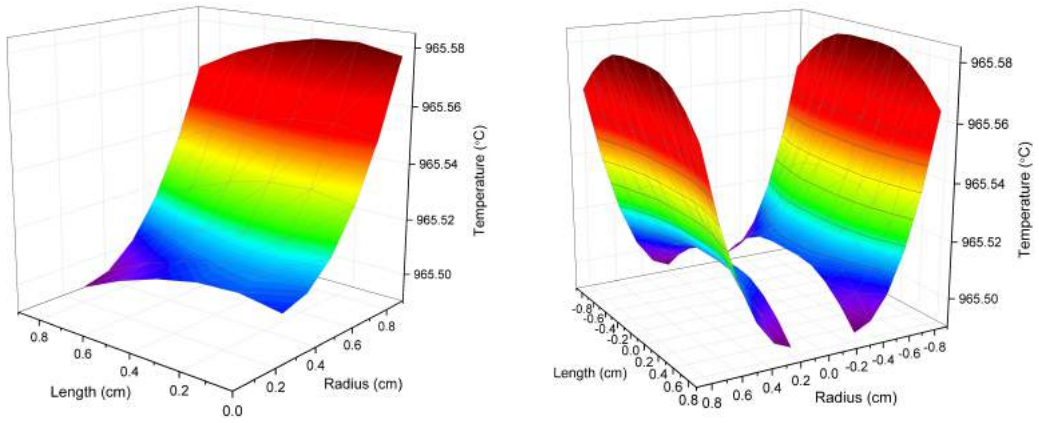

(a) Across a quarter of the plane.

(b) Multiplied along radial and axial lines of symmetry.

Figure 7.22: Temperature profiles across the cross-sectional plane through an axisymmetric, annular pellet as outlined in Figure 7.7, at $t = 2\,\mathrm{h}$.

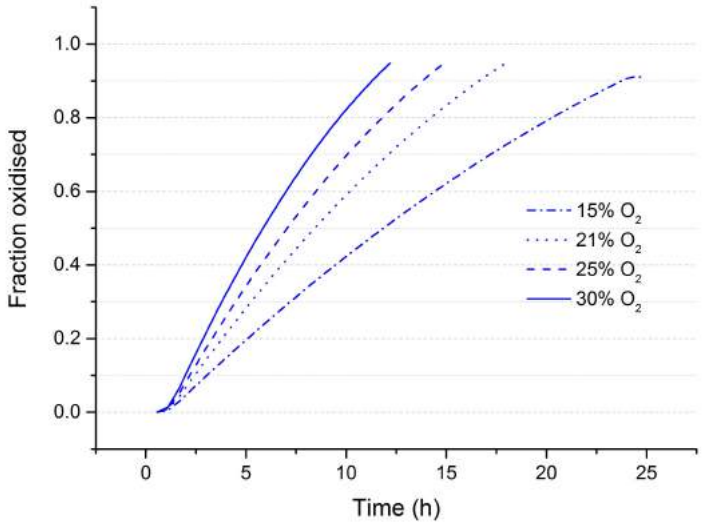

Figure 7.23: Oxidation curves of the annular UC pellet at different O_2 concentrations.

against experimental data, a sensitivity study on the effect of the O_2 concentration was carried out with the results presented in Figure 7.23. The same gas temperature and pellet dimensions were used as in the previous results. To complete these simulations, calculation of the gas traces was omitted due to them being computationally limiting and as after the kinetics constants have been fit they are not as important. Increasing the O_2 concentration was again shown to significantly decrease the oxidation completion time from 24.8 h at 15 % O_2 to 12.2 h at 30 % O_2.

7.6 Conclusions

The purpose of the model described in this chapter was to build on the results presented in Chapter 4 by adding an additional spatial dimension. Developing the oxidation model to two dimensions allowed the UC pellet to be considered as a cylinder, rather than a sphere, assuming it is axisymmetrical. Given that the majority of nuclear fuel pellets are cylindrical, this allowed a more realistic form of the UC pellet to be oxidised.

The production of a two-dimensional model required a significantly more complex mathematical description of the system. Heat transfer, mass transfer and reaction effects had to be considered in both spatial dimensions, resulting in the number of boundary conditions necessary for solution increasing from two to eight. A more complex numerical solution was also necessary due to their being an equation matrix solving heat transfer in both the x and y directions. A numerical method known as the alternating directions method (Smith, 1965) was therefore employed to allow an approximated solution using the FIB finite difference method to the heat transfer.

The resulting model is capable of predicting the temperature distribution across a two-dimensional plane taken to represent the cylinder, and reaction rates and completion times can be calculated under different temperatures and O_2 concentrations. The results were found to differ quite significantly from those predicted by the one-dimensional, spherical model, due to multiple heat fluxes experienced at the pellet corners by the two-dimensional model. This led to the

predicted temperatures being hotter in the two-dimensional model, which in turn led to faster predicted reaction completion times.

The difference in the predictions made by the two-dimensional model emphasises the necessity of increasing the model's complexity. A Biot number significantly smaller than 0.1, as demonstrated in Eq. 5.1 on Page 109 for the spherical case, for both the spherical and cylindrical systems implies that the pellet geometry shouldn't be significant and a reduced model could be used in either case. The temperature profiles in Figure 7.16, however, indicate that a lump model would not predict the higher temperature obtained by the two-dimensional model due to the multiple heat fluxes experienced around the pellet surface. Therefore, it is imperative that a two-dimensional model is employed to demonstrate that the reduced model is applicable only to the one-dimensional case, and that the equivalent volume sphere assumption itself is inaccurate.

The two-dimensional model was then modified to consider the oxidation of an axisymmetric UC cylinder with an annulus, allowing calculation of reaction variables, namely the rate constant, k_1, and the activation energy, E_A, through fitting to BNFL experimental data by Copperswhaite and Semeraz (Coppersthwaite & Semeraz, 2003). The fit was obtained though the modelling of the gas released by the oxidation and plotting it against experimental observation. Values of $k_1 = 23.0\,\mathrm{m\,s^{-1}}$ and $E_A = 93.0\,\mathrm{kJ\,mol^{-1}}$ were found to give the best fit. These values are quite different to those given by Scott (Scott, 1966) of $k_1 = 200\ \mathrm{m\,s^{-1}}$ and $E_A = 177.8\,\mathrm{kJ\,mol^{-1}}$, as a result of the longer reaction completion times observed by Copperswhaite and Semeraz (Coppersthwaite & Semeraz, 2003) in the BNFL report. The difference, however, may not be as significant as the values may suggest, as a lower activation energy to some extent mitigates the effect the slower reaction rate constant has on the oxidation rate. The new value for the activation energy shows closer agreement with other published values, displayed in Table 2.9 on Page 23, than Scott's much higher value, lending some support to the new kinetics values with a lower activation energy and rate constant.

Since, like its one-dimensional counterpart in Chapter 4, this model does not have an adherent product layer, it is applicable only to the higher O_2 partial pressures. It is also subject to some of the same limitations, such as simplified reaction kinetics, being dependent on the UC cylinder retaining axisymmetry

and the pellet being suspended in the bulk gas. However, it still contributes a excellent simulation tool for predicting temperatures reached by a UC pellet oxidation and therefore recommending safe operating conditions. The fitting of important parameters to experimental data helps to support these predictions, and also contributes to understanding the kinetics of UC oxidation.

Chapter 8

Advanced modelling techniques

8.1 Introduction

The work described in this chapter involves the use of DigiDiss^{TM} software and the modifications made to it necessary for simulating the oxidation of UC. Once these modifications were made and the initial results checked against the earlier models, this method allowed the oxidation to be considered in three dimensions, and also allowed the inclusion of fluid flow simulated using the LBM and batch processes using the DigiPac^{TM} packing algorithm.

8.2 Description of modifications

This section will include a description of the methods used to modify the DigiDiss^{TM} source code, written in C++, so that it was able to simulate the oxidation of UC. The necessary changes to be made to the code can be listed as follows:

1. Replacement of the Noyes-Whitney dissolution equation with a first order reaction equation, of the form of Eq. 4.5 on Page 85, to represent the reaction kinetics.

2. Coupling of the heat transfer code in DigiThem^{TM} to the kinetics module, DigiDiss^{TM}.

3. Introduction of thermal radiation, heat of reaction and heat transfer through the fluid to the heat transfer code

The core aspects of DigiPac^{TM}, such as the digitisation of solid structures into a finite number of voxels, remain, meaning that the modifications had to be made in the same fashion. For example, the three-dimensional nature of the code meant that modelling the heat transfer required further elaboration on the finite difference methods described in earlier chapters.

8.2.1 Reaction kinetics

The first, and simplest, modification to be discussed is the replacement of the DigiDiss^{TM} reaction kinetics. As described in Section 3.2.3 by Eq. 3.24, the rate of weight loss of the UC solid using DigiDiss^{TM} would be expressed by the Noyes-Whitney equation, repeated as:

$$\frac{\mathrm{d}W}{\mathrm{d}t} = -kS\left(C_{sat} - C_B\right)$$

This equation, being based on the difference between the solid concentration and its saturation concentration in the solvent, is unsuitable to describe an oxidation in a gaseous fluid as there is no saturation concentration. Therefore, the oxidation rate equation provided by Scott (Scott, 1966) in Eq. 4.5 used in previous models is applied. In order to ease its introduction into the source code, it requires expressing as a rate of the UC weight loss in $\mathrm{kg\,s^{-1}}$ rather than a rate of O_2 consumption in $\mathrm{mol\,s^{-1}}$:

$$\frac{\mathrm{d}W}{\mathrm{d}t} = -2k_C A C_{O_2} \tag{8.1}$$

where C_{O_2} is the O_2 concentration at the position at which the reaction is occurring.

Maintaining the assumption that the oxidation reaction occurs at the UC surface, Eq. 8.1 is applied at each node amongst the voxels where there is an interface between a solid UC voxel and a fluid voxel representing air. The total weight lost by a particular solid voxel over a give time step is therefore the sum of the reactions occurring at each of its faces that are exposed to the fluid. Given

the naming convention illustrated in Figure 3.10 on Page 77, this summation can be expressed as:

$$\frac{W_0^{n+1} - W_0^n}{\Delta t} = -2\Big(k_{C_1}^n \Delta x^2 C_1^n + k_{C_2}^n \Delta x^2 C_2^n + k_{C_3}^n \Delta x^2 C_3^n + k_{C_4}^n \Delta x^2 C_4^n + k_{C_5}^n \Delta x^2 C_5^n + k_{C_6}^n \Delta x^2 C_6^n\Big) \quad (8.2)$$

where W_0 is the UC weight at (i, j, k), the model's point of interest, n represents the time step, $k_{C_1} - k_{C_6}$ are the temperature dependent oxidation rate coefficients at positions 1 to 6 and $C_1 - C_6$ are the O_2 concentrations at positions 1 to 6.

Eq. 8.2 is representative of a solid voxel experiencing an oxidation at each of its six faces. The equation is of a different form depending on how many faces are exposed to the fluid and which faces these are. The calculation in Eq. 8.2 is completed at every solid voxel in the domain at each time step, reducing the weights of different voxels independently often at different rates. A threshold is input by the user to define a minimum weight, generally $< 1\%$ of the original value, below which the solid voxel is considered depleted and redefined as a fluid voxel. Due to the fixed spatial increment size in DigiDiss^{TM} and hence fixed voxel volume, the decreasing weight of a voxel manifests as a density decrease in the voxel.

8.2.2 Heat transfer

In order to calculate the various temperature dependent coefficients required to simulate the oxidation reaction, the temperature distribution through the simulation domain must be known. Eq. 3.34 in Section 3.2.4 details the finite difference approximation used in DigiTherm^{TM} to calculate heat conduction through a solid structure and the convective heat transfer at its surfaces. This method was therefore coupled to the DigiDiss^{TM} module with modified reaction kinetics by a number of additions to the source code.

After inclusion into the software simulating an oxidation, Eq. 3.34 was then elaborated on to include radiative heat transfer and the heat of reaction into the simulation. Similarly to the existing solution examining internal conduction and

convective heat transfer, these effects had to have the potential to occur at each of a voxel's six faces. Eq. 8.3 describes how these effects are included taking into account the possibility of each heat transfer phenomenon occurring at any of the voxel faces. The naming convention applied is again that illustrated in Figure 3.10.

$$
\begin{aligned}
C_p\frac{T_0^{t+\Delta t}-T_0}{\Delta t} = \\
&\underbrace{\begin{aligned}&+k_1\frac{T_1-T_0}{\Delta x^2}+k_2\frac{T_2-T_0}{\Delta x^2}+k_3\frac{T_3-T_0}{\Delta x^2}\\&+k_4\frac{T_4-T_0}{\Delta x^2}+k_5\frac{T_5-T_0}{\Delta x^2}+k_6\frac{T_6-T_0}{\Delta x^2}\end{aligned}}_{\text{Internal conduction}}\\
&\underbrace{\begin{aligned}&+h_1\frac{T_1-T_0}{\Delta x}+h_2\frac{T_2-T_0}{\Delta x}+h_3\frac{T_3-T_0}{\Delta x}\\&+h_4\frac{T_4-T_0}{\Delta x}+h_5\frac{T_5-T_0}{\Delta x}+h_6\frac{T_6-T_0}{\Delta x}\end{aligned}}_{\text{Convective heat transfer with fluid}}\\
&\underbrace{\begin{aligned}&+\epsilon_{UC}\sigma\frac{T_1^4-T_0^4}{\Delta x}+\epsilon_{UC}\sigma\frac{T_2^4-T_0^4}{\Delta x}+\epsilon_{UC}\sigma\frac{T_3^4-T_0^4}{\Delta x}\\&+\epsilon_{UC}\sigma\frac{T_4^4-T_0^4}{\Delta x}+\epsilon_{UC}\sigma\frac{T_5^4-T_0^4}{\Delta x}+\epsilon_{UC}\sigma\frac{T_6^4-T_0^4}{\Delta x}\end{aligned}}_{\text{Radiative heat transfer with fluid}}\\
&\underbrace{\begin{aligned}&-\frac{\Delta H_R k_{g_1}k_1C_1}{\Delta x(k_{g_1}+k_1)}-\frac{\Delta H_R k_{g_2}k_2C_2}{\Delta x(k_{g_2}+k_2)}-\frac{\Delta H_R k_{g_3}k_3C_3}{\Delta x(k_{g_3}+k_3)}\\&-\frac{\Delta H_R k_{g_4}k_4C_4}{\Delta x(k_{g_4}+k_4)}-\frac{\Delta H_R k_{g_5}k_5C_5}{\Delta x(k_{g_5}+k_5)}-\frac{\Delta H_R k_{g_6}k_6C_6}{\Delta x(k_{g_6}+k_6)}\end{aligned}}_{\text{Heat of reaction}}\\
&+e_xC_p\frac{T_1-T_0}{\Delta x}-e_xC_p\frac{T_2-T_0}{\Delta x}+e_yC_p\frac{T_3-T_0}{\Delta x}\\
&\qquad\qquad\underbrace{-e_yC_p\frac{T_4-T_0}{\Delta x}+e_zC_p\frac{T_5-T_0}{\Delta x}-e_zC_p\frac{T_6-T_0}{\Delta x}}_{\text{Heat transfer due to gas flow}}
\end{aligned}
\tag{8.3}
$$

where k_{g_1}-k_{g_6} are the mass transfer coefficients at each face and e_x, e_y and e_z are the fluid velocities in each direction.

With different combinations of solid and fluid voxels, Eq. 8.3 can function in a number of different ways that is dictated in the software by Boolean logic. For

Table 8.1: The terms that are removed from Eq. 8.3 depending on the phase of the voxels involved.

Voxel phase at (i, j, k)	Adjacent voxel phase	
	Solid	Liquid
Solid	convective, radiative, heat of reaction and fluid velocity	conductive
Liquid	conductive	convective, radiative and heat of reaction

example, if the voxel of interest at position '0' (i, j, k) is solid, and the voxel at position '1' $(i+1, j, k)$ is also solid, there is no exposure to the oxidant and hence no heat of reaction, no convective or radiative heat transfer and no effect of the fluid flow. The effect of the phases of relevant voxels on Eq. 8.3 is qualitatively described in Table 8.1.

In order to calculate the heat and mass transfer coefficients, h_1-h_6 and k_{g_1}-k_{g_6}, at the faces at which they are required, a subroutine was added that calculated the size of the solid in the direction normal to the heat and mass transfer at that point. These calculations also required calculation of the Nusselt, Nu, and Sherwood, Sh, numbers, respectively, that are both dependent on the Reynolds number. In order to obtain values for Nu and Sh, the Reynolds number is calculated as a function of the fluid flow velocity:

$$\mathrm{Re} = \frac{\rho_{fluid} e_{max} L_d}{\mu} \tag{8.4}$$

where ρ_{fluid} is the fluid density, e_{max} is the maximum of e_x, e_y and e_z and assumed to represent a freestream velocity, L_d is the characteristic length taken to be the length of the domain given the freestream velocity assumption and μ is the dynamic viscosity of the fluid.

Assuming that the heat transfer coefficient represents forced convection of a fluid over the surface of a cylinder, the Nusselt number can then be expressed in

Table 8.2: The dependence of the values of C and n on the Reynolds number (Hilpert, 1933).

Reynolds number	C	n
$0.4 < \mathrm{Re} < 4.0$	0.891	0.339
$4.0 < \mathrm{Re} < 40.0$	0.821	0.385
$40.0 < \mathrm{Re} < 4000.0$	0.615	0.466
$4000.0 < \mathrm{Re} < 40000.0$	0.174	0.618
$40000.0 < \mathrm{Re} < 400000.0$	0.024	0.805

terms of the Reynolds number as (Hilpert, 1933):

$$\mathrm{Nu} = C\mathrm{Re}^n \tag{8.5}$$

where C and n are dimensionless values dependent on the Reynolds number and provided in Table 8.2.

The heat transfer coefficient at each voxel face is then expressed in the usual fashion. For example, at position '1' it is given as:

$$h_1 = \frac{\lambda_{fluid}\mathrm{Nu}}{L_x} \tag{8.6}$$

where L_x is the characteristic length of the solid in the direction normal to the heat transfer; the x direction in this case.

The Sherwood number is calculated in the same manner as the Nusselt number, and is therefore written as:

$$\mathrm{Sh} = C\mathrm{Re}^n \tag{8.7}$$

The mass transfer coefficient is then also expressed as it has been previously. At position '1', it would be given as:

$$k_{g_1} = \frac{D_{O_2-CO}\mathrm{Sh}}{L_x} \tag{8.8}$$

The general heat transfer equation given in Eq. 8.3, coupled to the methodology for calculating heat and mass transfer coefficients in Eqs. 8.4 to 8.8 and a number of Boolean logic operators dependent on the phases of the voxels under

consideration at a particular position, allows calculation of the temperature distribution throughout the DigiDiss^{TM} domain. Therefore, the oxidation rates at each surface position can be calculated and simulations of the oxidation of UC can now be carried out using the modified DigiDiss^{TM} software.

8.2.3 Correcting for geometric difficulties

During initial oxidation simulations by the modified DigiDiss^{TM} software, it was noticed that the results predicted were consistently different to those predicted by the one-dimensional sphere model described in Chapter 4. Figure 8.1 is a plot of an oxidation curve produced by the modified DigiDiss^{TM} code compared to one from the one-dimensional sphere model using identical input parameters, illustrating the faster reaction rate predicted by the modified DigiDiss^{TM} model. The faster oxidation rate and associated higher pellet temperatures were predicted across a range of input parameters, with the discrepancy always being roughly constant despite debugging efforts indicating that the constants and calculated coefficients were virtually identical in each case. Therefore, it was suspected that the differing predictions were linked to the methodology employed in the finite difference solution in each case, particularly in how a sphere is represented in DigiPac^{TM} software as a collection of cubic voxels as illustrated in Figure 8.2.

A perfect sphere with a radius of 9.35×10^{-3} m has a surface area of 1.10×10^{-3} m^2. However, calculating the surface area of the spheres generated from cubic voxels reveals that the surface areas are generally around 1.65×10^{-3} m^2 with small variation dependent on the resolution of the sphere. Figure 8.3 is a plot of the calculated surface areas of spheres comprised of different numbers of voxels, revealing that the surface area is consistently larger than that of a perfect sphere of the same diameter. This larger surface area, therefore, was taken as explanation for the faster oxidation predicted by the modified DigiDiss^{TM} model.

Also included in Figure 8.3 is a measure of the sphericity (Wadell, 1935) of the generated spheres, calculated as:

$$\Psi_s = \frac{\pi^{\frac{1}{3}}(6V_s)^{\frac{2}{3}}}{A_s} \tag{8.9}$$

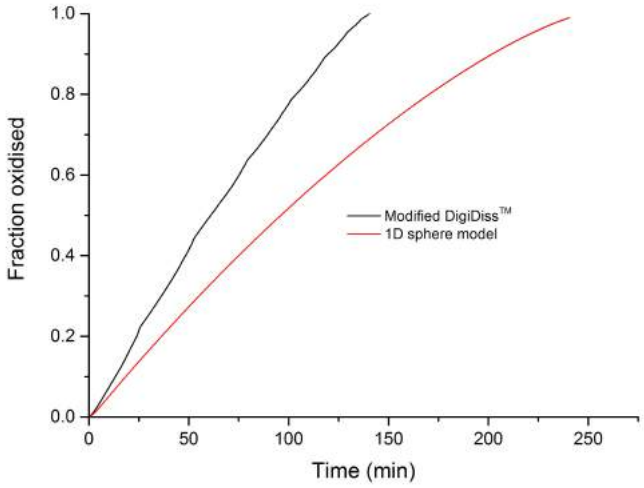

Figure 8.1: A comparison of oxidation curves produced by the DigiDiss^{TM} code and the 1D spherical model with identical input parameters that demonstrates the faster oxidation rate predicted by the DigiDiss^{TM} code.

where Ψ_s is the sphericity of a DigiPac^{TM} generated sphere, V_s its volume and A_s its surface area.

The sphericity of a particle is a measure of how close its volume to surface area ratio is to that of a perfect sphere, which has a sphericity of 1.0. Given that the spheres used in the modified DigiDiss^{TM} model have sphericity values between 0.66 and 0.68, the cause for the discrepancy in the oxidation rate between the two models is quantifiable. The issue can therefore be rectified by the inclusion

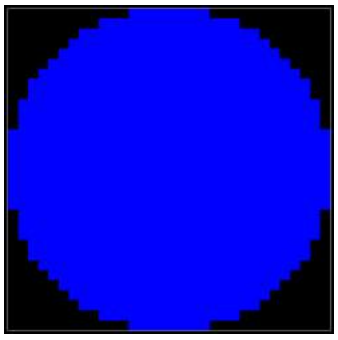

Figure 8.2: A cross section of a sphere discretised into voxels illustrating the inherent inaccuracy of representing rounded surfaces as cubic voxels.

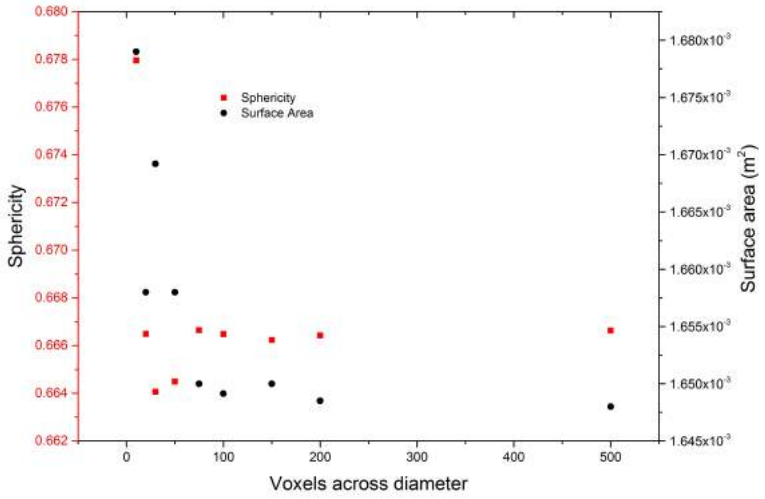

Figure 8.3: The effect of resolution on the surface area and sphericity of DigiPac^{TM} generated spheres.

of a factor of $1/\Psi_s$, the inverse of the sphericity of the voxel-based spheres, into any equation with a surface area dependence used by the modified DigiDiss^{TM} code. For example, Eq. 8.2 describing the weight loss of a voxel over a time step becomes:

$$\frac{W_0^{n+1} - W_0^n}{\Delta t} = -\frac{2}{\Psi_s}\Big(k_{C_1}^n \Delta x^2 C_1^n + k_{C_2}^n \Delta x^2 C_2^n + k_{C_3}^n \Delta x^2 C_3^n + k_{C_4}^n \Delta x^2 C_4^n + k_{C_5}^n \Delta x^2 C_5^n + k_{C_6}^n \Delta x^2 C_6^n\Big) \quad (8.10)$$

A similar effect was observed when comparing the results of oxidising a UC cylinder using the modified DigiDiss^{TM} model and the two-dimensional, axisymmetric cylinder model described in Chapter 7. The results of calculating the surface areas of cylinders generated using DigiPac^{TM} software and comparing them to the expected surface area of a cylinder of the same dimensions is included in Figure 8.4. Again, but to a lesser extent due to fewer rounded in edges in a cylinder than a sphere, the geometric shape generated from voxels has an overestimated surface area that results in the prediction of faster oxidation rates. Similar measures therefore had to be taken when oxidising cylinders, requiring the inclusion of a factor of $1/\Psi_c$ to compensate for the differences in surface area. Ψ_c, not necessarily the sphericity but a similar metric, is calculated from the ratio of the

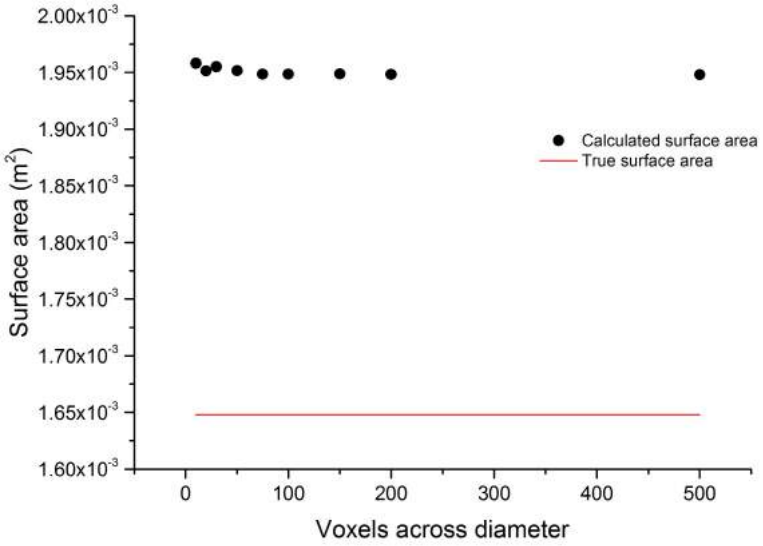

Figure 8.4: The effect of resolution on the surface area of DigiPac^{TM} generated cylinders.

true cylindrical surface area to the surface area of the voxel-based cylinder.

$$\Psi_c = \frac{A_c}{A} \tag{8.11}$$

where A_c is the calculated surface area of the generated cylinder and A is the surface area of the equivalent perfect cylinder.

This correction factor is included into the source code in the same fashion as Ψ_s. For example, when oxidising a cylinder, Eq. 8.2 becomes:

$$\frac{W_0^{n+1} - W_0^n}{\Delta t} = -\frac{2}{\Psi_c}\Big(k_{C_1}^n \Delta x^2 C_1^n + k_{C_2}^n \Delta x^2 C_2^n + k_{C_3}^n \Delta x^2 C_3^n + k_{C_4}^n \Delta x^2 C_4^n + k_{C_5}^n \Delta x^2 C_5^n + k_{C_6}^n \Delta x^2 C_6^n\Big) \tag{8.12}$$

Therefore, when using the modified DigiDiss^{TM} software to oxidise rounded geometric shapes such as spheres and cylinders, it is necessary to input the shape being used so that the appropriate correction factor can be applied by the software. This is a fairly awkward necessity that limits the variety of shapes that can be oxidised by the software without calculation of further correction factors, but is apparently unavoidable when representing objects with rounded surfaces as cubic voxels.

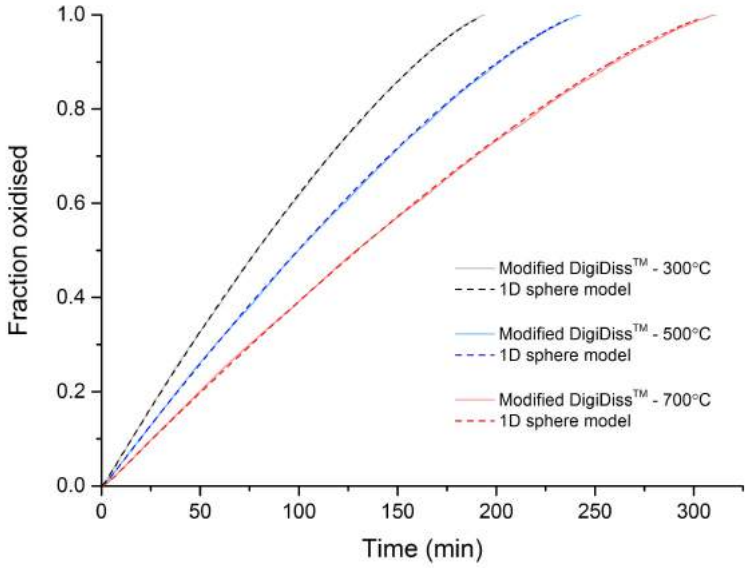

Figure 8.5: A comparison between the oxidation curves produced by the modified DigiDiss^{TM} software and the one-dimensional spherical model from Section 4. The O_2 concentration of the bulk gas was held constant at 3.15 mol m^{-3}, with an initial pellet radius of 0.935 cm.

8.2.4 Validation against previous models

The additions described in Sections 8.2.1, 8.2.2 and 8.2.3 allow the predictions of the DigiDiss^{TM} software to be compared to the results from the models in Chapters 4 and 7 in order to ensure it is simulating an oxidation in the same manner and that the changes to the source code have been implemented successfully. Figure 8.5 is a plot of the fraction of a spherical UC pellet oxidised against time at different temperatures, comparing the results of the modified DigiDiss^{TM} software to the one-dimensional model described in Chapter 4. The conditions were identical for both models, with a spherical UC pellet of radius 9.35×10^{-3} m at an initial temperature of 25 °C exposed to a bulk gas with an O_2 concentration of 3.15 mol m^{-3} and a fixed temperature of either 300, 500 or 700 °C.

The results displayed in Figure 8.5 reveal that the modified DigiDiss^{TM} software predicts a virtually identical oxidation rate to the one-dimensional model, indicating that the oxidation reaction kinetics and heat transfer have been in-

Table 8.3: A quantitative comparison of the maximum temperatures reached within the UC pellet and reaction completion times predicted by the modified DigiDiss^{TM} software and the one-dimensional spherical model.

Bulk gas temperature (°C)	Peak UC temperature (°C)		Reaction completion time (min)	
	1D sphere	DigiDiss^{TM}	1D sphere	DigiDiss^{TM}
300	1259		290	286
500	1350	1465	225	221
700	1425		187	176

corporated into the software successfully. The temperature dependencies of the two models can also be confirmed to agree as the oxidation curves at different temperatures all align smoothly.

Table 8.3 provides quantification for the results displayed in Figure 8.5, providing further detail on the similarities of the reaction completion times predicted by each model. Table 8.3 also includes the maximum temperature within the UC pellet predicted by each model, where the predictions diverge significantly. This disagreement between the two models on pellet temperature can be investigated by examining the average temperature within the pellet over time, as displayed in Figure 8.6. The pellet temperature predicted by the DigiDiss^{TM} software can be seen to be significantly discretised, increasing in temperature in a stepwise fashion and plateauing at a number of values in contrast to the more continuous temperature change predicted by the one-dimensional model. This phenomenon is explained by the manner in which the pellet changes in shape during the course of the oxidation in each model. The models described in Chapters 4, 5, 6 and 7 all have increment sizes that are allowed to change at each time step, resulting in the solid structure shrinking in small, manageable increments. Solid structures depleting in DigiDiss^{TM} software, however, do so by the removal of voxels from their structure once they have been reduced below a density threshold. This results in a staggered, less continuous change in the shape of the solid structure. Since the heat fluxes in and out of the solid are dependent on the surface area of the solid, and hence its shape and size, the predicted solid temperature is therefore also likely to be less continuous when using DigiDiss^{TM}.

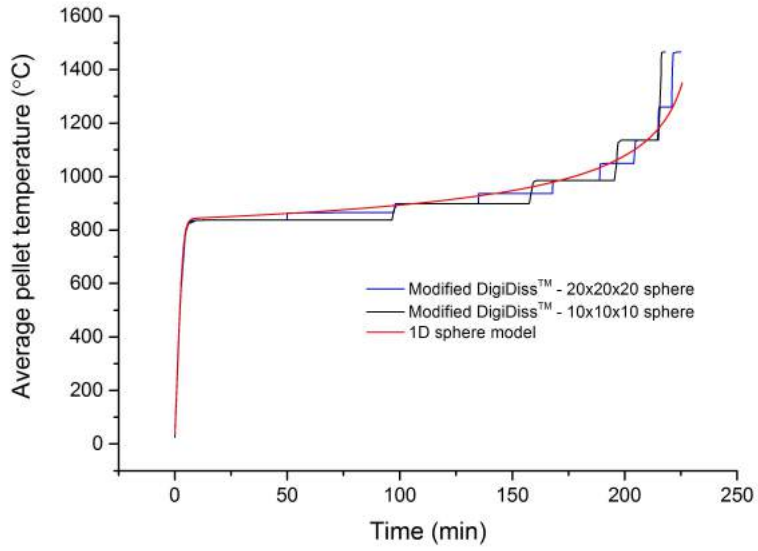

Figure 8.6: A comparison between the average pellet temperatures predicted by the modified DigiDiss^{TM} software and the one-dimensional spherical model from Section 4. The O_2 concentration of the bulk gas was held constant at $3.15\,\mathrm{mol\,m^{-3}}$, with an initial pellet radius of 0.935 cm.

Predictably, the discontinuities in DigiDiss's^{TM} temperature predictions are highly dependent on the number of voxels constituting the solid. Figure 8.6 also illustrates the effect of the number of voxels on the number and degree of the discontinuities in the pellet temperature. It suggests that the more voxels are included, the closer the prediction matches that of the one-dimensional sphere model and the staggering effect is reduced, confirming that it is the voxel-based nature of DigiDiss^{TM} causing the discretised temperature changes. Therefore, an accurate temperature prediction requires compromise with the lengthy computational times that are introduced with larger numbers of voxels.

Nonetheless, both the temperature and the reaction completion times predicted by the modified DigiDiss^{TM} software are satisfactorily close to the original predictions made by the one-dimensional spherical model, given that the two modelling techniques are quite different. Therefore, DigiDiss^{TM} can be said to have been modified to perform oxidation simulations successfully, and its more advanced capabilities can now be employed.

Table 8.4: Testing the modified DigiDiss^{TM} model for convergence by varying the number of voxels comprising the sphere and observing the effect on the predicted oxidation time.

Number of voxels along sphere diameter	Oxidation completion time (min)	Computational time (h)
10	218	0.77
20	221	17.4
40	229	430

8.2.5 Ensuring numerical stability and convergence

Since DigiDiss^{TM} employs finite difference methods in calculating its solutions, it is necessary to ensure stability and to check that its predictions converge. The stability criteria built into the modified DigiDiss^{TM} code again uses the form of the Courant-Friedrichs-Lewy rule, expressed as:

$$\Delta t \leq \frac{\Delta x^2}{6\alpha + \Delta x e_{max}} \tag{8.13}$$

where a factor of 6 is present due to the three-dimensionality of the system and α is the thermal diffusivity of either the solid being oxidised or the oxidising fluid, whichever is greater.

Unlike the models in previous chapters, the spatial increment size, representing the width of a voxel, is unchanged throughout the simulation. Therefore, the time step size is calculated using Eq. 8.13 at the beginning of the simulation only.

The modified DigiDiss^{TM} code was tested by convergence by carrying out identical simulations using a different number of voxels, and hence a different value for Δx, to represent a sphere being oxidised. Table 8.4 displays the effect of using different voxel resolutions on the predicted oxidation completion time and the computational time used, and Figure 8.7 provides images of how these spheres are represented in the code. Using Richardson's deferred approach to the limit (Smith, 1965) given in Eqs. 6.51 and 6.52, a prediction for the solution given an infinite number of voxels can be attained to confirm the solution is converging.

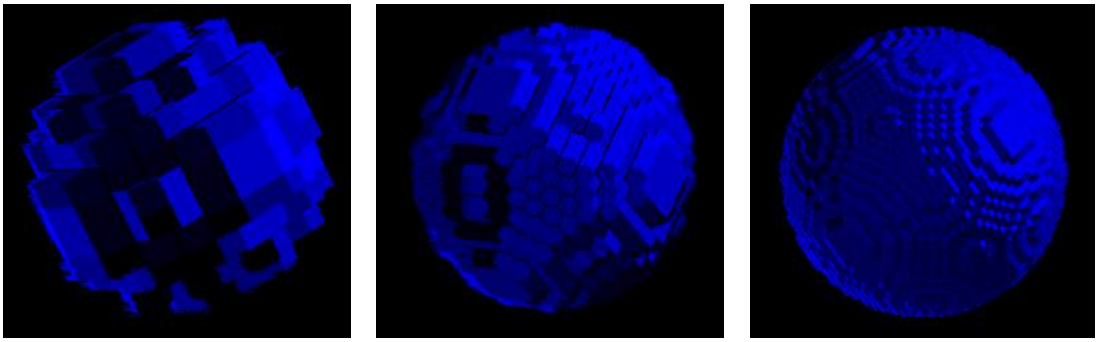

(a) 10 voxels in diameter. (b) 20 voxels in diameter. (c) 40 voxels in diameter.

Figure 8.7: Images of spherical inputs to DigiDiss^{TM} at different resolutions.

Applying this to the results in Table 8.4 gives a solution of an oxidation completion time of $u = 234\,\text{min}$. Given that increasing the resolution of the sphere in DigiDiss^{TM} causes the predicted completion time to tend towards this value of u, as indicated by the results in Table 8.4, the modified DigiDiss^{TM} code can be said to be convergent.

8.3 Application of advanced modelling techniques

The DigiDiss^{TM} software, with the modifications described in Section 8.2 checked against earlier results and for convergence, can now be used to take advantage of its additional functionality. In particular, batch oxidations using packed structures comprising multiple UC pellets can be exported from DigiPac^{TM} into the modified DigiDiss^{TM} software and oxidised. Additionally, the prediction of fluid flow behaviour using the LBM method, as described in Section 3.2.2, can be used to investigate the effects of flow rate on the oxidation rate and temperature distributions through the system.

8.3.1 Batch oxidation

In order to consider how the oxidation of UC fuel may be realistically carried out in an industrial setting, it was thought necessary to examine a batch process oxidising a number of UC pellets simultaneously. This can be completed in

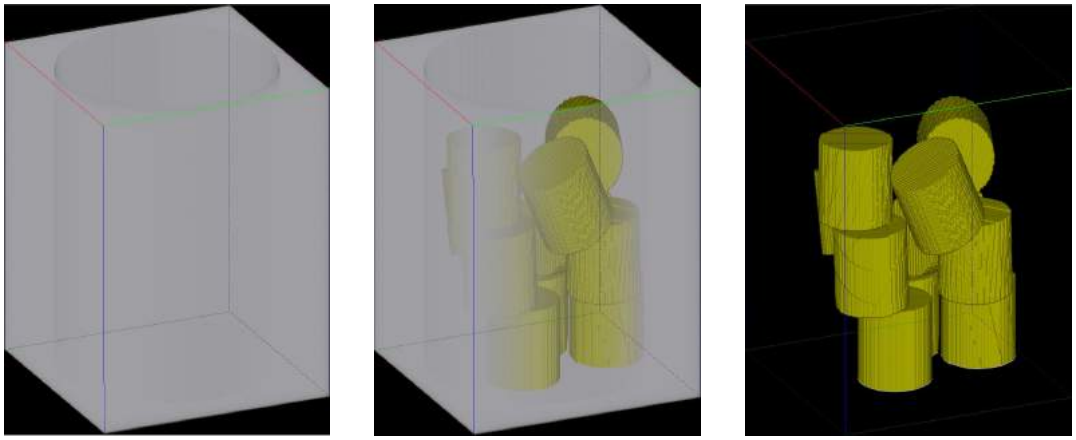

(a) The container

(b) Ten cylindrical pellets packed into the container.

(c) Pellets after removal of the container, ready for input into DigiDiss^{TM}.

Figure 8.8: The process of preparing a batch input for DigiDiss^{TM} using DigiPac^{TM}.

DigiDiss^{TM} due to the three-dimensionality of the code and the ability to oxidise any solid structure.

In order to simulate a batch oxidation DigiDiss^{TM}, a solid structure representing the batch must be generated using DigiPac^{TM}. For the purposes of this work, this involved inserting a number of cylindrical solids representing UC pellets into a cuboidal container with a hollow, cylindrical centre with an open face facing upwards. According to DigiPac's^{TM} packing algorithm, detailed in Figure 3.7, cylinders are then inserted at the top of the domain and allowed to fall under approximated gravity and arrange within the cylindrical centre. After halting of the algorithm, the container was removed to give a packing of cylindrical pellets suitable for oxidation in DigiDiss^{TM}. An example of this process is illustrated in Figure 8.8.

The solid input is then oxidised in DigiDiss^{TM} in the same manner as single solid would be with its component voxels becoming fluid after being depleted below a density criterion. One limitation of this method is that if a lower pellet in the packing were to oxidise first due to greater exposure to the fluid, for example, pellets above it would not collapse due to gravity not being accounted

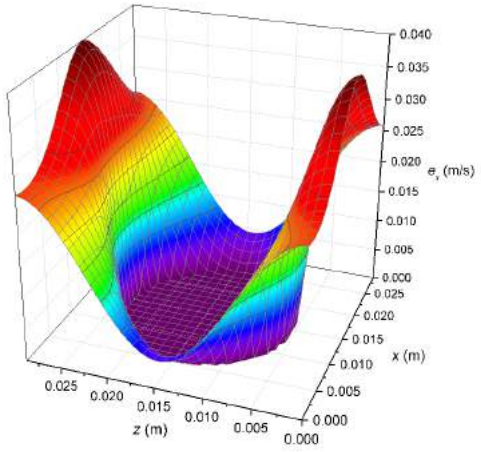

Figure 8.9: An example of flow velocity calculation using DigiDiss^{TM}. A sphere suspended in a cubic domain is subjected to a flow in the x direction with a maximum velocity of $e_{max} = 0.04\,\mathrm{m\,s^{-1}}$.

for in DigiDiss^{TM}. This method assumes that the batch process it is simulating places the UC pellets to be oxidised in a sieve-like container that allows essentially free access of the oxidising fluid to the pellets.

8.3.2 Flow around the pellet

Modelling of fluid flow through packed and single pellet structures was achieved through the use of DigiDiss^{TM}'s ability to apply the LBM. The maximum linear velocity, e_{max}, is specified prior to the simulation and is generally achieved by fluid flowing freely at the edges of the domain. The flow direction is established through the input of the body force in the x, y and z directions. A body force, or a long-range force, is a force acting uniformly on the whole volume, or body, of interest with an origin far away. An example of a typical body force would be gravity.

Alternatively, the flow velocities in each direction, e_x, e_y and e_z, at the relevant domain boundary can be input. The software then calculates the flow velocity in each direction, calculating the effect it has on the convective heat transfer as included in Eq. 8.3, Page 223. The calculation of the flow velocities across the volume (flow field) is completed after a particular number of time steps set by

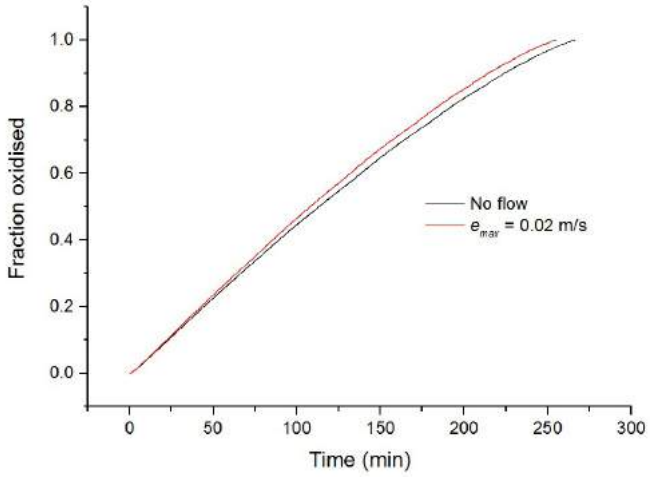

Figure 8.10: Fraction of the UC cylinder oxidised over time, with and without a fluid flow in the x direction

the user in order to save computational time. The flow velocity also has an effect on the Reynolds number calculation as described in Eq. 8.4, affecting the heat and mass transfer coefficients.

An example of a DigiDiss^{TM} flow distribution is presented in Figure 8.9, a plot of the fluid velocity in the x direction across the xz plane. In this case, a body force has been applied in the x direction only. A circular depression in the middle of the plot indicates the position of the cross-section through the sphere. The flow is fastest at the edges of the domain, where $e_x \approx e_{max}$.

8.4 Results

The modified DigiDiss^{TM} software is now capable of oxidising pellets singularly or as a batch. It can predict the temperature distribution through the domain and also simulate fluid flow around the solid structure(s). Demonstrations of these capabilities and the results from single and batch simulations are included in this section.

The first simulations completed in the software were the oxidation of single, cylindrical pellets with and without a fluid flow to examine the effect on the reaction rate. The pellets used were of a diameter and length of 1.87 cm and had

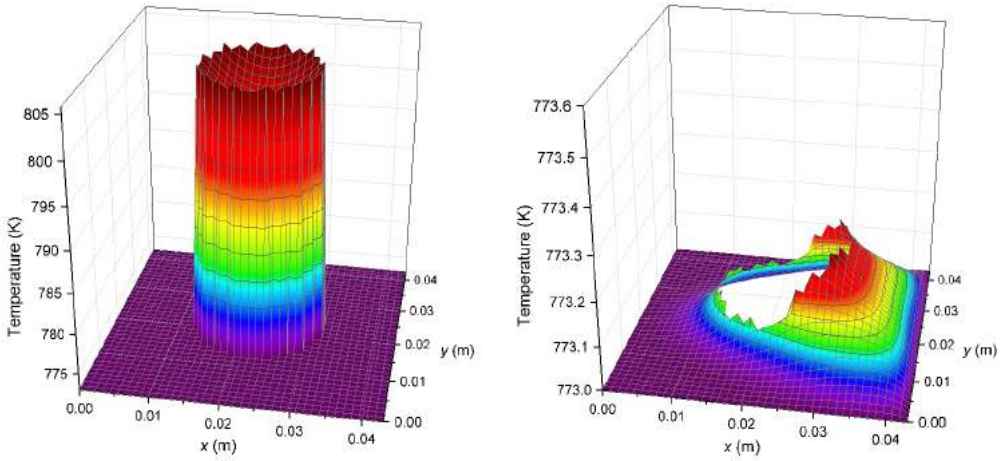

(a) Including pellet temperature. (b) Not including pellet temperature.

Figure 8.11: The temperature distribution across the xy plane through the DigiDiss^{TM} domain at $t = 2.90\,\text{min}$, with a cylindrical pellet with its length axis extending in the z direction is in the centre. The plot on the right has the pellet temperature removed to allow a rescale of the temperature axis to illustrate the gas temperature.

an initial temperature of 25 °C. The gas temperature was initially 500 °C and the O_2 concentration was held at $3.15\,\text{mol}\,\text{m}^{-3}$ across the fluid voxels, representative of air. A maximum fluid velocity, e_{max}, was then specified to prompt DigiDiss ^{TM} to include fluid flow simulation. The resulting oxidation curves are displayed in Figure 8.10. When a flow with $e_{max} = 0.02\,\text{m}\,\text{s}^{-1}$ is applied in the x direction, the oxidation completion time reduces from 267 min to 255 min as a result of the increased heat and mass transfer coefficient.

Figure 8.11 includes two cross-sectional temperature distributions output at $t = 2.90\,\text{min}$ during the simulation of the oxidation of a cylinder with a flow of $e_{max} = 0.02\,\text{m}\,\text{s}^{-1}$ in the x direction included. The cross-sections are taken through the xy plane of the DigiDiss^{TM} domain at the z midpoint, and the cylinder is positioned in the centre of the domain with its longitudinal axis extending in the z direction. Figure 8.11a displays the effect of the pellet heating due to the exothermic oxidation to become significantly hotter than the surrounding air. As the pellet is currently undergoing rapid temperature rise, a slight temperature

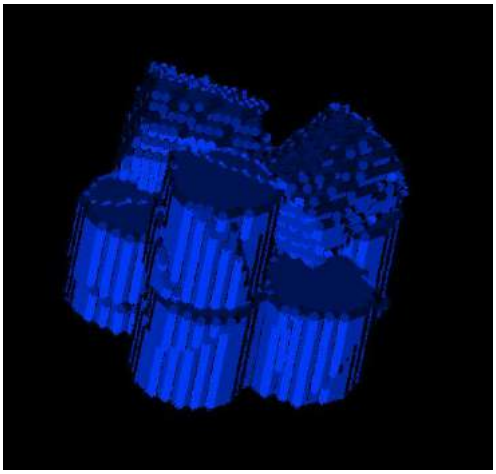

Figure 8.12: Eight, digitised cylindrical pellets packed into a single structure using DigiPac^{TM}, ready for input into the modified DigiDiss^{TM} software.

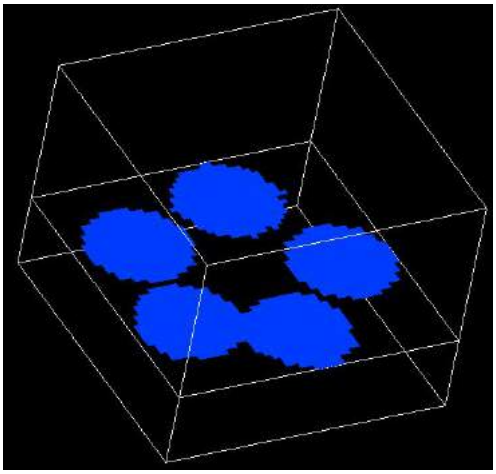

Figure 8.13: A cross-section taken through the packed pellet structure.

gradient can be seen between the surface of the pellet and the centre as the heat conducts inwards. Figure 8.11b is the same plot, but with the pellet temperature removed and rescaled to allow visualisation of the effects of the hotter pellet and the fluid flow on the gas temperature. Since the fluid is flowing in the x direction, heat emitted from the pellet can be seen to be transferred more significantly in the $+x$ direction. Note that for this simulation, the boundaries of the domain were fixed at a temperature of 500 °C (773 K).

A batch oxidation was carried out on eight cylindrical UC pellets of a length and diameter of 1.87 cm. The pellets were packed using the methodology described in Section 8.3.1 and the resulting structure, illustrated in Figure 8.12, was imported into the modified DigiDiss^{TM} software. Initially, the gas temperature was 500 °C and the pellet temperature was 25 °C. The O_2 concentration was held at 3.15 mol m^{-3} across the fluid voxels, representative of air. The batch simulation was completed both with and without a fluid flow. When a flow was applied, it was given a maximum velocity of $e_{max} = 0.02\,\mathrm{m\,s^{-1}}$. A qualitative example of the effect this flow has on the temperature distribution through the solid structure is illustrated in Figure 8.14a, a plot of the temperature profile

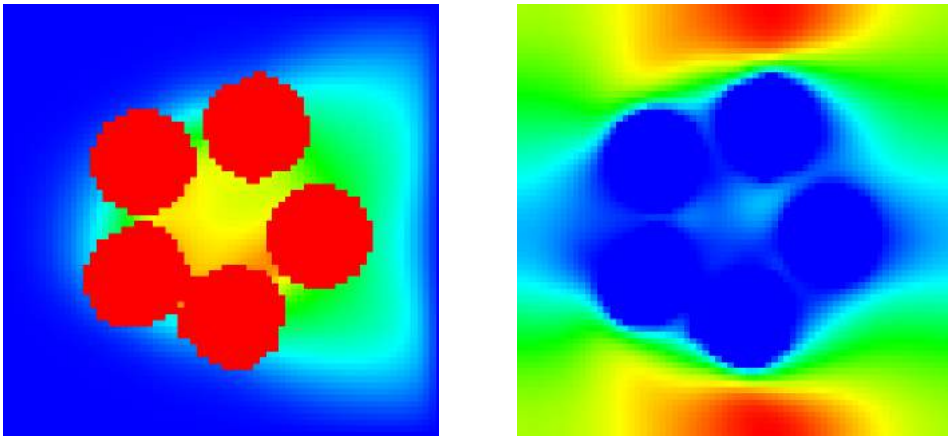

(a) Temperature distribution.

(b) Velocity in x direction distribution.

Figure 8.14: Examples of cross-sectional images taken during a batch oxidation of eight cylindrical UC pellets.

along the cross-section displayed in Figure 8.13. Figure 8.14b is a similar qualitative example of a velocity distribution through the packing as displayed by DigiDiss^{TM}.

The fraction of the overall solid volume present within the domain oxidised over time with and without the fluid flow present is included in Figure 8.15. Fluid flow has an initial effect of increasing the oxidation rate that eventually reduces causing the oxidation curves to align eventually. The re-alignment suggests that at some point the flow must have slowed the oxidation to counter the initial rate increase. This could be a result of the increased higher heat transfer coefficient cooling the pellets at a later stage in the reaction when they are hotter than the surrounding gas, reducing the reaction rate at their surface. This idea is supported by the faster reaction rate at the start of the oxidation, also likely to be a result of the higher heat transfer coefficient heating the pellet faster initially.

Table 8.5 allows the observation to be made that a batch pellet oxidation takes longer, 353 min, than an oxidation of a single pellet of the same shape and size under the same conditions, 267 min. This is likely because the surface area exposed to mass ratio is greater in the single pellet case, as in the batch structure

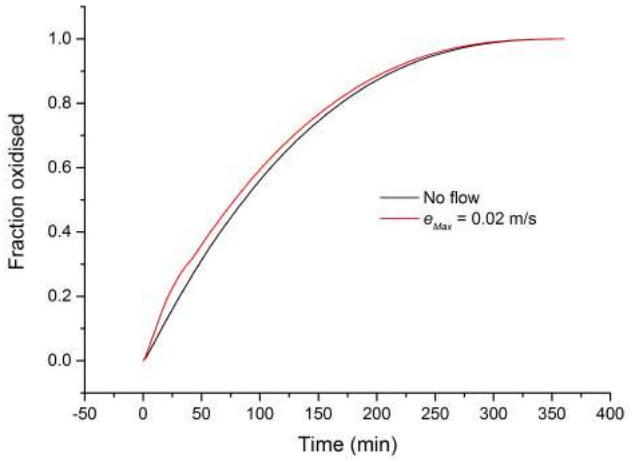

Figure 8.15: Fraction of the batch of UC pellets oxidised over time, with and without a fluid flow in the x direction present.

Table 8.5: Oxidation completion times of batch and single pellet oxidations with and without fluid flow.

e_{max}	Oxidation completion time (min)	
$(\mathrm{m\,s^{-1}})$	Batch	Single
0.00	353	267
0.02	360	255

any pellet-pellet contact reduces the area of UC open to air. Table 8.5 also highlights the different effect that introducing a flow rate has on each oxidation process. The slowing of the oxidation in the batch process could be a result of both the inter-pellet and pellet-air heat transfer being affected by the higher heat transfer coefficient, resulting in relatively more significant cooling effect on the batch than the single pellet that only undergoes pellet-air heat transfer. Figures 8.16, 8.17 and 8.18 are surface plots of DigiDiss$^{\mathrm{TM}}$ outputs taken during the batch oxidation simulation with flow present presented in Figure 8.15. Each figure displays a distribution through the xy cross section of the domain at different time intervals of temperature, UC density/concentration and flow velocity in the x direction, respectively.

Figure 8.16, the temperature distributions, illustrates the increase in pellet

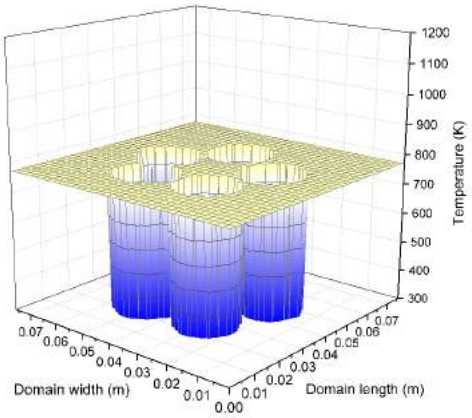

(a) $t = 0.02\,\text{min}$

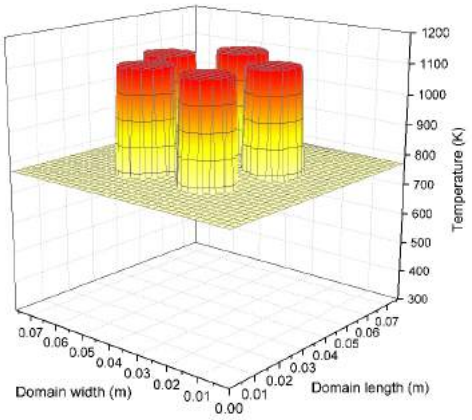

(b) $t = 77.27\,\text{min}$

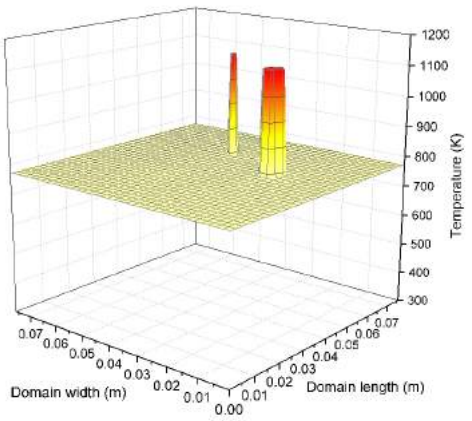

(c) $t = 209.83\,\text{min}$

Figure 8.16: The temperature distribution through the xy cross-section of the simulation domain at different times during the batch oxidation.

temperature as a result of the oxidation. In Figure 8.16a, five circular depressions in the temperature surface plot represent the presence of the initially colder relative to the surrounding air UC pellets. Figure 8.13, the cross-section through the packed structure, helps to visualise the pellet position within surface plots such as Figure 8.16a. As the oxidation proceeds and heats the UC pellets, their temperature surpasses the bulk gas temperature which heats up at a much slower rate, as displayed in Figure 8.16b. Finally, Figure 8.16c displays the remaining, mostly depleted pellets maintaining the higher temperature above the bulk gas.

The temperatures reached by the pellets in the batch system are very similar to those achieved by the single pellet under the same conditions. For example, after 77.27 min, the pellets in the batch are all at roughly 846 °C. At the same time, the single pellet is at 865 °C, which, given that it is a slightly faster reaction, is essentially the same. The predicted uniformity of the pellet temperatures in the batch system and the fairly minimal heating of the gaseous voidage between the pellets would also suggest that the pellet temperatures will be equivalent to single pellet system.

Figure 8.17, surface plots of the UC density in the solid voxels representing the UC, visualises the depleting UC pellets. Initially, in Figure 8.17a, all of the solid voxels comprising the five pellets in this particular cross section have densities of $1.363 \times 10^4\,\mathrm{kg\,m^{-3}}$, equivalent to the density of solid UC. Figure 8.17b displays the same pellets 77.27 min into the oxidation. Since the oxidation occurs at the pellet surface, the solid density at the centre of the pellets is unchanged whilst the outer voxels have been either removed entirely or significantly reduced in density as a result of the reaction. At 209.83 min, as the reaction is nearly complete, Figure 8.17c illustrates the last remaining two pellets that have had their densities throughout greatly reduced.

Distributions of the fluid velocity in the x direction are included in Figure 8.18. The position of the pellets can be inferred from the depressions as the result of their being solid. In all of the distributions, the flow can be seen to be faster further from the pellet. Low flow velocity is observed in-between the pellets at roughly the centre of the cross-section that increases as the pellets are depleted and present less of an obstacle to the fluid flow.

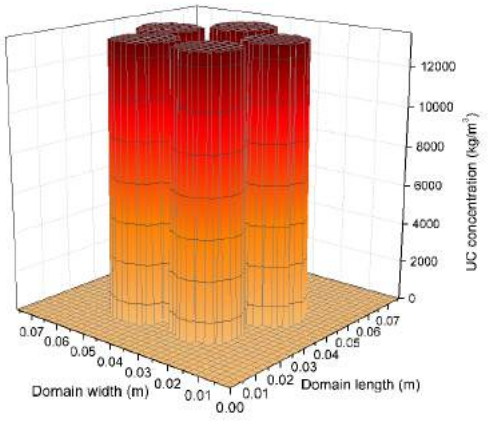

(a) $t = 0.02\,\text{min}$

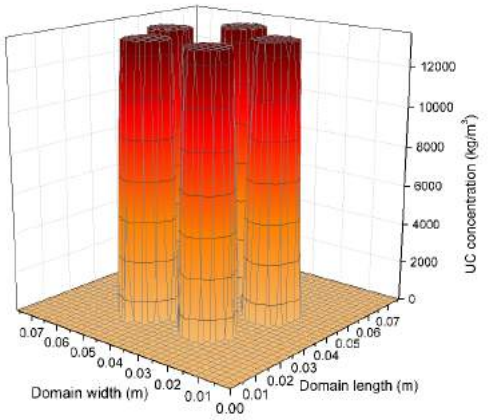

(b) $t = 77.27\,\text{min}$

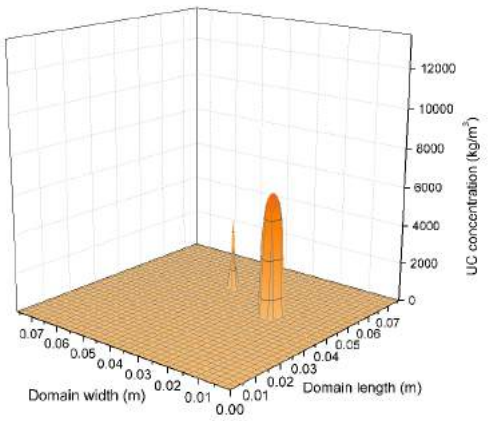

(c) $t = 209.83\,\text{min}$

Figure 8.17: The UC concentration distribution through the xy cross-section of the simulation domain at different times during the batch oxidation, illustrating the depletion of the pellets.

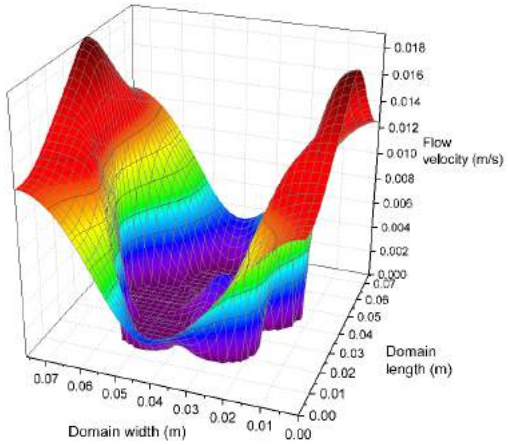

(a) $t = 0.02\,\text{min}$

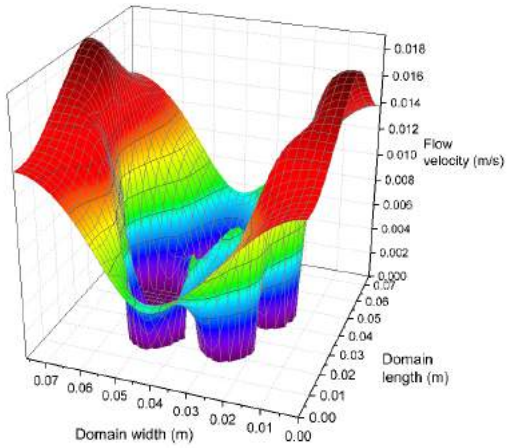

(b) $t = 77.27\,\text{min}$

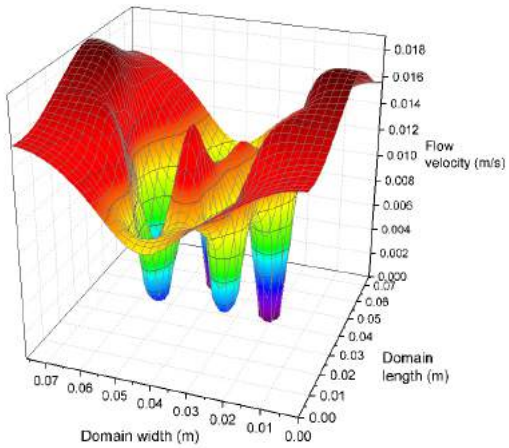

(c) $t = 209.83\,\text{min}$

Figure 8.18: The fluid velocity in the x direction through the xy cross-section of the simulation domain at different times during the batch oxidation.

8.5 Conclusions

This chapter has described the modifications made to a commercial dissolution code, DigiDiss^{TM}, to allow more advanced modelling techniques to be applied to simulating the oxidation of UC. The required modifications involved the coupling of a heat transfer code, DigiTherm^{TM}, to DigiDiss^{TM} and the inclusion of thermal radiation to the software. Additionally, the dissolution reaction kinetics were modified to represent an oxidation reaction using kinetics provided by Scott (Scott, 1966).

These modifications allowed a more advanced model of the oxidation of UC to be produced. The simulations are completed in three-dimensions, and are able to include the effects of fluid flow calculated using the LBM and to examine batch systems built in DigiPac^{TM}. The modified software was validated against the model produced in Chapter 4 to ensure that the significantly different simulation methodologies predicted the same results.

The resulting model is therefore capable of predicting three-dimensional distributions of temperature and fluid flow velocity throughout the domain, as well as visualising the depletion of the solid(s) undergoing oxidation. Oxidation completion times can be predicted and the fraction of UC oxidised over time plotted to illustrate the changing reaction rate.

Simulations were completed oxidising both single, cylindrical pellets and batch systems using pellets of the same shape and size. It was found that a batch system of eight pellets took 353 min, longer than the single pellet oxidation of 267 min predicted under identical conditions. This is suggested to be a result of the smaller surface area to volume ratio of the batch system resulting in less area available for the surface reaction. The temperatures reached by the batch system are calculated to be similar to single pellet, with minimal heating of the fluid in-between the pellets predicted.

Simulations applying a fluid flow to both the single pellet and batch systems were also completed, with a specified maximum velocity of $0.02\,\mathrm{m\,s^{-1}}$ used in each case. Due to the effect it has on increasing heat convection and heat and mass transfer coefficients, fluid flow was observed to accelerate the oxidation of the single UC pellet. However, for the batch system, the presence of a flow in fact

slowed the reaction. This is thought to be a result of the more complex cooling process affecting the batch pellets as they reach temperatures significantly greater than the surrounding fluid.

Chapter 9

Conclusions and Recommendations

9.1 Conclusions

The work included in this thesis has been the development of mathematical models designed to simulate the oxidation and dissolution of UC fuel. The motivation to produce these models is a result of a wider movement investigating the feasibility of different fuel types for Generation IV nuclear fission reactors. The models were designed to predict the completion times of each process under different reaction conditions, and also examine temperatures reached by the systems in order to outline and recommend safe operating conditions.

A literature review was carried out that focusses on previous experimental and modelling work in publications on oxidations and dissolutions of UC. A number of variables required to simulate the reactions were obtained from literature values for use in the initial models. Then, where possible, novel experimental data provided by collaborating researchers was used to fit kinetics constants to empirical observation and derive new values for these variables. Completed models, using either derived or literature-sourced variables, were then subjected to sensitivity studies to examine the effects of a number of initial conditions on the reaction.

All the models produced in this study use finite difference methods to approximate solutions to complex, non-linear partial and ordinary differential equations. These equations are implemented to describe physical processes such as heat and

mass transfer and changes in the shape of the solid UC structure. Stability of the finite difference solution is ensured using the Courant-Friedrichs-Lewy rule, and convergence is checked in each case through the use of Richardson's deferred approach to the limit to estimate the analytical solution.

The following two sections will summarise the most important conclusions from the dissolution and oxidation model chapters, respectively.

9.1.1 Dissolution

There are three dissolution models of increasing complexity included in Chapter 5: one using kinetics based on penetration of the solid by the solvent published by Hodgson (Hodgson, 1987), one using kinetics published by Maslennikov *et al.* (Maslennikov *et al.*, 2009) that include modelling of the HNO_2 concentration, and a final model using kinetics derived from novel data provided by the NNL.

The first two models are capable of reproducing the results produced by the respective publications that provide their reaction kinetics. Mathematical expression of the variation of the rate constants with either temperature or HNO_3 concentration allows extrapolation of these results to provide additional results to those in publication.

The third model produced through fitting to novel empirical data, however, is far more original. The most important aspect of this model is possibly the inclusion of the HNO_2 decomposition, observed to be significant in the NNL experiments at temperatures of 100 °C and above. This is included in the model as a temperature-dependent bi-exponential function capable of simulating the HNO_2 concentration between 6 M to 14 M HNO_3 and 80 °C to 110 °C. Therefore, the dissolution rate can also be simulated between these ranges, showing excellent agreement with the experimental data.

Through coupling to a reduced version of the heat transfer model developed for use in the oxidation models, the dissolution models are also able to predict an averaged pellet temperature, accurate due to the high thermal conductivity of UC resulting in minimal internal thermal gradients, during the dissolution.

9.1.2 Oxidation

The oxidation model is introduced in one-dimensional, spherical form in Chapter 4, with a number of different elaborations included in Chapters 6, 7 and 8. The first instance of the oxidation model uses kinetics published by Scott (Scott, 1966) to calculate a surface reaction rate and hence an oxidation completion time, as well as transient temperature distributions through the solid. The difficulty faced by this model, and the following iterations, is the presence of a highly non-linear boundary condition at the solid surface belonging to the heat transfer solution. The exothermic reaction rate included in this boundary condition is both dependent on the surface temperature and markedly affects it, necessitating the incorporation of an iterative loop into the model to enable a stable and convergent solution.

The resulting solution of the one-dimensional model predicts a steep temperature rise in the UC pellet caused by the exothermicity of the reaction. Generally, the temperature reaches a plateau around 700 °C, maintaining it until completion of the reaction where a degree of thermal runaway is predicted as the UC approaches depletion. These final temperatures reach as high as 1458 °C under the conditions used, and the completion time of the reaction is generally around 200 min to 400 min in air.

Chapter 6 then considers the effect on an adherent U_3O_8 product layer on the oxidation, claimed to be present by some literature sources. This came with the added complication of solving mass transfer through the product layer and the introduction of an additional, non-linear heat transfer boundary. The numerical solution predicted a greater reaction completion time as a result of the added barrier to the mass transfer of O_2 to the reaction site, suggesting it to be the rate-limiting process. The presence of a product layer slowing the reaction rate had the accompanying effect of lower temperatures reached by the UC pellet.

A two-dimensional solution to the UC oxidation is described in Chapter 7, allowing the UC pellet to be approximated as an axisymmetric cylinder as opposed to an equivalent volume sphere. The addition of another spatial dimensional required the alternating directions method to be employed in the numerical solution. The results that can be predicted by the two-dimensional model are similar:

temperature distributions through the solid and oxidation completion times being of the most interest. An unexpected prediction by the two-dimensional model was consistently higher temperatures and faster reaction rates than equivalent simulations made by the one-dimensional model. Examining the mathematics behind the heat transfer description reveals that the corners of the pellet in the two-dimensional solution are exposed to the heat of reaction and heat transfer with the bulk gas in both the r and x directions, resulting in higher temperatures reached that are then conducted throughout the solid. This leads to the conclusion that approximating a UC cylinder as an equivalent volume sphere is an inaccurate assumption in this context and highlights the importance of producing a two-dimensional model.

The final oxidation model is produced using an altogether different methodology described in Chapter 8. The capability of this model to simulate the oxidation in three-dimensions of arbitrarily shaped, digitised solids whilst including fluid flow simulation is demonstrated through the results included in Chapter 8. The software employed in this model allows the oxidation of batches of UC pellets, and comparison to equivalent oxidations of single pellets reveals the completion time is significantly longer due to a reduced surface area to volume ratio caused by pellet-pellet contact. The effect of fluid flow is more difficult to qualify, as it accelerates a single pellet oxidation whilst slowing the batch process at the flow velocity considered in this case.

9.2 Impact of the research

The research included in this thesis offers a significant contribution to the field of carbide fuel reprocessing. A number of oxidation models, each offering their own novel improvement on the single UC oxidation model in publication (Scott, 1966) and the accompanying stable and convergent numerical solutions are described. This provides an invaluable decision-making tool to the nuclear industry in predicting the behaviour of UC fuels undergoing oxidation, in both powdered and pellet form, and therefore determining the feasibility of pre-oxidation as a reprocessing step.

Fitting of these models to experimental data has shed light on the kinetics of the reaction, enabling this study to present its own calculated parameters for the activation energy and rate constant of the oxidation. For pellet oxidation, these parameters agree well with other, empirical observations of the activation energy, despite being in disagreement with those used by Scott's oxidation model (Scott, 1966). Therefore, this suggests that the kinetics derived for use in the models in this work are an improvement upon those used in the existing model.

A dissolution model has also been produced from novel experimental data carried out by collaborators, the NNL, that is able to predict the time taken for complete dissolution of a UC pellet across a range of temperatures and HNO_3 concentrations. This also constitutes a helpful tool in deciding upon the dissolution conditions necessary for an efficient reprocessing step. Whilst there are some UC dissolution models in publication, none provide predictions across both temperature and HNO_3 concentration ranges, making this new model more versatile. Additionally, it is the first UC dissolution model to include the effect of HNO_2 decomposition at high temperatures.

9.3 Recommendations for future work

Research into the oxidation and dissolution of UC fuel is a field expected to grow rapidly over the coming decades as more technologically advanced nuclear reactors are developed. As such, there is a huge amount of scope and demand for advancement of the findings included in this report.

One particular recommendation is the application of a stress model to examine the stability of the UC and U_3O_8 interface during oxidation. Such an investigation could provide further detail on the conditions when the product layer can be expected to adhere and when it can be expected to shatter and fall away from the UC core.

Another worthwhile investigation would be to consider the effects of the UC samples being irradiated on both the dissolution and oxidation reactions. Irradiation would likely cause significant changes to both the physical structure of fuel pellets, such as increasing its porosity and volume and causing cracks, and to their chemical composition through the introduction of various actinides. The

effect these changes have on the reactions would need to be considered and then also incorporated into the relevant models.

Further implementation of the modified DigiDiss^{TM} software is also recommended, as it is an exceptionally versatile tool in simulating UC fuel as a result of using digitised solids. More specific oxidations could be carried out on single or batch UC pellets of essentially any shape or size positioned within a domain of equally flexible shape. For example, a set up similar to that in 7.9 on Page 203 could be constructed in DigiPac^{TM} and imported for a simulation in DigiDiss^{TM}. Fluid flow through the work tube could be included as well as the heat evolved, allowing for a comprehensive simulation of the process.

The dissolution model described in this work does not predict the reaction products present in the resulting solution. Viewing the dissolution as part of the larger process, it would be very helpful to be able to make this prediction under certain temperatures and concentrations given the disruptive effect of carbon remaining in the solution. Some relationships between temperature and percentage of carbon remaining in solution have been established (e.g. Table 2.2 on Page 10, (Ferris & Bradley, 1965)), and using them to include predictions of the reaction products would greatly improve the dissolution model.

References

Aidun, C.K. & Clausen, J.R. (2010). Lattice-Boltzmann method for complex flows. *Annual Review of Fluid Mechanics*, **42**, 439–472.

Berryman, J.G. (1983). Random close packing of hard spheres and disks. *Physical Review A*, **27**, 1053–1061.

Berthinier, C., Coullomb, S., Rado, C., Le Guyadec, F., Chatillon, C., Blanquet, E. & Boichot, R. (2009). Experimental thermal analysis of uranium carbide powder ignition. In *Proceedings of Global 2009*, vol. 6131.

Berthinier, C., Coullomb, S., Rado, C., Blanquet, E., Boichot, R. & Chatillon, C. (2011). Experimental study of uranium carbide pyrophoricity. *Powder Technology*, **208**, 312 – 317.

Berthinier, C., Rado, C., Chatillon, C. & Hodaj, F. (2013). Thermodynamic assessment of oxygen diffusion in non-stoichiometric $UO_{2\pm x}$ from experimental data and frenkel pair modeling. *Journal of Nuclear Materials*, **433**, 265–286.

Bhattacharyya, R., Bhanja, K. & Mohan, S. (2015). Mathematical analysis of reduction of copper oxide pellets by hydrogen using the shrinking core model. *Fusion Engineering and Design*, **100**, 560 – 564.

Blin, L., Hadjadj, A. & Vervisch, L. (2003). Large eddy simulation of turbulent flows in reversing systems. *Journal of Turbulence*, **4**, 1–1.

Borchardt, H. (1959). Observations on reactions of uranium compounds. *Journal of Inorganic and Nuclear Chemistry*, **12**, 113 – 121.

Caboussat, A., Jouvet, G., Picasso, M. & Rappaz, J. (2011). *LES, variational multiscale LES and hybrid models*, 205–261. Chapman & Hall/CRC Numerical Analy & Scient Comp. Series, Chapman and Hall/CRC.

Caulkin, R., Jia, X., Xu, C., Fairweather, M., Williams, R.A., Stitt, H., Nijemeisland, M., Aferka, S., Crine, M., Lonard, A., Toye, D. & Marchot, P. (2009). Simulations of structures in packed columns and validation by x-ray tomography. *Industrial & Engineering Chemistry Research*, **48**, 202–213.

Caulkin, R., Jia, X., Fairweather, M. & Williams, R.A. (2012). Predictions of porosity and fluid distribution through nonspherical-packed columns. *AIChE Journal*, **58**, 1503–1512.

Chang, H.Y. (1981). *Selected Numerical Methods and Computer Programs for Chemical Engineers*. Sterling Swift Pub Co.

Chen, H., Chen, S. & Matthaeus, W.H. (1992). Recovery of the navier-stokes equations using a lattice-gas boltzmann method. *Phys. Rev. A*, **45**, R5339–R5342.

Chen, S. & Doolen, G.D. (1998). Lattice boltzmann method for fluid flows. *Annual review of fluid mechanics*, **30**, 329–364.

Coelho, D., Thovert, J.F. & Adler, P.M. (1997). Geometrical and transport properties of random packings of spheres and aspherical particles. *Physical Review E*, **55**, 1959–1978.

Coppersthwaite, D.P. & Semeraz, J.T. (2003). Uranium carbide oxidation. phase 2 trials. Tech. Rep. NSTS 4815, BNFL.

Cumberland, D. & Crawford, R. (1987). *The packing of particles*. Handbook of powder technology, Elsevier.

Davis, I.L. & Carter, R.G. (1990). Random particle packing by reduced dimension algorithms. *Journal of Applied Physics*, **67**.

De Coninck, R., Van Lierde, W. & Gijs, A. (1975). Uranium carbide: Thermal diffusivity, thermal conductivity and spectral emissivity at high temperatures. *Journal of Nuclear Materials*, **57**, 69–76.

Dell, R.M. & Wheeler, V.J. (1967). The ignition of uranium mononitride and uranium monocarbide in oxygen. *Journal of Nuclear Materials*, **21**, 328–336.

Donaldson, D., Hartley, K., Lees, P. & Parkinson, N. (1963). Reprocessing fast reactor fuels at dounreay. *Journal Name: Trans. AIME; Journal Volume: Vol: 227; Other Information: Orig. Receipt Date: 31-DEC-63*, 191–202.

Ewart, F.T. & Findlay, J.R. (1972). The ignition behaviour of irradiated carbide fuel material. *AERE-R 7192*.

Farr, J.D., Huber, E.J., Head, E.L. & Holley, C.E. (1959). The preparation of uranium monocarbide and its heat of formation. *The Journal of Physical Chemistry*, **63**, 1455–1456.

Ferreol, B. & Rothman, D.H. (1995). Lattice-boltzmann simulations of flow through fontainebleau sandstone. In *Multiphase Flow in Porous Media*, 3–20, Springer.

Ferris, L.M. & Bradley, M.J. (1965). Reactions of uranium carbides with nitric acid. *The Journal of American Chemistry*, **87**.

Ferris, L.M., Bradley, M.J. & Commission, U.S.A.E. (1964). *Off-gases from the reactions of uranium carbides with nitric acid at* 90 °C. ORNL ;3719, Oak Ridge National Laboratory, Oak Ridge, Tenn., tID-4500 (35th ed.). Bibliography references : p. 17-18.

Ferziger, J.H. & Peric, M. (2012). *Computational methods for fluid dynamics*. Springer Science & Business Media.

Fink, J. (2000). Thermophysical properties of uranium dioxide. *Journal of Nuclear Materials*, **279**, 1 – 18.

Flanary, J.R., Goode, J.H., Bradley, M.J., Ullmann, J.W., Ferris, L.M., Wall, G.C. & Commission, U.S.A.E. (1964). *Hot-cell studies of aqueous dissolution processes for irradiated carbide reactor fuels*. ORNL ;3660, Oak Ridge National Laboratory, Oak Ridge, Tenn., bibliography references : p. 33.

Flanary, J.R., Goode, J.H., Bradley, M.J., Ferris, L.M. & Ullmann, J.W. (1965). Head end dissolution for UC processes and UC-PuC reactor fuels. *Nuclear Applications*, **1**, 219.

Fogler, S.H. (1999). Elements of chemical reaction engineering.

Fox, D. & Maher, C.J. (2007). Reprocessing options for gcfr fuel. Tech. rep.

Fukasawa, T. & Ozawa, Y. (1986). Relationship between dissolution rate of uranium dioxide pellets in nitric acid solutions and their porosity. *Journal of Radioanalytical and Nuclear Chemistry*, **106**, 345–356.

Fukasawa, T., Ozawa, Y. & Kawamura, F. (1991). Generation and decomposition behavior of nitrous acid during dissolution of UO_2 pellets by nitric acid. *Nuclear Technology*, **94**, 108–113.

Ganguly, C., Hegde, P.V., Jain, G.C., Basak, U., Mehrotra, R.S., Majumdar, S. & Roy, P.R. (1986). Development and fabrication of 70% PuC - 30% UC fuel for the fast breeder test reactor in india. *Nuclear technology*, **72**, 59–69.

Gatski, T.B. & Bonnet, J.P. (2009). Chapter 5 - prediction strategies and closure models. In T.B. Gatski & J.P. Bonnet, eds., *Compressibility, Turbulence and High Speed Flow*, 117 – 160, Elsevier, Amsterdam.

Germano, M., Piomelli, U., Moin, P. & Cabot, W.H. (1991). A dynamic subgridscale eddy viscosity model. *Physics of Fluids A*, **3**.

Glatz, J.P., Bokelund, H. & Zierfuss, S. (1990). Analysis of the off-gas from dissolution of nuclear oxideand carbide fuels in nitric acid. *Radiochimica Acta*, **51**, 17–22.

Gopinathan, N., Fairweather, M. & Jia, X. (2003). Computational modelling of packed bed systems. In A. Kraslawski & I. Turunen, eds., *European Symposium on Computer Aided Process Engineering-1336th European Symposium of the Working Party on Computer Aided Process Engineering*, vol. 14 of *Computer Aided Chemical Engineering*, 647 – 652, Elsevier.

Gorlé, F., Coheur, L. & Timmermans, W. (1974). Uranium carbide fuel technology. *Journal of Nuclear Materials*, **51**, 343 – 353.

Gray, W. (1968). *The packing of solid particles*. Powder technology series, Chapman & Hall.

Grenthe, I., Drozdzynski, J., Fujino, T., Buck, E.C., Albrecht-Schmitt, T.E. & Wolf, S.F. (2010). Uranium. In L.R. Morss, N.M. Edelstein & J. Fuger, eds., *The chemistry of the actinide and transactinide elements*, vol. 1, Springer, Dordrecht.

Hilpert, R. (1933). Wärmeabgabe von geheizten drähten und rohren. *Forschung Gebeite Ingenieurw*, **4**, 215.

Hodgson, T. (1987). A model for fuel dissolution via fragmentation. In *Proc. of International Conference on Nuclear Fuel Reprocessing and Waste Management RECOD '87*.

Howard, J.B., Williams, G.C. & Fine, D.H. (1973). Kinetics of carbon monoxide oxidation in postflame gases. *Symposium (International) on Combustion*, **14**, 975–986.

Huwyler, S. & Bischoff, K. (1980). Recycling of (U, Pu)C scrap by incineration in a controlled atmosphere. *IAEA, Vienna*, 313.

Iyer, V.S., Mukerjess, S.K., Kamat, R.V., Pillai, K.T., Kumar, N., Vaidya, V.N. & Sood, D.D. (1990). Oxidation behaviour of carbide fuels. *Journal of Nuclear Technology*, **91**, 338.

Jeong, S.M., Kwon, K.C., Park, B.H. & Seo, C.S. (2006). A kinetic study of the oxidation of uranium dioxide. *Reaction Kinetics and Catalysis Letters*, **89**, 269–275.

Jia, X. & Williams, R.A. (2001). A packing algorithm for particles of arbitrary shapes. *Powder Technology*, **120**, 175 – 186.

Jia, X. & Williams, R.A. (2007). A hybrid mesoscale modelling approach to dissolution of granules and tablets. *Chemical Engineering Research and Design*, **85**, 1027–1038.

Jia, X., Gopinathan, N. & Williams, R. (2002). Modeling complex packing structures and their thermal properties. *Advanced Powder Technology*, **13**, 55 – 71.

Johnson, G.K. & Steele, W.V. (1981). The standard enthalpy of formation of uranium dioxide by fluorine bomb calorimetry. *The Journal of Chemical Thermodynamics*, **13**, 717–723.

Jones, R.W. & Crosthwaite, J.L. (1973). Uranium carbide fuel for organics cooled reactors. Tech. rep., Atomic Energy of Canada Ltd., Pinawa, Manitoba. Whiteshell Nuclear Research Establishment.

Junk, M., Klar, A. & Luo, L.S. (2005). Asymptotic analysis of the lattice boltzmann equation. *Journal of Computational Physics*, **210**, 676 – 704.

Kansal, A.R., Torquato, S. & Stillinger, F.H. (2002). Computer generation of dense polydisperse sphere packings. *The Journal of Chemical Physics*, **117**.

Kobayashi, H., Takezawa, N., Hara, K., Niki, T. & Kitano, K. (1976). The mechanism of nitrous acid decomposition. *Nippon Kagaku Kaishi*, **1976**, 383–387.

Kumar, V., Kleissl, J., Meneveau, C. & Parlange, M.B. (2006). Large-eddy simulation of a diurnal cycle of the atmospheric boundary layer: Atmospheric stability and scaling issues. *Water resources research*, **42**.

Le Guyadec, F., Rado, C., Joffre, S., Coullomb, S., Chatillon, C. & Blanquet, E. (2009). Thermodynamic and experimental study of UC powders ignition. *Journal of Nuclear Materials*, **393**, 333–342.

Legand, S., Bouyer, C., Dauvois, V., Casanova, F., Lebeau, D. & Lamouroux, C. (2014). Uranium carbide dissolution in nitric acid: speciation of organic compounds. *Journal of Radioanalytical and Nuclear Chemistry*, **302**, 27–39.

Mantle, M., Sederman, A. & Gladden, L. (2001). Single- and two-phase flow in fixed-bed reactors: {MRI} flow visualisation and lattice-Boltzmann simulations. *Chemical Engineering Science*, **56**, 523 – 529, 16th International Conference on Chemical Reactor Engineering.

Marchand, M., Fiquet, O. & Brothier, M. (2013). Oxidation kinetic analysis of a mixed uranium dicarbide and graphite compound. *Journal of Nuclear Materials*, **437**, 310–316.

Maslennikov, A., Genin, X., Vermeleun, J. & Moisy, P. (2009). UC oxidation with HNO_2 in aqueous solutions of HNO_3 and $HClO_4$. *Radiochimica Acta*, **97**, 571–580.

Mazaudier, F., Tamani, C., Galerie, A. & Marc, Y. (2010). On the oxidation of (U, Pu)C fuel: Experimental and kinetic aspects, practical issues. *JNM*, **406**, 277–284.

Mellor, G.L. & Herring, H.J. (1973). A survey of the mean turbulent field closure models. *AIAA journal*, **11**, 590–599.

Missen, R.W., Mims, C.A. & Savile, B.A. (1999). *Introduction to Chemical Reaction Engineering and Kinetics*. Wiley.

Moeng, C.H. & Sullivan, P. (2002). Large eddy simulation. *Encyclopedia of Atmospheric Sciences*, **1140**, 1150.

Mohammadi, B. & Pironneau, O. (1993). Analysis of the k-epsilon turbulence.

Moin, P. & Mahesh, K. (1998). Direct numerical simulation: a tool in turbulence research. *Annual review of fluid mechanics*, **30**, 539–578.

Mukerjee, S.K., Rao, G.A.R., Dehadraya, J.V., Vaidya, V.N., Venugopal, V. & Sood, D.D. (1994). The oxidation of uranium monocarbide microspheres. *Journal of Nuclear Materials*, **210**, 97–106.

Murbach, E. & Turner, W. (1962). Oxidation of uranium carbide by carbon dioxide. Tech. rep., Atomics International. Div. of North American Aviation, Inc., Canoga Park, Calif.

Naito, K., Kamegashira, N., Kondo, T. & Takeda, S. (1976). Isothermal oxidation, of uranium monocarbide powder under controlled oxygen partial pressures. *Journal of Nuclear Science and Technology*, **13**, 260–267.

Nawada, H.P., Murti, P.S., Seenivasan, G., Anthonysamy, S. & Mathews, C.K. (1989). Thermogravimetric study of the oxidation behaviour of uranium dicarbide. *Journal of thermal analysis*, **35**, 1145–1155.

Nayak, S., Srinivasan, T., Vasudeva Rao, P. & Mathews, C. (1988). Photochemical destruction of organic compounds formed during dissolution of uranium carbide in nitric acid. *Separation Science and Technology*, **23**, 1551–1561.

Nolan, G. & Kavanagh, P. (1992). Computer simulation of random packing of hard spheres. *Powder Technology*, **72**, 149 – 155.

Nolan, G. & Kavanagh, P. (1995). Random packing of nonspherical particles. *Powder Technology*, **84**, 199 – 205.

Oakley, O.H., Constantinides, Y., Navarro, C. & Holmes, S. (2005). Modeling vortex induced motions of spars in uniform and stratified flows. In *ASME 2005 24th International Conference on Offshore Mechanics and Arctic Engineering*, 885–894, American Society of Mechanical Engineers.

Park, J.Y. & Lee, Y.N. (1988). Solubility and decomposition kinetics of nitrous acid in aqueous solution. *The Journal of Physical Chemistry*, **92**, 6294–6302.

Pauson, P.L., Clelland, W.J. & McLean, J. (1963). Acid leaching of uranium and thorium carbides. *Nature*, **197**.

Peakall, K.A. & Antill, J.E. (1962). Oxidation of uranium monocarbide. *Journal of the Less Common Metals*, **4**, 426–435.

Pillai, C.G.S., Dua, A.K. & Raj, P. (2001). Thermal conductivity of U_3O_8 from 300 to 1100K. *Journal of Nuclear Materials*, **288**, 87–91.

Popov, M.M. & Ivanov, M.I. (1957). Heats of formation of PuO_2 and U_3O_8. *The Soviet Journal of Atomic Energy*, **2**, 439–443.

Ramanujam, A. (2001). *Purex and Thorex Processes (Aqueous Reprocessing)*, 7918–7924. Elsevier Ltd.

Ranz, W.E. & Marshall, W.R. (1952). Evaporation from drops: Part 1. *Chemical Engineering Progress*, **48**, 141–146.

Rowe, P.N., Klaxton, K.T. & Lewis, J.B. (1965). Heat and mass transfer from a single sphere in an extensive flowing fluid. *Chemical Engineering Research and Design*, **43a**, 14–31.

Royal Society (2011). Fuel cycle stewardship in a nuclear renaissance. Tech. rep., The Royal Society: London.

Rundle, R.E., Baenziger, N.C., Wilson, A.S. & McDonald, R.A. (1948). The structures of the carbides, nitrides and oxides of uranium1. *Journal of the American Chemical Society*, **70**, 99–105.

Rwifa, S.B. (2000). *Mean voidage and momentum transfer in packed beds*. Ph.D. thesis.

Safari, V., Arzpeyma, G., Rashchi, F. & Mostoufi, N. (2009). A shrinking particleshrinking core model for leaching of a zinc ore containing silica. *International Journal of Mineral Processing*, **93**, 79 – 83.

Scott, C.D. (1966). Analysis of combustion of graphite-uranium fuels in a fixed bed or moving bed. *Industrial & Engineering Chemistry Process Design and Development*, **5**, 223–233.

Sieder, E.N. & Tate, G.E. (1936). Heat transfer and pressure drop of liquids in tubes. *Industrial & Engineering Chemistry*, **28**, 1429–1435.

Simms, D.A., Hand, M., Fingersh, L. & Jager, D. (1999). *Unsteady aerodynamics experiment phases II-IV test configurations and available data campaigns*. National Renewable Energy Laboratory.

Smagorinsky, J. (1963). General circulation experiments with the primitive equations: I. the basic experiment*. *Monthly weather review*, **91**, 99–164.

Smith, G.D. (1965). *Numerical Solution of Partial Differential Equations*. Oxford University Press.

Smith, J.M. (1970). *Chemical Engineering Kinetics*. McGraw-Hill.

Soll, W., Chen, S., Eggert, K., Grunau, D. & Janecky, D. (1994). Application of the lattice boltzmann/lattice gas technique to multi-fluid flow in porous media. Tech. rep., Los Alamos National Lab., NM (United States).

Soppe, W. (1990). Computer simulation of random packings of hard spheres. *Powder Technology*, **62**, 189 – 197.

Sowden, R.G., Hodge, N., Moreton-Smith, M.J. & White, D.B. (1964). *Carbides in Nuclear Energy*. Macmillan & Co Ltd.

Spaid, M.A. & Phelan Jr, F.R. (1997). Lattice boltzmann methods for modeling microscale flow in fibrous porous media. *Physics of Fluids (1994-present)*, **9**, 2468–2474.

Speziale, C.G. (1991). Analytical methods for the development of reynolds-stress closures in turbulence. *Annual review of fluid mechanics*, **23**, 107–157.

Storms, E.K. & Huber Jr, E.J. (1967). The heat of formation of uranium carbide. *Journal of Nuclear Materials*, **23**, 19–24.

Structure Vision Ltd. (2012). *DigiTherm^{TM} Release 2 Users Guide*.

Structure Vision Ltd. (2013). *DigiDiss^{TM} Release 2 Users Guide*.

Succi, S., Foti, E. & Higuera, F. (1989). Three-dimensional flows in complex geometries with the lattice Boltzmann method. *EPL (Europhysics Letters)*, **10**, 433.

Tsubokura, M., Kobayashi, T., Taniguchi, N. & Jones, W. (2003). A numerical study on the eddy structures of impinging jets excited at the inlet. *International journal of heat and fluid flow*, **24**, 500–511.

Tu, J., Yeoh, G.H. & Liu, C. (2008). *Computational Fluid Dynamics - A Practical Approach*. Elsevier.

Wadell, H. (1935). Volume, shape, and roundness of quartz particles. *The Journal of Geology*, **43**, pp. 250–280.

Webb, M. & Davis, I.L. (2006). Random particle packing with large particle size variations using reduced-dimension algorithms. *Powder Technology*, **167**, 10 – 19.

Xu, C., Jia, X., Williams, R., Stitt, E., Nijemeisland, M., El-Bachir, S., Sederman, A. & Gladden, L. (2006). Property predictions for packed columns using random and distinct element digital packing algorithms. In *Fifth World Congress on Particle Technology, Orlando, FL*, Citeseer.

Zhao, S., Mei, G., Sun, J., Yang, W. & Xie, Z. (2012). Estimation of Effective Diffusion Coefficient of Gaseous Species in MgO-C Refractories by Shrinking Core Model. *ISIJ INTERNATIONAL*, **52**, 1186–1195.